UNIVERSITÀ DEGLI STUDI DI PADOVA

Dipartimento di Fisica e Astronomia "Galileo Galilei"

Corso di Laurea Magistrale in Fisica

Tesi di Laurea

Probing Gravitational-Wave Extra Polarizations

with Ground-Based Interferometers

Relatore   Laureando

Prof. Nicola Bartolo   Loris Amalberti

Correlatore

Dr. Angelo Ricciardone

Anno Accademico 2019/2020

A mia madre Roberta e a mio padre Luca.

Contents

Introduction

Gravitational waves (GWs) were predicted by Albert Einstein in 1916 in his theory of General Relativity (GR), which is still considered to be the most accurate and well-tested theory of gravitation we have today. This prediction became truth in 2016, when it was announced that gravitational waves from the merging of a binary black hole system were directly observed by the LIGO-Virgo collaboration for the first time [1], opening up new horizons to allow us to better understand our Universe. At the same time, the last century saw the rise (and possibly fall) of a wide number of theories of gravitation alternative to General Relativity. Since GR gives such a valid description of gravity, most of these alternatives today are not meant to completely replace Einstein's theory, but rather to extend it by focusing on scales far beyond those where it has been correctly tested, such as the solar system scale, and/or considering different stages of our Universe, with modifications motivated by other branches of physics, such as cosmology and particle physics. Such alternative theories of gravity do indeed feature some specific predictions that can distinguish them from GR. In particular when generic metric theories of gravity are considered, at most 6 gravitational wave polarization modes are allowed and classified as follows: 2 tensor modes (usually called plus and cross), already predicted by GR, 2 scalar modes (called breathing and longitudinal) and 2 vector modes (called vector-x and vector-y). Therefore the importance of testing for the presence of such extra-polarization modes is clear: if they are detected new physics is discovered and alternative theories need to be taken into account. The possibility to perform such a test with present and future ground-based interferometers is the focus of this Thesis.

Detectors which aim to detect gravitational waves are ground-based interferometers on Earth and future space-based interferometers. Ground-based are usually distinguished in 2nd-generation detectors, such as Advanced LIGO [8, 9] (which includes both observatories in Hanford and Livingston in North America), Advanced VIRGO [10] in Italy and KAGRA [11] in Japan, and future 3rd-generation interferometers, such as Einstein Telescope (ET) [14, 15] and Cosmic Explorer (CE) [16], which are expected to begin their operations in the 2030's. All these detectors exploit the basic functioning of a Michelson interferometer,

although they are built with high-finesse Fabry–Pérot resonant arm cavities and adopt signal recycling systems to extend light travel-time along the arms, thus its interaction with gravitational waves. While working with these kind of interferometers, the biggest problem arises from the fact that gravitational waves are very weak and it is very difficult for us to separate their true signal from the detector noise. As far as spaceborne interferometers are concerned we can mention the Laser Interferometer Space Antenna (LISA) [12, 13] that will be launched in the 2030's.

The Thesis is structured as follws. In the first chapter of this thesis, we give a short introduction about the theory of GR and we show how gravitational waves arise from linear perturbations of the metric tensor. We further introduce the reader to some of the most popular alternative theories of gravity and we briefly show how they are generated by introducing additional scalar/vector fields that mediate gravity and modifying the gravitational action from which field equations are obtained. Then we consider a Cosmological Stochastic Gravitational Wave Background (SGWB) involving a mixture of all possible tensor, vector and scalar polarization modes and we list its properties. In particular, the Cosmological Background is among the target of upcoming 3rd-generation detectors.

In the second chapter we analyze detection techniques for the SGWB exploiting ground-based interferometers. Initially, we investigate how detector responses significantly vary depending on both detector geometry and incoming gravitational wave frequency: in particular we show how for sufficiently low values of the latter the response is frequency independent. Whenever this condition is no longer valid, detector responses have to account for transfer functions, which in general depend on both detector geometry and GW frequency. Transfer functions show different behaviours for Michelson and Fabry-Pèrot inteferometers, althoug their presence always implies detector sensitivity losses above some critical frequency. Since in realistic situations GWs are very hard to distinguish from detector background noises, we proceed by covering the issue of detector correlation which allows to match two detector outputs to "filter" true GW signals. The measure of correlation between two interferometers with different locations and orientations is given by overlap reduction functions: these key objects are different for tensor, vector and scalar polarization modes respectively and while considering correlations between two detectors in this work we always provide their plots. Finally, we show how three detector networks can be exploited in order to separate stochastic background energy density contributions for tensor, vector and scalar modes using 2nd-generation interferometers.

In the third and last chapter we focus on future ground-based detector Einstein Telescope. We investigate some of its properties derived by its proposed triangular configuration with three interferometers in order to understand its benefits in terms of sensitivity to gravitational waves. After considering detector networks involving both 2nd-generation interferometers and the Einstein Telescope, we mainly focus on the interplays between the latter and the Cosmic Explorer: we find that detector networks involving 3rd-generation interferometers improve sensitivity to the SGWB roughly by a factor of 10^3 for each polarization mode with respect to the old generation. In the context of GW polarization modes separation,

we show how the Einstein Telescope alone cannot exploit its three detectors to distinguish energy density contributions to the SGWB from tensor, vector and scalar modes, thus only two ET interferometers can be considered to work independently in a network. Finally we show a possible method to break the existing degeneracy between breathing and longitudinal polarization modes exploiting both the Einstein Telescope and the Cosmic Explorer, which are expected to be sensitive to higher frequencies with respect to current interferometers.

Chapter 1

Gravitational Waves and Stochastic Backgrounds

Since 2016 binary mergers have been observed [2, 3, 4, 5, 6] by LIGO and Virgo through gravitational waves (GWs) detection. Therefore, in this chapter we wish to give the reader a basic introduction to Einstein's theory of General Relativity (GR) to better understand how GWs emerge and what are their properties. Defining a particular gauge choice, this can be achieved by "perturbing" the flat Minkowski spacetime metric and subsequently linearizing Einstein field equations to obtain a wave equation. It is a well-known result that GR predicts the existence of *plus* and *cross* polarization modes; however standard tools of GR such as the geodesic equation and the geodesic deviation equation allow us to understand how four independent extra polarization modes may ultimately arise. Moreover, alternative theories of gravitation might predict the existence of such modes, thus measuring GW polarizations provide a useful tool to test gravity. It turns out that more than one possible GW source exists: in this work we focus on a Cosmological Stochastic Gravitational Wave Background (SGWB). In direct analogy with the Cosmic Microwave Background [17, 69] for electromagnetic radiation, the detection of such background would give us information on the primordial phase of our Universe, possibly up to the inflation time scale [19, 25, 26, 27].

1.1 Gravitational Waves in General Relativity

We consider our spacetime to be a 4-dimensional manifold on which we set a generic coordinate system $x^\mu = (x^0, x^1, x^2, x^3)$; we further assume $g_{\mu\nu}(x)$ to be the metric tensor through which we define the line element

$$ds^2 = g_{\mu\nu}dx^\mu dx^\nu. \tag{1.1.1}$$

To understand how GWs are produced in GR, we follow [72] and we begin writing down the gravitational action

$$S = S_{EH} + S_M(\psi_M, g_{\mu\nu}), \tag{1.1.2}$$

where

$$S_{EH} = \frac{c^3}{16\pi G_N} \int d^4x \sqrt{-g} R, \tag{1.1.3}$$

is the Einstein-Hilbert action, S_M is the matter action which couples the matter field ψ_M to the metric tensor, g is determinant of the metric tensor, c is the speed of light and G_N is Newton's gravitational constant. The key object used in GR to measure the local spacetime curvature is the Riemann tensor

$$R_{\mu\nu}{}^{\rho}{}_{\sigma} = \partial_\mu \Gamma^{\rho}_{\nu\sigma} - \partial_\nu \Gamma^{\rho}_{\mu\sigma} + \Gamma^{\rho}_{\mu\alpha}\Gamma^{\alpha}_{\nu\sigma} - \Gamma^{\rho}_{\nu\alpha}\Gamma^{\alpha}_{\mu\sigma}, \tag{1.1.4}$$

where we have introduced the Christoffel symbols

$$\Gamma^{\rho}_{\mu\nu} = \frac{1}{2}g^{\rho\sigma}\left(\partial_\mu g_{\nu\sigma} + \partial_\nu g_{\mu\sigma} - \partial_\sigma g_{\mu\nu}\right), \tag{1.1.5}$$

and $g_{\mu\nu}$ are the metric tensor entries. The Ricci tensor and the Ricci scalar are then given by the following contractions

$$R_{\mu\nu} = R_{\alpha\mu}{}^{\alpha}{}_{\nu}, \qquad R = g^{\mu\nu}R_{\mu\nu}. \tag{1.1.6}$$

Einstein field equations are obtained taking the variation of the gravitational action with respect to the inverse metric and together they represent a tensorial equation that relates the metric tensor with matter

$$R_{\mu\nu} - \frac{1}{2}g_{\mu\nu}R = \frac{8\pi G}{c^4}T_{\mu\nu}, \tag{1.1.7}$$

where $T_{\mu\nu}$ is the stress-energy tensor. These equations are often written down this way to underline the fact that the left hand-side term gives us geometrical informations about the spacetime and its curvature, while the right-hand side term tells us informations about the gravitational field source. If no matter is present, then $T_{\mu\nu} = 0$ and Eq. (1.1.7) reduces[1] to

$$R_{\mu\nu} = 0, \tag{1.1.8}$$

which are the vacuum Einstein field equations. Gravitational waves are found by considering Einstein field equations in the *weak field limit* [20], which is valid when we consider nearly flat regions spacetime, meaning we can decompose the metric tensor as a sum of two terms

$$g_{\mu\nu} = \eta_{\mu\nu} + h_{\mu\nu}(x), \qquad |h_{\mu\nu}| \ll 1, \tag{1.1.9}$$

---

[1] We have $R_{\mu\nu} - \frac{1}{2}g_{\mu\nu}R = 0$, thus considering the contraction with the inverse metric tensor we get $g^{\mu\nu}(R_{\mu\nu} - \frac{1}{2}g_{\mu\nu}R) = R - 2R = -R = 0$.

where

$$\eta_{\mu\nu} = \begin{pmatrix} -1 & 0 & 0 & 0 \\ 0 & 1 & 0 & 0 \\ 0 & 0 & 1 & 0 \\ 0 & 0 & 0 & 1 \end{pmatrix}, \tag{1.1.10}$$

is the Minkowski metric for a flat spacetime, while $h_{\mu\nu}$ is the perturbative term which denotes small deviations from it. Under these assumptions, we wish to solve Eq. (1.1.8). Since the gravitational field is weak, we are justified to neglect all 2nd or higher order terms in $h_{\mu\nu}$ while computing all the quantities we need. This means that Christoffel symbols become

$$\Gamma^{\mu}_{\nu\rho}(h) = \frac{1}{2}\eta^{\mu\sigma}\left(\partial_{\nu}h_{\rho\sigma} + \partial_{\rho}h_{\nu\sigma} - \partial_{\sigma}h_{\nu\rho}\right) + \mathcal{O}(h^2), \tag{1.1.11}$$

and the vacuum field equations become

$$R_{\mu\nu}(h) = R_{\alpha\mu}{}^{\alpha}{}_{\nu}(h) = \partial_{\alpha}\Gamma^{\alpha}_{\mu\nu}(h) - \partial_{\mu}\Gamma^{\alpha}_{\alpha\nu}(h) + \mathcal{O}(h^2)$$
$$= \frac{1}{2}\left(\partial_{\mu}\partial^{\nu}h_{\alpha\nu} + \partial_{\nu}\partial^{\alpha}h_{\mu\alpha} - \partial_{\alpha}\partial^{\alpha}h_{\mu\nu} - \partial_{\mu}\partial_{\nu}h^{\alpha}_{\alpha}\right) + \mathcal{O}(h^2) = 0. \tag{1.1.12}$$

Notice that the perturbative term $h_{\mu\nu}(x)$ depends on the frame of reference we choose and if we wish to decompose the metric tensor we need Eq.(1.1.9) to hold on sufficiently large regions of spacetime. Inside these regions, we can always consider an infinitesimal coordinate transformation $\tilde{x}^{\mu} = x^{\mu} + \epsilon^{\mu}$, with $|\epsilon^{\mu}| = \mathcal{O}(h)$, thus the metric tensor transforms as

$$g_{\mu\nu} = \frac{\partial\tilde{x}^{\rho}}{\partial x^{\mu}}\frac{\partial\tilde{x}^{\sigma}}{\partial x^{\nu}}\tilde{g}_{\rho\sigma}$$
$$= (\delta^{\rho}_{\mu} + \partial_{\mu}\epsilon^{\rho})(\delta^{\sigma}_{\nu} + \partial_{\nu}\epsilon^{\sigma})\tilde{g}_{\rho\sigma}, \tag{1.1.13}$$

where $\tilde{g}_{\rho\sigma}$ is the metric tensor in the new frame of reference, which we rewrite as

$$\tilde{g}_{\mu\nu} = \eta_{\mu\nu} + \tilde{h}_{\mu\nu}(x), \qquad |\tilde{h}_{\mu\nu}| \ll 1. \tag{1.1.14}$$

This means that if we move to another frame of reference describing the same physical problem, we get the following relation between the two perturbative terms

$$\tilde{h}_{\mu\nu} = h_{\mu\nu} - \partial_{\mu}\epsilon_{\nu} - \partial_{\nu}\epsilon_{\mu} = h_{\mu\nu} - \delta h_{\mu\nu}. \tag{1.1.15}$$

This is the manifestation of the well known Gauge invariance[2] in the context of GR. To get rid of this freedom, we choose the x^{μ} coordinate system and we fix the gauge by picking the *de Donder gauge* [], which states

$$D^{\mu}D_{\mu}x^{\nu} = 0 = -g^{\rho\sigma}\Gamma^{\nu}_{\rho\sigma}, \tag{1.1.16}$$

---

[2]In electromagnetism the Gauge invariance denotes the transformation $A_{\mu} \to A_{\mu} + \partial_{\mu}f$, with f scalar function, which leaves the electromagnetic tensor $F_{\mu\nu} = \partial_{\mu}A_{\nu} - \partial_{\nu}A_{\mu}$ invariant. Similarly, in General Relativity metric perturbations related by Eq.(1.1.15) satisfy $\delta R_{\mu\nu}{}^{\rho}{}_{\sigma} = 0$, leaving the linearized Riemann tensor invariant.

where D_μ is the covariant derivative, which acts on covariant and contravariant vectors as

$$D_\mu V^\nu = \partial_\mu V^\nu + \Gamma^\nu_{\mu\rho} V^\rho, \qquad D_\mu V_\nu = \partial_\mu V_\nu - \Gamma^\rho_{\mu\nu} V_\rho. \tag{1.1.17}$$

It is straightforward to see that Eqs.(1.1.11) and (1.1.16) lead us to

$$\partial^\mu h_{\mu\nu} - \frac{1}{2}\partial_\nu h = 0, \tag{1.1.18}$$

where we have defined $h = h^\alpha_\alpha$, and from Eq.(1.1.12) we get

$$\begin{cases} \partial^\alpha \partial_\alpha h_{\mu\nu} = 0 \\ \partial^\mu h_{\mu\nu} - \frac{1}{2}\partial_\nu h = 0 \end{cases}. \tag{1.1.19}$$

In literature, the object $\bar{h}_{\mu\nu} = h_{\mu\nu} - \frac{1}{2}\eta_{\mu\nu}h$ called *trace-reversed* perturbation is often used to get the following system

$$\begin{cases} \partial^\alpha \partial_\alpha \bar{h}_{\mu\nu} = 0 \\ \partial^\mu \bar{h}_{\mu\nu} = 0 \end{cases}, \tag{1.1.20}$$

where the first expression is the plane wave equation and the second one is the result of the de Donder gauge condition. This system obviously admits plane waves as elementary solutions, so we have

$$\bar{h}_{\mu\nu} = C_{\mu\nu} e^{ik_\rho x^\rho}, \tag{1.1.21}$$

with the 4-momentum $k^2 = k^\mu k_\mu = 0$, suggesting that GWs travel at the speed of light, while the de Donder gauge condition gives us

$$k^\mu C_{\mu\nu} = 0, \tag{1.1.22}$$

with $C_{\mu\nu} = C_{\nu\mu}$ due to the metric tensor being simmetric, meaning we are now left with 6 degrees of freedom, starting from the possible initial 16. If we perform an infinitesimal coordinate transformation $x'^\mu = x^\mu + \epsilon^\mu$ we can still take the de Donder gauge condition to be valid as long as $D^\mu D_\mu \epsilon^\nu = 0$ is also satisfied and admits a solution $\epsilon_\mu = G_\mu e^{ik_\rho x^\rho}$. We rewrite Eq.(1.1.15) using the trace reversed perturbation to get

$$\bar{h}'_{\mu\nu} = \bar{h}_{\mu\nu} - \partial_\mu \epsilon_\nu - \partial_\nu \epsilon_\mu + \eta_{\mu\nu}\partial_\alpha \epsilon^\alpha, \tag{1.1.23}$$

which in terms of plane wave solutions gives us

$$\begin{aligned} C'_{\mu\nu} &= C_{\mu\nu} - ik_\mu G_\nu - ik_\nu G_\mu + i\eta_{\mu\nu}k_\alpha G^\alpha \\ &= \tilde{C}_{\mu\nu} + i\delta C_{\mu\nu}. \end{aligned} \tag{1.1.24}$$

Let us finally find the degrees of freedom of GWs in GR. We can set $c = 1$ for simplicity, thus the wave vector $k^\mu = \omega(1, 0, 0, 1)^T$ [3] denotes a GW propagating along the z-axis: with this specific choice, from $k^\mu C_{\mu\nu} = 0$ we get

$$C_{3\mu} = -C_{0\mu}. \tag{1.1.25}$$

---

[3]The dispersion relation for plane waves propagating at the speed of light in vacuum is $\omega = ck$.

We now proceed by choosing G^μ in order to fix $C_{0\mu} = 0 = C_{3\mu}$ in Eq.(1.1.24), we have

$$
\begin{aligned}
\delta C_{00} &= G_3 - G_0 = -\delta C_{03} \\
\delta C_{01} &= -G_1 = -\delta C_{31} \\
\delta C_{02} &= -G_2 = -\delta C_{32} \\
\delta C_{12} &= 0 \\
\delta C_{33} &= G_3 - G_0 \\
\delta C_{11} &= -(G_0 + G_3) = \delta C_{22},
\end{aligned}
\tag{1.1.26}
$$

and we can set $(G_3 - G_0)$ to fix $C'_{00} = C'_{03} = C'_{33} = 0$, G_1 to fix $C'_{01} = C'_{31} = 0$ and G_2 to fix $C'_{02} = C'_{32} = 0$. In the end we consider the object[4] $\delta(C^\mu_\mu) = -2(G_0 + G_3)$ and we set it to fix $C'^\mu_\mu = 0$, which implies $C'_{11} = -C'_{22}$. With no gauge freedom left to exploit, we rename $C' \equiv C$ and the only nonzero components are then C_{11}, C_{12}, C_{21} and C_{22} for the traceless and symmetric tensor $C_{\mu\nu}$, which can be written as

$$
C_{\mu\nu} = \begin{pmatrix} 0 & 0 & 0 & 0 \\ 0 & C_{11} & C_{12} & 0 \\ 0 & C_{12} & -C_{11} & 0 \\ 0 & 0 & 0 & 0 \end{pmatrix}.
\tag{1.1.27}
$$

In the end we are left with only 2 degrees of freedom. C_{11} and C_{22} completely characterize a GW propagating at the speed of light along the z-axis and correspond to the *plus* and *cross* polarization modes represented in the *transverse traceless gauge*, since the metric perurbation is traceless and perpendicular to the wave vector [72]. The metric tensor in Eq. (1.1.9) can now be written as

$$
g_{\mu\nu} = \begin{pmatrix} 1 & 0 \\ 0 & \delta_{ij} + h_{ij} \end{pmatrix},
\tag{1.1.28}
$$

where we have defined

$$
h_{ij} = \begin{pmatrix} C_{11} & C_{12} & 0 \\ C_{12} & -C_{11} & 0 \\ 0 & 0 & 0 \end{pmatrix} \operatorname{Re}(e^{ik_\rho x^\rho}),
\tag{1.1.29}
$$

which is the expression of the perturbation term in the *transverse-traceless gauge*, while the line element in Eq.(1.1.1) becomes

$$
\begin{aligned}
ds^2 = -dt^2 + dz^2 &+ \big(1 + C_{11}\cos\omega(t-z)\big)dx^2 + \big(1 - C_{11}\cos\omega(t-z)\big)dy^2 + \\
&+ 2C_{12}\big(\cos\omega(t-z)\big)dxdy.
\end{aligned}
\tag{1.1.30}
$$

---

[4]Recall we have just fixed $C'_{00} = C'_{33} = 0$.

Since Eqs.(1.1.19) still hold, h_{ij} satisfies the plane wave equation, meaning that superpositions of elementary solutions of the equation are still solutions. This means that the spatial part of the tensorial perturbation can be written down as

$$h_{ij}(t,\bar{\mathbf{x}}) = \sum_{A=+,\times} \int_{-\infty}^{+\infty} df \int_{S^2} d\Omega \big(\tilde{\mathbf{e}}_{ij}^A(\hat{\boldsymbol{\Omega}}) h_A(f,\hat{\boldsymbol{\Omega}})\big) e^{i2\pi f(t-\hat{\boldsymbol{\Omega}}\cdot\frac{\bar{\mathbf{x}}}{c})}, \qquad (1.1.31)$$

where $\hat{\boldsymbol{\Omega}}$ denotes the GW direction, amplitudes $h_A(f,\hat{\boldsymbol{\Omega}})$ are complex functions satisfying $h_A(-f,\hat{\boldsymbol{\Omega}}) = h_A^*(f,\hat{\boldsymbol{\Omega}})$ due to the reality of $h_{ij}(t,\bar{\mathbf{x}})$, $\tilde{\mathbf{e}}_{ij}^A \tilde{\mathbf{e}}_{A'}^{ij} = 2\delta_{AA'}$ and we restored the constant c. Although plus and cross polarization modes are the only one predicted by GR, we shall see in the next section how in alternative metric theories other modes are expected to exist and how it turns out that as long as we are in the weak field limit the metric tensor can be decomposed as in Eq.(1.1.28) with a different form for h_{ij}.

1.2 Gravitational Waves in Alternative Metric Theories of Gravity

Since GR was developed many observations have confirmed its correctness [21, 22, 23, 24]. However, when alternative metric theories of gravity are considered, other polarization modes might appear and, if these theories happen to be accurate, they might lead us to new physical considerations and results, causing an inevitable extension of GR. In this section we wish to give a simple and useful introduction to extra polarization modes by showing how they arise and affect test particles, while in the next section we show a few examples of alternative theories.

Freely-falling particles in a curved spacetime move along curves called geodesics, which represent the particle worldlines minimising the distance between two points. The evolution of a particle path $x^\mu(\tau)$ is dictated by the *geodesic equation*

$$\frac{d^2 x^\mu}{d\tau^2} + \Gamma^\mu_{\nu\rho} \frac{dx^\nu}{d\tau} \frac{dx^\rho}{d\tau} = 0, \qquad (1.2.1)$$

where the equality holds if τ is an affine parameter. We begin by considering nearby geodesics [45] for two massive test particles in a general, possibly curved, 4 dimensional spacetime and we identify them as $x^\mu(\tau_x)$ and $y^\mu(\tau_y)$, where $\tau_{x,y}$ denotes each particle proper time. Once we evaluate both geodesics for a specific value $\tau = \tau_x = \tau_y$, we can define

$$\epsilon^\mu(\tau) = y^\mu(\tau) - x^\mu(\tau), \qquad (1.2.2)$$

which gives a measure of how the two geodesics approach or deviate from each other; to be more precise, we need to evaluate $\epsilon^\mu(\tau)$ along one of the two geodesics, say $x^\mu(\tau)$, so that it represents the deviation of the second geodesic from the first one. Assuming this is the

case, we wish to study how this deviation evolves in terms of proper time. To simplify the
computation, we choose locally flat coordinates along $x^\mu(\tau)$, thus we have

$$\partial_\mu g_{\nu\rho}(x(\tau)) = 0 \implies \Gamma^\rho_{\mu\nu}(x(\tau)) = 0, \tag{1.2.3}$$

and the geodesic equations for $x^\mu(\tau)$ and $y^\mu(\tau)$ become

$$\frac{d^2x^\mu}{d\tau^2} = 0, \qquad \frac{d^2y^\mu}{d\tau^2} + \Gamma^\mu_{\nu\rho}(y)\frac{dy^\nu}{d\tau}\frac{dy^\rho}{d\tau} = 0, \tag{1.2.4}$$

while ϵ^μ satisfies

$$\begin{aligned}
\frac{d^2\epsilon^\mu}{d\tau^2} &= \frac{d^2y^\mu}{d\tau^2} - \frac{d^2x^\mu}{d\tau^2} = \frac{d^2y^\mu}{d\tau^2} \\
&= -\Gamma^\mu_{\nu\rho}(x+\epsilon)\frac{d(x+\epsilon)^\nu}{d\tau}\frac{d(x+\epsilon)^\rho}{d\tau} \\
&= -\epsilon^\sigma\partial_\sigma\Gamma^\mu_{\nu\rho}(x)\frac{dx^\nu}{d\tau}\frac{dx^\rho}{d\tau} + \mathcal{O}(\epsilon^2).
\end{aligned} \tag{1.2.5}$$

In the context of GR, we are interested in the evolution of vectors along geodesics, thus we
need the covariant derivative to accurately describe the evolution of the deviation vector

$$\begin{aligned}
\frac{D^2\epsilon^\mu}{D\tau^2} &= \frac{d^2\epsilon^\mu}{d\tau^2} + \frac{dx^\sigma}{d\tau}\partial_\sigma\Gamma^\mu_{\nu\rho}(x)\frac{dx^\nu}{d\tau}\epsilon^\rho \\
&= \left(-\partial_\sigma\Gamma^\mu_{\nu\rho}(x) + \partial_\nu\Gamma^\mu_{\sigma\rho}(x)\right)\frac{dx^\nu}{d\tau}\frac{dx^\rho}{d\tau}\epsilon^\sigma \\
&= -R_{\sigma\nu}{}^\mu{}_\rho(x)\epsilon^\sigma\frac{dx^\nu}{d\tau}\frac{dx^\rho}{d\tau},
\end{aligned} \tag{1.2.6}$$

where in the final step we add $-\Gamma^\mu_{\sigma\alpha}\Gamma^\alpha_{\nu\rho}$ and $\Gamma^\mu_{\nu\alpha}\Gamma^\alpha_{\sigma\rho}$ to the quantity between parenthesis,
since in locally flat coordinates they are null. This way we obtained the *geodesic deviation
equation* in a covariant form, thus valid in any frame of reference. Since we are interested in
small perturbations of the metric, we consider once again the weak field limit and we wish to
see how particles initially at rest[5] are affected by a passing GW. Under these assumptions,
we decompose the spatial part of the metric tensor as

$$g_{ij} = \delta_{ij} + h_{ij}, \qquad i,j = 1,2,3. \tag{1.2.7}$$

and Eq.(1.2.6) reduces to

$$\frac{D^2\epsilon^i}{Dt^2} = -R_{j0}{}^i{}_0(h)\epsilon^j(\tau) = \left(\frac{\partial^2}{\partial t^2}h^{ij}(t)\right)\epsilon_j(t). \tag{1.2.8}$$

---

[5]Under these assumptions the 4-velocity of a stationary observer is $u^\mu = (1,0,0,0)^T$ and the proper
time τ coincides with the coordinate time t.

Recall that h_{ij} reduces to Eq.(1.1.29) in GR, but it might be different for alternative metric theories, where more than two polarization modes for GWs can exist. We also notice that gravitational waves are related to linearized Riemann tensor components R_{j0i0} (sometimes called "electric" components of the Riemann tensor), which can be used to identify their polarization states. If we take plane waves propagating along the z-axis at the speed of light, then the electric components are only functions of $\xi(t, z) = t - \frac{z}{c}$. It was pointed out in [41] by Newmann and Penrose that there exist only 6 algebraically independent components[6] of the Riemann tensor in vacuum, corresponding to the same amount of possible polarization modes; we use the same notation introduced in their paper and we follow [18] to manage these components in order to define the following 4 objects

$$
\begin{aligned}
\Psi_2(\xi) &= -\frac{1}{6}R_{z0z0} \\
\Psi_3(\xi) &= -\frac{1}{2}R_{x0z0} + \frac{i}{2}R_{y0z0} \\
\Psi_4(\xi) &= -R_{x0x0} + R_{y0y0} + i2R_{x0y0} \\
\Phi_{22}(\xi) &= -R_{x0x0} - R_{y0y0},
\end{aligned}
\tag{1.2.9}
$$

where $\Psi_{3,4}(\xi)$ are complex functions and can be seen as the sum of two real independent ones. We introduce the square matrix $Z_{ij} = R_{j0i0}$, which may be written as

$$
\mathbf{Z} = \begin{pmatrix}
-\frac{1}{2}(\mathrm{Re}\,\Psi_4 + \Phi_{22}) & \frac{1}{2}\mathrm{Im}\,\Psi_4 & -2Re\Psi_3 \\
\frac{1}{2}\mathrm{Im}\,\Psi_4 & \frac{1}{2}(\mathrm{Re}\,\Psi_4 - \Phi_{22}) & 2\,\mathrm{Im}\,\Psi_3 \\
-2\,\mathrm{Re}\,\Psi_3 & 2\,\mathrm{Im}\,\Psi_3 & -6\Psi_2
\end{pmatrix},
\tag{1.2.10}
$$

then, as in [42], we define[7]

$$
\begin{aligned}
q_1 &= -3\sqrt{2}\Psi_2, & q_2 &= -2\,\mathrm{Re}\,\Psi_3, \\
q_3 &= 2\,\mathrm{Im}\,\Psi_3, & q_4 &= -\frac{1}{2}\,\mathrm{Re}\,\Psi_4, \\
q_5 &= \frac{1}{2}\,\mathrm{Im}\,\Psi_4, & q_6 &= -\frac{1}{2}\Phi_{22},
\end{aligned}
\tag{1.2.11}
$$

---

[6]From R_{j0i0} they are R_{x0x0}, R_{x0y0}, R_{x0z0}, R_{y0y0}, R_{y0z0}, R_{z0z0}.
[7]The constants are choosen in a way to already obtain the normalization we want for the GW polarization tensors.

thus we can write $\mathbf{Z} = \sum_{n=1}^{6} q_{(n)} \tilde{\mathbf{e}}_{ij}^{(n)}$, where we have defined

$$
\tilde{\mathbf{e}}_{ij}^{(1)} = \sqrt{2} \begin{pmatrix} 0 & 0 & 0 \\ 0 & 0 & 0 \\ 0 & 0 & 1 \end{pmatrix} = \tilde{\mathbf{e}}_{ij}^{l}, \qquad
\tilde{\mathbf{e}}_{ij}^{(2)} = \begin{pmatrix} 0 & 0 & 1 \\ 0 & 0 & 0 \\ 1 & 0 & 0 \end{pmatrix} = \tilde{\mathbf{e}}_{ij}^{x},
$$

$$
\tilde{\mathbf{e}}_{ij}^{(3)} = \begin{pmatrix} 0 & 0 & 0 \\ 0 & 0 & 1 \\ 0 & 1 & 0 \end{pmatrix} = \tilde{\mathbf{e}}_{ij}^{y}, \qquad
\tilde{\mathbf{e}}_{ij}^{(4)} = \begin{pmatrix} 1 & 0 & 0 \\ 0 & -1 & 0 \\ 0 & 0 & 0 \end{pmatrix} = \tilde{\mathbf{e}}_{ij}^{+},
$$

$$
\tilde{\mathbf{e}}_{ij}^{(5)} = \begin{pmatrix} 0 & 1 & 0 \\ 1 & 0 & 0 \\ 0 & 0 & 0 \end{pmatrix} = \tilde{\mathbf{e}}_{ij}^{\times}, \qquad
\tilde{\mathbf{e}}_{ij}^{(6)} = \begin{pmatrix} 1 & 0 & 0 \\ 0 & 1 & 0 \\ 0 & 0 & 0 \end{pmatrix} = \tilde{\mathbf{e}}_{ij}^{b},
$$

$$\tag{1.2.12}$$

which constitute the bases of all the possible polarization tensors for a metric theory of gravity of a 4 dimensional spacetime. In particular, looking at $\tilde{\mathbf{e}}_{ij}^{(4)}$ and $\tilde{\mathbf{e}}_{ij}^{(5)}$ we have found once again the plus $(+)$ and cross $(\times)$ polarization modes predicted by GR, which can be grouped together as *tensor modes*. However, four additional modes appear: $\tilde{\mathbf{e}}_{ij}^{(2)}$ and $\tilde{\mathbf{e}}_{ij}^{(3)}$ are called respectively *vector-x* (x) and *vector-y* (y) modes, belonging to the *vector modes*, while $\tilde{\mathbf{e}}_{ij}^{(1)}$ and $\tilde{\mathbf{e}}_{ij}^{(6)}$ are called *longitudinal* (l) and *breathing* (b) modes and they form the *scalar modes*. Each polarization mode is orthogonal to all the other ones, meaning that $\tilde{\mathbf{e}}_{ij}^{A} \tilde{\mathbf{e}}_{A'}^{ij} = 2\delta_{AA'}$ with $A, A' = +, \times, x, y, b, l$; moreover tensor and vector polarizations are traceless, while the scalar ones are not. Besides the way they affect test particles as shown in Fig.1.1, we have that tensor, vector and scalar modes are also distinguished by their relative GW helicity values, which are respectively $s = \pm 2$, $s = \pm 1$ and $s = 0$.

1.3 Examples of Alternative Metric Theories of Gravity

Despite the fact that today GR is the best description we have for gravity, alternative metric theories of gravity have been developed in order to extend Einstein's theory and describe possible physical effects that GR cannot. In the context of gravitational waves, different theories allow the existence of specific polarization modes, meaning that GWs provide a very useful tool to test the correctness of the theory itself. In this section we first show some examples of alternative theories generated by introducing additional scalar or vector fields that mediate gravitational interactions besides the metric tensor, then we give a brief introduction to the so-called $f(R)$ and Quadratic Gravity theories.

Scalar-Tensor theories. Scalar-Tensor theories are based on the presence of an additional scalar field ϕ, besides the metric tensor $g_{\mu\nu}$ [48, 49]. The gravitational action is now replaced by

$$
S = \frac{1}{16\pi G} \int d^4 x \sqrt{-g} \left[\phi R - \frac{\omega(\phi)}{\phi} g^{\mu\nu}(\partial_\mu \phi)(\partial_\nu \phi) - U(\phi) \right] + S_M(\psi_M, g_{\mu\nu}), \tag{1.3.1}
$$

where $U(\phi)$ is the scalar field potential and $\omega(\phi)$ is a coupling function. We proceed in the same way we did for GR and we take the variation of this action with respect to the inverse metric and ϕ to get the field equations

$$R_{\mu\nu} - \frac{1}{2}g_{\mu\nu}R = \frac{8\pi G}{\phi}T_{\mu\nu} + \frac{\omega(\phi)}{\phi^2}\big[(\partial_\mu\phi)(\partial_\nu\phi) - \frac{1}{2}g_{\mu\nu}(\partial_\alpha\phi)(\partial^\alpha\phi)\big] + \frac{1}{\phi}(\partial_\mu\partial_\nu\phi - g_{\mu\nu}\Box\phi),$$
$$(1.3.2a)$$

$$\Box\phi = \frac{1}{3 + 2\omega(\phi)}\big[8\pi G_N g^{\mu\nu}T_{\mu\nu} - \frac{d\omega}{d\phi}(\partial_\alpha\phi)(\partial^\alpha\phi) + \frac{d}{d\phi}(\phi^2 U(\phi))\big],\qquad(1.3.2b)$$

where $\Box$ is the d'Alambertian operator and $T_{\mu\nu}$ is the stress-energy tensor. Another formulation of the theory can be provided by introducing the following transformation for the metric tensor

$$\tilde{g}_{\mu\nu} = \frac{\phi}{\phi_0}g_{\mu\nu},\qquad(1.3.3)$$

where ϕ_0 is a constant and represents the asymptotic value of the scalar field today. Thus we get the action

$$S = \frac{1}{16\pi\tilde{G}}\int d^4x\sqrt{-\tilde{g}}\big(\tilde{R} - \frac{3 + 2\omega(\phi)}{2\phi^2}\tilde{g}^{\mu\nu}(\partial_\mu\phi)(\partial_\nu\phi) - V(\phi)\big) + S_M(\psi_M, \phi^{-1}\tilde{g}_{\mu\nu}),\ (1.3.4)$$

where $\tilde{R}$ is the Ricci scalar obtained from $\tilde{g}_{\mu\nu}$, $\tilde{G}_N = \frac{G_N}{\phi_0}$ and $V(\phi) = \frac{\phi_0 U(\phi)}{\phi^2}$. Eq.(1.3.1) and Eq.(1.3.4) are two different representations of the same theory, which are called respectively *Jordan frame* and *Einstein frame* and are used for different purposes. One particular example among scalar-tensor theories is the *Brans-Dicke theory* [52], which forecasts a constant value of the coupling function $\omega(\phi) \equiv \omega_{BD}$ and reduces to GR in the limit $\omega \to \infty$. This theory predicts the existence of scalar polarization modes, GW detection can be a good way to investigate the problem.

Vector-Tensor theories.   Vector-Tensor theories provide the presence of a vector field B^μ and of the usual metric tensor $g_{\mu\nu}$ [50, 51]. This time the gravitational action is given by

$$S = \frac{1}{16\pi G_N}\int d^4x\sqrt{-g}\big((1+\omega B_\mu B^\mu)R - Q_{\alpha\beta}^{\mu\nu}(D_\mu B^\alpha)(D_\nu B^\beta) + \lambda(B_\mu B^\mu + 1)\big) + S_M(\psi_M, g_{\mu\nu}),$$
$$(1.3.5)$$

where

$$Q_{\alpha\beta}^{\mu\nu} = c_1 g^{\mu\nu}g_{\alpha\beta} + c_2\delta_\alpha^\mu\delta_\beta^\nu + c_3\delta_\beta^\mu\delta_\alpha^\nu - c_4 B^\mu B^\nu g_{\alpha\beta},\qquad(1.3.6)$$

with c_j, $j = 1, 2, 3$ arbitrary. Depending on a specific model of such theories, the vector field B^μ can be uncostrained or can be constrained to have unit norm. A particular example of (constrained) vector-tensor theory is the Einstein–æther one [54], which was introduced to explore the possible violation of Lorentz invariance in the context of gravity. Unconstrained theories instead are characterized by $\lambda = 0$ and an arbitrary parameter ω.

f(R) theories. $f(R)$ theories replace the Ricci scalar appearing in the Einstein-Hilbert action with a function of R itself [60, 61]. The gravitational action then becomes

$$S = \frac{1}{16\pi G_N} \int d^4x \sqrt{-g} f(R) + S_M(\psi_M, g_{\mu\nu}). \qquad (1.3.7)$$

These theories are often used in cosmology, where $f(R)$ is chosen in a way to explain the present accelerated expansion of the Universe on cosmological scales without taking into account the cosmological constant Λ or dark energy. Tipically this kind of theories are studied by substituing $f(R)$ with $f(\tau) - \frac{df(\tau)}{d\tau}(R - \tau)$, where τ is a scalar field, we can take the variation of the action with respect to τ to find $\tau = R$. Next, we set $\phi \equiv -\frac{df(\tau)}{d\tau}$ and it is possible to show that we obtain a scalar-tensor theory action with coupling function $\omega(\phi) = 0$ and potential defined from $\phi^2 U(\phi) = \phi\tau(\phi) - f(\tau(\phi))$ [44].

Quadratic Gravity and Chern-Simons theories. Quadratic gravity models add to Einstein-Hilbert action quadratic terms in R, $R_{\mu\nu}$, $R_{\mu\nu}{}^\rho{}_\sigma$, thus the gravitational action becomes [44]

$$S = \int d^4x \sqrt{-g} \{ \kappa R + \alpha_1 f_1(\phi) R^2 + \alpha_2 f_2(\phi) R_{\alpha\beta} R^{\alpha\beta} + \alpha_3 f_3(\phi) R_{\alpha\beta\gamma\delta} R^{\alpha\beta\gamma\delta} +$$

$$+ \alpha_4 f_4(\phi)(\frac{1}{2}\epsilon^{\gamma\delta\rho\sigma} R^\alpha_{\beta\rho\sigma} R^\beta_{\alpha\gamma\delta}) - \frac{\beta}{2} \big(g^{\mu\nu}(\partial_\mu\phi)(\partial_\nu\phi) + 2V(\phi) \big) \} + S_M(\psi_M, g_{\mu\nu}), \quad (1.3.8)$$

where $\kappa = \frac{1}{16\pi G_N}$, α_i are coupling constants, ϕ is a scalar field and β is a constant. Different values of α_i and β corresponds to different theories: in the special case of $\alpha_1 = \alpha_2 = \alpha_3 = 0$ we recover the so-called *Chern-Simons* gravity theory [58]. This may appear from anomaly cancellation schemes in the standard model, from string theory, or from quantum loop gravity [70, 71].

There is a wide number of metric theories of gravity in addition to the ones we briefly discussed, although it is not in our interest to list all of them. We have just shown how in the last century alternative models beyond GR were introduced and how we can exploit GWs as a tool to test them. In Tab.2.1 we give some references and some properties about such models.

1.4 Cosmological and Astrophysical Stochastic Backgrounds

A stochastic background of gravitational waves (SGWB) [72, 7] is defined as a superposition of waves, the general direction of which is given by the unit vector $\hat{\mathbf{\Omega}}$, and is expected to be produced by a wide number of independent and unresolved astrophysical sources and by cosmological sources ([43, 73]). In the context of SGWB of cosmological origin we are interested in primordial GW production processes,
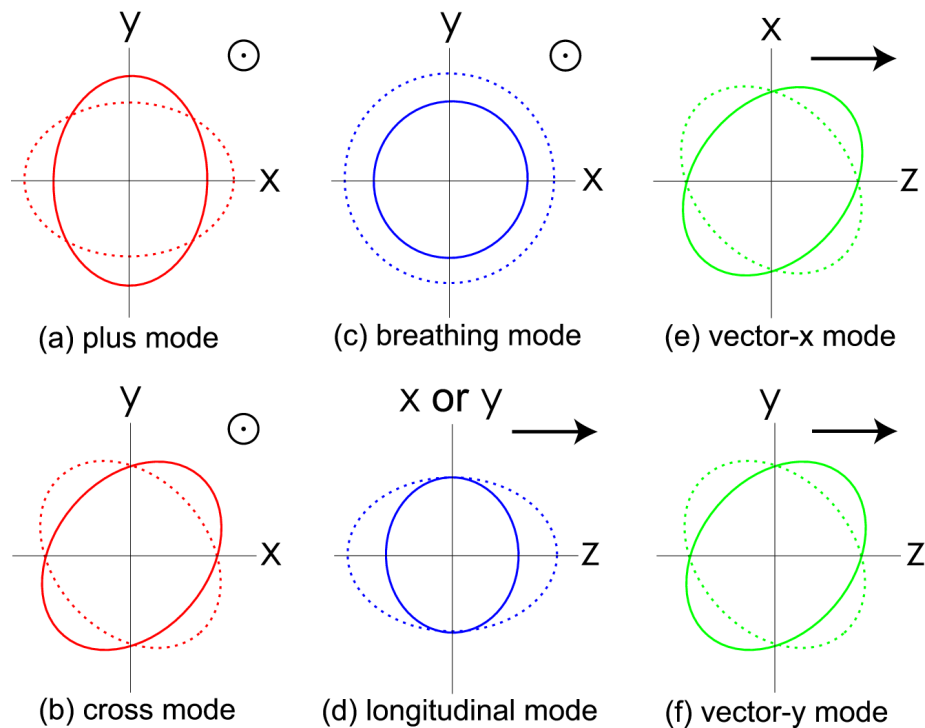
Figure 1.1: Effects of passing GWs on test masses. The symbols $\odot$ and $\rightarrow$ denote the propagating direction of the GW, while its effects on test masses are shown by the two ellipses/circles. This picture was taken from [86].

Gravitational theory	Gravitational fields	$\tilde{\mathbf{e}}_{ij}^{+}$	$\tilde{\mathbf{e}}_{ij}^{\times}$	$\tilde{\mathbf{e}}_{ij}^{x}$	$\tilde{\mathbf{e}}_{ij}^{y}$	$\tilde{\mathbf{e}}_{ij}^{b}$	$\tilde{\mathbf{e}}_{ij}^{l}$
General relativity [46, 47]	$g_{\mu\nu}$	✓	✓	×	×	×	×
Brans-Dicke theory [52]	$g_{\mu\nu}, \phi$	✓	✓	×	×	✓	✓
4-Vector gravity [53]	B^{μ}	×	×	✓	✓	×	×
Horndesk theory [55, 56]	$g_{\mu\nu}, \phi$	✓	✓	×	×	✓	✓
Einstein-æther theory [55, 54]	$g_{\mu\nu}, B^{\mu}$	✓	✓	✓	✓	✓	✓
dCS gravity [57, 58]	$g_{\mu\nu}, \phi$	✓	✓	×	×	×	×
EdGB gravity [57, 59]	$g_{\mu\nu}, \phi$	✓	✓	×	×	×	×
$f(R)$ gravity [55, 60, 61]	$- - -$	✓	✓	×	×	✓	✓

Table 1.1: Polarization modes of GWs and gravitational fields predicted in different metric theories of gravity where $g_{\mu\nu}$ is the metric tensor, B^{μ} is a vector field and ϕ is a scalar field. Longitudinal mode existence strongly depends on the mass of the graviton: if the graviton is massless, then only the breathing mode is present, meanwhile if the graviton has mass, both scalar modes exist.

These include the SGWB produced by the standard amplification of vacuum metric tensor modes, due to the accelerated inflationary[8] expansion in the early universe, but also many processes related to inflation models beyond the standard mechanism which could produce detectable signals (e.g. from the couplings of the inflaton field to extra fields, to new symmetry patterns underlying the inflationary mechanism or a mass of the graviton or Primordial Black Holes formation, see, e.g. [62] Post-inflationary, early universe mechanisms can also source GWs with a large amplitude, like strong first order phase transitions. All these SGWB once produced, would afterwards propagate freely until today. Thus, the detection of the SGWB coming from the primordial universe could provide us very interesting information on the status of the universe in its early years. Stochastic backgrounds may also have astrophysical origin, being produced by a large number of weak, independent, and unresolved astrophysical sources. A clear example may be the astrophysical background arising from stellar mass binary black hole coalescences[34, 35, 36], core-collapse supernovae [37, 38] or GWs coming from rotating neutron stars [39, 40].
In the rest of this section we work in the transverse-tracelesse gauge and we assume the existence of all the possible polarization modes $A = (+, \times, x, y, b, l)$ given by Eq.(1.2.12) to introduce some general results for the SGWB. The metric perturbation appearing in Eq.(1.1.31) must be replaced by

$$h_{ij}(t, \bar{\mathbf{x}}) = \sum_{A} \int_{-\infty}^{+\infty} df \int_{S^2} d\Omega \big(\tilde{\mathbf{e}}_{ij}^{A}(\hat{\mathbf{\Omega}}) h_A(f, \hat{\mathbf{\Omega}}) \big) e^{i2\pi f(t - \hat{\mathbf{\Omega}} \cdot \frac{\bar{\mathbf{x}}}{c})}. \qquad (1.4.1)$$

---

[8]For energies comprised between the scale of inflation, processes such as particle production during inflation [26], cosmic strings [28, 29] and first order phase transitions [30, 31] could be cosmological sources of GWs.

Since we have only one Universe to work with, the ensemble average of the amplitudes $h_A(f, \hat{\boldsymbol{\Omega}})$, which are now random variables, is replaced by a time average invoking the ergodic hypothesis [32]. We list here some properties we expect to be true for a stochastic background of gravitational waves:

- We assume the stochastic background to be Gaussian. This means that SGWB statistical properties are described by the mean value $\langle h_A(f, \hat{\boldsymbol{\Omega}}) \rangle$ and the two-point correlator $\langle h_A^*(f, \hat{\boldsymbol{\Omega}}) h_{A'}(f', \hat{\boldsymbol{\Omega}}') \rangle$, where $\langle \cdot \rangle$ denotes the ensemble average. This assumption is sustained by central limit theorem, which states that a large number of random uncorrelated events produces a random event, indipendently of the probability distribution of the random events. We further assume that $\langle h_A(f, \hat{\boldsymbol{\Omega}}) \rangle = 0$ and consequently we focus on the two-point correlator.[9]

- Similarly to the CMB radiation, we expect the stochastic background to be highly isotropic in a first approximation[10]. Recent studies to quantify non-Gaussianity in the cosmological SGWB are reported in [33]. Thus, we expect waves coming from different directions not to be correlated, meaning that considering the two-point correlator $\langle h_A^*(f, \hat{\boldsymbol{\Omega}}) h_{A'}(f', \hat{\boldsymbol{\Omega}}') \rangle$ this is proportional to

$$\delta(\hat{\boldsymbol{\Omega}}, \hat{\boldsymbol{\Omega}}') = \delta(\phi - \phi')\delta(\cos\theta - \cos\theta'), \tag{1.4.2}$$

  with (θ, ϕ) standard spherical coordinates.

- The SGWB is stationary, which means that all the background statistical properties must depend on the difference between times, but not on the time origin. In the time domain, the two-point correlator $\langle h_A(t) h_{A'}(t') \rangle$ may be proportional to $t - t'$, while moving to the frequency domain, this means that $\langle h_A^*(f, \hat{\boldsymbol{\Omega}}) h_{A'}(f', \hat{\boldsymbol{\Omega}}') \rangle$ is proportional to $\delta(f - f')$.

- Since nature has no preferences, we assume an unpolarized SGWB, meaning that GWs have statistically equivalent components of tensor, vector and scalar modes. This also implies that the two-point correlator is proportional to $\delta_{AA'}$.

It is now time to discuss if these conditions are valid for both cosmological and astrophysical backgrounds. The Gaussian SGWB assumption is expected to be true for a background of cosmological origin, due to the large number of possible sources needed for the central limit theorem to work (see footnote 8.). On the other hand, if the number of GW sources contributing to the astrophysical background is small, the assumption may not hold for the astrophysical background. The isotropy expectation seems reasonable for GWs of cosmological origin (see footnote 9) coming from early universe sources, but it may not be valid

---

[9]See however the discussion in [63, 64, 65] and the recent work about non-Gaussianities in the space of distribution of the SGWB energy density [33, 66, 67]

[10]Of course small anisotropies might be present analogously to the CMB, where $\frac{\Delta T}{T} \approx 10^{-5}$. For recenet works in the direction of the SGWB see [66, 68]

if we consider GWs relative to astrophysical processes: in this case the gravitational background would be more intense when looking in the direction of the galactic plane where these processes are supposed to take place, breaking the isotropy. Finally, a cosmological background is expected to vary on time-scales comparable to the age of the universe, which is several orders of magnitude larger than both GW period and observation time, and the stationary assumption can be taken to be true for it. In the end, a background of cosmological origin in a first approximation satisfies all the conditions we discussed, while an astrophysical background presents some issues and his nature cannot always be defined stochastic according to the properes described above. From now on, when we consider a stochastic background of gravitational waves, we shall focus only on the one of cosmological origin. Putting together all four assumptions, the two-point correlator is given by

$$\langle h_A^*(f, \hat{\mathbf{\Omega}}) h_{A'}(f', \hat{\mathbf{\Omega}}') \rangle = \frac{1}{4\pi} \delta(\hat{\mathbf{\Omega}}, \hat{\mathbf{\Omega}}') \delta(f - f') \delta_{AA'} \frac{1}{2} S^A(f), \tag{1.4.3}$$

where $S^A(f)$ is a real function called *spectral density*[11], relative to the polarization mode A, it satisfies $S^A(f) = S^A(-f)$ and its dimensions are Hz^{-1}. The factor $1/4\pi$ comes from a normalization choice so that

$$\int d\Omega \int d\Omega' \langle h_A^*(f, \hat{\mathbf{\Omega}}) h_{A'}(f', \hat{\mathbf{\Omega}}') \rangle = \delta(f - f') \delta_{AA'} \frac{1}{2} S^A(f). \tag{1.4.4}$$

To get a proper description of the SGWB it is useful to keep track of its energy density, whose contributions can be found in the transverse-traceless gauge for each polarization mode from [72]

$$\rho_{gw}^A \equiv \int_{f=0}^{f=\infty} d(\ln f) \frac{d\rho_{gw}^A}{d\ln f}, \tag{1.4.5}$$

which is the energy density contained in a logarithmic frequency bin corresponding to A-polarized GWs and

$$\Omega_{gw}^A(f) \equiv \frac{1}{\rho_c} \frac{d\rho_{gw}^A}{d\ln f}, \tag{1.4.6}$$

where ρ_c is the so-called critical energy density i.e. the cosmological quantity defined as the energy density needed today to close the Universe

$$\rho_c = \frac{3c^2 H_0^2}{8\pi G} \approx 1.688 \times 10^{-8} h_0^2, \tag{1.4.7}$$

where H_0 is the today value of the Hubble parameter [78] (i.e. the Universe expansion rate) which is parametrized via $H_0 = (67.27 \pm 0.60) \mathrm{km\, s^{-1} Mpc^{-1}}$. It is straightforward to define

$$\Omega_{gw}^A = \frac{1}{\rho_c} \int_{f=0}^{f=\infty} d(\ln f) \Omega_{gw}^A(f), \tag{1.4.8}$$

---

[11]Due to the presence of the $1/2$ factor, $S(f)$ should be called *one-sided spectral density* (in opposition to the *double-sided spectral density* $S_{double}^A(f) = \frac{1}{2} S^A(f)$), to highlight the fact that when computing an integration over the whole frequency range $\int_{-\infty}^{\infty} df S_{double}(f) = \int_0^{\infty} df S(f)$. However, we omit the "one-sided" adjective for simplicity from now on.

which denotes the adimensional quantity used to keep track of the gravitational radiation energy density. Since we are considering logarithmic frequency intervals, both Ω_{gw}^A and $\Omega_{gw}^A(f)$ are dimensionless. There is a precise relation between $\Omega_{gw}^A(f)$, related to the GW background energy density, and $S^A(f)$, which uniquely characterizes the statistical properties of the background itself, that we now wish to find. Using Eqs.(1.4.1) and (1.4.3) it is possible to get a second expression [72] for the energy density given by

$$\rho_{gw}^A = \frac{c^2}{16\pi G} \int_{f=0}^{f=\infty} d(\ln f) 4\pi^2 f^3 S^A(f). \tag{1.4.9}$$

We now compare Eqs.(1.4.5)-(1.4.9) to finally get the following relation

$$\Omega_{gw}^A(f) = \frac{2\pi^2}{3H_0^2} f^3 S^A(f). \tag{1.4.10}$$

Chapter 2

2nd-generation Ground Based Interferometers

In this chapter we introduce the physics behind ground-based GW interferometers in order to understand how GWs from a Cosmological Stochastic Background can be detected ([72, 73]). The major issue concerning GW signals is their incredible weakness which makes them really hard to distinguish from the background detector noise; to avoid this problem at least two detectors need to be cross-correlated to filter the GW signal. Moreover, to separate tensor, vector and scalar polarization mode contributions to the background energy density we need at least three detectors, thus we can build detector networks with interferometers on Earth. In order to prepare ourselves to upcoming future ground-based detectors, in this section we wish to better understand these problems considering 2nd-generation interferometers, which represent a valid starting point.

2.1 Detector Signal and Angular Pattern Functions

We now wish to understand how GWs can be detected and how we can distinguish their weak signal from the noise background. We begin the discussion by considering 2nd-generation ground-based interferometers, while upcoming future detectors will be discussed in the next chapter. As suggested by Eqs. (1.1.9) and (1.4.1), the nature of GWs is tensorial. However, in real life situations, we expect the output of a detector to be a scalar quantity given by the sum of two time-dependent terms: the first one, which we denote $h(t)$, relative to the real GW signal and the second one, $n(t)$, relative to the detector noise. To derive those, we introduce the rank-2 *detector tensor* $\mathbf{D}$, which depends on the detector geometry, in such a way that

$$h(t) = D^{ij} h_{ij}(t, \bar{\mathbf{x}}), \tag{2.1.1}$$

where $\bar{\mathbf{x}}$ denotes the detector location and the signal will be given by

$$s(t) = h(t) + n(t). \tag{2.1.2}$$

If the detector is a GW interferometer of arm length L, then $\mathbf{D}$ is the trace-free tensor

$$\mathbf{D} = \frac{1}{2}\big\{\hat{\mathbf{u}} \otimes \hat{\mathbf{u}} - \hat{\mathbf{v}} \otimes \hat{\mathbf{v}}\big\}, \tag{2.1.3}$$

where $\hat{\mathbf{u}}$ and $\hat{\mathbf{v}}$ are unit vectors directed along the interferometer arms and $\otimes$ denotes the tensor product. This expression is valid if the GW reduced wavelenght[1] $\lambdabar$ is greater than the interferometer arm length L. This working regime is sometimes referred to as *long wavelength limit*. Analogously we can define a characteristic frequency $f_* = \frac{c}{2\pi L}$ and reproduce the previous limit whenever $f \ll f_*$, where f is the GW frequency: in Tab.2.1 we list both arm length and characteristic frequency of 2nd-generation ground-based interferometers.

Detector	Arm Length	f_*
Ligo Hanford (LH)	4 Km	11937 Hz
Ligo Livingston (LL)	4 Km	11937 Hz
Virgo (V)	3 Km	15915 Hz
Kagra (K)	3 Km	15915 Hz

Table 2.1: Arm length and characteristic frequency of 2nd-generation ground-based interferometers.

We now define for each polarization mode the detector *angular pattern functions*

$$F^A(\hat{\mathbf{\Omega}}) = D^{ij}e_{ij}^A(\hat{\mathbf{\Omega}}), \qquad A = +, \times, x, y, b, l. \tag{2.1.4}$$

thus the GW true signal can be written as

$$h(t) = \sum_A \int_{-\infty}^{+\infty} df \int_{S^2} d\Omega \big(F^A(\hat{\mathbf{\Omega}})h_A(f,\hat{\mathbf{\Omega}})\big)e^{i2\pi f(t-\hat{\mathbf{\Omega}}\cdot\frac{\bar{\mathbf{x}}}{c})}. \tag{2.1.5}$$

Angular pattern functions are key objects in data analysis and they encode information on both GW direction and polarization and detector geometry. We now wish to find a possible analytic expression of F^A for an L-shaped[2] interferometer ([86, 72]) and we begin by defining the following orthonormal coordinate system

$$\begin{cases} \hat{\mathbf{u}} = (1,0,0)^T \\ \hat{\mathbf{v}} = (0,1,0)^T \\ \hat{\mathbf{z}} = (0,0,1)^T \end{cases}. \tag{2.1.6}$$

---

[1]We define $\lambdabar = \frac{\lambda}{2\pi}$.
[2]GW interferometer with an internal angle of $\frac{\pi}{2}$ between its arms.

We assume that the first arm of the interferometer is directed along $\hat{\mathbf{u}}$, while the second one is directed along $\hat{\mathbf{v}}$, thus the detector tensor is given by

$$\mathbf{D} = \frac{1}{2} \begin{pmatrix} 1 & 0 & 0 \\ 0 & -1 & 0 \\ 0 & 0 & 0 \end{pmatrix}. \tag{2.1.7}$$

Starting from Eq.(2.1.6), we define a second orthonormal coordinate system rotated by angles $\{\theta \in [0,\pi], \phi \in [0,2\pi]\}$ given by

$$\begin{cases} \hat{\mathbf{u}}' = (\cos\theta\cos\phi, \cos\theta\sin\phi, -\sin\theta)^T \\ \hat{\mathbf{v}}' = (-\sin\phi, \cos\phi, 0)^T \\ \hat{\mathbf{z}}' = (\sin\theta\cos\phi, \sin\theta\sin\phi, \cos\theta)^T \end{cases}, \tag{2.1.8}$$

and we identify $\hat{\mathbf{z}}'$ with the GW direction $\hat{\boldsymbol{\Omega}}$. Polarization tensors can be defined through tensor products between $\hat{\boldsymbol{\Omega}}$ and two orthogonal unit vectors lying on its transverse plane: to put ourselves in the most general situation, we can perform a rotation by an angle ψ around the axis identified by the unit vector $\hat{\boldsymbol{\Omega}}$, thus rotated unit vectors are given by

$$\begin{pmatrix} \hat{\mathbf{m}} \\ \hat{\mathbf{n}} \\ \hat{\boldsymbol{\Omega}} \end{pmatrix} = \begin{pmatrix} \cos\psi & \sin\psi & 0 \\ -\sin\psi & \cos\psi & 0 \\ 0 & 0 & 1 \end{pmatrix} \begin{pmatrix} \hat{\mathbf{u}}' \\ \hat{\mathbf{v}}' \\ \hat{\boldsymbol{\Omega}}' \end{pmatrix} \implies \begin{cases} \hat{\mathbf{m}} = \hat{\mathbf{u}}'\cos\psi + \hat{\mathbf{v}}'\sin\psi \\ \hat{\mathbf{n}} = -\hat{\mathbf{u}}'\sin\psi + \hat{\mathbf{v}}'\cos\psi \\ \hat{\boldsymbol{\Omega}} = \hat{\mathbf{z}}' \end{cases}. \tag{2.1.9}$$

While the detector tensor remains unaffected, clearly this change of coordinates leads to the following new expressions for the polarization tensors

$$\tilde{\mathbf{e}}_+ = \hat{\mathbf{m}} \otimes \hat{\mathbf{m}} - \hat{\mathbf{n}} \otimes \hat{\mathbf{n}},$$
$$\tilde{\mathbf{e}}_\times = \hat{\mathbf{m}} \otimes \hat{\mathbf{n}} + \hat{\mathbf{n}} \otimes \hat{\mathbf{m}},$$
$$\tilde{\mathbf{e}}_b = \hat{\mathbf{m}} \otimes \hat{\mathbf{m}} + \hat{\mathbf{n}} \otimes \hat{\mathbf{n}},$$
$$\tilde{\mathbf{e}}_l = \sqrt{2}\,\hat{\boldsymbol{\Omega}} \otimes \hat{\boldsymbol{\Omega}},$$
$$\tilde{\mathbf{e}}_x = \hat{\mathbf{m}} \otimes \hat{\boldsymbol{\Omega}} + \hat{\boldsymbol{\Omega}} \otimes \hat{\mathbf{m}},$$
$$\tilde{\mathbf{e}}_y = \hat{\mathbf{n}} \otimes \hat{\boldsymbol{\Omega}} + \hat{\boldsymbol{\Omega}} \otimes \hat{\mathbf{n}}, \tag{2.1.10}$$

According to Eq.(2.1.8) and Eq.(2.1.9), we may express all these tensor products in terms

of unit vectors $\hat{\mathbf{u}}', \hat{\mathbf{v}}'$, and $\hat{\boldsymbol{\Omega}}$, as we show here

$$
\begin{cases}
\hat{\mathbf{m}} \otimes \hat{\mathbf{m}} = \hat{\mathbf{u}}' \otimes \hat{\mathbf{u}}' \cos^2 \psi + \hat{\mathbf{v}}' \otimes \hat{\mathbf{v}}' \sin^2 \psi + \hat{\mathbf{u}}' \otimes \hat{\mathbf{v}}' \sin \psi \cos \psi + \hat{\mathbf{v}}' \otimes \hat{\mathbf{u}}' \sin \psi \cos \psi \\
\hat{\mathbf{n}} \otimes \hat{\mathbf{n}} = \hat{\mathbf{u}}' \otimes \hat{\mathbf{u}}' \sin^2 \psi + \hat{\mathbf{v}}' \otimes \hat{\mathbf{v}}' \cos^2 \psi - \hat{\mathbf{u}}' \otimes \hat{\mathbf{v}}' \sin \psi \cos \psi - \hat{\mathbf{v}}' \otimes \hat{\mathbf{u}}' \sin \psi \cos \psi \\
\hat{\mathbf{m}} \otimes \hat{\mathbf{n}} = -\hat{\mathbf{u}}' \otimes \hat{\mathbf{u}}' \sin \psi \cos \psi + \hat{\mathbf{v}}' \otimes \hat{\mathbf{v}}' \sin \psi \cos \psi + \hat{\mathbf{u}}' \otimes \hat{\mathbf{v}}' \cos^2 \psi - \hat{\mathbf{v}}' \otimes \hat{\mathbf{u}}' \sin^2 \psi \\
\hat{\mathbf{n}} \otimes \hat{\mathbf{m}} = -\hat{\mathbf{u}}' \otimes \hat{\mathbf{u}}' \sin \psi \cos \psi + \hat{\mathbf{v}}' \otimes \hat{\mathbf{v}}' \sin \psi \cos \psi - \hat{\mathbf{u}}' \otimes \hat{\mathbf{v}}' \sin^2 \psi + \hat{\mathbf{v}}' \otimes \hat{\mathbf{u}}' \cos^2 \psi \\
\hat{\boldsymbol{\Omega}} \otimes \hat{\boldsymbol{\Omega}} = \hat{\mathbf{z}}' \otimes \hat{\mathbf{z}}' \\
\hat{\mathbf{m}} \otimes \hat{\boldsymbol{\Omega}} = \hat{\mathbf{u}}' \otimes \hat{\mathbf{z}}' \cos \psi + \hat{\mathbf{v}}' \otimes \hat{\mathbf{z}}' \sin \psi \\
\hat{\boldsymbol{\Omega}} \otimes \hat{\mathbf{m}} = \hat{\mathbf{z}}' \otimes \hat{\mathbf{u}}' \cos \psi + \hat{\mathbf{z}}' \otimes \hat{\mathbf{v}}' \sin \psi \\
\hat{\mathbf{n}} \otimes \hat{\boldsymbol{\Omega}} = -\hat{\mathbf{u}}' \otimes \hat{\mathbf{z}}' \sin \psi + \hat{\mathbf{v}}' \otimes \hat{\mathbf{z}}' \cos \psi \\
\hat{\boldsymbol{\Omega}} \otimes \hat{\mathbf{n}} = -\hat{\mathbf{z}}' \otimes \hat{\mathbf{u}}' \sin \psi + \hat{\mathbf{z}}' \otimes \hat{\mathbf{v}}' \cos \psi.
\end{cases}
$$

$$(2.1.11)$$

We now need to find the form of all the possible tensor product combinations involving unit vectors $\hat{\mathbf{u}}', \hat{\mathbf{v}}'$, and $\hat{\mathbf{z}}'$. With a little work it can be shown that

$$
\hat{\mathbf{u}}' \otimes \hat{\mathbf{u}}' = \begin{pmatrix} \cos^2 \theta \cos^2 \phi & \cos^2 \theta \sin \phi \cos \phi & -\sin \theta \cos \theta \cos \phi \\ \cos^2 \theta \sin \phi \cos \phi & \cos^2 \theta \sin^2 \phi & -\sin \theta \cos \theta \sin \phi \\ -\sin \theta \cos \theta \cos \phi & -\sin \theta \cos \theta \sin \phi & \sin^2 \theta \end{pmatrix}, \qquad (2.1.12)
$$

$$
\hat{\mathbf{u}}' \otimes \hat{\mathbf{v}}' = \begin{pmatrix} -\cos \theta \sin \phi \cos \phi & \cos \theta \cos^2 \phi & 0 \\ -\cos \theta \sin^2 \phi & \cos \theta \sin \phi \cos \phi & 0 \\ \sin \theta \sin \phi & -\sin \theta \cos \phi & 0 \end{pmatrix}, \qquad (2.1.13)
$$

$$
\hat{\mathbf{v}}' \otimes \hat{\mathbf{u}}' = \begin{pmatrix} -\cos \theta \sin \phi \cos \phi & -\cos \theta \sin^2 \phi & \sin \theta \sin \phi \\ \cos \theta \cos^2 \phi & \cos \theta \sin \phi \cos \phi & -\sin \theta \cos \phi \\ 0 & 0 & 0 \end{pmatrix}, \qquad (2.1.14)
$$

$$
\hat{\mathbf{v}}' \otimes \hat{\mathbf{v}}' = \begin{pmatrix} \sin^2 \phi & -\sin \phi \cos \phi & 0 \\ -\sin \phi \cos \phi & \cos^2 \phi & 0 \\ 0 & 0 & 0 \end{pmatrix}, \qquad (2.1.15)
$$

$$
\hat{\mathbf{z}}' \otimes \hat{\mathbf{z}}' = \begin{pmatrix} \sin^2 \theta \cos^2 \phi & \sin^2 \theta \sin \phi \cos \phi & \sin \theta \cos \theta \cos \phi \\ \sin^2 \theta \sin \phi \cos \phi & \sin^2 \theta \sin^2 \phi & \sin \theta \cos \theta \sin \phi \\ \sin \theta \cos \theta \cos \phi & \sin \theta \cos \theta \sin \phi & \cos^2 \theta \end{pmatrix}, \qquad (2.1.16)
$$

$$
\hat{\mathbf{u}}' \otimes \hat{\mathbf{z}}' = \begin{pmatrix} \sin \theta \cos \theta \cos^2 \phi & \sin \theta \cos \theta \sin \phi \cos \phi & \cos^2 \theta \cos \phi \\ \sin \theta \cos \theta \sin \phi \cos \phi & \sin \theta \cos \theta \sin^2 \phi & \cos^2 \theta \sin \phi \\ -\sin^2 \theta \cos \phi & -\sin^2 \theta \sin \phi & -\sin \theta \cos \theta \end{pmatrix}, \qquad (2.1.17)
$$

$$
\hat{\mathbf{z}}' \otimes \hat{\mathbf{u}}' = \begin{pmatrix} \sin \theta \cos \theta \cos^2 \phi & \sin \theta \cos \theta \sin \phi \cos \phi & -\sin^2 \theta \cos \phi \\ \sin \theta \cos \theta \sin \phi \cos \phi & \sin \theta \cos \theta \sin^2 \phi & -\sin^2 \theta \sin \phi \\ \cos^2 \theta \cos \phi & \cos^2 \theta \sin \phi & -\sin \theta \cos \theta \end{pmatrix}, \qquad (2.1.18)
$$

24

$$\hat{\mathbf{v}}' \otimes \hat{\mathbf{z}}' = \begin{pmatrix} -\sin\theta\sin\phi\cos\phi & -\sin\theta\sin^2\phi & -\cos\theta\sin\phi \\ \sin\theta\cos^2\phi & \sin\theta\sin\phi\cos\phi & \cos\theta\cos\phi \\ 0 & 0 & 0 \end{pmatrix}, \qquad (2.1.19)$$

$$\hat{\mathbf{z}}' \otimes \hat{\mathbf{v}}' = \begin{pmatrix} -\sin\theta\sin\phi\cos\phi & \sin\theta\cos^2\phi & 0 \\ -\sin\theta\sin^2\phi & \sin\theta\sin\phi\cos\phi & 0 \\ \sin\theta\cos\theta & \cos\theta\cos\phi & 0 \end{pmatrix}. \qquad (2.1.20)$$

Finally we can plug Eqs.(2.1.12)-(2.1.20) into Eq.(2.1.11) to get the most general expression for our polarization tensors and we can compute the angular pattern function for each polarization mode. We get

- for the $+$ and $\times$ tensor modes

$$F^+(\hat{\mathbf{\Omega}}, \psi) = D^{ij}\tilde{e}_{ij}^+ = \frac{1}{2}\left[(\hat{\mathbf{m}}\otimes\hat{\mathbf{m}} - \hat{\mathbf{n}}\otimes\hat{\mathbf{n}})_{11} - (\hat{\mathbf{m}}\otimes\hat{\mathbf{m}} - \hat{\mathbf{n}}\otimes\hat{\mathbf{n}})_{22}\right] =$$
$$= \frac{1}{2}(1+\cos^2\theta)\cos 2\phi\cos 2\psi - \cos\theta\sin 2\phi\sin 2\psi, \qquad (2.1.21)$$

$$F^\times(\hat{\mathbf{\Omega}}, \psi) = D^{ij}\tilde{e}_{ij}^\times = \frac{1}{2}\left[(\hat{\mathbf{m}}\otimes\hat{\mathbf{n}} + \hat{\mathbf{m}}\otimes\hat{\mathbf{n}})_{11} - (\hat{\mathbf{m}}\otimes\hat{\mathbf{n}} + \hat{\mathbf{m}}\otimes\hat{\mathbf{n}})_{22}\right] =$$
$$= -\frac{1}{2}(1+\cos^2\theta)\cos 2\phi\sin 2\psi - \cos\theta\sin 2\phi\cos 2\psi, \qquad (2.1.22)$$

- for the breathing and longitudinal scalar modes

$$F^b(\hat{\mathbf{\Omega}}) = D^{ij}\tilde{e}_{ij}^b = \frac{1}{2}\left[(\hat{\mathbf{m}}\otimes\hat{\mathbf{m}} + \hat{\mathbf{n}}\otimes\hat{\mathbf{n}})_{11} - (\hat{\mathbf{m}}\otimes\hat{\mathbf{m}} + \hat{\mathbf{n}}\otimes\hat{\mathbf{n}})_{22}\right] =$$
$$= -\frac{1}{2}\sin^2\theta\cos 2\phi, \qquad (2.1.23)$$

$$F^l(\hat{\mathbf{\Omega}}) = D^{ij}\tilde{e}_{ij}^l = \frac{\sqrt{2}}{2}\left[(\hat{\mathbf{z}}'\otimes\hat{\mathbf{z}}')_{11} - (\hat{\mathbf{z}}'\otimes\hat{\mathbf{z}}')_{22}\right] =$$
$$= \frac{1}{\sqrt{2}}\sin^2\theta\cos 2\phi, \qquad (2.1.24)$$

- and for the x and y vector modes

$$F^x(\hat{\mathbf{\Omega}}, \psi) = D^{ij}\tilde{e}_{ij}^x = \frac{1}{2}\left[(\hat{\mathbf{m}}\otimes\hat{\mathbf{\Omega}} + \hat{\mathbf{\Omega}}\otimes\hat{\mathbf{m}})_{11} - (\hat{\mathbf{m}}\otimes\hat{\mathbf{\Omega}} + \hat{\mathbf{\Omega}}\otimes\hat{\mathbf{m}})_{22}\right] =$$
$$= \sin\theta(\cos\theta\cos 2\phi\cos\psi - \sin 2\phi\sin\psi), \qquad (2.1.25)$$

$$F^y(\hat{\mathbf{\Omega}}, \psi) = D^{ij}\tilde{e}_{ij}^y = \frac{1}{2}\left[(\hat{\mathbf{n}}\otimes\hat{\mathbf{\Omega}} + \hat{\mathbf{\Omega}}\otimes\hat{\mathbf{n}})_{11} - (\hat{\mathbf{n}}\otimes\hat{\mathbf{\Omega}} + \hat{\mathbf{\Omega}}\otimes\hat{\mathbf{n}})_{22}\right] =$$
$$= -\sin\theta(\cos\theta\cos 2\phi\sin\psi + \sin 2\phi\cos\psi). \qquad (2.1.26)$$

25

We notice that angular pattern functions corresponding to tensor and vector modes are functions of the polarization angle ψ, while scalar modes are not. Moreover breathing and longitudinal modes only differ for a constant multiplicative factor and they are not distinguishable, thus completely degenerate. We mentioned how angular pattern functions are a measure of the detector sensitivity to GWs of different polarizations and directions. In Fig.2.1-2.3 we show their plots with $\psi = 0$ for each polarization mode in our $3D$ space and their projection on a $2D$ plane for fixed values of θ. Let us consider Fig.2.1c for a clear example: due to detector geometry, a GW with plus polarization coming from the direction $(\theta, \phi = \frac{\pi}{4})$ is not detected by the interferometer. This happens because the incoming wave induces the same phase shift to the light running along both interferometer arms so that the relative phase difference becomes zero, making this direction blind. Similar scenarios can happen for other polarizations and blind directions correspond to $F^A = 0$.

2.2 Transfer Function of a Michelson Interferometer

All previous results were found considering GW frequencies smaller than f_* and it now seems legit to explore how Eq.(2.1.3) changes if the long wavelength limit can no longer be taken as valid. Let us consider the arm of an interferometer with two masses (m_1, m_2) at its ends: m_1 and m_2 are located respectively at $\bar{\mathbf{x}}$ and $\bar{\mathbf{x}} + L \cdot \hat{\mathbf{e}}_1$, where L is the arm length and $\hat{\mathbf{e}}_1$ is the unit vector directed along the arm. The passage of a gravitational wave described by Eq.(1.4.1) affects the travel of a photon emitted at $\bar{\mathbf{x}}$ at time $t - \frac{L}{c}$ and arriving at $\bar{\mathbf{x}} + L \cdot \hat{\mathbf{e}}_1$ at time t. The time-travel change ([87]) is given by

$$\Delta T = \frac{(\hat{\mathbf{e}}_1 \otimes \hat{\mathbf{e}}_1)^{ij}}{2c} \int_0^L ds \big(h_{ij}(t(s), \bar{\mathbf{x}}(s)) \big), \tag{2.2.1}$$

where we are using the position and time parametrizations [88]

$$t(s) = \big(t - \frac{L}{c} \big) + \frac{s}{c}, \qquad \bar{\mathbf{x}}(s) = \bar{\mathbf{x}} + s \cdot \hat{\mathbf{e}}_1. \tag{2.2.2}$$

Putting together Eqs.(1.4.1) and (2.2.1) we get

$$\begin{aligned} \Delta T &= \frac{(\hat{\mathbf{e}}_1 \otimes \hat{\mathbf{e}}_1)^{ij}}{2c} \int_0^L ds \sum_A \int_{-\infty}^{+\infty} df \int_{S^2} d\Omega \big(\tilde{\mathbf{e}}_{ij}^A(\hat{\mathbf{\Omega}}) h_A(f, \hat{\mathbf{\Omega}}) \big) e^{i2\pi f(t - \hat{\mathbf{\Omega}} \cdot \frac{\bar{\mathbf{x}}}{c})} e^{i2\pi f \frac{s}{c}(1 - \hat{\mathbf{\Omega}} \cdot \hat{\mathbf{e}}_1)} e^{-i2\pi f \frac{L}{c}} \\ &= \frac{(\hat{\mathbf{e}}_1 \otimes \hat{\mathbf{e}}_1)^{ij}}{2c} \big(\sum_A \int_{-\infty}^{+\infty} df \int_{S^2} d\Omega \big(\tilde{\mathbf{e}}_{ij}^A(\hat{\mathbf{\Omega}}) h_A(f, \hat{\mathbf{\Omega}}) \big) e^{i2\pi f(t - \hat{\mathbf{\Omega}} \cdot \frac{\bar{\mathbf{x}}}{c})} \big) \times \\ &\times \int_0^L ds \big(e^{i2\pi f \frac{s}{c}(1 - \hat{\mathbf{\Omega}} \cdot \hat{\mathbf{e}}_1)} \big) e^{-i2\pi f \frac{L}{c}}, \end{aligned}$$
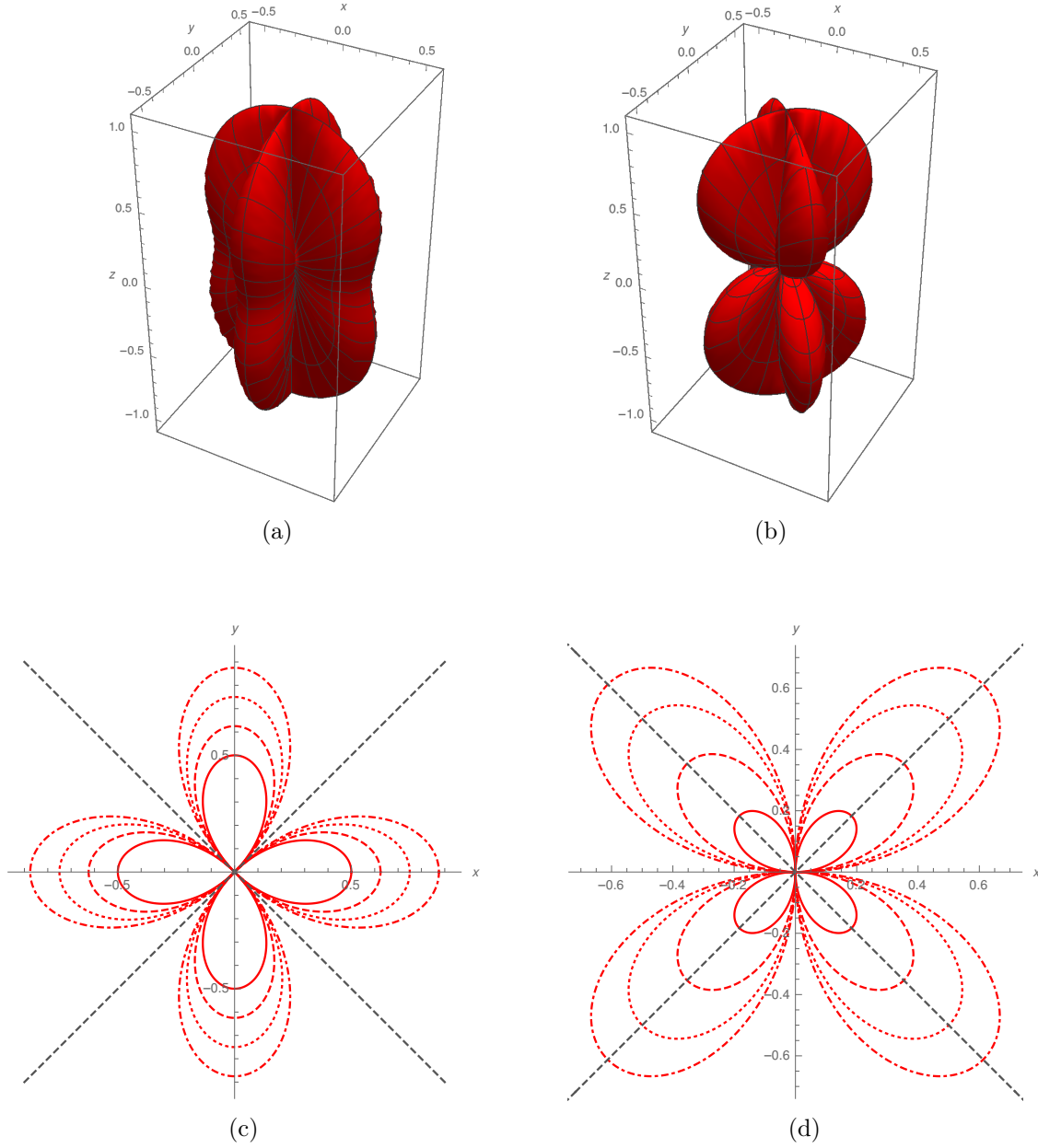
$$\tag{2.2.3}$$

(a)

(b)

(c)

(d)

Figure 2.1: Angular pattern functions for plus (left) and cross (right) polarization of an L-shaped interferometer with arms directed along the x-axis and y-axis respectively. In (a), (b) the $3D$ plots of $|F^+|$ and $|F^\times|$ are shown, while their projections on a $2D$ plane for different fixed values of θ (($\frac{\pi}{6}$, dot-dashed), ($\frac{\pi}{4}$, dotted), ($\frac{\pi}{3}$, dashed), ($\frac{5\pi}{12}$, solid)) are shown in (c), (d).
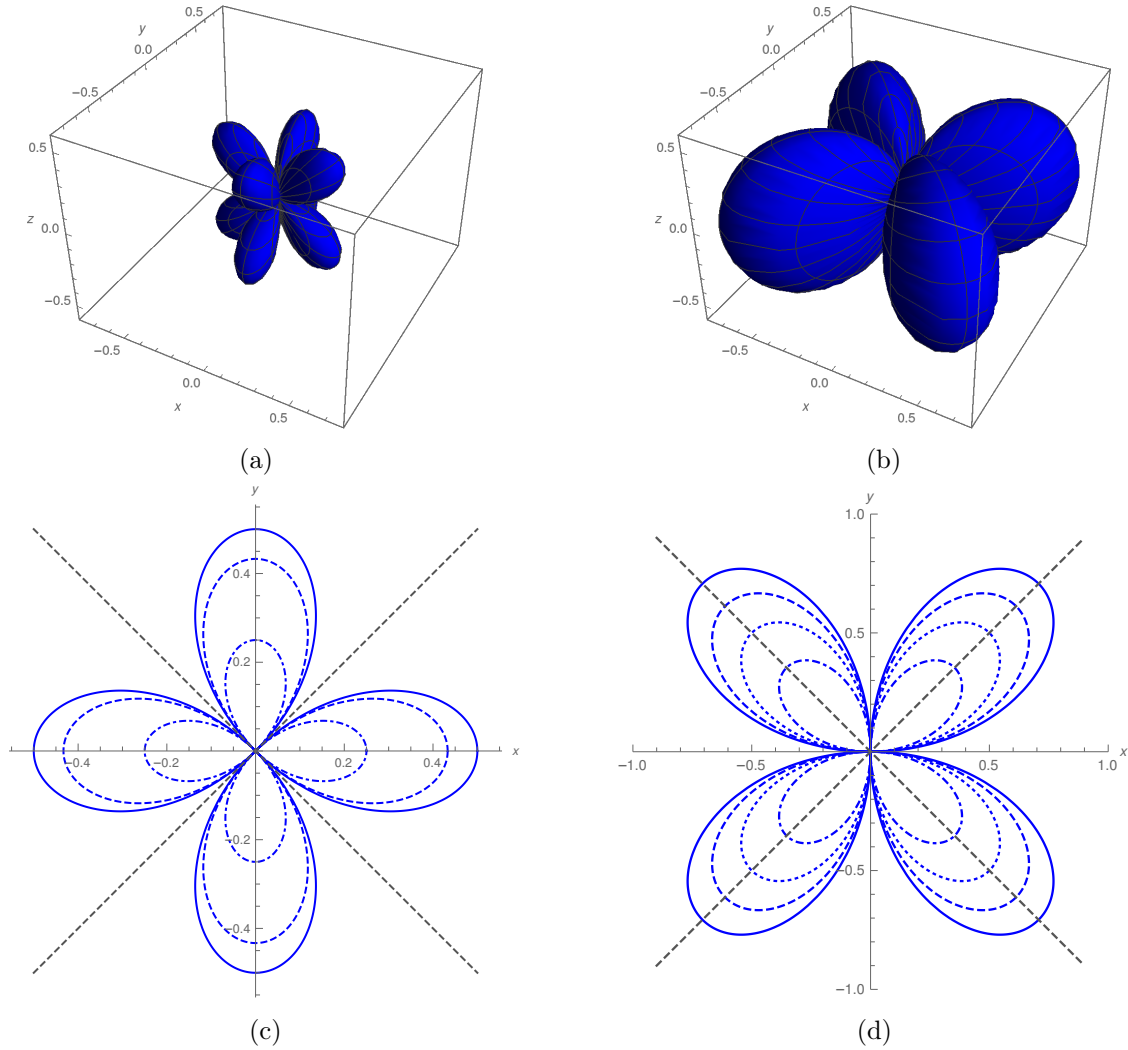
27

(a)

(b)

(c)

(d)

Figure 2.2: Angular pattern functions for vector-x (left) and vector-y (right) polarization modes of an L-shaped interferometer with arms directed along the x-axis and y-axis respectively. In (a), (b) the $3D$ plots of $|F^x|$ and $|F^y|$ are shown, while their projections on a $2D$ plane for different fixed values of θ (vector-x: $(\frac{\pi}{12}$, dot-dashed), $(\frac{\pi}{6}$, dashed), $(\frac{\pi}{4}$, solid), vector-y: $(\frac{\pi}{6}$, dot-dashed), $(\frac{\pi}{4}$, dotted), $(\frac{\pi}{3}$, dashed), $(\frac{\pi}{2}$, solid)) are shown in (c), (d).
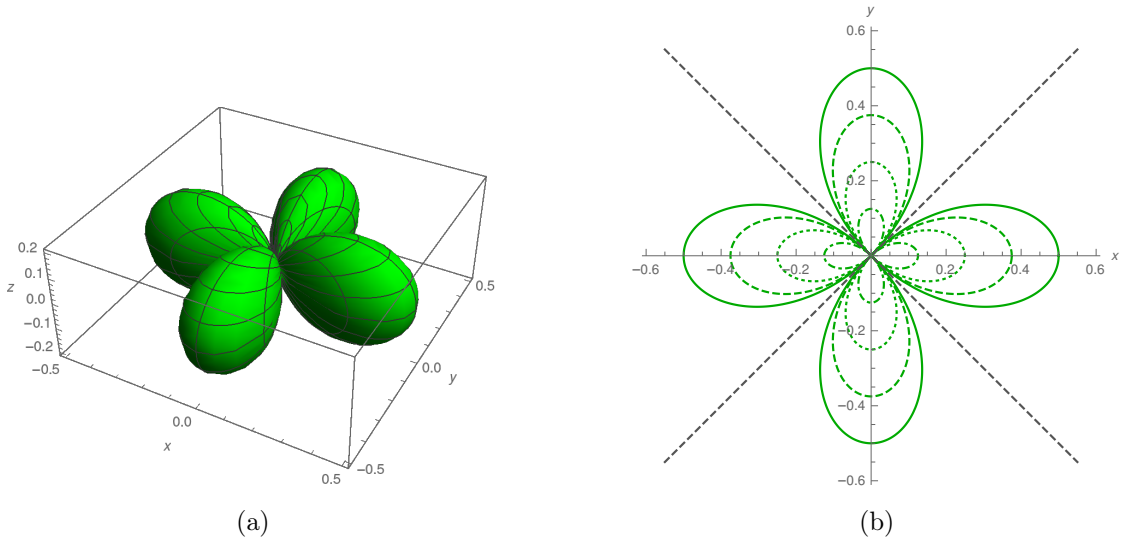
(a)   (b)

Figure 2.3: Angular pattern functions for the breathing polarization mode of an L-shaped interferometer with arms directed along the x-axis and y-axis respectively. In (a) the $3D$ plots of $|F^b|$ is shown, while its projection on a $2D$ plane for different fixed values of θ (($\frac{\pi}{6}$, dot-dashed), ($\frac{\pi}{4}$, dotted), ($\frac{\pi}{3}$, dashed), ($\frac{\pi}{2}$, solid)) are shown in (b). $|F^l|$ differs from $|F^b|$ by a $\sqrt{2}$ constant factor.

where $A = +, \times, x, y, b, l$. We now need to compute the integration over the parameter s before going on, thus we have

$$
\int_0^L ds \big(e^{i2\pi f \frac{s}{c}(1-\hat{\mathbf{\Omega}}\cdot\hat{\mathbf{e}}_1)} \big) = \frac{e^{i2\pi f \frac{L}{c}(1-\hat{\mathbf{\Omega}}\cdot\hat{\mathbf{e}}_1)} - 1}{i2\frac{\pi f}{c}(1 - \hat{\mathbf{\Omega}}\cdot\hat{\mathbf{e}}_1)} =
$$

$$
= \frac{e^{i\pi f \frac{L}{c}(1-\hat{\mathbf{\Omega}}\cdot\hat{\mathbf{e}}_1)}}{\frac{\pi f}{c}(1 - \hat{\mathbf{\Omega}}\cdot\hat{\mathbf{e}}_1)} \frac{e^{i\pi f \frac{L}{c}(1-\hat{\mathbf{\Omega}}\cdot\hat{\mathbf{e}}_1)} - e^{-i\pi f \frac{L}{c}(1-\hat{\mathbf{\Omega}}\cdot\hat{\mathbf{e}}_1)}}{2i} =
$$

$$
= \frac{\sin\big(\frac{\pi L f}{c}(1 - \hat{\mathbf{\Omega}}\cdot\hat{\mathbf{e}}_1)\big)}{\frac{\pi f}{c}(1 - \hat{\mathbf{\Omega}}\cdot\hat{\mathbf{e}}_1)} e^{i\pi f \frac{L}{c}(1-\hat{\mathbf{\Omega}}\cdot\hat{\mathbf{e}}_1)}
$$

$$
= L\frac{\sin\big(\frac{f}{2f_*}(1 - \hat{\mathbf{\Omega}}\cdot\hat{\mathbf{e}}_1)\big)}{\frac{f}{2f_*}(1 - \hat{\mathbf{\Omega}}\cdot\hat{\mathbf{e}}_1)} e^{i\frac{f}{2f_*}(1-\hat{\mathbf{\Omega}}\cdot\hat{\mathbf{e}}_1)}
$$

$$
= L\,\mathrm{sinc}\big(\frac{f}{2f_*}(1 - \hat{\mathbf{\Omega}}\cdot\hat{\mathbf{e}}_1)\big) e^{i\frac{f}{2f_*}(1-\hat{\mathbf{\Omega}}\cdot\hat{\mathbf{e}}_1)}, \tag{2.2.4}
$$

where we have used $\mathrm{sinc}(x) = \frac{\sin x}{x}$. Finally we define the following tensor

$$
D^{ij}(\hat{\mathbf{\Omega}}\cdot\hat{\mathbf{e}}_1, f) = \frac{1}{2}(\hat{\mathbf{e}}_1 \otimes \hat{\mathbf{e}}_1)^{ij} \mathcal{T}(\hat{\mathbf{\Omega}}\cdot\hat{\mathbf{e}}_1, f), \tag{2.2.5}
$$

where

$$
\mathcal{T}(\hat{\mathbf{\Omega}}\cdot\hat{\mathbf{e}}_1, f) = \mathrm{sinc}\big(\frac{f}{2f_*}(1 - \hat{\mathbf{\Omega}}\cdot\hat{\mathbf{e}}_1)\big) e^{-i\frac{f}{2f_*}(1+\hat{\mathbf{\Omega}}\cdot\hat{\mathbf{e}}_1)}, \tag{2.2.6}
$$

is the *one-arm transfer function*. When GW frequencies are lower than f_* we have $\mathcal{T} \approx 1$, while for $f \approx f_*$ transfer functions start to oscillate and the interferometer suffers a loss of sensitivity to GWs of higher frequencies. This behaviour is shown in Fig.2.4. In the end we show that the time-travel change can be written as

$$
\Delta T = \sum_A \left(\frac{L}{c} \int_{-\infty}^{+\infty} df \int_{S^2} d\Omega \big(\tilde{\mathbf{e}}_{ij}^A(\hat{\mathbf{\Omega}}) D^{ij}(\hat{\mathbf{\Omega}}\cdot\hat{\mathbf{e}}_1, f) h_A(f, \hat{\mathbf{\Omega}}) \big) e^{i2\pi f(t - \hat{\mathbf{\Omega}}\cdot\frac{\bar{\mathbf{x}}}{c})} \right). \tag{2.2.7}
$$

Let us now assume we are working with a Michelson interferometer: we want to consider the whole photon time-travel along the first arm: the photon is emitted at $\bar{\mathbf{x}}_\mathbf{a}$ at time $t - \frac{2L}{c}$ and arrives at $\bar{\mathbf{x}}_\mathbf{b} = \bar{\mathbf{x}}_\mathbf{a} + L \cdot \hat{\mathbf{e}}_1$ at time $t - \frac{L}{c}$, then it goes back to $\bar{\mathbf{x}}_\mathbf{a}$ reaching this position at time t. Something analogous can be said for the second arm of the interferometer: two more masses m_3 adn m_4 are located respectively at $\bar{\mathbf{x}}_\mathbf{c}$ and $\bar{\mathbf{x}}_\mathbf{d} = \bar{\mathbf{x}}_\mathbf{c} + L \cdot \hat{\mathbf{e}}_2$, where once again L is the arm length and $\hat{\mathbf{e}}_2$ is the versor directed along the second arm. This way we are able to consider the signal

$$
s(t) = \frac{c}{2L} \big\{ \big[\Delta T_{ab}(t - 2\frac{L}{c}) + \Delta T_{ba}(t - \frac{L}{c}) \big] - \big[\Delta T_{cd}(t - 2\frac{L}{c}) + \Delta T_{dc}(t - \frac{L}{c}) \big] \big\}. \tag{2.2.8}
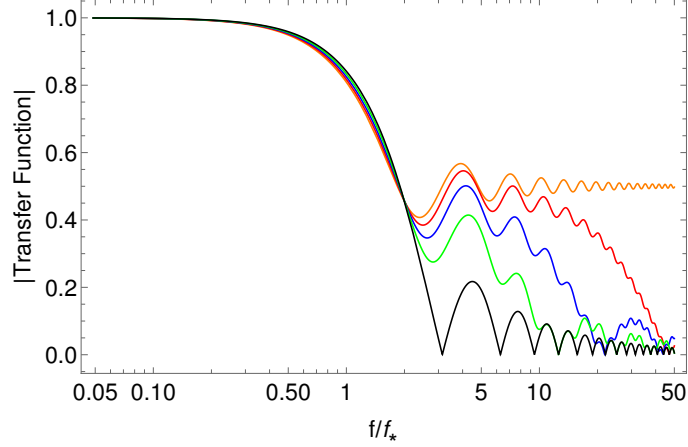$$

Figure 2.4: Absolute value of the one-arm transfer function for a Michelson interferometer for different values of the angle $\hat{\boldsymbol{\Omega}} \cdot \hat{\mathbf{e}}_1$ ($(2\pi$,Orange), $(\frac{\pi}{6}$,Red), $(\frac{\pi}{4}$,Blue), $(\frac{\pi}{3}$,Green), $(\frac{\pi}{2}$,Black)).

Starting with the first arm we define the following parametrizations for the $a \to b$ travel

$$\Delta T_{ab}(t - 2\frac{L}{c}), \qquad t(s) = \left(t - \frac{2L}{c}\right) + \frac{s}{c}, \qquad \bar{\mathbf{x}}(s) = \bar{\mathbf{x}}_1 + s\hat{\mathbf{e}}_1, \qquad (2.2.9)$$

and repeating the steps done for the one-arm transfer function we obtain

$$\Delta T_{ab}(t - 2\frac{L}{c}) =$$
$$= \frac{(\hat{\mathbf{e}}_1 \otimes \hat{\mathbf{e}}_1)^{ij}}{2c} \int_0^L ds \sum_A \int_{-\infty}^{+\infty} \int_{S^2} d\Omega \left(\tilde{\mathbf{e}}_{ij}^A(\hat{\boldsymbol{\Omega}}) h_A(f,\hat{\boldsymbol{\Omega}})\right) e^{i2\pi f(t - \hat{\boldsymbol{\Omega}} \cdot \frac{\bar{\mathbf{x}}_1}{c})} e^{i2\pi f \frac{s}{c}(1 - \hat{\boldsymbol{\Omega}} \cdot \hat{\mathbf{e}}_1)} e^{-i4\pi f \frac{L}{c}}$$
$$= L\frac{(\hat{\mathbf{e}}_1 \otimes \hat{\mathbf{e}}_1)^{ij}}{2c} \int_{-\infty}^{+\infty} df \int_{S^2} d\Omega \left(\sum_A (\tilde{\mathbf{e}}_{ij}^A(\hat{\boldsymbol{\Omega}}) h_A(f,\hat{\boldsymbol{\Omega}})) e^{i2\pi f(t - \hat{\boldsymbol{\Omega}} \cdot \frac{\bar{\mathbf{x}}_1}{c})}\right) \times$$
$$\times \operatorname{sinc}\left(\frac{f}{2f_*}(1 - \hat{\boldsymbol{\Omega}} \cdot \hat{\mathbf{e}}_1)\right) e^{-i\frac{f}{2f_*}(3 + \hat{\boldsymbol{\Omega}} \cdot \hat{\mathbf{e}}_1)}.$$
$$(2.2.10)$$

Moving on to the $b \to a$ travel we have

$$\Delta T_{ba}(t - \frac{L}{c}), \qquad t(s) = \left(t - \frac{L}{c}\right) + \frac{s}{c}, \qquad \bar{\mathbf{x}}(s) = (\bar{\mathbf{x}}_1 + L\hat{\mathbf{e}}_1) - s\hat{\mathbf{e}}_1, \qquad (2.2.11)$$

so we get

$$\Delta T_{ba}(t - \frac{L}{c}) =$$
$$= \frac{(\hat{\mathbf{e}}_1 \otimes \hat{\mathbf{e}}_1)^{ij}}{2c} \int_0^L ds \sum_A \int_{-\infty}^{+\infty} \int_{S^2} d\Omega (\tilde{\mathbf{e}}_{ij}^A(\hat{\boldsymbol{\Omega}}) h_A(f, \hat{\boldsymbol{\Omega}})) e^{i2\pi f(t - \hat{\boldsymbol{\Omega}} \cdot \frac{\bar{\mathbf{x}}_1}{c})} e^{i2\pi f \frac{s}{c}(1 + \hat{\boldsymbol{\Omega}} \cdot \hat{\mathbf{e}}_1)} e^{-i2\pi f \frac{L}{c}} e^{-i2\pi f \frac{L}{c} \hat{\boldsymbol{\Omega}} \cdot \hat{\mathbf{e}}_1}$$
$$= L \frac{(\hat{\mathbf{e}}_1 \otimes \hat{\mathbf{e}}_1)^{ij}}{2c} \int_{-\infty}^{+\infty} df \int_{S^2} d\Omega \left(\sum_A (\tilde{\mathbf{e}}_{ij}^A(\hat{\boldsymbol{\Omega}}) h_A(f, \hat{\boldsymbol{\Omega}})) e^{i2\pi f(t - \hat{\boldsymbol{\Omega}} \cdot \frac{\bar{\mathbf{x}}_1}{c})} \right) \times$$
$$\times \operatorname{sinc}\left(\frac{f}{2f_*}(1 + \hat{\boldsymbol{\Omega}} \cdot \hat{\mathbf{e}}_1) \right) e^{-i \frac{f}{2f_*}(1 + \hat{\boldsymbol{\Omega}} \cdot \hat{\mathbf{e}}_1)}.$$

$$(2.2.12)$$

Summing up these two contributions we find the total delay in time-travel relative to the first arm

$$\Delta T_{ab}(t - 2\frac{L}{c}) + \Delta T_{ba}(t - \frac{L}{c}) =$$
$$= L \frac{(\hat{\mathbf{e}}_1 \otimes \hat{\mathbf{e}}_1)^{ij}}{2c} \int_{-\infty}^{+\infty} df \int_{S^2} d\Omega \left(\sum_A (\tilde{\mathbf{e}}_{ij}^A(\hat{\boldsymbol{\Omega}}) h_A(f, \hat{\boldsymbol{\Omega}})) e^{i2\pi f(t - \hat{\boldsymbol{\Omega}} \cdot \frac{\bar{\mathbf{x}}_1}{c})} \right) \times$$
$$\times \left[\operatorname{sinc}\left(\frac{f}{2f_*}(1 - \hat{\boldsymbol{\Omega}} \cdot \hat{\mathbf{e}}_1) \right) e^{-i \frac{f}{2f_*}(3 + \hat{\boldsymbol{\Omega}} \cdot \hat{\mathbf{e}}_1)} + \operatorname{sinc}\left(\frac{f}{2f_*}(1 + \hat{\boldsymbol{\Omega}} \cdot \hat{\mathbf{e}}_1) \right) e^{-i \frac{f}{2f_*}(1 + \hat{\boldsymbol{\Omega}} \cdot \hat{\mathbf{e}}_1)} \right]$$
$$= \frac{L}{c} (\hat{\mathbf{e}}_1 \otimes \hat{\mathbf{e}}_1)^{ij} \int_{-\infty}^{+\infty} df \int_{S^2} d\Omega \left(\sum_A (\tilde{\mathbf{e}}_{ij}^A(\hat{\boldsymbol{\Omega}}) h_A(f, \hat{\boldsymbol{\Omega}})) e^{i2\pi f(t - \hat{\boldsymbol{\Omega}} \cdot \frac{\bar{\mathbf{x}}_1}{c})} \right) \mathcal{T}_1(\hat{\boldsymbol{\Omega}} \cdot \hat{\mathbf{e}}_1, f),$$

$$(2.2.13)$$

where we have defined the two-arms transfer function

$$\mathcal{T}_{Mich,1}(\hat{\boldsymbol{\Omega}} \cdot \hat{\mathbf{e}}_1, f) = \frac{1}{2} \left[\operatorname{sinc}\left(\frac{f}{2f_*}(1 - \hat{\boldsymbol{\Omega}} \cdot \hat{\mathbf{e}}_1) \right) e^{-i \frac{f}{2f_*}(3 + \hat{\boldsymbol{\Omega}} \cdot \hat{\mathbf{e}}_1)} + \operatorname{sinc}\left(\frac{f}{2f_*}(1 + \hat{\boldsymbol{\Omega}} \cdot \hat{\mathbf{e}}_1) \right) e^{-i \frac{f}{2f_*}(1 + \hat{\boldsymbol{\Omega}} \cdot \hat{\mathbf{e}}_1)} \right],$$

$$(2.2.14)$$

which also reduces to unity for $f \ll f_*$ and starts to oscillate when $f \approx f_*$. Let us focus on the second arm of the interferometer now: we only need to switch $\hat{\mathbf{e}}_1$ with $\hat{\mathbf{e}}_2$ to get the proper result, we have

$$\Delta T_{cd}(t - 2\frac{L}{c}) + \Delta T_{dc}(t - \frac{L}{c}) =$$
$$= \frac{L}{c} (\hat{\mathbf{e}}_2 \otimes \hat{\mathbf{e}}_2)^{ij} \int_{-\infty}^{+\infty} df \int_{S^2} d\Omega \left(\sum_A (\tilde{\mathbf{e}}_{ij}^A(\hat{\boldsymbol{\Omega}}) h_A(f, \hat{\boldsymbol{\Omega}})) e^{i2\pi f(t - \hat{\boldsymbol{\Omega}} \cdot \frac{\bar{\mathbf{x}}_1}{c})} \right) \mathcal{T}_2(\hat{\boldsymbol{\Omega}} \cdot \hat{\mathbf{e}}_2, f),$$

$$(2.2.15)$$

32

where the transfer function relative to the second arm was also defined

$$\mathcal{T}_{Mich,2}(\hat{\boldsymbol{\Omega}} \cdot \hat{\mathbf{e}}_2, f) = \frac{1}{2}\Big[\mathrm{sinc}\big(\frac{f}{2f_*}(1 - \hat{\boldsymbol{\Omega}} \cdot \hat{\mathbf{e}}_2)\big)e^{-i\frac{f}{2f_*}(3 + \hat{\boldsymbol{\Omega}} \cdot \hat{\mathbf{e}}_2)} + \mathrm{sinc}\big(\frac{f}{2f_*}(1 + \hat{\boldsymbol{\Omega}} \cdot \hat{\mathbf{e}}_2)\big)e^{-i\frac{f}{2f_*}(1 + \hat{\boldsymbol{\Omega}} \cdot \hat{\mathbf{e}}_2)}\Big].$$
(2.2.16)

The signal in Eq.(2.2.8) is then given by

$$s(t) = \int_{-\infty}^{+\infty} df \int_{S^2} d\Omega \bigg(\sum_A \big(\tilde{\mathbf{e}}_{ij}^A(\hat{\boldsymbol{\Omega}}) D^{ij}(\hat{\boldsymbol{\Omega}} \cdot \hat{\mathbf{e}}_1, \hat{\boldsymbol{\Omega}} \cdot \hat{\mathbf{e}}_2, f) h_A(f, \hat{\boldsymbol{\Omega}})\big)e^{i2\pi f(t - \hat{\boldsymbol{\Omega}} \cdot \frac{\bar{\mathbf{x}}_1}{c})}\bigg). \quad (2.2.17)$$

where we have finally introduced the complete expression of the detector tensor

$$D^{ij}(\hat{\boldsymbol{\Omega}} \cdot \hat{\mathbf{e}}_1, \hat{\boldsymbol{\Omega}} \cdot \hat{\mathbf{e}}_2, f) = \frac{(\hat{\mathbf{e}}_1 \otimes \hat{\mathbf{e}}_1)^{ij}\mathcal{T}_{Mich,1}(\hat{\boldsymbol{\Omega}} \cdot \hat{\mathbf{e}}_1, f) - (\hat{\mathbf{e}}_2 \otimes \hat{\mathbf{e}}_2)^{ij}\mathcal{T}_{Mich,2}(\hat{\boldsymbol{\Omega}} \cdot \hat{\mathbf{e}}_2, f)}{2}.$$
(2.2.18)

When GW frequencies approache f_* or higher values, transfer functions cannot be ignored anymore and their effects must be considered; in particular we now have frequency-dependent angular pattern functions for each polarization mode

$$F^A(\hat{\boldsymbol{\Omega}}, f) = D^{ij}(\hat{\boldsymbol{\Omega}} \cdot \hat{\mathbf{e}}_1, \hat{\boldsymbol{\Omega}} \cdot \hat{\mathbf{e}}_2, f) e_{ij}^A(\hat{\boldsymbol{\Omega}}). \quad (2.2.19)$$

When $f \ll f_*$, transfer function effects are negligible and the detector tensor does not depend on the GW frequency anymore. Moreover, if we set $\hat{\mathbf{e}}_1 = (1, 0, 0)^T$ and $\hat{\mathbf{e}}_2 = (0, 1, 0)^T$ we see that Eqs.(2.1.3) and (2.1.4) are recovered.

2.3 Transfer Function of a Fabry-Pèrot Interferometer

All 2nd-generation ground based interferometers have Fabry-Pèrot cavities built in both arms: the idea is to extend the interaction between GWs and light by forcing the latter to "bounce" inside the cavity for a longer period of time before recombining the two beams: this is achieved by "trapping" photons using highly reflective mirrors [74]. We now wish to understand how this behaviour affects the transfer function of such interferometers. We begin by considering the more manageable fourier transform of Eq.(2.2.1)

$$\Delta\widetilde{T} = \frac{L}{c}(\hat{\mathbf{e}}_1 \otimes \hat{\mathbf{e}}_1)^{ij} \int_{S^2} d\Omega \bigg(\sum_A \big(\tilde{\mathbf{e}}_{ij}^A(\hat{\boldsymbol{\Omega}}) h_A(f, \hat{\boldsymbol{\Omega}})\big)e^{-i2\pi f(\hat{\boldsymbol{\Omega}} \cdot \frac{\bar{\mathbf{x}}_a}{c})}\mathcal{T}_{Mich}(\hat{\boldsymbol{\Omega}} \cdot \hat{\mathbf{e}}_1, f)\bigg), \quad (2.3.1)$$

and with a little abuse of notation we rename $\Delta\widetilde{T} \equiv \Delta T$. In order to properly understand the light phase shift induced by cavities, we shall start with the case of a multi-round trip photon using a Michelson interferometer where we assume we can control the number of back and forth bounces made by photons. Then, we move on to the case of a Fabry-Pérot interferometer.

Multi-round trip Michelson interferometer. Let us consider the general case where a photon is emitted at time $t_m = t - \frac{2L}{c}m$ at $\bar{\mathbf{x}}_{\mathbf{a}}$, reaches at $\bar{\mathbf{x}}_{\mathbf{b}}$ at $t_m + \frac{L}{c}$ and then gets back to $\bar{\mathbf{x}}_{\mathbf{a}}$ at $t_m + \frac{2L}{c}$, with $m \in \{1, 2, 3, ..., \infty\}$. Recalling that ΔT denotes a single round-trip for a Michelson-interferometer, we find the following relation

$$\Delta T_m = e^{-i\frac{2f}{f_*}(m-1)}\Delta T, \tag{2.3.2}$$

where we notice that for $m = 1$ we get a trivial identity[3]. Let us further assume that a photon emitted at t_m makes exactly m round trips before reaching the position $\bar{\mathbf{x}}_{\mathbf{a}}$ at time t and exiting the cavity. This means that its total time travel change can be expressed as the sum of each change acquired along every loop, we have

$$\begin{aligned}
\Delta T_m^{tot} &= \Delta T_m + \Delta T_{m-1} + ... + \Delta T_2 + \Delta T_1 \\
&= e^{-i\frac{2f}{f_*}(m-1)}\Delta T_1 + e^{-i\frac{2f}{f_*}(m-2)}\Delta T_1 + ... + e^{-i\frac{2f}{f_*}}\Delta T_1 + \Delta T_1 \\
&= \left(\sum_{n=0}^{m-1} e^{-i\frac{2f}{f_*}n}\right)\Delta T_1 = \frac{\sin\left(\frac{f}{f_*}m\right)}{\sin\left(\frac{f}{f_*}\right)}e^{-i\frac{f}{f_*}(m-1)}\Delta T,
\end{aligned} \tag{2.3.3}$$

where in the second step we used Eq.(2.3.2) and the subscript m in ΔT_m^{tot} denotes the number of round trips carried out by the photon. Indeed the time travel change acquired by a photon coming from m round trips can be related to the one relative to a single round trip by multiplying for a factor

$$g(m,f) = \frac{\sin\left(\frac{f}{f_*}m\right)}{\sin\left(\frac{f}{f_*}\right)}e^{-i\frac{f}{f_*}(m-1)}. \tag{2.3.4}$$

Looking at Eq.(2.3.1) we can re-define the transfer function so that this factor is now included, we get

$$\mathcal{T}_{MultiMich}(\hat{\mathbf{\Omega}} \cdot \hat{\mathbf{e}}_{\mathbf{1}}, f) = \frac{\sin\left(\frac{f}{f_*}m\right)}{\sin\left(\frac{f}{f_*}\right)}e^{-i\frac{f}{f_*}(m-1)}\mathcal{T}_{Mich}(\hat{\mathbf{\Omega}} \cdot \hat{\mathbf{e}}_{\mathbf{1}}, f). \tag{2.3.5}$$

While considering a Michelson interferometer, we mentioned how transfer functions collapse to unity when GW frequencies are lower than f_*. Due to the presence of $g(m,f)$, this is no longer true and we now wish to restore our previous result for a multi-round trip interferometer as well. Let us consider the following limit

$$\lim_{\frac{f}{f_*} \to 0} g(m,f) = m. \tag{2.3.6}$$

---

[3]In the new notation $\Delta T_1 = \Delta T$

It is then possible to introduce the one-arm normalized transfer function of a multi-round trip Michelson interferometer as

$$\mathcal{T}_{MultiMich}^{Norm}(\hat{\mathbf{\Omega}} \cdot \hat{\mathbf{e}}_1, f) = \frac{\sin\left(\frac{f}{f_*}m\right)}{m\sin\left(\frac{f}{f_*}\right)} e^{-i\frac{f}{f_*}(m-1)} \mathcal{T}_{Mich}(\hat{\mathbf{\Omega}} \cdot \hat{\mathbf{e}}_1, f). \tag{2.3.7}$$

Unfortunately, in real life scenarios we cannot control the exact number of loops made by a photon inside a Fabry-Pérot cavity, meaning that we need to approach the problem from a probabilistic point of view.

Fabry-Pérot interferometer. We now wish to understand how light behaves inside a Fabry-Pérot cavity: we follow [72] for a proper discussion. Let us assume that light of frequency f_L is emitted by a laser towards a Fabry-Pérot cavity. Let us further consider the electric field coming out from the cavity, which is given by the superposition of all the fields that entered the cavity at a time $t_m = t - \frac{2L}{c}m$, $m \in \{1, 2, 3, ..., \infty\}$, and are coming out at time t. Assuming no GWs are present, the general expression for a field that entered the cavity at time t_m and went through m round trips before coming out is given by

$$E_m^{cavity} = \left(-r_1^{m-1}r_2^m t_1^2 e^{i2m\frac{f_L}{f_*}}\right) E_{in} e^{-i\omega_L t}, \tag{2.3.8}$$

where $r_{1,2}$ and t_1 are the reflection and transmission coefficients of the mirrors inside the cavity and facing the inside of the cavity itself, $\omega_L = 2\pi f_L$ and $E_{in}e^{-i\omega_L t}$ is the electric field entering the cavity corresponding to the laser light. Reflection coefficients are used to define the cavity finesse as

$$\mathcal{F} = \frac{\pi\sqrt{r_1 r_2}}{1 - r_1 r_2}. \tag{2.3.9}$$

The electric field about to exit the cavity at time t is then given by

$$E_{tot}^{cavity} = \left(\sum_{m=1}^{\infty} E_m^{cavity}\right) = -\left(\frac{r_2 t_1^2 e^{i2\frac{f_L}{f_*}}}{1 - r_1 r_2 e^{i2\frac{f_L}{f_*}}}\right) E_{in} e^{-i\omega_L t}, \tag{2.3.10}$$

thus the total reflected electric field given by the sum of the electric field immediately reflected back and the electric field coming out of the cavity [72] is

$$E_{refl}^{tot} = r_1 E_{in} e^{-i\omega_L t} + E_{tot}^{cavity} = E_{in} e^{-i\omega_L t} \frac{r_1 - r_2 e^{i2\frac{f_L}{f_*}}}{1 - r_1 r_2 e^{i2\frac{f_L}{f_*}}} = R(f_L) E_{in} e^{-i\omega_L t}, \tag{2.3.11}$$

where $R(f_L)$ can be interpreted as the reflection coefficient associated to the cavity. Let us now assume a GW is present: for a single loop it produces a phase shift $\Delta\phi = 2\pi f_L \Delta T$, meaning that after m round trips we have

$$\Delta\phi_m^{tot} = 2\pi f_L \Delta T_m^{tot} = 2\pi f_L \frac{\sin\left(\frac{f}{f_*}m\right)}{\sin\left(\frac{f}{f_*}\right)} e^{-i\frac{f}{f_*}(m-1)} \Delta T_1 = \frac{\sin\left(\frac{f}{f_*}m\right)}{\sin\left(\frac{f}{f_*}\right)} e^{-i\frac{f}{f_*}(m-1)} \Delta\phi, \tag{2.3.12}$$

where we used Eq.(2.3.3). Small values of $\Delta\phi$ imply small values of $\Delta\phi_m^{tot}$), thus for the electric field coming out of the cavity we get

$$
\begin{aligned}
E_m^{cav,GW} &= \left(-r_1^{m-1}r_2^m t_1^2 e^{i2m\frac{f_L}{f_*}} e^{i\Delta\phi_m^{tot}}\right) E_{in} e^{-i\omega_L t} \\
&\approx \left(-r_1^{m-1}r_2^m t_1^2 e^{i2m\frac{f_L}{f_*}}(1+i\Delta\phi_m^{tot})\right) E_{in} e^{-i\omega_L t},
\end{aligned}
\tag{2.3.13}
$$

which is now different from Eq.(2.3.8). The reflected field then becomes

$$
\begin{aligned}
E_{refl}^{tot,GW} &= r_1 E_{in} e^{-i\omega_L t} + \left(\sum_{m=1}^{\infty} E_m^{cav,GW}\right) \\
&= E_{in} e^{-i\omega_L t} \frac{r_1 - r_2 e^{i2\frac{f_L}{f_*}}}{1 - r_1 r_2 e^{i2\frac{f_L}{f_*}}} \left(1 + i\frac{1 - r_1 r_2 e^{i2\frac{f_L}{f_*}}}{r_1 - r_2 e^{i2\frac{f_L}{f_*}}} \sum_{m=1}^{\infty}\left(-r_1^{m-1}r_2^m t_1^2 e^{i2m\frac{f_L}{f_*}}\Delta\phi_m^{tot}\right)\right) \\
&\approx E_{in} e^{-i\omega_L t} \frac{r_1 - r_2 e^{i2\frac{f_L}{f_*}}}{1 - r_1 r_2 e^{i2\frac{f_L}{f_*}}} e^{i\Delta\phi_{FP}},
\end{aligned}
\tag{2.3.14}
$$

where

$$
\begin{aligned}
\Delta\phi_{FP} &= \frac{1 - r_1 r_2 e^{i2\frac{f_L}{f_*}}}{r_1 - r_2 e^{i2\frac{f_L}{f_*}}} \sum_{m=1}^{\infty}\left(-r_1^{m-1}r_2^m t_1^2 e^{i2m\frac{f_L}{f_*}}\Delta\phi_m^{tot}\right)\right) \\
&= \frac{1 - r_1 r_2 e^{i2\frac{f_L}{f_*}}}{r_1 - r_2 e^{i2\frac{f_L}{f_*}}} \sum_{m=1}^{\infty}\left(-r_1^{m-1}r_2^m t_1^2 e^{i2m\frac{f_L}{f_*}} \frac{\sin\left(\frac{f}{f_*}m\right)}{\sin\left(\frac{f}{f_*}\right)} e^{-i\frac{f}{f_*}(m-1)}\Delta\phi_1\right)\right) \\
&= \frac{r_2 t_1^2 e^{i2\frac{f_L}{f_*}}}{\left(r_1 - r_2 e^{i2\frac{f_L}{f_*}}\right)\left(1 - r_1 r_2 e^{i2\left(\frac{f_L}{f_*} - \frac{f}{f_*}\right)}\right)}\Delta\phi,
\end{aligned}
\tag{2.3.15}
$$

is the phase change induced by a GW affecting the path of photons inside the cavity. Notice that Eq.(2.3.14) shows how the effect of a GW on light inside a Fabry-Pérot cavity might be expressed as the perturbation of the reflection coefficient $R(f_L) \to R'(f_L, f) = R(f_L) + \alpha(f_L, f)$, where in general $\alpha \in \mathbb{C}$ and $|\alpha| \ll 1$. Once again we found that $\Delta\phi_{FP}$ can be related to the phase change induced by a Michelson interferometer. Moreover, we focus on the GW-frequency dependent term and ignore the rest of the amplification factor, this way we can define the transfer function for a Fabry-Pérot interferometer

$$
\mathcal{T}_{FP}(\hat{\mathbf{\Omega}} \cdot \hat{\mathbf{e}}_1, f) = \frac{\mathcal{T}_{Mich}(\hat{\mathbf{\Omega}} \cdot \hat{\mathbf{e}}_1, f)}{1 - r_1 r_2 e^{i2\left(\frac{f_L}{f_*} - \frac{f}{f_*}\right)}}.
\tag{2.3.16}
$$

We want to define the normalized transfer function for a Fabry-Pérot interferometer in a way that reduces to unity when $f \ll f_*$, this time we have

$$\lim_{\frac{f}{f_*} \to 0} \frac{\mathcal{T}_{Mich}(\hat{\mathbf{\Omega}} \cdot \hat{\mathbf{e}}_1, f)}{1 - r_1 r_2 e^{i2\left(\frac{f_L}{f_*} - \frac{f}{f_*}\right)}} = \frac{1}{1 - r_1 r_2 e^{i2\frac{f_L}{f_*}}}, \tag{2.3.17}$$

which leads us to the following relation

$$\mathcal{T}_{FP}^{Norm}(\hat{\mathbf{\Omega}} \cdot \hat{\mathbf{e}}_1, f) = \frac{1 - r_1 r_2 e^{i2\frac{f_L}{f_*}}}{1 - r_1 r_2 e^{i2\left(\frac{f_L}{f_*} - \frac{f}{f_*}\right)}} \mathcal{T}_{Mich}(\hat{\mathbf{\Omega}} \cdot \hat{\mathbf{e}}_1, f). \tag{2.3.18}$$

Both normalized transfer functions given by Eqs.(2.3.7) and (2.3.16) are in good agreement with results found in [89] and [90] and two example plots are shown in Fig.2.5. Let us further assume that $f_L/f_* = 2n\pi$; this condition can be achieved setting the proper laser frequency. The detector tensor is given by

$$D^{ij}(\hat{\mathbf{\Omega}} \cdot \hat{\mathbf{e}}_1, \hat{\mathbf{\Omega}} \cdot \hat{\mathbf{e}}_2, f) = C(f) \frac{(\hat{\mathbf{e}}_1 \otimes \hat{\mathbf{e}}_1)^{ij} \mathcal{T}_{Mich,1}(\hat{\mathbf{\Omega}} \cdot \hat{\mathbf{e}}_1, f) - (\hat{\mathbf{e}}_2 \otimes \hat{\mathbf{e}}_2)^{ij} \mathcal{T}_{Mich,2}(\hat{\mathbf{\Omega}} \cdot \hat{\mathbf{e}}_2, f)}{2},$$
$$\tag{2.3.19}$$

which differs from Eq.(2.2.18) only for a GW frequency dependent factor

$$C(f) = \frac{1 - r_1 r_2}{1 - r_1 r_2 e^{i2\left(\frac{f_L}{f_*} - \frac{f}{f_*}\right)}}. \tag{2.3.20}$$

It is worth noting that all the information relative to GW direction and detector geometry were already contained in the transfer function of a Michelson interferometer. The detector output has the same form of Eq.(2.2.17), although the detector tensor that appears in the equation is now given by Eq.(2.3.19). Let us focus on the absolute value of the unnormalized transfer function and assume for simplicity $r_2 = 1$, $\frac{2f_L}{f_*} = 2n\pi$ and rename $r_1 \equiv r$. Taking Eq.(2.3.16) and considering the absolute value of the denominator of the right handside term we have

$$\sqrt{\left(1 - r\cos\left(2\frac{f}{f_*}\right)\right)^2 + r^2 \sin^2\left(2\frac{f}{f_*}\right)} = \sqrt{(1 + r^2) - 2r\cos\left(2\frac{f}{f_*}\right)}. \tag{2.3.21}$$

When $f \ll f_*$ we can expand $2r\cos\left(2\frac{f}{f_*}\right) = 2r(1 - \frac{1}{2}\left(2\frac{f}{f_*}\right)^2)$, thus we get

$$\sqrt{(1 + r^2) - 2r\cos\left(2\frac{f}{f_*}\right)} = \sqrt{(1 - r^2) + r\left(2\frac{f}{f_*}\right)^2} = (1 - r)\sqrt{\left(1 + r\frac{16\pi^2 L^2 f^2}{(1 - r)^2 c^2}\right)}$$

$$= (1 - r)\sqrt{\left(1 + r\left(\frac{f}{f_p}\right)^2\right)}, \tag{2.3.22}$$

where we have defined the pole frequency and the storage time[4]

$$f_p = \frac{1}{4\pi\tau}, \qquad \tau = \frac{2L}{c}\frac{1}{1-r^2} \approx \frac{L}{c}\frac{1}{1-r}, \tag{2.3.23}$$

meaning that the absolute value of Eq.(2.3.16) can be expressed as

$$|\mathcal{T}_{FP}^{norm}(\hat{\mathbf{\Omega}} \cdot \hat{\mathbf{e}}_1, f)| \approx \frac{|\mathcal{T}_{Mich}(\hat{\mathbf{\Omega}} \cdot \hat{\mathbf{e}}_1, f)|}{(1-r)\sqrt{\left(1 + r\left(\frac{f}{f_p}\right)^2\right)}}. \tag{2.3.24}$$

We found that with Fabry-Pérot interferometers, if the period of the GW becomes comparable to the storage time there is another contribution to the detector sensitivity loss, besides the loss due to the *sinc* function in the Michelson transfer function.

2.4   Two-Detector Correlation and Signal-to-Noise ratio

In the first chapter we mentioned how the SGWB can be considered as a superposition of waves produced by a huge number of unresolved sources: it is then impossible to determine the form of the true GW signal $h(t)$, since by definition it is considered an unpredictable fluctuating variable. As a consequence we expect a single detector to be useless while detecting gravitational radiation from stochastic backgrounds. Moreover, in realistic situations gravitational waves can be buried deep in noise, with the latter being larger than the actual signal itself, making possible GW detections really hard to see. We now wish to understand how we may overcome this issue: following [43, 72] the idea is to work with at least two interferometers which allow us to match the output of the first detector to the output of the second one, so we can actually see if a GW signal is detected from both interferometers. We also wish to show how this allow us to neglect noise terms by considering ensamble averages. We further assume that the long wavelength limit is valid, all possible modes exist and we consider the signal to be given by Eq.(2.1.2) for both detectors

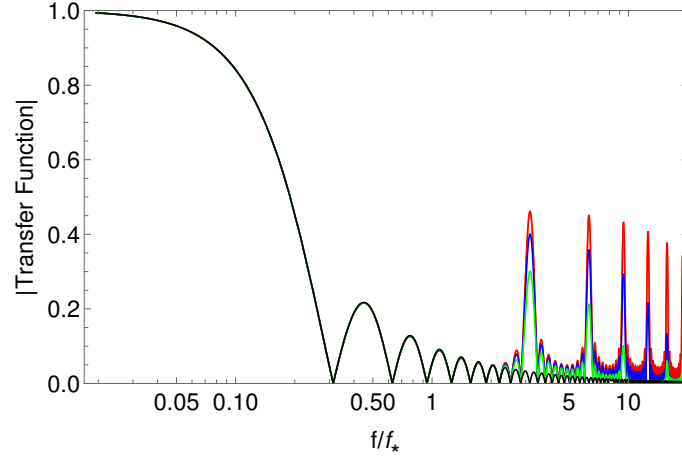$$s_j(t) = h_j(t) + n_j(t), \qquad j = 1, 2. \tag{2.4.1}$$

with

$$h_j(t, \bar{\mathbf{x}}_j) = \sum_A \int_{-\infty}^{+\infty} df \int_{S^2} d\Omega \left(F_j^A(\hat{\mathbf{\Omega}})h_A(f, \hat{\mathbf{\Omega}})\right)e^{i2\pi f(t - \hat{\mathbf{\Omega}}\cdot\frac{\bar{\mathbf{x}}_j}{c})}, \tag{2.4.2}$$

where $\bar{\mathbf{x}}_j$ is the j-th detector location while $F_j^A(\hat{\mathbf{\Omega}})$, $A = +, \times, x, y, b, l$, are its angular pattern functions. In correlation analysis detector outputs are related defining the quantity
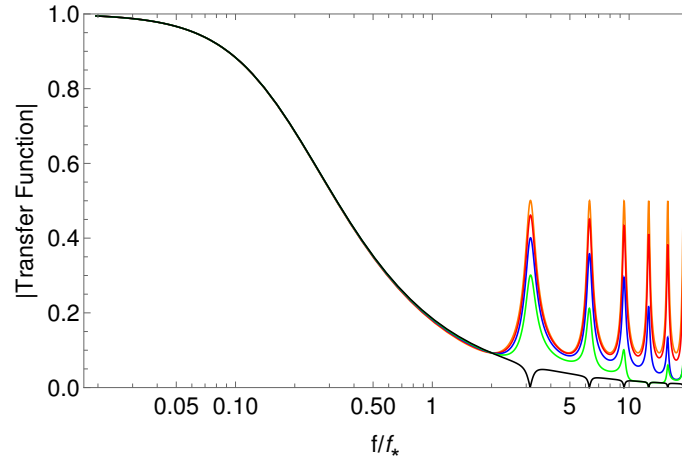
$$Y = \int_{-T/2}^{T/2} dt \int_{-T/2}^{+T/2} dt' s_1(t)s_2(t')Q(t - t'), \tag{2.4.3}$$

---

[4]Time needed to reduce the number of photons inside the cavity of a factor $1/e$

(a)

(b)

Figure 2.5: Absolute value of the normalized one-arm transfer function for a multi-round trip Michelson interferometer (a) and a Fabry-Pèrot interferometer (finesse=10 and $f_L/f_* = 2n\pi$) (b) for different values of the angle $\hat{\boldsymbol{\Omega}} \cdot \hat{\mathbf{e}}_{\mathbf{1}}$ ((2π,Orange), ($\frac{\pi}{6}$,Red), ($\frac{\pi}{4}$,Blue), ($\frac{\pi}{3}$,Green), ($\frac{\pi}{2}$,Black)).

where T is the total observation time and $Q(t)$ is the *filter function* [72]. However, it is more convenient to switch to the frequency space considering the Fourier transform[5] of Eq.(2.4.2)

$$\tilde{h}_j(f,\bar{\mathbf{x}}_j) = \sum_A \int_{S^2} d\Omega \big(F_j^A(\hat{\mathbf{\Omega}})h_A(f,\hat{\mathbf{\Omega}})\big)e^{-i2\pi f\hat{\mathbf{\Omega}}\cdot\frac{\bar{\mathbf{x}}_j}{c}}, \tag{2.4.4}$$

expressing the signal as $s_j(f) = \tilde{h}_j + n_j(f)$, with $n_j(f)$ Fourier transform of the time dependent noise function. In terms of frequency, we can exploit the following identity

$$\delta_T(f) \equiv \int_{-T/2}^{T/2} dt e^{i2\pi ft} = \frac{\sin(\pi fT)}{fT}, \tag{2.4.5}$$

which is equivalent to the Dirac delta for $fT\to\infty$[6], thus Eq.(2.4.3) becomes

$$Y = \int_{-\infty}^{+\infty} df \int_{-\infty}^{+\infty} df' \int_{-\infty}^{+\infty} df''\delta_T(f-f'')\delta_T(f'-f'')s_1^*(f)s_2(f')Q(f'')$$
$$= \int_{-\infty}^{+\infty} df s_1^*(f)s_2(f)Q(f), \tag{2.4.6}$$

where $Q(f)$ is the Fourier transform of the time dependent filter function. If we consider the following ensemble average[7]

$$\langle s_1^*(f)s_2(f)\rangle = \langle\tilde{h}_1^*(f)h_2(f)\rangle + \langle\tilde{h}_1^*(f)n_2(f)\rangle + \langle n_1^*(f)\tilde{h}_2(f)\rangle + \langle n_1^*(f)n_2(f)\rangle, \tag{2.4.7}$$

a reasonable assumption is that different detector noises are uncorrelated and so are the true GW signal detected by one interferometer and the noise of the other, meaning that $\langle n_1^*(f)n_2(f)\rangle = 0$ and $\langle\tilde{h}_i^*(f)n_j(f)\rangle = \langle n_i^*(f)\tilde{h}_j(f)\rangle = 0$, $i,j = \{1,2\}$, $i\neq j$. Indeed, we define the signal S as the ensemble average[8] of Y and we get

$$S = \langle Y\rangle = \int_{-\infty}^{+\infty} df\langle s_1^*(f)s_2(f)\rangle Q(f) = \int_{-\infty}^{\infty} df\langle\tilde{h}_1^*(f)\tilde{h}_2(f)\rangle Q(f)$$
$$= \int_{-\infty}^{+\infty} df \sum_{A,A'} \int d\Omega \int d\Omega' \int_0^{2\pi} \frac{d\psi}{2\pi} F_1^A(\hat{\mathbf{\Omega}})F_2^{A'}(\hat{\mathbf{\Omega}}')\langle h_A^*(f,\hat{\mathbf{\Omega}})h_{A'}(f,\hat{\mathbf{\Omega}}')\rangle e^{i2\pi f(\hat{\mathbf{\Omega}}'\cdot\frac{\bar{\mathbf{x}}_2}{c}-\hat{\mathbf{\Omega}}\cdot\frac{\bar{\mathbf{x}}_1}{c})}Q(f)$$
$$= \frac{T}{2}\sum_A \int_{-\infty}^{+\infty} df S^A(f) \int_0^{2\pi} \frac{d\psi}{2\pi} \int_{S^2} \frac{d\Omega}{4\pi} e^{i2\pi f\hat{\mathbf{\Omega}}\cdot\frac{\Delta\bar{\mathbf{x}}}{c}} \big(F_i^A(\hat{\mathbf{\Omega}},\psi)F_j^A(\hat{\mathbf{\Omega}},\psi)\big)Q(f), \tag{2.4.8}$$

---

[5]We have $G(t) = \int_{-\infty}^{\infty} df\tilde{G}(f)e^{i2\pi ft}$.

[6]2nd-generation ground based interferometers are sensible to frequencies ranging from $1-10^3$ Hz. For sufficiently large observation periods we are justified to assume this limit to be true.

[7]We recall that the ergodic assumption must be used here, thus the ensemble average is replaced by a time average.

[8]We recall that angular pattern functions for tensor and vector polarization modes depend on the angular variable ψ, meaning that also the average over this angle must be included.

where we have used Eq.(1.4.3) and Eq.(2.4.5), with $\delta(0) = T$ and $\Delta\bar{\mathbf{x}} = \bar{\mathbf{x}}_J - \bar{\mathbf{x}}_I$ is the distance betwen the two detectors. Let us now consider Eq.(1.4.10): since we are considering an unpolarized background, we are justified to assume that

$$\Omega_{gw}^+(f) = \Omega_{gw}^\times(f) \rightarrow \Omega_{gw}^T(f) = \Omega_{gw}^+(f) + \Omega_{gw}^\times(f)$$
$$\Omega_{gw}^x(f) = \Omega_{gw}^y(f) \rightarrow \Omega_{gw}^V(f) = \Omega_{gw}^x(f) + \Omega_{gw}^y(f), \tag{2.4.9}$$

both for tensor and vector modes. Something different needs to be said for scalar modes: through Eqs.(2.1.23)-(2.1.24) we showed that breathing and longitudinal polarization modes are degenerate when $f \ll f_*$ and it is not possible for us to separate their contribution to the SGWB energy density. Longitudinal mode contributions can be expressed as a fraction of the breathing ones, thus we have

$$\Omega_{gw}^l(f) = \kappa(f)\Omega_{gw}^b(f) \rightarrow \Omega_{gw}^S(f) = \Omega_{gw}^b(f) + \Omega_{gw}^l(f) = \Omega_{gw}^b(f)(1 + \kappa(f)). \tag{2.4.10}$$

Recalling Eq.(1.4.10), we finally rewrite Eq.(2.4.8) as

$$S = \frac{3H_0^2 T}{4\pi^2} \sum_A \int_{-\infty}^{+\infty} df\, f^{-3} \Omega_{gw}^A(f) \int_0^{2\pi} \frac{d\psi}{2\pi} \int_{S^2} \frac{d\Omega}{4\pi} e^{i2\pi f \hat{\mathbf{\Omega}} \cdot \frac{\Delta\bar{\mathbf{x}}}{c}} \left(F_i^A(\hat{\mathbf{\Omega}}, \psi) F_j^A(\hat{\mathbf{\Omega}}, \psi) \right) Q(f)$$
$$= \frac{3H_0^2 T}{8\pi^2} \int_{-\infty}^{+\infty} df\, f^{-3} \left(\Omega_{gw}^T(f)\Gamma^T(f) + \Omega_{gw}^V(f)\Gamma^V(f) + \frac{2}{1+\kappa}\Omega_{gw}^S(f)\Gamma^S(f) \right) Q(f), \tag{2.4.11}$$

where for tensor, vector and scalar modes we have defined the corresponding *overlap reduction function*[9]

$$\Gamma_{IJ}^T = \int_0^{2\pi} \frac{d\psi}{2\pi} \int_{S^2} \frac{d\Omega}{4\pi} e^{i2\pi f \hat{\mathbf{\Omega}} \cdot \frac{\Delta\bar{\mathbf{x}}}{c}} \Big(\sum_{A=+,\times} F_I^A(\hat{\mathbf{\Omega}}, \psi) F_J^A(\hat{\mathbf{\Omega}}, \psi) \Big), \tag{2.4.12}$$

$$\Gamma_{IJ}^V = \int_0^{2\pi} \frac{d\psi}{2\pi} \int_{S^2} \frac{d\Omega}{4\pi} e^{i2\pi f \hat{\mathbf{\Omega}} \cdot \frac{\Delta\bar{\mathbf{x}}}{c}} \Big(\sum_{A=x,y} F_I^A(\hat{\mathbf{\Omega}}, \psi) F_J^A(\hat{\mathbf{\Omega}}, \psi) \Big), \tag{2.4.13}$$

$$\Gamma_{IJ}^S = \int_{S^2} \frac{d\Omega}{4\pi} e^{i2\pi f \hat{\mathbf{\Omega}} \cdot \frac{\Delta\bar{\mathbf{x}}}{c}} \Big(F_I^b(\hat{\mathbf{\Omega}}) F_J^b(\hat{\mathbf{\Omega}}) + \kappa F_I^l(\hat{\mathbf{\Omega}}) F_J^l(\hat{\mathbf{\Omega}}) \Big), \tag{2.4.14}$$

Overlap reduction functions are key objects in the context of cross correlation because they are a measure of the correlation between two interferometers. We now wish to investigate their properties and we begin by noticing that they are dimensionless, they show oscillatory behaviours at high frequencies and they contain information on both GW polarization and

---

[9]As we shall see, the ψ-dependence in $\sum_A F_i^A(\hat{\mathbf{\Omega}}, \psi) F_j^A(\hat{\mathbf{\Omega}}, \psi)$ cancels out: this is why we usually omit this angular variable in angular pattern function expressions, although we decided to show it in this instance for completeness.

frequency, but also information on detector geometry and angular sensitivity, since angular pattern functions appear in their definitions. Moreover, when we consider a detector pair, overlap reduction functions are suggesting that different interferometers detect a different GW signal both because of their different locations and orientations. Let us now discuss their oscillatory behaviour: the complex exponential factor forces us to introduce a new characteristic frequency $f_c = \frac{c}{2\pi|\Delta\overline{\mathbf{x}}|}$. When $f \gg f_c$[10] we see that $\Gamma_{ij}(f)$ starts to oscillate very rapidly and the signal S tends to zero. However, 2nd-generation interferometers are located sufficiently far apart from each other, thus inducing f_c to be approximately two order of magnitude smaller than f_*, meaning that if GW frequencies reach f_*, then the overlap function is very close to zero and so is the signal S. This is the reason why we feel safe to work in the long wavelength limit with ground-based interferometers.

We further introduce *normalized overlap reduction functions*

$$\gamma^N(f) = \frac{\Gamma_{IJ}^N(f)}{F_{IJ}^N}, \qquad\qquad N = T, V, S \qquad\qquad (2.4.15)$$

where F_{IJ}^N is obtained computing Γ_{IJ}^N in the scenario where the two detectors are of the same type[11] and share both location and orientation. In the following, while computing F_{IJ}^N we use the subscript "$I = J$" to underline these assumptions: we get

$$F_{IJ}^T = \int_0^{2\pi} \frac{d\psi}{2\pi} \int_{S^2} \frac{d\Omega}{4\pi} \Big(\sum_{A=+,\times} F_I^A(\hat{\mathbf{\Omega}}, \psi) F_J^A(\hat{\mathbf{\Omega}}, \psi) \Big)\Big|_{\mathbf{I=J}} =$$

$$= \int_0^{2\pi} \frac{d\psi}{2\pi} \int_{S^2} \frac{d\Omega}{4\pi} \big[(F^+(\theta, \phi, \psi))^2 + (F^\times(\theta, \phi, \psi))^2 \big] =$$

$$= \int \frac{d\psi}{2\pi} \int_{S^2} \frac{d\Omega}{4\pi} \Big\{ \frac{1}{4}[(1 + \cos^2\theta)\cos 2\phi]^2 \cos^2 2\psi + \cos^2\theta \sin^2 2\phi \sin^2 2\psi +$$

$$- (1 + \cos^2\theta)\cos\theta\sin 2\phi\cos 2\phi\sin 2\psi\cos 2\psi \Big\} + \int \frac{d\psi}{2\pi} \int_{S^2} \frac{d\Omega}{4\pi} \Big\{ \frac{1}{4}[(1 + \cos^2\theta)\cos 2\phi]^2 \sin^2 2\psi +$$

$$+ \cos^2\theta \sin^2 2\phi \cos^2 2\psi + (1 + \cos^2\theta)\cos\theta\sin 2\phi\cos 2\phi\sin 2\psi\cos 2\psi \Big\} =$$

$$= \int \frac{d\psi}{2\pi} \int_{S^2} \frac{d\Omega}{4\pi} \Big\{ \frac{1}{4}[(1 + \cos^2\theta)\cos 2\phi]^2 \overbrace{(\cos^2 2\psi + \sin^2 2\psi)}^{=1} + \cos^2\theta \sin^2 2\phi \overbrace{(\cos^2 2\psi + \sin^2 2\psi)}^{=1} \Big\} =$$

$$= \frac{1}{4\pi} \int_0^{2\pi} d\phi \int_0^\pi d\theta \sin\theta \Big\{ \frac{1}{4}[(1 + \cos^2\theta)\cos 2\phi]^2 + \cos^2\theta \sin^2 2\phi \Big\} = \frac{2}{5},$$

$$(2.4.16)$$

---

[10] Once again, the analogous limit in terms of the reduced wavelength is $\lambdabar \ll |\Delta\overline{\mathbf{x}}|$.

[11] for example it cpuld be the case of two two L shaped interferometers.

$$F_{IJ}^V = \int_0^{2\pi} \frac{d\psi}{2\pi} \int_{S^2} \frac{d\Omega}{4\pi} \Big(\sum_{A=x,y} F_I^A(\hat{\mathbf{\Omega}},\psi)F_J^A(\hat{\mathbf{\Omega}},\psi)\Big)\Big|_{\mathbf{I}=\mathbf{J}} =$$

$$= \int_0^{2\pi} \frac{d\psi}{2\pi} \int_{S^2} \frac{d\Omega}{4\pi} \big[(F^x(\theta,\phi,\psi))^2 + (F^y(\theta,\phi,\psi))^2\big] =$$

$$= \int \frac{d\psi}{2\pi} \int_{S^2} \frac{d\Omega}{4\pi} \big[\sin^2\theta(\cos^2\theta\cos^2 2\phi\cos^2\psi + \sin^2 2\phi\sin^2\psi - 2\cos\theta\sin 2\phi\cos 2\phi\sin\psi\cos\psi)\big] +$$

$$+ \int \frac{d\psi}{2\pi} \int_{S^2} \frac{d\Omega}{4\pi} \big[\sin^2\theta(\cos^2\theta\cos^2 2\phi\cos^2\psi + \sin^2 2\phi\sin^2\psi + 2\cos\theta\sin 2\phi\cos 2\phi\sin\psi\cos\psi)\big] =$$

$$= \int \frac{d\psi}{2\pi} \int_{S^2} \frac{d\Omega}{4\pi} \Big\{ \sin^2\theta[\cos^2\theta\cos^2 2\phi \overbrace{(\cos^2 2\psi + \sin^2 2\psi)}^{=1} + \sin^2 2\phi \overbrace{(\cos^2 2\psi + \sin^2 2\psi)}^{=1}]\Big\} =$$

$$= \frac{1}{4\pi} \int_0^{2\pi} d\phi \int_0^{\pi} d\theta \sin^3\theta[\cos^2\theta\cos^2 2\phi + \sin^2 2\phi] = \frac{2}{5},$$

$$(2.4.17)$$

$$F_{IJ}^S = \int_0^{2\pi} \frac{d\psi}{2\pi} \int_{S^2} \frac{d\Omega}{4\pi} \big[F_I^b(\hat{\mathbf{\Omega}})F_J^b(\hat{\mathbf{\Omega}}) + \kappa F_I^l(\hat{\mathbf{\Omega}})F_J^l(\hat{\mathbf{\Omega}})\big]\Big|_{\mathbf{I}=\mathbf{J}} =$$

$$= \int_0^{2\pi} \frac{d\psi}{2\pi} \int_{S^2} \frac{d\Omega}{4\pi} \big[(F^b(\theta,\phi))^2 + \kappa(F^l(\theta,\phi))^2\big] =$$

$$= \frac{1}{4\pi} \int_0^{2\pi} d\phi \int_0^{\pi} d\theta \sin\theta \big(\frac{1}{2} + \kappa\big) \frac{1}{2} \sin^4\theta \cos^2 2\phi = \frac{1+2\kappa}{15}. \qquad (2.4.18)$$

It is worth noting how Eqs.(2.4.16)-(2.4.17) do not depend on the polarization angle ψ and the integration over this variable becomes trivial and can be omitted: this is due to the fact that the objects $(F^+)^2 + (F^\times)^2$, $(F^x)^2 + (F^y)^2$ are ψ-invariant. Although we showed this in the particular case of two identical detectors in the same location and identically oriented, it is straightforward to show this is true in general: under the assumptions made for a SGWB it seems reasonable to expect the physics of the the problem not to depend on the rotation of the axes lying on the plane orthogonal to $\hat{\mathbf{\Omega}}$ with respect to the GW direction itself[12]. In the limit where $I = J$, we recover the quantity $\sum_A F_I^A(\hat{\mathbf{\Omega}})F_I^A(\hat{\mathbf{\Omega}})$ which is the *antenna power pattern* of a single detector and represents its maximum detection reach along different angular directions. In Fig. 2.6, 2.7, 2.8 we show 3D plots related to antenna power pattern square root for tensor, vector and scalar polarization modes along with their 2D projections for some fixed values of θ. Finally, from Eq.(2.4.15) we find the normalized overlap reduction functions for each mode

$$\gamma_{IJ}^T = \frac{5}{2} \int_{S^2} \frac{d\Omega}{4\pi} e^{i2\pi f\hat{\mathbf{\Omega}}\cdot\frac{\Delta\overline{\mathbf{X}}}{c}} \Big(\sum_{A=+,\times} F_I^A(\hat{\mathbf{\Omega}})F_J^A(\hat{\mathbf{\Omega}})\Big), \qquad (2.4.19)$$

---

[12] These axes still need to be orthogonal to each other to properly define polarization tensors.
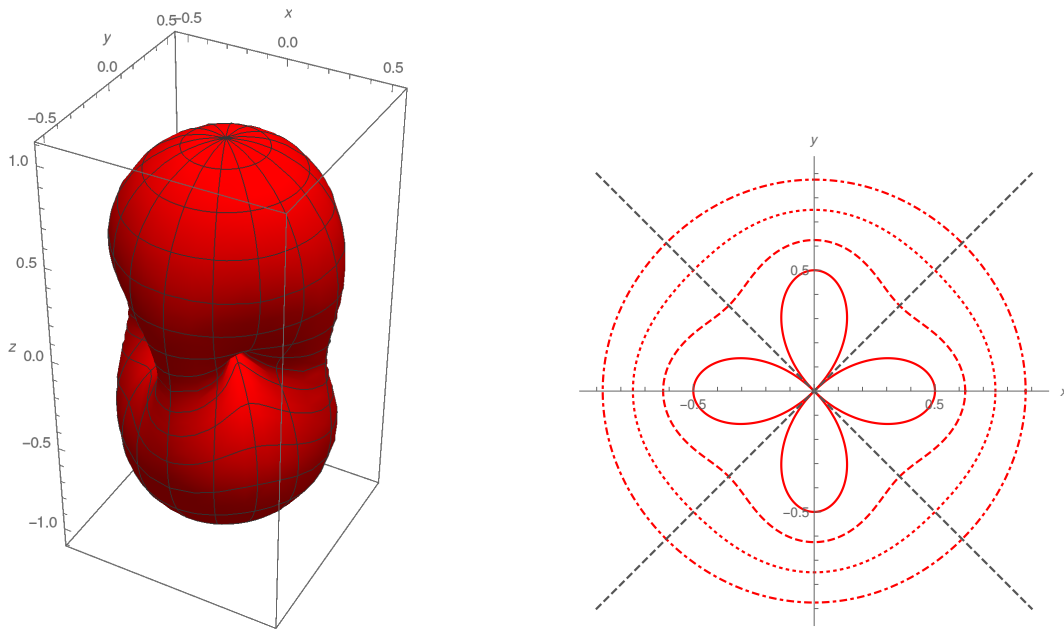
Figure 2.6: $3D$ plot of $\sqrt{(F^+)^2 + (F^\times)^2}$ (peanut diagram), and relative projection on a $2D$ plane for different fixed values of θ (($\frac{\pi}{6}$, dot-dashed), ($\frac{\pi}{4}$, dotted), ($\frac{\pi}{3}$, dashed), ($\frac{\pi}{2}$, solid).
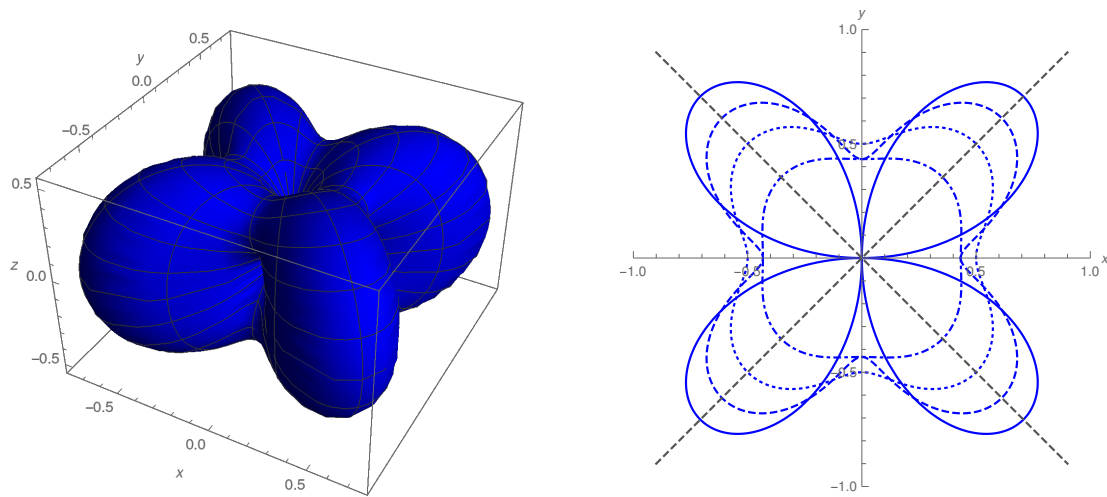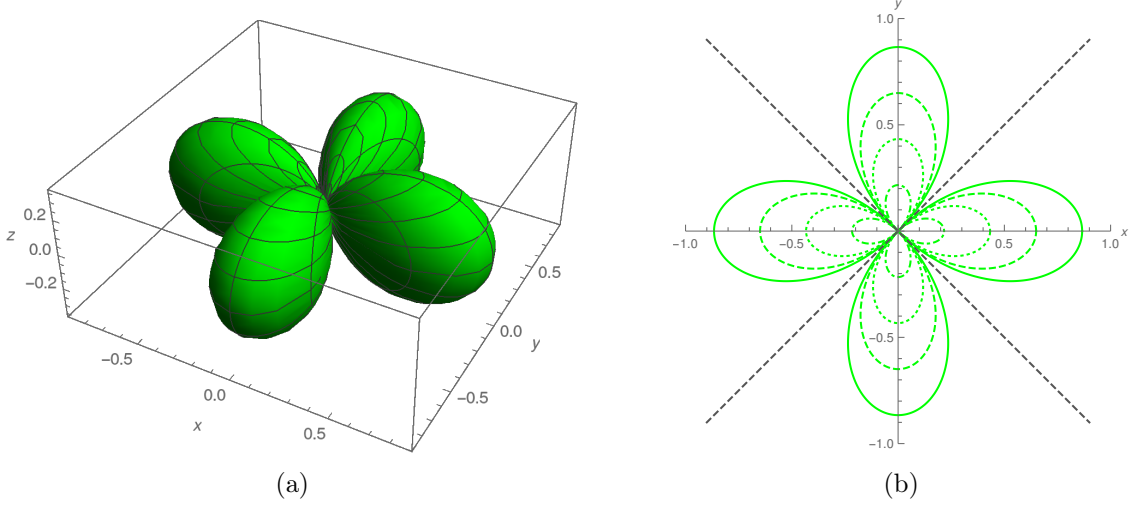

Figure 2.7: $3D$ plot of $\sqrt{(F^x)^2 + (F^y)^2}$, and relative projection on a $2D$ plane for different fixed values of θ (($\frac{\pi}{6}$, dot-dashed), ($\frac{\pi}{4}$, dotted), ($\frac{\pi}{3}$, dashed), ($\frac{\pi}{2}$, solid).

(a)   (b)

Figure 2.8: $3D$ plot of $\sqrt{(F^b)^2 + (F^l)^2}$, and relative projection on a $2D$ plane for different fixed values of θ (($\frac{\pi}{6}$, dot-dashed), ($\frac{\pi}{4}$, dotted), ($\frac{\pi}{3}$, dashed), ($\frac{\pi}{2}$, solid).

$$\gamma_{IJ}^{V} = \frac{5}{2} \int_{S^2} \frac{d\Omega}{4\pi} e^{i2\pi f \hat{\mathbf{\Omega}} \cdot \frac{\Delta \overline{\mathbf{X}}}{c}} \Big(\sum_{A=x,y} F_I^A(\hat{\mathbf{\Omega}}) F_J^A(\hat{\mathbf{\Omega}}) \Big), \tag{2.4.20}$$

$$\gamma_{IJ}^{S} = \frac{15}{1+2\kappa} \int_{S^2} \frac{d\Omega}{4\pi} e^{i2\pi f \hat{\mathbf{\Omega}} \cdot \frac{\Delta \overline{\mathbf{X}}}{c}} \big(F_I^b(\hat{\mathbf{\Omega}}) F_J^b(\hat{\mathbf{\Omega}}) + \kappa F_I^l(\hat{\mathbf{\Omega}}) F_J^l(\hat{\mathbf{\Omega}}) \big), \tag{2.4.21}$$

and Eq.(2.4.11) can be rewritten as

$$S = \frac{3H_0^2 T}{20\pi^2} \int_{-\infty}^{+\infty} df f^{-3} \big(\Omega_{gw}^T(f)\gamma^T(f) + \Omega_{gw}^V(f)\gamma^V(f) + \tau(f)\Omega_{gw}^S(f)\gamma^S(f) \big) Q(f), \tag{2.4.22}$$

where

$$\tau(f) = \frac{1}{3} \left(\frac{1 + 2\kappa(f)}{1 + \kappa(f)} \right), \qquad \frac{1}{3} \leq \tau(f) \leq \frac{2}{3}. \tag{2.4.23}$$

Up to now we mainly focused on GW signals and we removed noise contributions considering the ensemble average given by Eq.(2.4.7). However, since a possible GW signal is expected to be very weak, distinguishing the latter from the background noise can be very challenging. Indeed we account for the presence of a background noise by considering Y in the absence

of a GW signal and then compute

$$
\begin{aligned}
N^2 &= \langle Y^2 \rangle - \langle Y \rangle^2 \\
&= \int_{-\infty}^{+\infty} df \int_{-\infty}^{+\infty} df' \left(\langle n_1^*(f) n_2(f) n_1(f') n_2^*(f') \rangle - \langle n_1^*(f) n_2(f) \rangle \langle n_1(f') n_2^*(f') \rangle \right) Q(f) Q(f') \\
&= \int_{-\infty}^{+\infty} df \int_{-\infty}^{+\infty} df' \left(\langle n_1^*(f) n_1(f') \rangle \langle n_2(f) n_2^*(f') \rangle \right),
\end{aligned}
$$
(2.4.24)

where again we assumed noises of different detectors to be uncorrelated. We assume the detector noise to be stationary, thus we may consider the ensemble average

$$
\langle n^*(f) n(f') \rangle = \delta(f - f') \frac{1}{2} S_n(f),
$$
(2.4.25)

meaning that noise and sensitivity of the interferometer are completely specified by the function $S_n(f)$, which is called *power spectral density* (PSD) and has dimension Hz^{-1}. Since we expect $n(t)$ to be real we have $n^*(f) = n(-f)$ and $S_n(f) = S_n(-f)$. We can now use Eq.(2.4.25) to get

$$
N^2 = \frac{T}{4} \int_{-\infty}^{\infty} df \, S_{1n}(f) S_{2n}(f) |Q(f)|^2
$$
(2.4.26)

and we finally define the *Signal-to Noise Ratio* (SNR) as

$$
\begin{aligned}
\frac{S}{N} &= \frac{3 H_0^2 \sqrt{T}}{10 \pi^2} \frac{\int_{-\infty}^{+\infty} df \, f^{-3} \left(\Omega_{gw}^T(f) \gamma^T(f) + \Omega_{gw}^V(f) \gamma^V(f) + \tau(f) \Omega_{gw}^S(f) \gamma^S(f) \right) Q(f)}{\left(\int_{-\infty}^{\infty} df \, S_{1n}(f) S_{2n}(f) |Q(f)|^2 \right)^{\frac{1}{2}}} \\
&= \frac{3 H_0^2 \sqrt{T}}{10 \pi^2} \frac{\int_{-\infty}^{+\infty} df \, f^{-3} \left(\Omega_{gw}^T(f) \gamma^T(f) + \Omega_{gw}^V(f) \gamma^V(f) + \tau(f) \Omega_{gw}^S(f) \gamma^S(f) \right) Q(f)}{\left(\int_{-\infty}^{\infty} df \, S_n^2(f) |Q(f)|^2 \right)^{\frac{1}{2}}},
\end{aligned}
$$
(2.4.27)

where in the last step we have defined the function

$$
S_n(f) = \left(S_{1n}(f) S_{2n}(f) \right)^{\frac{1}{2}}.
$$
(2.4.28)

Since the signal S depends on T, while N depends on its square root, so does the SNR, meaning that the greater the observation time, the better the SNR would be. To maximize the SNR we need to find the optimal form for the filter function $Q(f)$: there is a simple way to show how this is done which we report here. We begin by introducing the following scalar product involving two general complex functions $H(f)$ and $G(f)$, we have

$$
H \cdot G = \int_{-\infty}^{\infty} df \, H^*(f) G(f) S_n^2(f),
$$
(2.4.29)

and we define for simplicity $\Omega_{gw}(f)\gamma(f) = \Omega_{gw}^T(f)\gamma^T(f) + \Omega_{gw}^V(f)\gamma^V(f) + \tau(f)\Omega_{gw}^S(f)\gamma^S(f)$, meaning that Eq.(2.4.27) becomes

$$\frac{S}{N} = \frac{3H_0^2\sqrt{T}}{10\pi^2}\left(\frac{Q(f)\cdot\left(\frac{\gamma_{IJ}(f)\Omega_{gw}(f)}{f^3 S_n^2}\right)}{\sqrt{Q(f)\cdot Q(f)}}\right),$$
(2.4.30)

where we used I and J to denote detectors of the pair. Similarly to the case of two parallel vectors in linear algebra, the previous scalar product is maximized when

$$Q(f) \propto \left(\frac{\gamma_{IJ}(f)\Omega_{gw}(f)}{f^3 S_n^2(f)}\right).$$
(2.4.31)

Finally, using this expression for the filter function, Eq.(2.4.27) may be written as

$$
\begin{aligned}
\frac{S}{N} &= \frac{3H_0^2\sqrt{T}}{10\pi^2}\left(\int_{-\infty}^{+\infty} df \frac{(\Omega_{gw}^T(f)\gamma^T(f) + \Omega_{gw}^V(f)\gamma^V(f) + \tau(f)\Omega_{gw}^S(f)\gamma^S(f))^2}{f^6 S_{1n}(f)S_{2n}(f)}\right)^{\frac{1}{2}} \\
&= \frac{3H_0^2\sqrt{T}}{10\pi^2}\left(\int_{-\infty}^{+\infty} df \frac{(\gamma(f)\Omega_{gw}(f))^2}{f^6 S_{1n}(f)S_{2n}(f)}\right)^{\frac{1}{2}} \\
&= \frac{3H_0^2\sqrt{T}}{10\pi^2}\left(\int_{-\infty}^{+\infty} df \frac{(\gamma(f)\Omega_{gw}(f))^2}{f^6 S_n^2(f)}\right)^{\frac{1}{2}}.
\end{aligned}
$$
(2.4.32)

2.5 Analytic Overlap Function for Two L-shaped Interferometers on Earth

2nd-generation interferometers like LIGO, Virgo or KAGRA are sensitive to GW frequencies ranging from 10 Hz to a few kHz and since $f_* \approx 10^4$ Hz (see Tab. 2.1) we can always work in the long wavelength limit. Under this assumption, we now wish to investigate overlap reduction functions to find a possible analytical expression for each polarization mode. In the following, we proceed as in [43] for the tensor modes, then we extend the results to vector and scalar modes as in [86].

Let us consider a GW detector pair on Earth: we define the unit vector $\hat{\mathbf{d}} = \frac{\Delta\overline{\mathbf{x}}}{|\Delta\overline{\mathbf{x}}|}$, where $\Delta\overline{\mathbf{x}}$ denotes the distance between the two detector locations, and $\alpha \equiv \frac{f}{f_c} = \frac{2\pi f|\Delta\overline{\mathbf{x}}|}{c}$. Appealing to Eqs.(2.1.3), (2.1.4) and (2.4.15) we obtain a second expression for the normalized overlap reduction function for each polarization mode

$$\gamma^N(f) = D^{ij}D^{kl}\Gamma_{ijkl}^N(\alpha, \hat{\mathbf{d}}), \qquad\qquad N = T, V, S$$
(2.5.1)

where

$$\Gamma_{ijkl}^T(\alpha, \hat{\mathbf{d}}) \equiv \frac{5}{2}\sum_{A=+,\times}\int_{S^2}\frac{d\Omega}{4\pi}e^{i\alpha\hat{\mathbf{\Omega}}\cdot\hat{\mathbf{d}}}\tilde{e}_{ij}^A(\hat{\mathbf{\Omega}})\tilde{e}_{kl}^A(\hat{\mathbf{\Omega}}),$$
(2.5.2)

$$\Gamma^V_{ijkl}(\alpha, \hat{\mathbf{d}}) \equiv \frac{5}{2} \sum_{A=x,y} \int_{S^2} \frac{d\Omega}{4\pi} e^{i\alpha\hat{\mathbf{\Omega}}\cdot\hat{\mathbf{d}}} \tilde{e}^A_{ij}(\hat{\mathbf{\Omega}}) \tilde{e}^A_{kl}(\hat{\mathbf{\Omega}}), \tag{2.5.3}$$

and

$$\Gamma^S_{ijkl}(\alpha, \hat{\mathbf{d}}) \equiv \frac{15}{1+2k} \int_{S^2} \frac{d\Omega}{4\pi} e^{i\alpha\hat{\mathbf{\Omega}}\cdot\hat{\mathbf{d}}} \big(\tilde{e}^b_{ij}(\hat{\mathbf{\Omega}}) \tilde{e}^b_{kl}(\hat{\mathbf{\Omega}}) + \kappa \tilde{e}^l_{ij}(\hat{\mathbf{\Omega}}) \tilde{e}^l_{kl}(\hat{\mathbf{\Omega}})\big). \tag{2.5.4}$$

Since the following steps are the same for each polarization mode, for the rest of the discussion we shall omit the apex N for simplicity. Due to its construction, the rank-4 tensor $\Gamma_{ijkl}(\alpha, \hat{\mathbf{d}})$ is symmetric under exchanges of $i \leftrightarrow j$, $k \leftrightarrow l$ and $ij \leftrightarrow kl$: these properties lead to the most general tensor form for $\Gamma_{ijkl}(\alpha, \hat{\mathbf{d}})$, which can be written in terms of the Kronecker delta δ_{ij} and d_i

$$\begin{aligned}\Gamma_{ijkl}(\alpha, \hat{\mathbf{d}}) = {}& A(\alpha)\delta_{ij}\delta_{kl} + B(\alpha)\big(\delta_{ik}\delta_{jl} + \delta_{jk}\delta_{il}\big) + C(\alpha)\big(\delta_{ij}d_k d_l + \delta_{kl}d_i d_j\big) + \\ & + D(\alpha)\big(\delta_{ik}d_j d_l + \delta_{il}d_j d_k + \delta_{jk}d_i d_l + \delta_{jl}d_i d_k\big) + E(\alpha)d_i d_j d_k d_l.\end{aligned} \tag{2.5.5}$$

We now wish to find an expression for the functions $A(\alpha)$, $B(\alpha)$, $C(\alpha)$, $D(\alpha)$, $E(\alpha)$ and we begin by singularly taking the contraction between $\Gamma_{ijkl}(\alpha, \hat{\mathbf{d}})$ and the different rank-4 tensors appearing in the equation above, thus we define

$$\begin{aligned}\xi_1(\alpha) &\equiv \Gamma_{ijkl}\delta^{ij}\delta^{kl}, \\ \xi_2(\alpha) &\equiv \Gamma_{ijkl}\big(\delta^{ik}\delta^{jl} + \delta^{jk}\delta^{il}\big), \\ \xi_3(\alpha) &\equiv \Gamma_{ijkl}\big(\delta^{ij}d^k d^l + \delta^{kl}d^i d^j\big), \\ \xi_4(\alpha) &\equiv \Gamma_{ijkl}\big(\delta^{ik}d^j d^l + \delta^{il}d^j d^k + \delta^{jk}d^i d^l + \delta^{jl}d^i d^k\big), \\ \xi_5(\alpha) &\equiv \Gamma_{ijkl}d^i d^j d^k d^l.\end{aligned} \tag{2.5.6}$$

Since the Kronecker delta satisfies $\delta^{ij}\delta_{ij} = 3$ and $\delta^{ij}d_i d_j = d^j d_j = 1$, we get

$$\begin{aligned}\xi_1(\alpha) = {}& A(\alpha)\delta_{ij}\delta_{kl}\delta^{ij}\delta^{kl} + B(\alpha)\big(\delta_{ik}\delta_{jl} + \delta_{jk}\delta_{il}\big)\delta^{ij}\delta^{kl} + \\ & + C(\alpha)\big(\delta_{ij}d_k d_l + \delta_{kl}d_i d_j\big)\delta^{ij}\delta^{kl} + D(\alpha)\big(\delta_{ik}d_j d_l + \delta_{il}d_j d_k + \delta_{jk}d_i d_l + \delta_{jl}d_i d_k\big)\delta^{ij}\delta^{kl} + \\ & + E(\alpha)d_i d_j d_k d_l\delta^{ij}\delta^{kl} = \\ = {}& 9A(\alpha) + 6B(\alpha) + 6C(\alpha) + 4D(\alpha) + E(\alpha),\end{aligned}$$
$$\tag{2.5.7}$$

$$\begin{aligned}\xi_2(\alpha) = {}& A(\alpha)\delta_{ij}\delta_{kl}\big(\delta^{ik}\delta^{jl} + \delta^{jk}\delta^{il}\big) + B(\alpha)\big(\delta_{ik}\delta_{jl} + \delta_{jk}\delta_{il}\big)\big(\delta^{ik}\delta^{jl} + \delta^{jk}\delta^{il}\big) + \\ & + C(\alpha)\big(\delta_{ij}d_k d_l + \delta_{kl}d_i d_j\big)\big(\delta^{ik}\delta^{jl} + \delta^{jk}\delta^{il}\big) + \\ & + D(\alpha)\big(\delta_{ik}d_j d_l + \delta_{il}d_j d_k + \delta_{jk}d_i d_l + \delta_{jl}d_i d_k\big)\big(\delta^{ik}\delta^{jl} + \delta^{jk}\delta^{il}\big) + \\ & + E(\alpha)d_i d_j d_k d_l\big(\delta^{ik}\delta^{jl} + \delta^{jk}\delta^{il}\big) = \\ = {}& 6A(\alpha) + 24B(\alpha) + 4C(\alpha) + 16D(\alpha) + 2E(\alpha),\end{aligned} \tag{2.5.8}$$

48

$$\xi_3(\alpha) = A(\alpha)\delta_{ij}\delta_{kl}\big(\delta^{ij}d^kd^l + \delta^{kl}d^id^j\big) + B(\alpha)\big(\delta_{ik}\delta_{jl} + \delta_{jk}\delta_{il}\big)\big(\delta^{ij}d^kd^l + \delta^{kl}d^id^j\big) +$$
$$+ C(\alpha)\big(\delta_{ij}d_kd_l + \delta_{kl}d_id_j\big)\big(\delta^{ij}d^kd^l + \delta^{kl}d^id^j\big) +$$
$$+ D(\alpha)\big(\delta_{ik}d_jd_l + \delta_{il}d_jd_k + \delta_{jk}d_id_l + \delta_{jl}d_id_k\big)\big(\delta^{ij}d^kd^l + \delta^{kl}d^id^j\big) +$$
$$+ E(\alpha)d_id_jd_kd_l\big(\delta^{ij}d^kd^l + \delta^{kl}d^id^j\big) =$$
$$= 6A(\alpha) + 4B(\alpha) + 8C(\alpha) + 8D(\alpha) + 2E(\alpha), \tag{2.5.9}$$

$$\xi_4(\alpha) = A(\alpha)\delta_{ij}\delta_{kl}\big(\delta^{ik}d^jd^l + \delta^{il}d^jd^k + \delta^{jk}d^id^l + \delta^{jl}d^id^k\big) +$$
$$+ B(\alpha)\big(\delta_{ik}\delta_{jl} + \delta_{jk}\delta_{il}\big)\big(\delta^{ik}d^jd^l + \delta^{il}d^jd^k + \delta^{jk}d^id^l + \delta^{jl}d^id^k\big) +$$
$$+ C(\alpha)\big(\delta_{ij}d_kd_l + \delta_{kl}d_id_j\big)\big(\delta^{ik}d^jd^l + \delta^{il}d^jd^k + \delta^{jk}d^id^l + \delta^{jl}d^id^k\big) +$$
$$+ D(\alpha)\big(\delta_{ik}d_jd_l + \delta_{il}d_jd_k + \delta_{jk}d_id_l + \delta_{jl}d_id_k\big)\big(\delta^{ik}d^jd^l + \delta^{il}d^jd^k + \delta^{jk}d^id^l + \delta^{jl}d^id^k\big) +$$
$$+ E(\alpha)d_id_jd_kd_l\big(\delta^{ik}d^jd^l + \delta^{il}d^jd^k + \delta^{jk}d^id^l + \delta^{jl}d^id^k\big) =$$
$$= 4A(\alpha) + 16B(\alpha) + 8C(\alpha) + 24D(\alpha) + 4E(\alpha), \tag{2.5.10}$$

$$\xi_5(\alpha) = A(\alpha)\delta_{ij}\delta_{kl}d^id^jd^kd^l + B(\alpha)\big(\delta_{ik}\delta_{jl} + \delta_{jk}\delta_{il}\big)d^id^jd^kd^l + C(\alpha)\big(\delta_{ij}d_kd_l + \delta_{kl}d_id_j\big)d^id^jd^kd^l +$$
$$+ D(\alpha)\big(\delta_{ik}d_jd_l + \delta_{il}d_jd_k + \delta_{jk}d_id_l + \delta_{jl}d_id_k\big)d^id^jd^kd^l + E(\alpha)d_id_jd_kd_ld^id^jd^kd^l =$$
$$= A(\alpha) + 2B(\alpha) + 2C(\alpha) + 4D(\alpha) + E(\alpha). \tag{2.5.11}$$

Putting together Eqs.(2.5.7)-(2.5.11), we can write our results in a matrix form

$$\begin{pmatrix} \xi_1 \\ \xi_2 \\ \xi_3 \\ \xi_4 \\ \xi_5 \end{pmatrix} = \begin{pmatrix} 9 & 6 & 6 & 4 & 1 \\ 6 & 24 & 4 & 16 & 2 \\ 6 & 4 & 8 & 8 & 2 \\ 4 & 16 & 8 & 24 & 4 \\ 1 & 2 & 2 & 4 & 1 \end{pmatrix} \begin{pmatrix} A \\ B \\ C \\ D \\ E \end{pmatrix}, \tag{2.5.12}$$

and the coefficient matrix can be inverted, so that

$$\begin{pmatrix} A \\ B \\ C \\ D \\ E \end{pmatrix} = \frac{1}{8} \begin{pmatrix} 3 & -1 & -3 & 1 & 1 \\ -1 & 1 & 1 & -1 & 1 \\ -3 & 1 & 5 & -1 & -5 \\ 1 & -1 & -1 & 2 & -5 \\ 1 & 1 & -5 & -5 & 35 \end{pmatrix} \begin{pmatrix} \xi_1 \\ \xi_2 \\ \xi_3 \\ \xi_4 \\ \xi_5 \end{pmatrix}. \tag{2.5.13}$$

We now need to find an expression for ξ_1, ξ_2, ξ_3, ξ_4, ξ_5, thus considering Eq.(2.1.9) we introduce the angular coordinate η such that the unit vector $\hat{\mathbf{d}}$ satisfies

$$\begin{cases} \hat{\mathbf{m}} \cdot \hat{\mathbf{d}} = 0 \\ \hat{\mathbf{n}} \cdot \hat{\mathbf{d}} = -\sin\eta \\ \hat{\mathbf{\Omega}} \cdot \hat{\mathbf{d}} = \cos\eta \end{cases} \tag{2.5.14}$$

meaning that $\hat{\mathbf{d}}$ lies on the $\hat{\mathbf{n}}$-$\hat{\boldsymbol{\Omega}}$ plane and its components can be taken as $\hat{\mathbf{d}} = (0, -\sin\eta, \cos\eta)^T$. We set $x \equiv \cos\eta$ and we express ξ_j, $j = 1, ..., 5$ as proper combinations of spherical Bessel functions, which can be found in B.1. Finally we obtain

- for the tensor mode

$$\xi_1(\alpha) = \frac{5}{4} \int_{-1}^{1} dx e^{i\alpha x} \left(\tilde{e}_{ij}^+\tilde{e}_{kl}^+ + \tilde{e}_{ij}^\times\tilde{e}_{kl}^\times\right)\delta^{ij}\delta^{kl} = 0, \qquad (2.5.15)$$

$$\xi_2(\alpha) = \frac{5}{4} \int_{-1}^{1} dx e^{i\alpha x} \left(\tilde{e}_{ij}^+\tilde{e}_{kl}^+ + \tilde{e}_{ij}^\times\tilde{e}_{kl}^\times\right)\left(\delta^{ik}\delta^{jl} + \delta^{jk}\delta^{il}\right) = 20j_0(\alpha), \qquad (2.5.16)$$

$$\xi_3(\alpha) = \frac{5}{4} \int_{-1}^{1} dx e^{i\alpha x} \left(\tilde{e}_{ij}^+\tilde{e}_{kl}^+ + \tilde{e}_{ij}^\times\tilde{e}_{kl}^\times\right)\left(\delta^{ij}d^k d^l + \delta^{kl}d^i d^j\right) = 0, \qquad (2.5.17)$$

$$\xi_4(\alpha) = \frac{5}{4} \int_{-1}^{1} dx e^{i\alpha x} \left(\tilde{e}_{ij}^+\tilde{e}_{kl}^+ + \tilde{e}_{ij}^\times\tilde{e}_{kl}^\times\right)\left(\delta^{ik}d^j d^l + \delta^{il}d^j d^k + \delta^{jk}d^i d^l + \delta^{jl}d^i d^k\right) =$$
$$= 10 \int_{-1}^{1} dx e^{i\alpha x}(1 - x^2) = 40\frac{j_1(\alpha)}{\alpha}, \qquad (2.5.18)$$

$$\xi_5(\alpha) = \frac{5}{4} \int_{-1}^{1} dx e^{i\alpha x} \left(\tilde{e}_{ij}^+\tilde{e}_{kl}^+ + \tilde{e}_{ij}^\times\tilde{e}_{kl}^\times\right)d^i d^j d^k d^l =$$
$$= \frac{5}{4} \int_{-1}^{+1} dx e^{i\alpha x}(1 - x^2)^2 = 20\frac{j_2(\alpha)}{\alpha^2}, \qquad (2.5.19)$$

- for the vector mode

$$\xi_1(\alpha) = \frac{5}{4} \int_{-1}^{1} dx e^{i\alpha x} \left(\tilde{e}_{ij}^x\tilde{e}_{kl}^x + \tilde{e}_{ij}^y\tilde{e}_{kl}^y\right)\delta^{ij}\delta^{kl} = 0, \qquad (2.5.20)$$

$$\xi_2(\alpha) = \frac{5}{4} \int_{-1}^{1} dx e^{i\alpha x} \left(\tilde{e}_{ij}^x\tilde{e}_{kl}^x + \tilde{e}_{ij}^y\tilde{e}_{kl}^y\right)\left(\delta^{ik}\delta^{jl} + \delta^{jk}\delta^{il}\right) = 20j_0(\alpha), \qquad (2.5.21)$$

$$\xi_3(\alpha) = \frac{5}{4} \int_{-1}^{1} dx e^{i\alpha x} \left(\tilde{e}_{ij}^x\tilde{e}_{kl}^x + \tilde{e}_{ij}^y\tilde{e}_{kl}^y\right)\left(\delta^{ij}d^k d^l + \delta^{kl}d^i d^j\right) = 0, \qquad (2.5.22)$$

$$\xi_4(\alpha) = \frac{5}{4} \int_{-1}^{1} dx e^{i\alpha x} \left(\tilde{e}_{ij}^x\tilde{e}_{kl}^x + \tilde{e}_{ij}^y\tilde{e}_{kl}^y\right)\left(\delta^{ik}d^j d^l + \delta^{il}d^j d^k + \delta^{jk}d^i d^l + \delta^{jl}d^i d^k\right) =$$
$$= 5 \int_{-1}^{+1} dx e^{i\alpha x}\left[2 - (1 - x^2)\right] = 20\left(j_0(\alpha) - \frac{j_1(\alpha)}{\alpha}\right), \qquad (2.5.23)$$

$$\xi_5(\alpha) = \frac{5}{4} \int_{-1}^{1} dx\, e^{i\alpha x} \big(\tilde{e}_{ij}^x \tilde{e}_{kl}^x + \tilde{e}_{ij}^y \tilde{e}_{kl}^y\big) d^i d^j d^k d^l =$$

$$= 5 \int_{-1}^{+1} dx\, e^{i\alpha x} \big[(1-x^2) - (1-x^2)^2\big] = 20\left(\frac{j_1(\alpha)}{\alpha} - 4\frac{j_2(\alpha)}{\alpha^2}\right), \qquad (2.5.24)$$

- for the scalar mode

$$\xi_1(\alpha) = \frac{5}{4} \int_{-1}^{1} dx\, e^{i\alpha x} \big(\tilde{e}_{ij}^b \tilde{e}_{kl}^b + \kappa \tilde{e}_{ij}^l \tilde{e}_{kl}^l\big) \delta^{ij} \delta^{kl} = 30\left(\frac{2+\kappa}{1+2\kappa}\right) j_0(\alpha), \qquad (2.5.25)$$

$$\xi_2(\alpha) = \frac{5}{4} \int_{-1}^{1} dx\, e^{i\alpha x} \big(\tilde{e}_{ij}^b \tilde{e}_{kl}^b + \kappa \tilde{e}_{ij}^l \tilde{e}_{kl}^l\big) \big(\delta^{ik} \delta^{jl} + \delta^{jk} \delta^{il}\big) = 60\left(\frac{1+\kappa}{1+2\kappa}\right) j_0(\alpha), \;\; (2.5.26)$$

$$\xi_3(\alpha) = \frac{5}{4} \int_{-1}^{1} dx\, e^{i\alpha x} \big(\tilde{e}_{ij}^b \tilde{e}_{kl}^b + \kappa \tilde{e}_{ij}^l \tilde{e}_{kl}^l\big) \big(\delta^{ij} d^k d^l + \delta^{kl} d^i d^j\big) =$$

$$= \frac{30}{1+2\kappa} \int_{-1}^{+1} dx\, e^{i\alpha x} \big[\kappa + (1-\kappa)(1-x^2)\big] = \frac{60}{1+2\kappa}\left[\kappa j_0(\alpha) + 2(1-\kappa)\frac{j_1(\alpha)}{\alpha}\right],$$
$$(2.5.27)$$

$$\xi_4(\alpha) = \frac{5}{4} \int_{-1}^{1} dx\, e^{i\alpha x} \big(\tilde{e}_{ij}^b \tilde{e}_{kl}^b + \kappa \tilde{e}_{ij}^l \tilde{e}_{kl}^l\big) \big(\delta^{ik} d^j d^l + \delta^{il} d^j d^k + \delta^{jk} d^i d^l + \delta^{jl} d^i d^k\big) =$$

$$= \frac{30}{1+2\kappa} \int_{-1}^{+1} dx\, e^{i\alpha x} \big[2\kappa + (1-2\kappa)(1-x^2)\big] = \frac{120}{1+2\kappa}\left[\kappa j_0(\alpha) + (1-2\kappa)\frac{j_1(\alpha)}{\alpha}\right],$$
$$(2.5.28)$$

$$\xi_5(\alpha) = \frac{5}{4} \int_{-1}^{1} dx\, e^{i\alpha x} \big(\tilde{e}_{ij}^b \tilde{e}_{kl}^b + \kappa \tilde{e}_{ij}^l \tilde{e}_{kl}^l\big) d^i d^j d^k d^l =$$

$$= \frac{15}{2(1+2\kappa)} \int_{-1}^{+1} dx\, e^{i\alpha x} \big[2\kappa - 4\kappa(1-x^2) + (1+2\kappa)(1-x^2)^2\big] =$$

$$= \frac{30}{1+2\kappa}\left[\kappa j_0(\alpha) - 4\kappa\frac{j_1(\alpha)}{\alpha} + 4(1+2\kappa)\frac{j_2(\alpha)}{\alpha^2}\right], \qquad (2.5.29)$$

Considering Eq.(2.5.13) we can list our results in a cleaner way

- Tensor mode

$$\begin{pmatrix} A(\alpha) \\ B(\alpha) \\ C(\alpha) \\ D(\alpha) \\ E(\alpha) \end{pmatrix} = \frac{1}{2\alpha^2} \begin{pmatrix} -5\alpha^2 & 10\alpha & 5 \\ 5\alpha^2 & -10\alpha & 5 \\ 5\alpha^2 & -10\alpha & -25 \\ -5\alpha^2 & 20\alpha & -25 \\ 5\alpha^2 & -50\alpha & 175 \end{pmatrix} \begin{pmatrix} j_0(\alpha) \\ j_1(\alpha) \\ j_2(\alpha) \end{pmatrix} = \frac{1}{42} \begin{pmatrix} -28 & 80 & 3 \\ 42 & -60 & 3 \\ 0 & -120 & -15 \\ 0 & 90 & -15 \\ 0 & 0 & 105 \end{pmatrix} \begin{pmatrix} j_0(\alpha) \\ j_2(\alpha) \\ j_4(\alpha) \end{pmatrix} .$$
$$(2.5.30)$$

- Vector mode

$$
\begin{pmatrix} A(\alpha) \\ B(\alpha) \\ C(\alpha) \\ D(\alpha) \\ E(\alpha) \end{pmatrix} = \frac{5}{2\alpha^2} \begin{pmatrix} 0 & 0 & -4 \\ 0 & 2\alpha & -4 \\ 0 & -4\alpha & 20 \\ \alpha^2 & -7\alpha & 20 \\ -4\alpha^2 & 40\alpha & -140 \end{pmatrix} \begin{pmatrix} j_0(\alpha) \\ j_1(\alpha) \\ j_2(\alpha) \end{pmatrix} = \frac{1}{42} \begin{pmatrix} -28 & -40 & -12 \\ 42 & 30 & -12 \\ 0 & 60 & 60 \\ 0 & -45 & 60 \\ 0 & 0 & -420 \end{pmatrix} \begin{pmatrix} j_0(\alpha) \\ j_2(\alpha) \\ j_4(\alpha) \end{pmatrix} .
$$

$$(2.5.31)$$

- Scalar mode

$$
\begin{pmatrix} A(\alpha) \\ B(\alpha) \\ C(\alpha) \\ D(\alpha) \\ E(\alpha) \end{pmatrix} = \frac{15}{(1+2\kappa)\alpha^2} \begin{pmatrix} \alpha^2 & -2\alpha & (1+2\kappa) \\ 0 & 0 & (1+2\kappa) \\ -\alpha^2 & 2(2+\kappa)\alpha & -5(1+2\kappa) \\ 0 & (1+2\kappa)\alpha & -5(1+2\kappa) \\ (1+2\kappa)\alpha^2 & -10(1+2\kappa)\alpha & -35(1+2\kappa) \end{pmatrix} \begin{pmatrix} j_0(\alpha) \\ j_1(\alpha) \\ j_2(\alpha) \end{pmatrix} =
$$

$$
= \frac{1}{7(1+2\kappa)} \begin{pmatrix} 14(3+\kappa) & -20(3-\kappa) & 3(1+2\kappa) \\ 7(1+2\kappa) & 10(1+2\kappa) & 3(1+2\kappa) \\ 0 & 30(3-\kappa) & -15(1+2\kappa) \\ 0 & -15(1+2\kappa) & -15(1+2\kappa) \\ 0 & 0 & 105(1+2\kappa) \end{pmatrix} \begin{pmatrix} j_0(\alpha) \\ j_2(\alpha) \\ j_4(\alpha) \end{pmatrix} .
$$

$$(2.5.32)$$

Eqs.(2.5.30), (2.5.31) and (2.5.32) show two different forms of the same result and they are equivalent: it is possible to use Bessel functions j_0, j_1, j_2 or j_0, j_2, j_4 and we can switch from one expression to the other using the relations shown in Appendix B. In our case, we decided to stick to the j_0, j_2, j_4 notation. Let us consider Eq.(2.5.1) once again: this time we want to compute all the contractions that appear while reminding ourselves that the detector tensor is tracefree, thus $D^{ii} = 0$. We get

$$
\gamma^N(f) = A(\alpha)\underbrace{D_1^{ii}D_2^{jj}}_{0} + B(\alpha)\big(D_1^{ij}D_{2ij} + D_1^{ij}D_{2ij}\big) + C(\alpha)\big(\underbrace{D_1^{ii}D_2^{kl}d_kd_l}_{0} + \underbrace{D_1^{ij}D_2^{kk}d_id_j}_{0}\big)+
$$
$$
+ D(\alpha)\big(D_1^{ij}D_{2il}d_jd^l + D_1^{ij}D_{2ik}d_jd^k + D_1^{ij}D_{2jl}d_id^l + D_1^{ij}D_{2jk}d_id^k\big) + E(\alpha)D_1^{ij}D_2^{kl}d_id_jd_kd_l =
$$
$$
= 2B(\alpha)D_1^{ij}D_{2ij} + 4D(\alpha)D_1^{ij}D_{2il}d_jd^l + E(\alpha)D_1^{ij}D_2^{kl}d_id_jd_kd_l =
$$
$$
= \rho_1(\alpha)D_1^{ij}D_{2ij} + \rho_2(\alpha)D_1^{ij}D_{2il}d_jd^l + \rho_3(\alpha)D_1^{ij}D_2^{kl}d_id_jd_kd_l,
$$

$$(2.5.33)$$

where in the last line we have defined $\rho_1(\alpha) = 2B(\alpha)$, $\rho_2(\alpha) = 4D(\alpha)$ and $\rho_3(\alpha) = E(\alpha)$. In the end, our final coefficients are

- Tensor mode

$$\begin{pmatrix} \rho_1^T(\alpha) \\ \rho_2^T(\alpha) \\ \rho_3^T(\alpha) \end{pmatrix} = \frac{1}{2\alpha^2} \begin{pmatrix} 10\alpha^2 & -20\alpha & 10 \\ -20\alpha^2 & 80\alpha & -100 \\ 5\alpha^2 & -50\alpha & 175 \end{pmatrix} \begin{pmatrix} j_0(\alpha) \\ j_1(\alpha) \\ j_2(\alpha) \end{pmatrix} =$$

$$= \frac{1}{14} \begin{pmatrix} 28 & -40 & 2 \\ 0 & 120 & -20 \\ 0 & 0 & 35 \end{pmatrix} \begin{pmatrix} j_0(\alpha) \\ j_2(\alpha) \\ j_4(\alpha) \end{pmatrix}, \qquad (2.5.34)$$

- Vector mode

$$\begin{pmatrix} \rho_1^V(\alpha) \\ \rho_2^V(\alpha) \\ \rho_3^V(\alpha) \end{pmatrix} = \frac{10}{\alpha^2} \begin{pmatrix} 0 & \alpha & -2 \\ \alpha^2 & -7\alpha & 20 \\ -\alpha^2 & 10\alpha & -35 \end{pmatrix} \begin{pmatrix} j_0(\alpha) \\ j_1(\alpha) \\ j_2(\alpha) \end{pmatrix} =$$

$$= \frac{2}{7} \begin{pmatrix} 7 & 5 & -2 \\ 0 & -15 & 20 \\ 0 & 0 & -35 \end{pmatrix} \begin{pmatrix} j_0(\alpha) \\ j_2(\alpha) \\ j_4(\alpha) \end{pmatrix}, \qquad (2.5.35)$$

- Scalar mode

$$\begin{pmatrix} \rho_1^S(\alpha) \\ \rho_2^S(\alpha) \\ \rho_3^S(\alpha) \end{pmatrix} = \frac{15}{\alpha^2} \begin{pmatrix} 0 & 0 & 2 \\ 0 & 4\alpha & -20 \\ \alpha^2 & -10\alpha & 35 \end{pmatrix} \begin{pmatrix} j_0(\alpha) \\ j_1(\alpha) \\ j_2(\alpha) \end{pmatrix} =$$

$$= \frac{1}{7} \begin{pmatrix} 14 & 20 & 6 \\ 0 & -60 & -60 \\ 0 & 0 & 105 \end{pmatrix} \begin{pmatrix} j_0(\alpha) \\ j_2(\alpha) \\ j_4(\alpha) \end{pmatrix}. \qquad (2.5.36)$$

We notice that the parameter $\kappa(f)$ correctly disappears from the scalar mode coefficients: we have already mentioned that breathing and longitudinal polarization modes are degenerate in the long wavelength limit, thus $\kappa(f)$ must disappear as a manifestation of their indistinguishability[13]. We now compute Eq.(2.5.33) for a real detector pair on Earth[14]: we begin by introducing the coordinate system displayed in Fig.2.9. The angle β represents

---

[13]Indeed if the κ parameter was present, it would mean that we would be able to distinguish breathing and longitudinal mode contribution so the SGWB and break the degeneracy.

[14]We take the Earth to be a perfect sphere of radius $R = 6.371 \cdot 10^3$ km.
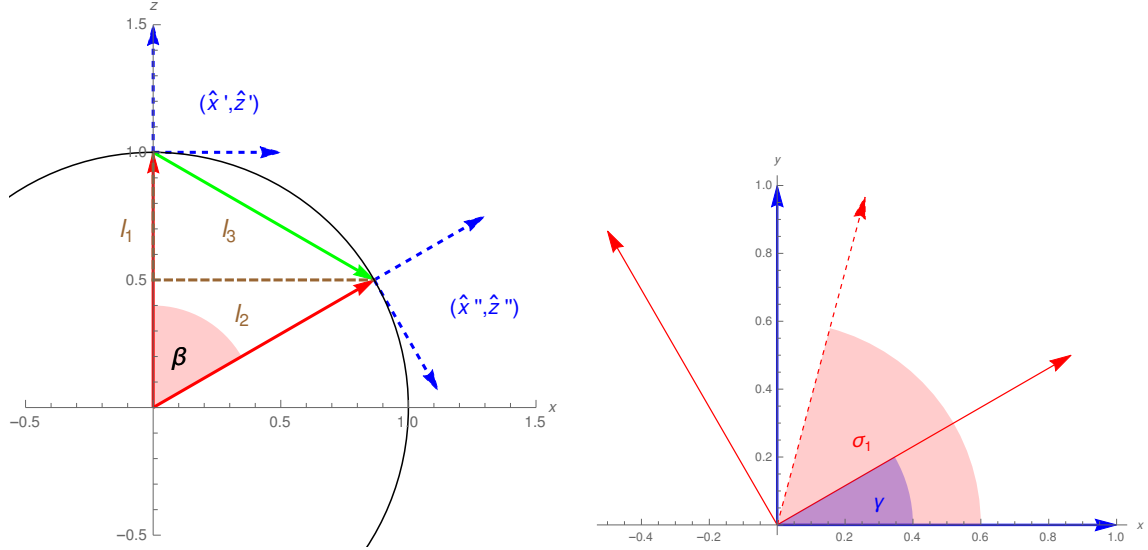
Figure 2.9: (Left) Representation of the relative position of a detector pair (blue arrows) lying on the surface of the Earth. (Right) Orientation of the detector arms (red, solid) and bisector (red, dashed) with respect to the vector (x axis) tangent to the circumference of radius R connecting the detector pair together.

the separation between two L-shaped interferometers I and J located on the surface of the Earth and is measured from its center, while σ_1 and σ_2 are the angles between the bisector of the angle between each of the two interferometer arms and the tangent to the circumference of radius R wrapping planet Earth and connecting the two detectors together at the detector locations. Angles σ_1 and σ_2 are measured in a counterclockwise manner relative to the vector tangent to the circumference and they are defined on the planes tangent to Earth at the detector positions, as seen in the right panel of Fig.2.9. This means that $\beta, \sigma_1, \sigma_2$ define the location and orientation of both detectors. Exploiting the simmetry of our problem, we can place the first detector at $\beta = 0$. We then introduce an orthonormal coordinate system $S' = (\hat{\mathbf{x}}', \hat{\mathbf{y}}', \hat{\mathbf{z}}')$ with its origin in the position of the I-th detector and then we define a second one $S'' = (\hat{\mathbf{x}}'', \hat{\mathbf{y}}'', \hat{\mathbf{z}}'')$ with its origin in the position of the J-th detector:

$$\begin{cases} \hat{\mathbf{x}}' = (1,0,0)^T \\ \hat{\mathbf{y}}' = (0,1,0)^T \\ \hat{\mathbf{z}}' = (0,0,1)^T \end{cases}, \qquad \begin{cases} \hat{\mathbf{x}}'' = (\cos\beta, 0, -\sin\beta)^T \\ \hat{\mathbf{y}}'' = (1,0,0)^T \\ \hat{\mathbf{z}}'' = (\sin\beta, 0, \cos\beta)^T \end{cases}. \qquad (2.5.37)$$

We introduce unit vectors $(\hat{\mathbf{u}}', \hat{\mathbf{v}}')$ directed along each I-th detector arm and $(\hat{\mathbf{u}}'', \hat{\mathbf{v}}'')$ directed along each J-th detector arm, with $\hat{\mathbf{u}}' \perp \hat{\mathbf{v}}'$ and $\hat{\mathbf{u}}'' \perp \hat{\mathbf{v}}''$. In the most general case we can express $(\hat{\mathbf{u}}', \hat{\mathbf{v}}')$ as a rotation of $(\hat{\mathbf{x}}'', \hat{\mathbf{y}}'')$ around $\hat{\mathbf{z}}'$ and $(\hat{\mathbf{u}}'', \hat{\mathbf{v}}'')$ as a rotation of

$(\hat{\mathbf{x}}'', \hat{\mathbf{y}}'')$ around $\hat{\mathbf{z}}''$:

$$
\begin{pmatrix} \hat{\mathbf{u}}' \\ \hat{\mathbf{v}}' \\ \hat{\mathbf{z}}' \end{pmatrix} = \begin{pmatrix} \cos\gamma & \sin\gamma & 0 \\ -\sin\gamma & \cos\gamma & 0 \\ 0 & 0 & 1 \end{pmatrix} \begin{pmatrix} \hat{\mathbf{x}}' \\ \hat{\mathbf{y}}' \\ \hat{\mathbf{z}}' \end{pmatrix}, \qquad \begin{pmatrix} \hat{\mathbf{u}}'' \\ \hat{\mathbf{v}}'' \\ \hat{\mathbf{z}}'' \end{pmatrix} = \begin{pmatrix} \cos\delta & \sin\delta & 0 \\ -\sin\delta & \cos\delta & 0 \\ 0 & 0 & 1 \end{pmatrix} \begin{pmatrix} \hat{\mathbf{x}}'' \\ \hat{\mathbf{y}}'' \\ \hat{\mathbf{z}}'' \end{pmatrix}.
$$
(2.5.38)

The internal angle of an L-shaped interferometer is $\frac{\pi}{2}$, so given the geometry of the problem we have $\gamma = \sigma_1 - \frac{\pi}{4}$ and $\delta = \sigma_2 - \frac{\pi}{4}$. Finally we can compute the two detector tensors

$$
\mathbf{D}_I = \frac{1}{2}\{\hat{\mathbf{u}}' \otimes \hat{\mathbf{u}}' - \hat{\mathbf{v}}' \otimes \hat{\mathbf{v}}'\}, \qquad \mathbf{D}_J = \frac{1}{2}\{\hat{\mathbf{u}}'' \otimes \hat{\mathbf{u}}'' - \hat{\mathbf{v}}'' \otimes \hat{\mathbf{v}}''\}.
$$
(2.5.39)

Starting with $\mathbf{D}_I$, we have

$$
\begin{cases} \hat{\mathbf{u}}' \otimes \hat{\mathbf{u}}' = \hat{\mathbf{x}}' \otimes \hat{\mathbf{x}}' \cos^2\gamma + \hat{\mathbf{y}}' \otimes \hat{\mathbf{y}}' \sin^2\gamma + \hat{\mathbf{x}}' \otimes \hat{\mathbf{y}}' \sin\gamma\cos\gamma + \hat{\mathbf{y}}' \otimes \hat{\mathbf{x}}' \sin\gamma\cos\gamma \\ \hat{\mathbf{v}}' \otimes \hat{\mathbf{v}}' = \hat{\mathbf{x}}' \otimes \hat{\mathbf{x}}' \sin^2\gamma + \hat{\mathbf{y}}' \otimes \hat{\mathbf{y}}' \cos^2\gamma - \hat{\mathbf{x}}' \otimes \hat{\mathbf{y}}' \sin\gamma\cos\gamma - \hat{\mathbf{y}}' \otimes \hat{\mathbf{x}}' \sin\gamma\cos\gamma \end{cases} .
$$
(2.5.40)

These tensor products can be computed using Eq.(2.5.37), and we obtain

$$
\hat{\mathbf{x}}' \otimes \hat{\mathbf{x}}' = \begin{pmatrix} 1 & 0 & 0 \\ 0 & 0 & 0 \\ 0 & 0 & 0 \end{pmatrix}, \quad \hat{\mathbf{y}}' \otimes \hat{\mathbf{y}}' = \begin{pmatrix} 0 & 0 & 0 \\ 0 & 1 & 0 \\ 0 & 0 & 0 \end{pmatrix},
$$

$$
\hat{\mathbf{x}}' \otimes \hat{\mathbf{y}}' = \begin{pmatrix} 0 & 1 & 0 \\ 0 & 0 & 0 \\ 0 & 0 & 0 \end{pmatrix}, \quad \hat{\mathbf{y}}' \otimes \hat{\mathbf{x}}' = \begin{pmatrix} 0 & 0 & 0 \\ 1 & 0 & 0 \\ 0 & 0 & 0 \end{pmatrix} .
$$
(2.5.41)

Putting together what we have found we get

$$
\mathbf{D}_I = \frac{1}{2} \begin{pmatrix} \cos^2\gamma - \sin^2\gamma & 2\sin\gamma\cos\gamma & 0 \\ 2\sin\gamma\cos\gamma & \sin^2\gamma - \cos^2\gamma & 0 \\ 0 & 0 & 0 \end{pmatrix}
$$

$$
= \frac{1}{2} \begin{pmatrix} \cos 2\gamma & \sin 2\gamma & 0 \\ \sin 2\gamma & -\cos 2\gamma & 0 \\ 0 & 0 & 0 \end{pmatrix},
$$
(2.5.42)

which is the expression for the I-th detector tensor located at $\beta = 0$.
Something similar can be done for $\mathbf{D}_J$. This time we start with

$$
\begin{cases} \hat{\mathbf{u}}'' \otimes \hat{\mathbf{u}}'' = \hat{\mathbf{x}}'' \otimes \hat{\mathbf{x}}'' \cos^2\delta + \hat{\mathbf{y}}'' \otimes \hat{\mathbf{y}}'' \sin^2\delta + \hat{\mathbf{x}}'' \otimes \hat{\mathbf{y}}'' \sin\delta\cos\delta + \hat{\mathbf{y}}'' \otimes \hat{\mathbf{x}}'' \sin\delta\cos\delta \\ \hat{\mathbf{v}}'' \otimes \hat{\mathbf{v}}'' = \hat{\mathbf{x}}'' \otimes \hat{\mathbf{x}}'' \sin^2\delta + \hat{\mathbf{y}}'' \otimes \hat{\mathbf{y}}'' \cos^2\delta - \hat{\mathbf{x}}'' \otimes \hat{\mathbf{y}}'' \sin\delta\cos\delta - \hat{\mathbf{y}}'' \otimes \hat{\mathbf{x}}'' \sin\delta\cos\delta \end{cases} ,
$$
(2.5.43)

Using Eq.(2.5.37) we obtain

$$\hat{\mathbf{x}}'' \otimes \hat{\mathbf{x}}'' = \begin{pmatrix} \cos^2\beta & 0 & -\sin\beta\cos\beta \\ 0 & 0 & 0 \\ -\sin\beta\cos\beta & 0 & \sin^2\beta \end{pmatrix} \quad , \quad \hat{\mathbf{y}}'' \otimes \hat{\mathbf{y}}'' = \begin{pmatrix} 0 & 0 & 0 \\ 0 & 1 & 0 \\ 0 & 0 & 0 \end{pmatrix} \quad ,$$

$$\hat{\mathbf{x}}'' \otimes \hat{\mathbf{y}}'' = \begin{pmatrix} 0 & \cos\beta & 0 \\ 0 & 0 & 0 \\ 0 & -\sin\beta & 0 \end{pmatrix} \quad , \quad \hat{\mathbf{y}}'' \otimes \hat{\mathbf{x}}'' = \begin{pmatrix} 0 & 0 & 0 \\ \cos\beta & 0 & -\sin\beta \\ 0 & 0 & 0 \end{pmatrix} \quad . \quad (2.5.44)$$

Finally we get

$$\mathbf{D}_J = \frac{1}{2} \begin{pmatrix} \cos^2\beta\cos 2\delta & \cos\beta\sin 2\delta & -\sin\beta\cos\beta\cos 2\delta \\ \cos\beta\sin 2\delta & -\cos 2\delta & -\sin\beta\sin 2\delta \\ -\sin\beta\cos\beta\cos 2\delta & -\sin\beta\sin 2\delta & \sin^2\beta\cos 2\delta \end{pmatrix}. \quad (2.5.45)$$

It is worth noting that for $\beta \to 0$ we have $\mathbf{D}_J \to \mathbf{D}_I$, which is the expected result. We still need an expression for the unit vector $\hat{\mathbf{d}}$. We have $|\Delta\bar{\mathbf{x}}| = 2R\sin\frac{\beta}{2} = l_3$ and considering the left panel of Fig.2.9 we get

$$\begin{cases} l_3 = 2R\sin\frac{\beta}{2}, \\ l_2 = R\sin\beta, \\ l_1 = R\sqrt{4\sin^2\frac{\beta}{2} - \sin^2\beta} = R\sqrt{4\sin^2\frac{\beta}{2} - 4\sin^2\frac{\beta}{2}\cos^2\frac{\beta}{2}} = 2R\sin^2\frac{\beta}{2}, \end{cases} \quad (2.5.46)$$

thus we find

$$\hat{\mathbf{d}} = \frac{1}{2R\sin\frac{\beta}{2}} \times (R\sin\beta, 0, -2R\sin^2\frac{\beta}{2})^T$$

$$= (\cos\frac{\beta}{2}, 0, -\sin\frac{\beta}{2})^T. \quad (2.5.47)$$

We may now proceed to insert the previous results in (2.5.33) to compute the tensor contractions. We get

- for $D_I^{ij} D_{Jij}$

$$D_I^{ij} D_{Jij} = D_I^{11} D_{J11} + D_I^{12} D_{J12} + D_I^{21} D_{J21} + D_I^{22} D_{J22}$$

$$= \frac{1}{4}\left(\cos 2\gamma\cos 2\delta + 2\cos\beta\sin 2\gamma\sin 2\delta + \cos^2\beta\cos 2\gamma\cos 2\delta\right), \quad (2.5.48)$$

- for $D^i_{Ik}D^{kj}_J d_i d_j$

$$D^i_{Ik}D^{kj}_J d_i d_j = D^1_{I1}D^{11}_J d_1 d_1 + D^1_{I1}D^{13}_J d_1 d_3 + D^1_{I2}D^{21}_J d_1 d_1 + D^1_{I2}D^{23}_J d_1 d_3$$

$$= \frac{1}{4}\Big(\cos\beta\cos^2\frac{\beta}{2}\sin 2\gamma\sin 2\delta + \overbrace{\sin\beta\sin\frac{\beta}{2}\cos\frac{\beta}{2}}^{1/2\sin^2\beta}\sin 2\gamma\sin 2\delta +$$

$$+ \cos^2\beta\cos^2\frac{\beta}{2}\cos 2\gamma\cos 2\delta + \overbrace{\sin\beta\cos\beta\sin\frac{\beta}{2}\cos\frac{\beta}{2}}^{1/2\cos\beta\sin^2\beta}\cos 2\gamma\cos 2\delta\Big),$$

$$(2.5.49)$$

- for $D^{ij}_I D^{kl}_J d_i d_j d_k d_l$

$$D^{ij}_I D^{kl}_J d_i d_j d_k d_l = D^{11}_I D^{11}_J d_1 d_1 d_1 d_1 + D^{11}_I D^{13}_J d_1 d_1 d_1 d_3 + D^{11}_I D^{31}_J d_1 d_1 d_3 d_1 + D^{11}_I D^{33}_J d_1 d_1 d_3 d_3$$

$$= \frac{1}{4}\Big(\cos^2\beta\cos^4\frac{\beta}{2}\cos 2\gamma\cos 2\delta + 2\sin\beta\cos\beta\sin\frac{\beta}{2}\cos^3\frac{\beta}{2}\cos 2\gamma\cos 2\delta +$$

$$+ \sin^2\beta\sin^2\frac{\beta}{2}\cos^2\frac{\beta}{2}\cos 2\gamma\cos 2\delta\Big).$$

$$(2.5.50)$$

We now introduce two new parameters

$$\sigma^+ \equiv \frac{\sigma_1 + \sigma_2}{2}, \qquad \sigma^- \equiv \frac{\sigma_1 - \sigma_2}{2}, \qquad (2.5.51)$$

thus we can use trigonometric identities listed in A.2 to find

$$\begin{cases} \cos 2\gamma\cos 2\delta = \frac{1}{2}\big(\cos(4\sigma^+ - \pi) + \cos 4\sigma^-\big) = \frac{1}{2}\big(\cos 4\sigma^- - \cos 4\sigma^+\big) \\ \sin 2\gamma\sin 2\delta = \frac{1}{2}\big(\cos 4\sigma^- - \cos(4\sigma^+ - \pi)\big) = \frac{1}{2}\big(\cos 4\sigma^- + \cos 4\sigma^+\big) \end{cases}. \qquad (2.5.52)$$

We finally have all the ingredients to reduce Eq.(2.5.33) to the following expression

$$\gamma^N(\alpha, \beta, \sigma^+, \sigma^-) = \Xi^+_N(\alpha, \beta)\cos 4\sigma^+ + \Xi^-_N(\alpha, \beta)\cos 4\sigma^-, \qquad (2.5.53)$$

with $N = T, V, S$. Let us start with the tensor mode: plugging Eqs.(3.1.9)-(3.1.11) and the second expression of Eq.(2.5.34) in Eq.(2.5.33) we get

$$
\gamma_{IJ}^{T}(\alpha) = \left(2j_0 - \frac{20}{7}j_2 + \frac{1}{7}j_4\right) \times \frac{1}{4}\left[\frac{1}{2}(\cos 4\sigma^- - \cos 4\sigma^+) + \cos\beta(\cos 4\sigma^- + \cos 4\sigma^+)+\right.
$$
$$
+ \frac{1}{2}\cos^2\beta(\cos 4\sigma^- - \cos 4\sigma^+)\Bigg] + \left(\frac{60}{7}j_2 - \frac{10}{7}j_4\right) \times \frac{1}{4}\left[\frac{1}{2}\cos\beta\cos^2\frac{\beta}{2}(\cos 4\sigma^- + \cos 4\sigma^+)+\right.
$$
$$
+ \frac{1}{4}\sin^2\beta(\cos 4\sigma^- + \cos 4\sigma^+) + \frac{1}{2}\cos^2\beta\cos^2\frac{\beta}{2}(\cos 4\sigma^- - \cos 4\sigma^+)+
$$
$$
\left.+ \frac{1}{4}\cos\beta\sin^2\beta(\cos 4\sigma^- - \cos 4\sigma^+)\right]+
$$
$$
+ \frac{35}{14}j_4 \times \frac{1}{4}\left[\frac{1}{2}\cos^2\beta\cos^4\frac{\beta}{2}(\cos 4\sigma^- - \cos 4\sigma^+) + \frac{1}{2}\sin^2\beta\sin^2\frac{\beta}{2}\cos^2\frac{\beta}{2}(\cos 4\sigma^- - \cos 4\sigma^+)+\right.
$$
$$
\left.+ \sin\beta\cos\beta\cos^3\frac{\beta}{2}\sin\frac{\beta}{2}(\cos 4\sigma^- - \cos 4\sigma^+)\right].
$$

$$(2.5.54)$$

We now look for $\Xi_T^+(\alpha, \beta)$, meaning we must focus on terms multiplying $\cos 4\sigma^+$. We then have

$$
\Xi_T^+(\alpha,\beta) = -\frac{1}{2}j_0\left[\frac{1}{2}\left(1 + \cos^2\beta\right) - \cos\beta\right] + \frac{5}{7}j_2\left[\frac{1}{2}\left(1 + \cos^2\beta\right) - \cos\beta + \frac{3}{2}\left(\cos\beta\cos^2\frac{\beta}{2}+\right.\right.
$$
$$
\left.+ \frac{1}{2}\sin^2\beta - \cos^2\beta\cos^2\frac{\beta}{2} - \frac{1}{2}\cos\beta\sin^2\beta\right)\Bigg] - \frac{1}{28}j_4\left[\frac{1}{2}\left(1 + \cos^2\beta\right) - \cos\beta + 5\left(\cos\beta\cos^2\frac{\beta}{2}+\right.\right.
$$
$$
\left.+ \frac{1}{2}\sin^2\beta - \cos^2\beta\cos^2\frac{\beta}{2} - \frac{1}{2}\cos\beta\sin^2\beta\right) + \frac{35}{2}\left(\frac{1}{2}\cos^2\beta\cos^4\frac{\beta}{2} + \frac{1}{2}\sin^2\beta\sin^2\frac{\beta}{2}\cos^2\frac{\beta}{2}+\right.
$$
$$
\left.\left.+ \cos\beta\sin\beta\cos^3\frac{\beta}{2}\sin\frac{\beta}{2}\right)\right].
$$

$$(2.5.55)$$

It is very useful to simplify all the following expressions using the following identities

- first identity

$$
\frac{1 + \cos^2\beta}{2} = \frac{1}{2} + \frac{1 + \cos 2\beta}{4} = \frac{3}{4} + \frac{\cos 2\beta}{4}, \tag{2.5.56}
$$

- second identity

$$\cos\beta\cos^2\frac{\beta}{2} + \frac{1}{2}\sin^2\beta - \cos^2\beta\cos^2\frac{\beta}{2} - \frac{1}{2}\cos\beta\sin^2\beta =$$
$$= \cos\beta\cos^2\frac{\beta}{2}(1-\cos\beta) + \frac{1}{2}\sin^2\beta - 2\cos\beta\cos^2\frac{\beta}{2}\sin^2\frac{\beta}{2} =$$
$$= 2\cos\beta\cancel{\cos^2\frac{\beta}{2}\sin^2\frac{\beta}{2}} - 2\cos\beta\cancel{\cos^2\frac{\beta}{2}\sin^2\frac{\beta}{2}} + \frac{1}{2}\sin^2\beta =$$
$$= \frac{1}{2}\sin^2\beta, \tag{2.5.57}$$

- third identity

$$\frac{1}{2}\cos^2\beta\cos^4\frac{\beta}{2} + \frac{1}{2}\sin^2\beta\sin^2\frac{\beta}{2}\cos^2\frac{\beta}{2} + \sin\beta\cos\beta\overbrace{\cos^3\frac{\beta}{2}\sin\frac{\beta}{2}}^{1/2\sin\beta\cos^2\frac{\beta}{2}} =$$
$$= \frac{1}{2}\left(\cos^2\beta\cos^4\frac{\beta}{2} + \sin^2\beta\cos^2\frac{\beta}{2}\overbrace{\left(\sin^2\frac{\beta}{2} + \cos\beta\right)}^{1/2-1/2\cos\beta+\cos\beta}\right) =$$
$$= \frac{1}{2}\cos^4\frac{\beta}{2}(\cos^2\beta + \sin^2\beta) = \frac{1}{2}\cos^4\frac{\beta}{2} =$$
$$= \frac{1}{8}(1+\cos\beta)^2 = \frac{1}{2}\left(\frac{3}{4} + \cos\beta + \frac{1}{4}\cos 2\beta\right), \tag{2.5.58}$$

which lead us to

$$\Xi_T^+(\alpha,\beta) = j_0\left(-\frac{3}{8} + \frac{1}{2}\cos\beta - \frac{1}{8}\cos 2\beta\right) + j_2\left(+\frac{45}{56} - \frac{5}{7}\cos\beta - \frac{5}{56}\cos 2\beta\right) +$$
$$- j_4\left(\frac{169}{896} + \frac{27}{224}\cos\beta + \frac{3}{896}\cos 2\beta\right) =$$
$$= -\left(\frac{3}{8}j_0 - \frac{45}{56}j_2 + \frac{169}{896}j_4\right) + \left(\frac{1}{2}j_0 - \frac{5}{7}j_2 - \frac{27}{224}j_4\right)\cos\beta +$$
$$- \left(\frac{1}{8}j_0 + \frac{5}{56}j_2 + \frac{3}{896}j_4\right)\cos 2\beta. \tag{2.5.59}$$

59

Let us now focus on terms multiplying $\cos 4\sigma^-$, this time we have

$$\Xi_T^-(\alpha,\beta) = \frac{1}{2}j_0\left[\frac{1}{2}(1+\cos^2\beta)+\cos\beta\right] + \frac{5}{7}j_2\left[-\frac{1}{2}(1+\cos^2\beta)-\cos\beta+\frac{3}{2}(\cos\beta\cos^2\frac{\beta}{2}+\frac{1}{2}\sin^2\beta+\right.$$

$$+\cos^2\beta\cos^2\frac{\beta}{2}+\frac{1}{2}\cos\beta\sin^2\beta)\Big] + \frac{1}{14}j_4\left[\frac{1}{2}(1+\cos^2\beta)+\cos\beta-5\big(\cos\beta\cos^2\frac{\beta}{2}+\right.$$

$$+\frac{1}{2}\sin^2\beta+\cos^2\beta\cos^2\frac{\beta}{2}+\frac{1}{2}\cos\beta\sin^2\beta\big) + \frac{35}{4}\big(\frac{1}{2}\cos^2\beta\cos^4\frac{\beta}{2}+\frac{1}{2}\sin^2\beta\sin^2\frac{\beta}{2}\cos^2\frac{\beta}{2}+$$

$$+\sin\beta\cos\beta\cos^3\frac{\beta}{2}\sin\frac{\beta}{2}\big)\Big].$$

$$(2.5.60)$$

Once again we may simplify the calculations

- first identity

$$\cos^4\frac{\beta}{2} = \frac{1}{4}(1+\cos^2\beta) = \frac{1}{2}\left[\cos\beta+\frac{1}{2}(1+\cos^2\beta)\right], \qquad (2.5.61)$$

- second identity

$$\cos\beta\cos^2\frac{\beta}{2}+\frac{1}{2}\sin^2\beta+\cos^2\beta\cos^2\frac{\beta}{2}+\frac{1}{2}\cos\beta\sin^2\beta =$$

$$= \cos\beta\cos^2\frac{\beta}{2}+\cos^2\beta\cos^2\frac{\beta}{2}+\frac{1}{2}\overbrace{\sin^2\beta}^{1-\cos^2\beta}(1+\cos\beta) =$$

$$= \cos\beta\cos^2\frac{\beta}{2}+\cos^2\frac{\beta}{2}+\cancel{\cos^2\beta\cos^2\frac{\beta}{2}}-\cancel{\cos^2\beta\cos^2\frac{\beta}{2}} =$$

$$= (1+\cos\beta)\cos^2\frac{\beta}{2} = 2\cos^4\frac{\beta}{2}, \qquad (2.5.62)$$

- third identity

$$\frac{1}{2}\cos^2\beta\cos^4\frac{\beta}{2}+\frac{1}{2}\sin^2\beta\sin^2\frac{\beta}{2}\cos^2\frac{\beta}{2}+\overbrace{\sin\beta\cos\beta\cos^3\frac{\beta}{2}\sin\frac{\beta}{2}}^{1/2\cos\beta\sin^2\beta\cos^2\beta/2} =$$

$$= \frac{1}{2}\cos^2\beta\cos^4\frac{\beta}{2}+\frac{1}{2}\sin^2\beta\cos^2\frac{\beta}{2}\overbrace{\big(\cos\beta+\sin^2\frac{\beta}{2}\big)}^{1/2(1+\cos\beta)} =$$

$$= \frac{1}{2}\cos^4\frac{\beta}{2}\big(\cos^2\beta+\sin^2\beta\big) = \frac{1}{2}\cos^4\frac{\beta}{2}, \qquad (2.5.63)$$

thus we get

$$\Xi_T^-(\alpha,\beta) = j_0\cos^4\frac{\beta}{2}+\frac{5}{7}j_2\cos^4\frac{\beta}{2}+\frac{3}{112}j_4\cos^4\frac{\beta}{2} = \left(j_0+\frac{5}{7}j_2+\frac{3}{112}j_4\right)\cos^4\frac{\beta}{2}. \quad (2.5.64)$$

Moving to vector modes, this time we need to plug the second expression of Eq.(2.5.35) into Eq.(2.5.33), so we get

$$
\begin{aligned}
\gamma_{IJ}^V(\alpha) = {} & \left(2j_0 + \frac{10}{7}j_2 - \frac{4}{7}j_4 \right) \times \frac{1}{4}\left[\frac{1}{2}(\cos 4\sigma^- - \cos 4\sigma^+) + \cos\beta(\cos 4\sigma^- + \cos 4\sigma^+) + \right. \\
& + \frac{1}{2}\cos^2\beta(\cos 4\sigma^- - \cos 4\sigma^+) \bigg] + \left(-\frac{30}{7}j_2 + \frac{40}{7}j_4 \right) \times \frac{1}{4}\left[\frac{1}{2}\cos\beta\cos^2\frac{\beta}{2}(\cos 4\sigma^- + \cos 4\sigma^+) + \right. \\
& + \frac{1}{4}\sin^2\beta(\cos 4\sigma^- + \cos 4\sigma^+) + \frac{1}{2}\cos^2\beta\cos^2\frac{\beta}{2}(\cos 4\sigma^- - \cos 4\sigma^+) + \\
& + \frac{1}{4}\cos\beta\sin^2\beta(\cos 4\sigma^- - \cos 4\sigma^+) \bigg] + \\
& - 10j_4 \times \frac{1}{4}\left[\frac{1}{2}\cos^2\beta\cos^4\frac{\beta}{2}(\cos 4\sigma^- - \cos 4\sigma^+) + \frac{1}{2}\sin^2\beta\sin^2\frac{\beta}{2}\cos^2\frac{\beta}{2}(\cos 4\sigma^- - \cos 4\sigma^+) + \right. \\
& + \cos\beta\sin\beta\cos^3\frac{\beta}{2}\sin\frac{\beta}{2}(\cos 4\sigma^- - \cos 4\sigma^+) \bigg].
\end{aligned}
$$
(2.5.65)

We can immediately spot a similarity: Eq.(2.5.65) differs from Eq.(2.5.54) only for the coefficients multiplying the Bessel functions j_0, j_2, j_4. This means that we can still use Eqs.(2.5.56)-(2.5.58) and Eqs.(2.5.61)-(2.5.63) to get the following results

$$
\begin{aligned}
\Xi_V^+(\alpha,\beta) = {} & -\left(\frac{3}{8}j_0 + \frac{45}{112}j_2 - \frac{169}{896}j_4 \right) + \left(\frac{1}{2}j_0 + \frac{5}{14}j_2 + \frac{27}{56}j_4 \right)\cos\beta + \\
& - \left(\frac{1}{8}j_0 - \frac{5}{112}j_2 - \frac{3}{224}j_4 \right)\cos 2\beta,
\end{aligned}
$$
(2.5.66)

and

$$
\Xi_V^-(\alpha,\beta) = \left(j_0 - \frac{5}{14}j_2 - \frac{3}{28}j_4 \right)\cos^4\frac{\beta}{2}.
$$
(2.5.67)

Something analogous is obtained for the scalar mode: pluggin the second expression of Eq.(2.5.36) into Eq.(2.5.33) we get

$$\gamma_{IJ}^S(\alpha) = \left(2j_0 + \frac{20}{7}j_2 + \frac{6}{7}j_4\right) \times \frac{1}{4}\left[\frac{1}{2}(\cos 4\sigma^- - \cos 4\sigma^+) + \cos\beta(\cos 4\sigma^- + \cos 4\sigma^+) + \right.$$

$$+ \frac{1}{2}\cos^2\beta(\cos 4\sigma^- - \cos 4\sigma^+)\bigg] + \left(-\frac{60}{7}j_2 - \frac{60}{7}j_4\right) \times \frac{1}{4}\left[\frac{1}{2}\cos\beta\cos^2\frac{\beta}{2}(\cos 4\sigma^- + \cos 4\sigma^+) + \right.$$

$$+ \frac{1}{4}\sin^2\beta(\cos 4\sigma^- + \cos 4\sigma^+) + \frac{1}{2}\cos^2\beta\cos^2\frac{\beta}{2}(\cos 4\sigma^- - \cos 4\sigma^+) + $$

$$+ \frac{1}{4}\cos\beta\sin^2\beta(\cos 4\sigma^- - \cos 4\sigma^+)\bigg] + $$

$$+ 15j_4 \times \frac{1}{4}\left[\frac{1}{2}\cos^2\beta\cos^4\frac{\beta}{2}(\cos 4\sigma^- - \cos 4\sigma^+) + \frac{1}{2}\sin^2\beta\sin^2\frac{\beta}{2}\cos^2\frac{\beta}{2}(\cos 4\sigma^- - \cos 4\sigma^+) + \right.$$

$$+ \cos\beta\sin\beta\cos^3\frac{\beta}{2}\sin\frac{\beta}{2}(\cos 4\sigma^- - \cos 4\sigma^+)\bigg],$$

$$(2.5.68)$$

and once again we can use Eqs.(2.5.56)-(2.5.58), (2.5.61)-(2.5.63) to help us with our computations. We finally get

$$\Xi_S^+(\alpha,\beta) = -\left(\frac{3}{8}j_0 + \frac{45}{56}j_2 + \frac{507}{448}j_4\right) + \left(\frac{1}{2}j_0 + \frac{5}{7}j_2 - \frac{81}{112}j_4\right)\cos\beta + $$

$$- \left(\frac{1}{8}j_0 - \frac{5}{56}j_2 + \frac{9}{448}j_4\right)\cos 2\beta, \tag{2.5.69}$$

and

$$\Xi_S^-(\alpha,\beta) = \left(j_0 - \frac{5}{7}j_2 + \frac{9}{56}j_4\right)\cos^4\frac{\beta}{2}. \tag{2.5.70}$$

All these results can be finally used to compute Eq.(2.5.53) for each polarization mode.

2.6 Detectable SGWB Energy Density and Mode Separation

We now consider the Earth-based coordinate system introduced in Appendix C: both location and orientation of 2nd-generation interferometers are well known [75, 76] and listed in Table 2.2 and the detailed procedure we used to compute β, σ^+ and σ^- is also reported in the same appendix. Numerical values of these angular parameters and characteristic frequencies f_c are shown in Table 2.3 and 2.4. Components of unit vectors directed along each interferometer arm with respect to the detector center are also listed in Table 2.2; we can use these values to compute the detector tensor and antenna power pattern for real GW interferometers on Earth. Mollweide projections of square root antenna power pattern functions are shown in Fig.2.10, 2.11 and 2.12 for tensor, vector and scalar modes respectively.
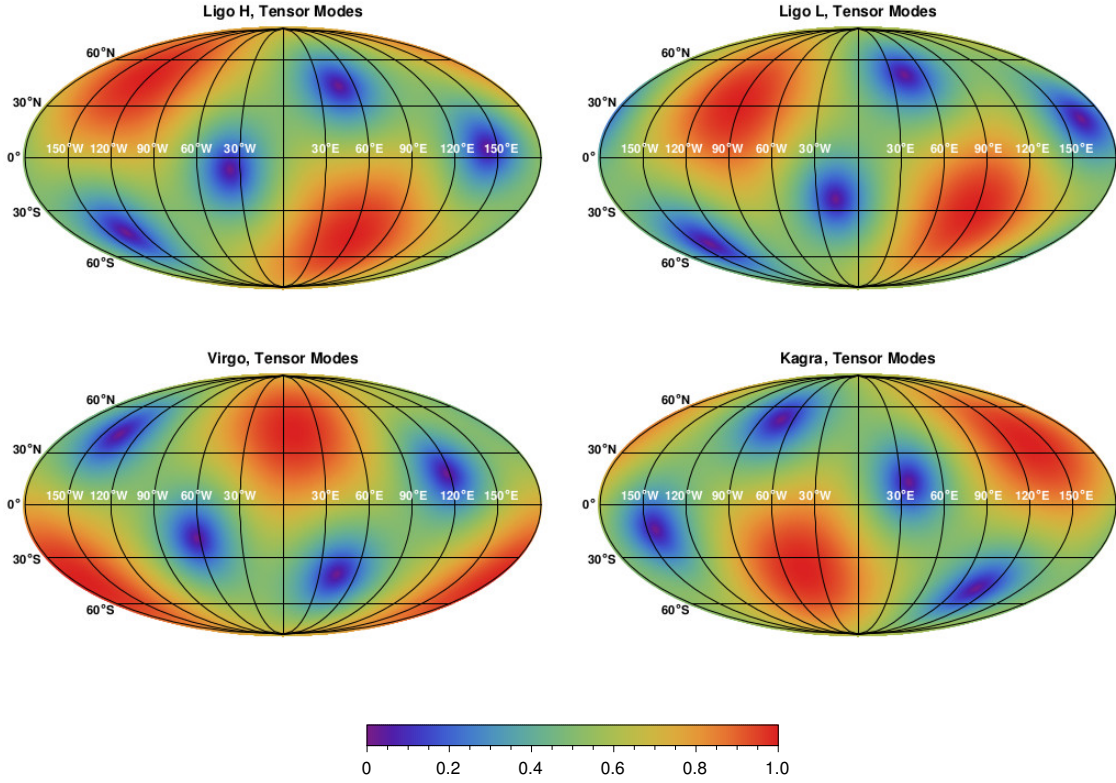
Figure 2.10: Mollweide projection of $\sqrt{(F^+)^2 + (F^\times)^2}$ for 2nd-generation interferometers Ligo-Hanford (top left), Ligo-Livingston (top right), Virgo (bottom left) and Kagra (bottom right). The coordinate system used is described in Appendix C. Unit vectors listed in Tab 2.2 were used to compute detector tensors.
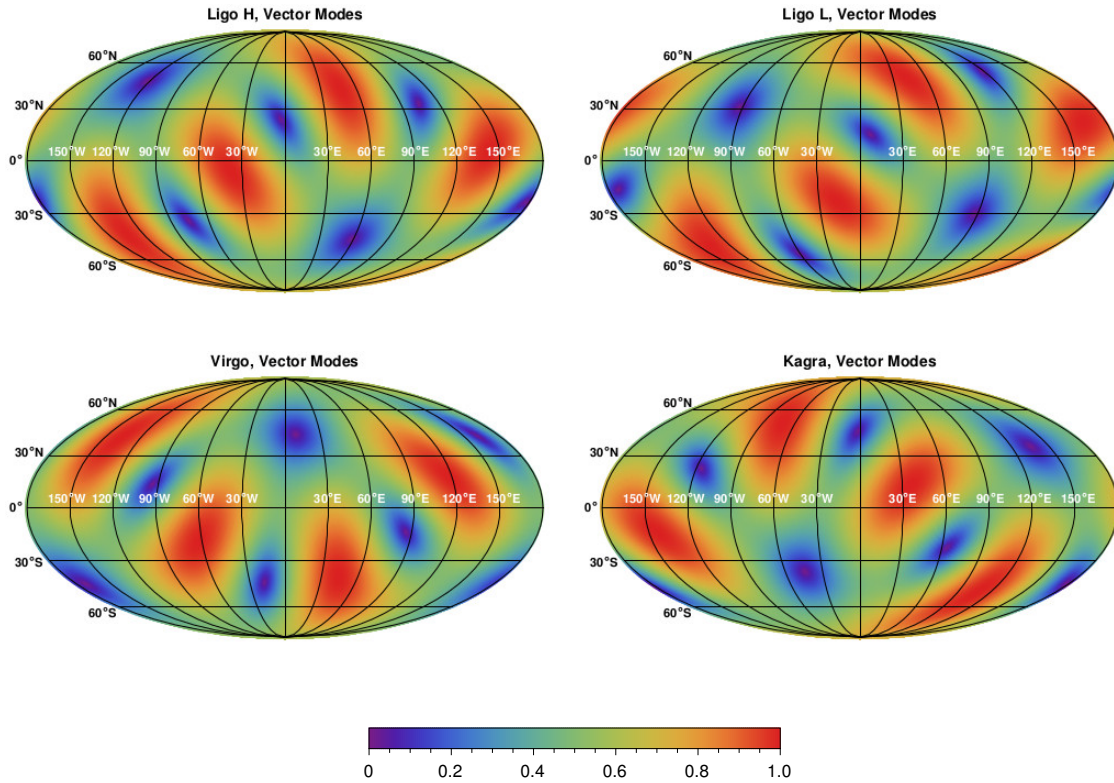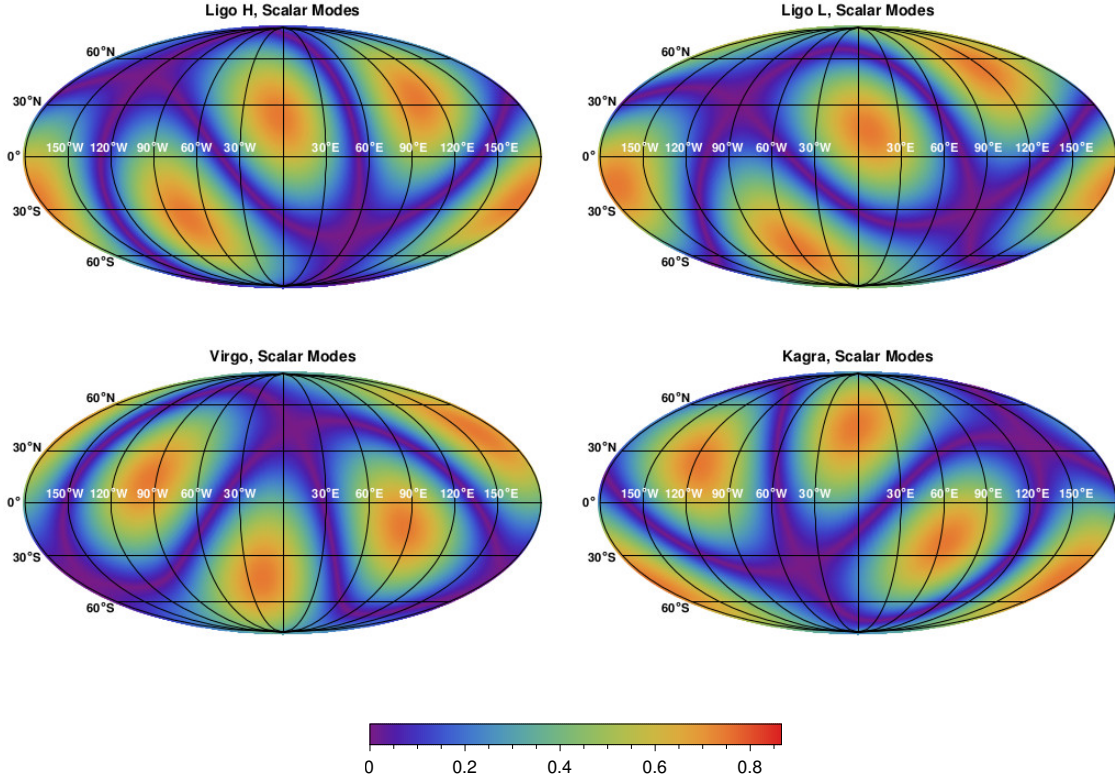
Figure 2.11: Mollweide projection of $\sqrt{(F^x)^2 + (F^y)^2}$ for 2nd-generation interferometers Ligo-Hanford (top left), Ligo-Livingston (top right), Virgo (bottom left) and Kagra (bottom right). The coordinate system used is described in Appendix C. Unit vectors listed in Tab 2.2 were used to compute detector tensors.

Figure 2.12: Mollweide projection of $\sqrt{(F^b)^2 + (F^l)^2}$ for 2nd-generation interferometers Ligo-Hanford (top left), Ligo-Livingston (top right), Virgo (bottom left) and Kagra (bottom right). The coordinate system used is described in Appendix C. Unit vectors listed in Tab 2.2 were used to compute detector tensors.

	Central Location	1st Arm	2nd Arm
LH	$\{-0.338, -0.6, 0.725\}$	$\{-0.224, 0.799, 0.557\}$	$\{-0.914, 0.0261, -0.405\}$
LL	$\{-0.0116, -0.861, 0.508\}$	$\{-0.953, -0.144, -0.266\}$	$\{0.302, -0.488, -0.819\}$
V	$\{0.712, 0.132, 0.690\}$	$\{-0.701, 0.201, 0.684\}$	$\{-0.0485, -0.971, 0.236\}$
K	$\{-0.591, 0.546, 0.594\}$	$\{-0.390, -0.838, 0.382\}$	$\{0.706, -0.00580, 0.709\}$

Table 2.2: Cartesian coordinates Ligo Hanford (LH), Ligo Livingston (LL), Virgo (V), Kagra (K) and unit vectors directed along each interferometer arm with respect to its center. The coordinate system used is described in Appendix C.

These results along with Eq.(2.5.53) allow us to explicitly compute overlap reduction functions for each detector pair: their plots are shown in Fig.2.14. Let us set the GW frequency to zero: we have that $j_0 = 1$ while $j_2 = 0 = j_4$. Since Eqs.(2.5.54),(2.5.65) and (2.5.68) have the same coefficients multiplying j_0 we get the same expression of Eq.(2.5.53) for tensor, vector and scalar modes

$$\gamma^N(f=0) = \cos^4\frac{\beta}{2}\cos 4\sigma^- - \sin^4\frac{\beta}{2}\cos 4\sigma^+, \qquad (2.6.1)$$

for $N = T, V, S$. This is the reason why for $f \ll f_c$ overlap functions behave in the same way for each polarization mode as shown in Fig.2.14. Notice that $\gamma^N(f=0) \neq 1$: this issue arises from the fact that the detectors of each pair are not in the same location and do not share the same orientation[15]. As we mentioned, overlap functions show an oscillatory behaviour once $f \approx f_c$ and approach 0 when $f \gg f_c$. We are finally ready to compute the

	β	σ_1	σ_2	σ^+	σ^-	f_c [Hz]
LH-LL	$27°14'24''$	$196°40'12''$	$286°52'12''$	$241°46'12''$	$-45°6'$	16.01
LH-V	$79°36'36''$	$173°31'12''$	$115°23'24''$	$144°27'36''$	$-29°42'$	5.85
LH-K	$72°22'12''$	$28°18'$	$205°47'24''$	$116°54'36''$	$-88°52'48''$	6.33
LL-V	$79°36'36''$	$145°49'48''$	$199°48'36''$	$172°49'12''$	$-26°59'24''$	6.03
LL-K	$99°18'$	$23°49'12''$	$295°40'12''$	$159°44'24''$	$-135°55'48''$	4.92
V-K	$86°30'$	$66°14'24''$	$127°49'48''$	$97°1'48''$	$-30°48'$	5.46

Table 2.3: Separation angle β between detector pairs on the surface of the Earth and bisector orientation σ_1, σ_2 relative to the circumference of radius R connecting the pair given in degrees. Parameters σ^+, σ^- are also shown. The coordinate system used is described in Appendix C.

SGWB energy density contributions for each polarization mode exploiting what we learned. We begin by considering the simplest scenario: we assume the existence of only one between

---

[15]Indeed, choosing $\beta = 0$ and $\sigma_1 = \sigma_2$ we obtain $\gamma^N(f=0) = 1$.

	β	σ_+	σ^-
LH-LL	27.2	241.8	-45.1
LH-V	79.6	144.5	29.1
LH-K	72.4	116.9	-88.9
LL-V	76.8	172.8	-27.0
LL-K	99.3	159.7	-135.9
V-K	86.5	97.0	-30.8

Table 2.4: Separation and relative orientations of major interferometers on Earth given in decimal degrees. The coordinate system used is described in Appendix C.

tensor, vector and scalar modes and a frequency independent GW-spectrum for each case, meaning that the parameter related the GW energy density defined in Eq.(1.4.6) can be taken outside the integral in Eq.(2.4.32). Secondly, we set $SNR = 5$ as a threshold and we consider a total observation time of three years, thus we can rewrite Eq.(2.4.32) as follows

$$h_0^2 \Omega_{gw}^N = 5 \times \left[\left(\frac{3(100 K m s^{-1} M p c^{-1})^2 \sqrt{3yrs}}{10\pi^2} \right)^{-1} \left(\int_{-\infty}^{+\infty} df \frac{(\gamma^N(f))^2}{f^6 S_n^2(f)} \right)^{-\frac{1}{2}} \right], \quad (2.6.2)$$

with $N = T, V, S$ and[16] $h_0^2 \Omega_{gw}^N \rightarrow \tau h_0^2 \Omega_{gw}^N$ if $N = S$. The noise power spectral density can be derived from detector sensitivity curves: these are usually constructed by taking the ratio of the PSD to the detector sky- and polarization-averaged response to a GW [77]. Sensitivity curves relative to 2nd-generation interferometers are public and provided by [79, 80] and their plots are shown in Fig.2.13. Numerical values of the SGWB detectable energy density Ω_{gw}^N are reported in Table 2.5. Combinations of interferometers more sensitive to GWs are between LIGO-Livingston, LIGO-Hanford and Virgo due to their better sensitivities. In the most general case of a GW signal, tensor, vector and scalar modes are all present at the same time and we need to consider the full form of Eq.(2.4.32), which mixes the three contributions making it impossible to distinguish their energy density contributions with only two interferometers. To overcome this issue, we need to consider a network of (at least) three detectors which we simply denote $1, 2, 3$: it is then possible to obtain three different signals related to three possible detector pairs $(1, 2)$, $(2, 3)$, $(3, 1)$, which we wish to manipulate in order to compute $\Omega_{gw}^N(f)$, with $N = T, V, S$. We show how this can be achieved follwing [86], then we list the results obtained using updated noise data provided by [79, 80]. We begin by considering Eqs.(2.4.8) and (2.4.22), we can deduce

$$\langle s_I^*(f) s_J(f) \rangle = \frac{3 H_0^2 T}{20\pi^2} f^{-3} \big(\Omega_{gw}^T(f) \gamma_{IJ}^T(f) + \Omega_{gw}^V(f) \gamma_{IJ}^V(f) + \tau(f) \Omega_{gw}^S(f) \gamma_{IJ}^S(f) \big), \quad (2.6.3)$$

---

[16]We recall that $\tau(f) = \frac{1}{3} \left(\frac{1+2\kappa(f)}{1+\kappa(f)} \right)$
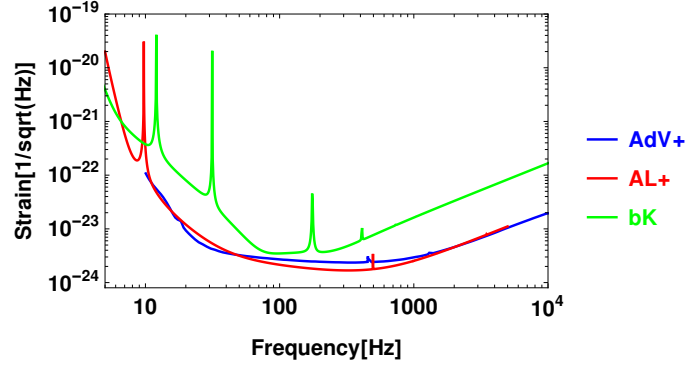
Figure 2.13: Sensitivity curves for 2nd-generation interferometers. Plots were realized with public data provided by [79, 80].

	$h_0^2 \Omega_{gw}^T$	$h_0^2 \Omega_{gw}^V$	$\tau h_0^2 \Omega_{gw}^S$
LH-LL	8.96×10^{-10}	1.20×10^{-9}	1.19×10^{-9}
LH-V	4.82×10^{-9}	6.39×10^{-9}	2.54×10^{-9}
LH-K	3.95×10^{-8}	2.58×10^{-8}	1.91×10^{-8}
LL-V	4.82×10^{-9}	4.86×10^{-9}	2.81×10^{-9}
LL-K	6.93×10^{-8}	7.57×10^{-8}	6.41×10^{-8}
V-K	2.02×10^{-8}	2.80×10^{-8}	2.01×10^{-8}

Table 2.5: SGWB detectable energy density contributions for tensor, vector and scalar modes if only one of these is present. A frequency independent GW-spectrum, and a total observational time of three years were assumed. The signal to noise ratio was set to 5. All detector pairs return similar values for each polarization SGWB energy density contribution.

with $I, J = 1, 2, 3$ denoting the three interferometers. We further introduce a new object G_{IJ} which satisfies

$$\langle G_{IJ} \rangle = \frac{20\pi^2}{3H_0^2 T} f^3 \langle s_I^*(f) s_J(f) \rangle = \left(\Omega_{gw}^T(f) \gamma_{IJ}^T(f) + \Omega_{gw}^V(f) \gamma_{IJ}^V(f) + \tau(f) \Omega_{gw}^S(f) \gamma_{IJ}^S(f) \right),$$
(2.6.4)

where ensemble averages were used in order to eliminate noise contributions, similarly to the two detectors scenario. We can express our result as

$$\begin{pmatrix} \langle G_{12} \rangle \\ \langle G_{23} \rangle \\ \langle G_{31} \rangle \end{pmatrix} = \begin{pmatrix} \gamma_{12}^T & \gamma_{12}^V & \gamma_{12}^S \\ \gamma_{23}^T & \gamma_{23}^V & \gamma_{23}^S \\ \gamma_{31}^T & \gamma_{31}^V & \gamma_{31}^S \end{pmatrix} \begin{pmatrix} \Omega_{gw}^T \\ \Omega_{gw}^V \\ \tau \Omega_{gw}^T \end{pmatrix} = \mathbf{\Lambda}(f) \begin{pmatrix} \Omega_{gw}^T \\ \Omega_{gw}^V \\ \tau \Omega_{gw}^T \end{pmatrix},$$
(2.6.5)

68
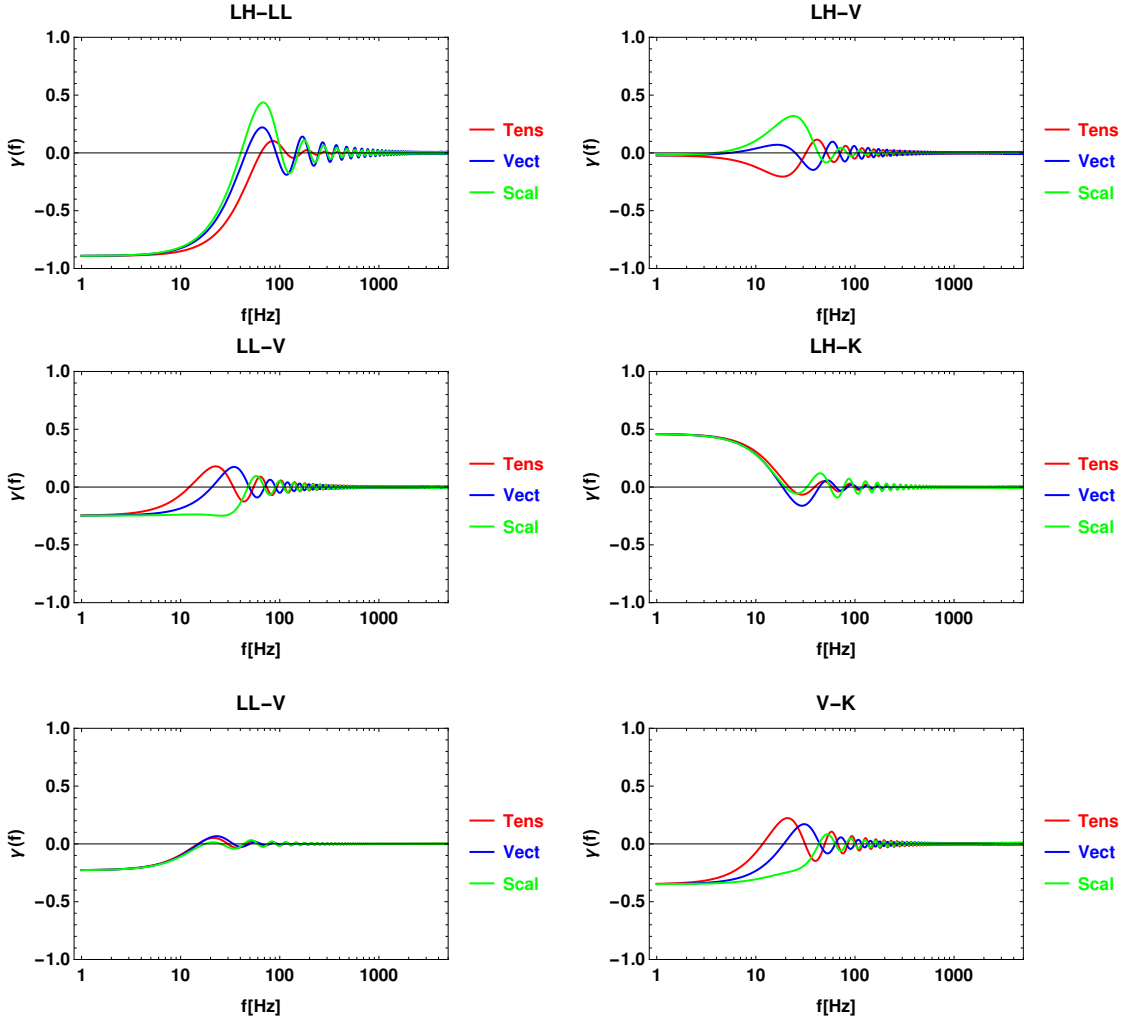
Figure 2.14: Overlap reduction functions of 2nd-generation ground-based interferometer pairs on Earth. Plots were obtained from Eq.(2.5.53) and data listed in Tab. 2.4.

where $\mathbf{\Lambda}$ is the *detector correlation matrix*. In case this matrix is invertible, we get

$$\begin{pmatrix} \Omega_{gw}^T \\ \Omega_{gw}^V \\ \tau\Omega_{gw}^T \end{pmatrix} = \mathbf{\Lambda}^{-1}(f) \begin{pmatrix} \langle G_{12} \rangle \\ \langle G_{23} \rangle \\ \langle G_{31} \rangle \end{pmatrix}, \tag{2.6.6}$$

where

$$\mathbf{\Lambda}^{-1} = \frac{1}{det\mathbf{\Lambda}} \begin{pmatrix} \gamma_{23}^V\gamma_{31}^S - \gamma_{23}^S\gamma_{31}^V & \gamma_{31}^V\gamma_{12}^S - \gamma_{31}^S\gamma_{12}^V & \gamma_{12}^V\gamma_{23}^S - \gamma_{12}^S\gamma_{23}^V \\ \gamma_{23}^S\gamma_{31}^T - \gamma_{23}^T\gamma_{31}^S & \gamma_{31}^S\gamma_{12}^T - \gamma_{31}^T\gamma_{12}^S & \gamma_{12}^S\gamma_{23}^T - \gamma_{12}^T\gamma_{23}^S \\ \gamma_{23}^T\gamma_{31}^V - \gamma_{23}^V\gamma_{31}^T & \gamma_{31}^T\gamma_{12}^V - \gamma_{31}^V\gamma_{12}^T & \gamma_{12}^T\gamma_{23}^V - \gamma_{12}^V\gamma_{23}^T \end{pmatrix}, \tag{2.6.7}$$

and

$$det\mathbf{\Lambda} = \gamma_{12}^T(\gamma_{23}^V\gamma_{31}^S - \gamma_{23}^S\gamma_{31}^V) + \gamma_{12}^V(\gamma_{23}^S\gamma_{31}^T - \gamma_{23}^T\gamma_{31}^S) + \gamma_{12}^S(\gamma_{23}^T\gamma_{31}^V - \gamma_{23}^V\gamma_{31}^T). \tag{2.6.8}$$

For $\mathbf{\Lambda}$ to be invertible, its determinant needs to satisfy $det\mathbf{\Lambda} \neq 0$: this condition is not trivial and needs to be verified investigating real networks. We can express the inverse matrix as

$$\mathbf{\Lambda}^{-1} = \begin{pmatrix} \beta_1^T & \beta_2^T & \beta_3^T \\ \beta_1^V & \beta_2^V & \beta_3^V \\ \beta_1^S & \beta_2^S & \beta_3^S \end{pmatrix}, \tag{2.6.9}$$

and define the new GW signal for each polarization mode as

$$S_N = \frac{3H_0^2 T}{20\pi^2} \int_{-\infty}^{\infty} df\, f^{-3}\big(\Omega_{gw}^N(f)Q(f)\big)$$

$$= \frac{3H_0^2 T}{20\pi^2} \int_{-\infty}^{\infty} df\, f^{-3}\big(\beta_1^N\langle G_{12}\rangle + \beta_2^N\langle G_{21}\rangle + \beta_3^N\langle G_{31}\rangle\big)Q(f), \tag{2.6.10}$$

while the noise becomes

$$N_N^2 = \frac{T}{4} \int_{-\infty}^{\infty} df\,\big[(\beta_1^N)^2 S_{n1}(f)S_{n2}(f) + (\beta_2^N)^2 S_{n2}(f)S_{n3}(f) + (\beta_3^N)^2 S_{n3}(f)S_{n1}(f)\big]Q^2(f), \tag{2.6.11}$$

with $N = T, V, S$. We then define

$$Z_N = \big[(\beta_1^N)^2 S_{n1}(f)S_{n2}(f) + (\beta_2^N)^2 S_{n2}(f)S_{n3}(f) + (\beta_3^N)^2 S_{n3}(f)S_{n1}(f)\big]^{\frac{1}{2}}, \tag{2.6.12}$$

and we introduce the analogous inner product of Eq.(2.4.29)

$$H \cdot G = \int_{-\infty}^{\infty} df\, H^*(f)G(f)Z_N^2(f). \tag{2.6.13}$$

It is straightforward to see that the SNR may be expressed as

$$\left(\frac{S}{N}\right)_{N=T,V,S} = \frac{3H_0^2\sqrt{T}}{10\pi^2}\left(\frac{Q(f) \cdot \left(\frac{\Omega_{gw}^N(f)}{f^3 Z_N^2}\right)}{\sqrt{Q(f) \cdot Q(f)}}\right), \tag{2.6.14}$$

and the filter function that maximizes the SNR

$$Q(f) \propto \frac{\Omega_{gw}^N(f)}{f^3 Z_n^2}. \tag{2.6.15}$$

In the end we obtain

$$\left(\frac{S}{N}\right)_{N=T,V,S} = \frac{3H_0^2\sqrt{T}}{10\pi^2}\left(\int_{-\infty}^{+\infty} df \frac{(\Omega_{gw}^N(f))^2}{f^6 Z_N^2(f)}\right)^{\frac{1}{2}}, \tag{2.6.16}$$

which is the formula we use to efficiently separate tensor, vector and scalar modes. As we mentioned, the condition $det\mathbf{\Lambda}(f) \neq 0$ needs to be satisfied: indeed, $Z_N(f) \propto (det\mathbf{\Lambda}(f))^{-1}$ and if the determinant is zero, so is the SNR. For each possible triad of 2nd-generation interferometers on Earth, we show how $det\mathbf{\Lambda}(f)$ behaves in Fig. 2.15: we mentioned how overlap functions have similar values for $f \ll f_c$ and reduce to zero for $f \gg f_c$, thus the determinant filters GW frequencies and allows a true mode separation only for finite ranges (10-100 Hz) far away from f_*: this is another instance that justifies us to use the long wavelength limit. We checked $Z_N(f)$ functions regularity and zeros and no anomalous behaviours were found. We finally list our results in Tab. 2.6 for the detectable energy density: once again we assumed a frequency independent GW-spectrum for each polarization mode. We notice that all networks return similar values for each polarization SGWB energy density contribution.

	$h_0^2\Omega_{gw}^T$	$h_0^2\Omega_{gw}^V$	$\tau h_0^2\Omega_{gw}^S$
LH-LL-V	4.36×10^{-9}	1.06×10^{-8}	3.75×10^{-9}
LH-LL-K	2.32×10^{-8}	4.09×10^{-8}	3.01×10^{-8}
V-K-LL	2.55×10^{-8}	5.04×10^{-8}	4.73×10^{-8}
V-K-LH	2.64×10^{-8}	2.69×10^{-8}	1.80×10^{-8}

Table 2.6: SGWB detectable energy density contributions for tensor, vector and scalar modes considering three detector networks. A frequency independent GW-spectrum, and a total observational time of three years is assumed. The SNR is set to 5. All possible networks return similar values for each polarization SGWB energy density contribution.
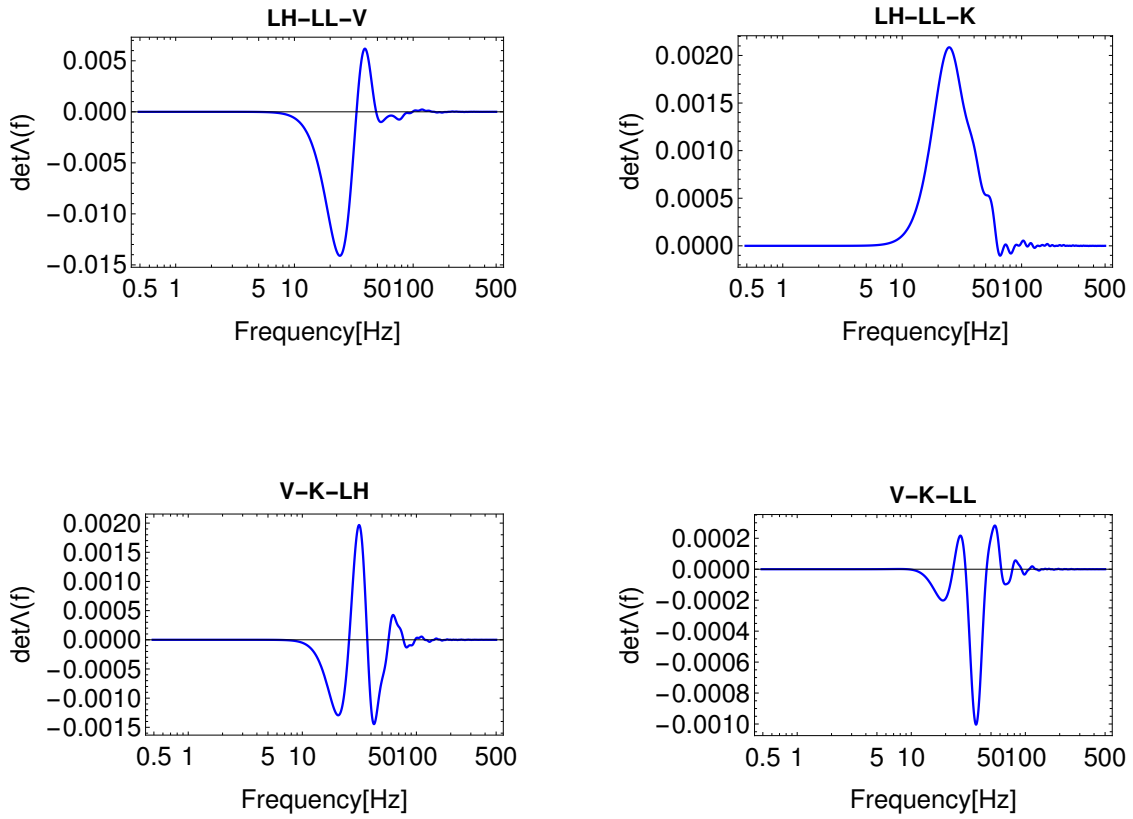
Figure 2.15: Plots of $det\mathbf{\Lambda}(f)$ defined in Eq.(2.6.8) for each possible network built with three 2nd-generation ground-based interferometers on Earth. Overlap reduction functions have similar values for $f \ll f f_c$ and collapse to zero for $f \gg f_c$, thus the determinant filters GW frequencies and allows a true mode separation only for finite frequency ranges.

Chapter 3

3nd-generation ground based interferometers

3.1 Response Functions of a V-shaped Interferometer

In this chapter we generalize some of the previously obtained results to the case of a V-shaped interferometer, like will probably be ET [14]. Once again we consider the orthonormal coordinate system shown in Eq.(2.1.6) and we proceed by finding the proper expression of the detector tensor. Let us first consider the case where the GW frequency $f \ll f_*$: assuming that versors directed along each detector arm are $\hat{\mathbf{e}}_1 = (1, 0, 0)$ and $\hat{\mathbf{e}}_2 = (\cos\eta, \sin\eta, 0)$ we have

$$D_{f \ll f_*} = \begin{pmatrix} \frac{1}{2}\sin^2\eta & -\frac{1}{2}\sin\eta\cos\eta & 0 \\ -\frac{1}{2}\sin\eta\cos\eta & -\frac{1}{2}\sin^2\eta & 0 \\ 0 & 0 & 0 \end{pmatrix}. \tag{3.1.1}$$

An example of this configuration is shown by blue versors in the left panel of Fig.3.1 for $\eta = \frac{\pi}{3}$. Let us further reconsider Eq.(2.1.4): angular pattern functions for a V-shaped
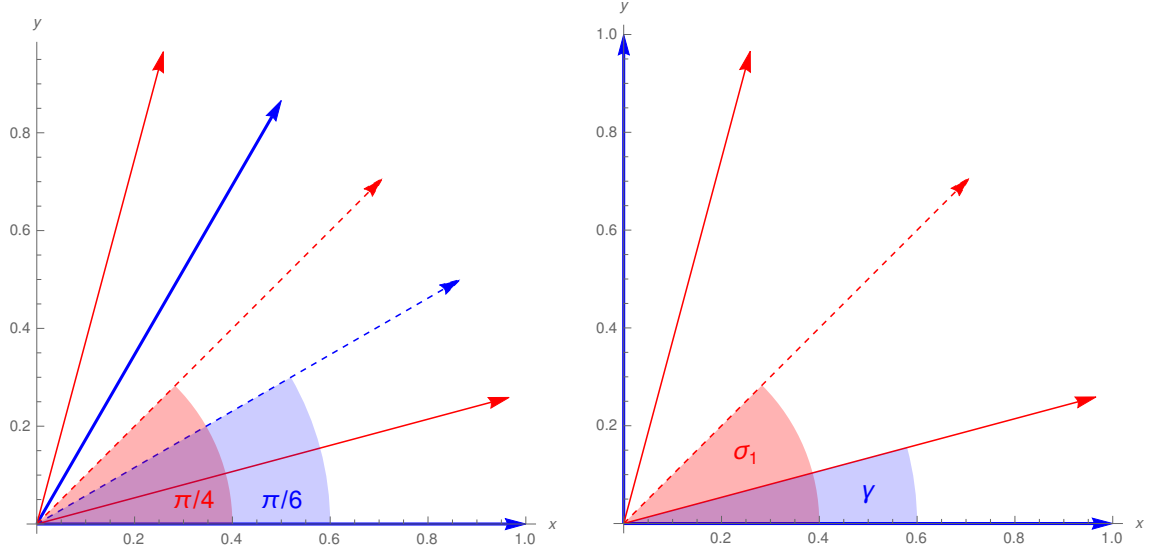
Figure 3.1: (Left) Example of possible configurations for a V-shaped detector with an internal angle of $\frac{\pi}{3}$. (Right) Orientation of the detector arms (red, solid) and bisector (red, dashed) with respect to the vector (x axis) tangent to the circumference connecting the detector pair together.

interferometer are then given by

$$
F^+(\theta, \phi, \psi, \eta) = \frac{1}{4} \sin \eta ((\cos 2\theta + 3) \cos 2\psi \sin(\eta - 2\phi) - 4 \cos \theta \sin 2\psi \cos(\eta - 2\phi))
$$

$$
F^\times(\theta, \phi, \psi, \eta) = \frac{1}{4} \sin \eta (-4 \cos \theta \cos 2\psi \cos(\eta - 2\phi) - (\cos 2\theta + 3) \sin 2\psi \sin(\eta - 2\phi))
$$

$$
F^b(\theta, \phi, \eta) = -\frac{1}{2} \sin \eta \sin^2 \theta \sin(\eta - 2\phi)
$$

$$
F^l(\theta, \phi, \eta) = \frac{1}{\sqrt{2}} \sin \eta \sin^2 \theta \sin(\eta - 2\phi)
$$

$$
F^x(\theta, \phi, \psi, \eta) = \sin \eta \sin \theta (\cos \theta \cos \psi \sin(\eta - 2\phi) - \sin \psi \cos(\eta - 2\phi))
$$

$$
F^y(\theta, \phi, \psi, \eta) = -\sin \eta \sin \theta (\cos \theta \sin \psi \sin(\eta - 2\phi) + \cos \psi \cos(\eta - 2\phi)).
$$

$$(3.1.2)$$

As a consistency check for $\eta = \frac{\pi}{2}$ we get expressions previously found for an L-shaped interferometer and given by Eqs.(2.1.21)-(2.1.26), which is an expected and correct result. We notice that $F^b(\theta, \phi, \eta)$ and $F^l(\theta, \phi, \eta)$ still differ only for a constant factor, thus considering different opening angles do not break the degeneracy between scalar modes. When $f \approx f_*$ the full form of the detector tensor is given by Eq.(2.2.18): transfer function effects

cannot be neglected this time, thus we have

$$
D = \begin{pmatrix} \frac{1}{2}\left(\mathcal{T}_1 - \mathcal{T}_2\cos^2\eta\right) & -\frac{1}{2}\mathcal{T}_2\sin\eta\cos\eta & 0 \\ -\frac{1}{2}\mathcal{T}_2\sin\eta\cos\eta & -\frac{1}{2}\mathcal{T}_2\sin^2\eta & 0 \\ 0 & 0 & 0 \end{pmatrix},
\tag{3.1.3}
$$

where $\mathcal{T}_i$, $i = 1, 2$, are transfer functions for each arm. The latter expression reduces to Eq.(3.1.1) in the long wavelength limit, where $\mathcal{T}_i \approx 1$. Angular pattern functions now depend on GW frequencies, thus we get

$$F^+(\theta,\phi,\psi,\eta,f) = \frac{1}{4}[\cos 2\psi(\cos^2\theta(\cos 2\phi(\mathcal{T}_1 - \mathcal{T}_2\cos 2\eta) + \mathcal{T}_1 - \mathcal{T}_2) + \cos 2\phi(\mathcal{T}_1 - \mathcal{T}_2\cos 2\eta)+$$

$$- \mathcal{T}_1 - \mathcal{T}_2\sin\eta\cos\eta(\cos 2\theta + 3)\sin 2\phi + \mathcal{T}_2) - 2\cos\theta\sin 2\psi(\mathcal{T}_1\sin 2\phi + \mathcal{T}_2\sin(2(\eta - \phi)))]$$

$$F^\times(\theta,\phi,\psi,\eta,f) = \frac{1}{8}[\sin 2\psi((\cos 2\theta + 3)\cos 2\phi(\mathcal{T}_2\cos 2\eta - \mathcal{T}_1) + 2(\mathcal{T}_1 - \mathcal{T}_2)\sin^2\theta+$$

$$+ \mathcal{T}_2\sin 2\eta(\cos 2\theta + 3)\sin 2\phi) - 4\cos\theta\cos 2\psi(\mathcal{T}_1\sin 2\phi + \mathcal{T}_2\sin(2(\eta - \phi)))]$$

$$F^b(\theta,\phi,\eta,f) = \frac{1}{8}[2\sin^2\theta(\mathcal{T}_2\cos(2(\eta - \phi)) - \mathcal{T}_1\cos 2\phi) + (\mathcal{T}_1 - \mathcal{T}_2)(\cos 2\theta + 3)]$$

$$F^l(\theta,\phi,\eta,f) = \frac{\sin^2\theta(\mathcal{T}_1\cos 2\phi + \mathcal{T}_1 - \mathcal{T}_2\cos(2(\eta - \phi)) - \mathcal{T}_2)}{2\sqrt{2}}$$

$$F^x(\theta,\phi,\psi,\eta,f) = \frac{1}{2}\sin\theta[\cos\theta\cos\psi(\mathcal{T}_1\cos 2\phi + \mathcal{T}_1 - \mathcal{T}_2\cos(2(\eta - \phi)) - \mathcal{T}_2)+$$

$$- \sin\psi(\mathcal{T}_1\sin 2\phi + \mathcal{T}_2\sin(2(\eta - \phi)))]$$

$$F^y(\theta,\phi,\psi,\eta,f) = \frac{1}{4}[\sin 2\theta\sin\psi(\mathcal{T}_1(-\cos 2\phi) - \mathcal{T}_1 + \mathcal{T}_2\cos(2(\eta - \phi)) + \mathcal{T}_2)+$$

$$- 2\sin\theta\cos\psi(\mathcal{T}_1\sin 2\phi + \mathcal{T}_2\sin(2(\eta - \phi)))].$$

$$\tag{3.1.4}$$

This result is very intriguing: it suggests that if $f \approx f_*$ or higher, then the degeneracy between breathing and longitudinal modes is broken. We merely assert this here, while we deeply investigate this behaviour at the end of this chapter using both Einstein Telescope and Cosmic Explorer interferometers. For the rest of this section we assume the condition $f \ll f_*$ to be valid instead. Since we are only changing the detector internal angle we expect Eq. (2.5.1) to be the same in form, although we recall that normalization factors appearing in Eqs.(2.5.2)-(2.5.4) were obtained considering two L shaped interferometers. To overcome this issue, we simply need to compute Eqs.(2.4.16)-(2.4.18) taking two interferometers with opening angles η and τ, with $\eta, \tau \in (0, \frac{\pi}{2}]$. From Eq.(3.1.2) it is straightforward to see that

$$
F_{IJ}^T = \frac{2}{5}\sin\eta\sin\tau, \qquad F_{IJ}^V = \frac{2}{5}\sin\eta\sin\tau, \qquad F_{IJ}^S = \frac{1 + 2\kappa}{15}\sin\eta\sin\tau, \tag{3.1.5}
$$

which are general normalization factors affected by the interferometer opening angle. We now wish to compute the overlap reduction function of a V-shaped interferometer pair on

Earth by retracing what we did in the previous chapter: detectors I and J now have opening angles η and τ and we choose unit vectors directed along their arms as $\hat{\mathbf{e}}_1'$, $\hat{\mathbf{e}}_2'$ and $\hat{\mathbf{e}}_1''$, $\hat{\mathbf{e}}_2''$. These unit vectors are expressed as a counterclowise rotation of the unit vectors $\hat{\mathbf{x}}'$ and $\hat{\mathbf{x}}''$ on the $(\hat{\mathbf{x}}', \hat{\mathbf{y}}')$ and $(\hat{\mathbf{x}}'', \hat{\mathbf{y}}'')$ planes with respect to the proper x-axis. Rotation angles are now $\gamma = \sigma_1 - \frac{\eta}{2}$ and $\delta = \sigma_2 - \frac{\tau}{2}$. Considering the left panel of Fig. 2.9 and the right panel of Fig. 3.1 this time we get

$$\hat{\mathbf{e}}_1' = (\cos\gamma, \sin\gamma, 0), \qquad\qquad \hat{\mathbf{e}}_2' = (\cos(\eta+\gamma), \sin(\eta+\gamma), 0),$$
$$\hat{\mathbf{e}}_1'' = (\cos\beta\cos\delta, \sin\delta, \sin\beta\cos\delta), \quad \hat{\mathbf{e}}_2'' = (\cos\beta\cos(\tau+\delta), \sin(\tau+\delta), \sin\beta\cos(\tau+\delta)),$$
$$\text{(3.1.6)}$$

and the following expressions for the detector tensors

$$\mathbf{D}_I = \frac{1}{2}\{\hat{\mathbf{e}}_1' \otimes \hat{\mathbf{e}}_1' - \hat{\mathbf{e}}_2' \otimes \hat{\mathbf{e}}_2'\} = \frac{\sin\eta}{2}\begin{pmatrix} \sin(\eta+2\gamma) & -\cos(\eta+2\gamma) & 0 \\ -\cos(\eta+2\gamma) & -\sin(\eta+2\gamma) & 0 \\ 0 & 0 & 0 \end{pmatrix}, \qquad \text{(3.1.7)}$$

and

$$\mathbf{D}_J = \frac{1}{2}\{\hat{\mathbf{e}}_1'' \otimes \hat{\mathbf{e}}_1'' - \hat{\mathbf{e}}_2'' \otimes \hat{\mathbf{e}}_2''\} =$$
$$= \frac{\sin\tau}{2}\begin{pmatrix} \cos^2\beta\sin(\tau+2\delta) & -\cos\beta\cos(\tau+2\delta) & -\sin\beta\cos\beta\sin(\tau+2\delta) \\ -\cos\beta\cos(\tau+2\delta) & -\sin(\tau+2\delta) & \sin\beta\cos(\tau+2\delta) \\ -\sin\beta\cos\beta\sin(\tau+2\delta) & \sin\beta\cos(\tau+2\delta) & \sin^2\beta\sin(\tau+2\delta) \end{pmatrix}.$$
$$\text{(3.1.8)}$$

We simply need to compute the same objects we met beofore, we get

- for $D_I^{ij}D_{Jij}$

$$D_I^{ij}D_{Jij} = D_I^{11}D_{J11} + D_I^{12}D_{J12} + D_I^{21}D_{J21} + D_I^{22}D_{J22}$$
$$= \frac{\sin\eta\sin\tau}{4}\big(\sin(\eta+2\gamma)\sin(\tau+2\delta) + 2\cos\beta\cos(\eta+2\gamma)\cos(\tau+2\delta)+$$
$$+ \cos^2\beta\sin(\eta+2\gamma)\sin(\tau+2\delta)\big),$$
$$\text{(3.1.9)}$$

- for $D_{Ik}^i D_J^{kj} d_i d_j$

$$D_{Ik}^i D_J^{kj} d_i d_j = D_{I1}^1 D_J^{11} d_1 d_1 + D_{I1}^1 D_J^{13} d_1 d_3 + D_{I2}^1 D_J^{21} d_1 d_1 + D_{I2}^1 D_J^{23} d_1 d_3$$
$$= \frac{\sin\eta\sin\tau}{4}\Big(\cos\beta\cos^2\frac{\beta}{2}\cos(\eta+2\gamma)\cos(\tau+2\delta)+$$
$$+ \sin\beta\sin\frac{\beta}{2}\cos\frac{\beta}{2}\cos(\eta+2\gamma)\cos(\tau+2\delta) + \cos^2\beta\cos^2\frac{\beta}{2}\sin(\eta+2\gamma)\sin(\tau+2\delta)+$$
$$+ \sin\beta\cos\beta\sin\frac{\beta}{2}\cos\frac{\beta}{2}\sin(\eta+2\gamma)\sin(\tau+2\delta)\Big),$$
$$\text{(3.1.10)}$$

- for $D_I^{ij} D_J^{kl} d_i d_j d_k d_l$

$$D_I^{ij} D_J^{kl} d_i d_j d_k d_l = D_I^{11} D_J^{11} d_1 d_1 d_1 d_1 + D_I^{11} D_J^{13} d_1 d_1 d_1 d_3 + D_I^{11} D_J^{31} d_1 d_1 d_3 d_1 + D_I^{11} D_J^{33} d_1 d_1 d_3 d_3$$

$$= \frac{\sin \eta \sin \tau}{4} \Big(\cos^2 \beta \cos^4 \frac{\beta}{2} \sin(\eta + 2\gamma) \sin(\tau + 2\delta) +$$

$$+ 2 \sin \beta \cos \beta \sin \frac{\beta}{2} \cos^3 \frac{\beta}{2} \sin(\eta + 2\gamma) \sin(\tau + 2\delta)$$

$$+ \sin^2 \beta \sin^2 \frac{\beta}{2} \cos^2 \frac{\beta}{2} \sin(\eta + 2\gamma) \sin(\tau + 2\delta) \Big).$$

$$(3.1.11)$$

Notice how the factor $\sin \eta \sin \tau$ is common between all these contractions. We define the two parameters $\sigma^+ \equiv \frac{\sigma_1 + \sigma_2}{2}$ and $\sigma^- \equiv \frac{\sigma_1 - \sigma_2}{2}$, this way can compute

$$\begin{cases} \cos(\eta + 2\gamma) \cos(\tau + 2\delta) = \frac{1}{2} \big(\cos 4\sigma^- + \cos 4\sigma^+ \big) \\ \sin(\eta + 2\gamma) \sin(\tau + 2\delta) = \frac{1}{2} \big(\cos 4\sigma^- - \cos 4\sigma^+ \big) \end{cases} . \qquad (3.1.12)$$

Considering Eqs.(2.5.1) and (3.1.5) we notice that factors $(\sin \eta \sin \tau)^{-1}$ relative to the overlap normalizations and the factor $\sin \eta \sin \tau$ relative to the detector tensor contractions perfectly elide each other, meaning that the overlap reduction function expression is still given by Eq.(2.5.53), computed for an L-shaped interferometer. Notice that this is due to the normalization choice we have made for overlap functions; although the SNR is reduced by a factor $\sin \eta \sin \tau$ with respect to the case of two L-shaped interferometers

$$\frac{S}{N} = \frac{3 H_0^2 \sqrt{T} \sin \eta \sin \tau}{10 \pi^2} \left(\int_{-\infty}^{+\infty} df \frac{(\gamma(f) \Omega_{gw}(f))^2}{f^6 S_n^2(f)} \right)^{\frac{1}{2}} . \qquad (3.1.13)$$

3.2 The Einstein Telescope

The Einstein Telescope Project (ET) is an upcoming third-generation ground-based gravitational wave detector. A possible configuration for [82, 83] ET adopts the *xylophone configuration* which consists of three underground detectors, each in turn composed of two aligned V-shaped interferometers with an opening angle $\eta = \frac{\pi}{3}$, arm length $L = 10$ Km and characteristic frequency $f_* \approx 4774$ Hz. One interferometer is optimized to detect low GW frequencies (1 Hz - 250 Hz), while the other one aims to detect GWs with higher frequencies (10 Hz - 10 kHz) and the two are expected to work together to extend ET detectors sensitivity to the whole allowed frequency range [82]. These three detectors are displaced in a triangular way as shown in Fig.3.2, where we decided to label them as A, B and C. We then consider the frame of reference introduced by Eq.(2.1.6), this way we can define
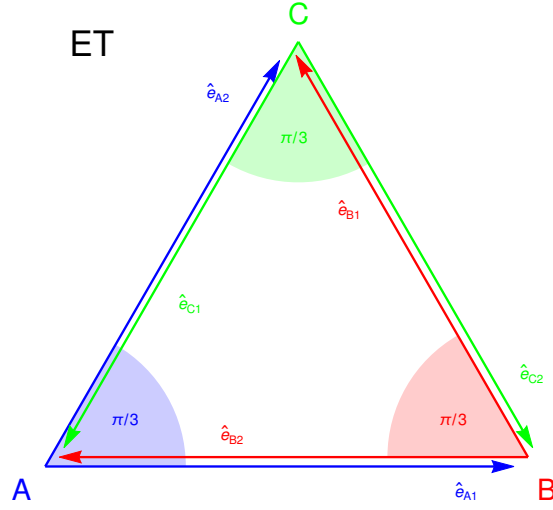
Figure 3.2: Einstein Telescope interferometers configuration.

versors directed along each interferometer arm

$$\hat{\mathbf{e}}_{\mathbf{A1}} = (\cos 0, \sin 0, 0)^T, \qquad\qquad \hat{\mathbf{e}}_{\mathbf{A2}} = (\cos\frac{\pi}{3}, \sin\frac{\pi}{3}, 0)^T, \qquad\qquad (3.2.1a)$$

$$\hat{\mathbf{e}}_{\mathbf{B1}} = \left(\cos\left(\pi - \frac{\pi}{3}\right), \sin\left(\pi - \frac{\pi}{3}\right), 0\right)^T, \qquad \hat{\mathbf{e}}_{\mathbf{B2}} = (\cos\pi, \sin\pi, 0)^T, \qquad\qquad (3.2.1b)$$

$$\hat{\mathbf{e}}_{\mathbf{C1}} = \left(\cos\left(\pi + \frac{\pi}{3}\right), \sin\left(\pi + \frac{\pi}{3}\right), 0\right)^T, \qquad \hat{\mathbf{e}}_{\mathbf{C2}} = \left(\cos\left(2\pi - \frac{\pi}{3}\right), \sin\left(2\pi - \frac{\pi}{3}\right), 0\right)^T.$$
$$(3.2.1c)$$

The Einstein Telescope can detect GWs with $f \lessgtr f_*$, thus in the following we need to consider two different working regimes.

3.2.1 Einstein Telescope at Low Frequencies

Let us start assuming the long wavelength limit is valid: we have three different detector tensors, one for each ET interferometer[1]

$$D^A_{f \ll f_*} = \begin{pmatrix} \frac{3}{8} & -\frac{\sqrt{3}}{8} & 0 \\ -\frac{\sqrt{3}}{8} & -\frac{3}{8} & 0 \\ 0 & 0 & 0 \end{pmatrix}, \tag{3.2.2a}$$

$$D^B_{f \ll f_*} = \begin{pmatrix} -\frac{3}{8} & -\frac{\sqrt{3}}{8} & 0 \\ -\frac{\sqrt{3}}{8} & \frac{3}{8} & 0 \\ 0 & 0 & 0 \end{pmatrix}, \tag{3.2.2b}$$

$$D^C_{f \ll f_*} = \begin{pmatrix} 0 & \frac{\sqrt{3}}{4} & 0 \\ \frac{\sqrt{3}}{4} & 0 & 0 \\ 0 & 0 & 0 \end{pmatrix}. \tag{3.2.2c}$$

As we did for 2nd-generation interferometers, it is straightforward to compute angular pattern functions for each mode using Eq.(2.1.4)

$$F^+_A(\theta, \phi, \psi) = \frac{\sqrt{3}}{8}((\cos 2\theta + 3) \cos 2\psi \sin\left(\frac{\pi}{3} - 2\phi\right) - 4 \cos\theta \sin 2\psi \cos\left(\frac{\pi}{3} - 2\phi\right)) \tag{3.2.3a}$$

$$F^+_B(\theta, \phi, \psi) = -\frac{\sqrt{3}}{8}((\cos 2\theta + 3) \cos 2\psi \sin\left(\frac{\pi}{3} + 2\phi\right) + 4 \cos\theta \sin 2\psi \cos\left(\frac{\pi}{3} + 2\phi\right)) \tag{3.2.3b}$$

$$F^+_C(\theta, \phi, \psi) = \frac{\sqrt{3}}{2}\left(\frac{1}{4}(\cos 2\theta + 3) \cos 2\psi \sin 2\phi + \cos\theta \sin 2\psi \cos 2\phi\right) \tag{3.2.3c}$$

$$F^\times_A(\theta, \phi, \psi) = -\frac{\sqrt{3}}{8}(4 \cos\theta \cos 2\psi \cos\left(\frac{\pi}{3} - 2\phi\right) + (\cos 2\theta + 3) \sin 2\psi \sin\left(\frac{\pi}{3} - 2\phi\right)) \tag{3.2.3d}$$

$$F^\times_B(\theta, \phi, \psi) = \frac{\sqrt{3}}{8}((\cos 2\theta + 3) \sin 2\psi \sin\left(\frac{\pi}{3} + 2\phi\right) - 4 \cos\theta \cos 2\psi \cos\left(\frac{\pi}{3} + 2\phi\right)) \tag{3.2.3e}$$

$$F^\times_C(\theta, \phi, \psi) = \frac{\sqrt{3}}{2}\left(\cos\theta \cos 2\psi \cos 2\phi - \frac{1}{4}(\cos 2\theta + 3) \sin 2\psi \sin 2\phi\right), \tag{3.2.3f}$$

---

[1]Each interferometer couple of the xylophone configuration can be considered as one interferometer sensible to GW frequencies ranging from 1-10 Hz.

$$F_A^x(\theta, \phi, \psi) = \frac{\sqrt{3}}{2} \sin \theta (\cos \theta \cos \psi \sin\left(\frac{\pi}{3} - 2\phi\right) - \sin \psi \cos\left(\frac{\pi}{3} - 2\phi\right)) \qquad (3.2.4a)$$

$$F_B^x(\theta, \phi, \psi) = -\frac{\sqrt{3}}{2} \sin \theta (\cos \theta \cos \psi \sin\left(\frac{\pi}{3} + 2\phi\right) + \sin \psi \cos\left(\frac{\pi}{3} + 2\phi\right)) \qquad (3.2.4b)$$

$$F_C^x(\theta, \phi, \psi) = \frac{1}{2} \sin \theta (\cos \theta \cos \psi \sin 2\phi + \sin \psi \cos 2\phi) \qquad (3.2.4c)$$

$$F_A^y(\theta, \phi, \psi) = -\frac{\sqrt{3}}{2} \sin \theta (\cos \theta \sin \psi \sin\left(\frac{\pi}{3} - 2\phi\right) + \cos \psi \cos\left(\frac{\pi}{3} - 2\phi\right)) \qquad (3.2.4d)$$

$$F_B^y(\theta, \phi, \psi) = \frac{\sqrt{3}}{2} \sin \theta (\cos \theta \sin \psi \sin\left(\frac{\pi}{3} + 2\phi\right) - \cos \psi \cos\left(\frac{\pi}{3} + 2\phi\right)) \qquad (3.2.4e)$$

$$F_C^y(\theta, \phi, \psi) = \frac{1}{2} \sin \theta (\cos \psi \cos 2\phi - 2 \cos \theta \sin \psi \sin \phi \cos \phi). \qquad (3.2.4f)$$

$$F_A^b(\theta, \phi) = -\frac{\sqrt{3}}{4} \sin^2 \theta \sin\left(\frac{\pi}{3} - 2\phi\right) \qquad (3.2.5a)$$

$$F_B^b(\theta, \phi) = \frac{\sqrt{3}}{4} \sin^2 \theta \sin\left(\frac{\pi}{3} + 2\phi\right) \qquad (3.2.5b)$$

$$F_C^b(\theta, \phi) = -\frac{\sqrt{3}}{2} \sin^2 \theta \sin \phi \cos \phi \qquad (3.2.5c)$$

$$F_A^l(\theta, \phi) = \frac{\sqrt{3} \sin^2 \theta \sin\left(\frac{\pi}{3} - 2\phi\right)}{2\sqrt{2}} \qquad (3.2.5d)$$

$$F_B^l(\theta, \phi) = -\frac{\sqrt{3} \sin^2 \theta \sin\left(\frac{\pi}{3} + 2\phi\right)}{2\sqrt{2}} \qquad (3.2.5e)$$

$$F_C^l(\theta, \phi) = \frac{1}{\sqrt{2}} \sin^2 \theta \sin \phi \cos \phi, \qquad (3.2.5f)$$

Notice how the following identities are satisfied due to ET geometrical configuration

$$F_B^Q(\theta, \phi, \psi) = F_A^Q\left(\theta, \phi - \frac{2\pi}{3}, \psi\right), \qquad F_C^Q(\theta, \phi, \psi) = F_A^Q\left(\theta, \phi + \frac{2\pi}{3}, \psi\right), \qquad (3.2.6)$$

with $Q = +, \times, b, l, x, y$. While discussing 2nd-generation interferometers we introduced antenna power pattern functions[2] and we mentioned they are ψ[3]-independent quantities representing the maximum detector reach along different angular directions. Since we now have three detectors, it is indeed useful to consider the network joint response to tensor,

---

[2]We recall that the antenna power pattern function represent the detector maximum detection reach along different angular directions.

[3]We recall that ψ is the polarization angle.

vector and scalar modes, which are defined as

$$F^T(\theta) = \sum_{k=A,B,C} \left((F_k^+)^2 + (F_k^\times)^2\right)$$

$$= \frac{9}{256}\left(35 + 28\cos 2\theta + \cos 4\theta\right), \tag{3.2.7}$$

$$F^V(\theta) = \sum_{k=A,B,C} \left((F_k^x)^2 + (F_k^y)^2\right)$$

$$= \frac{9}{16}\left(3 + \cos 2\theta\right)\sin^2\theta, \tag{3.2.8}$$

$$F^S(\theta) = \sum_{k=A,B,C} \left((F_k^b)^2 + (F_k^l)^2\right)$$

$$= \frac{27\sin^4\theta}{32}. \tag{3.2.9}$$

We appreciate how ET joint responses are independent from both angular variables ψ and ϕ for each polarization mode: relative plots are shown in Fig. 3.3, 3.4, 3.5. If we compare them to Fig. 2.6 and 2.8 we notice how the GWs detection reach is definitely improved for ET: starting from tensor modes, the Einstein Telescope presents no blind spots at all, making ET sensible to GWs incoming from every direction; moving on to vector and scalar modes, only GWs along directions perpendicular to the interferometer plane ($\theta = 0$, π) cannot be detected. Moreover, V-shaped interferometers suffer from an opening angle of $\frac{\pi}{3}$, but all three detectors combined enhance ET maximum detection reach by the following factors κ_N

$$\left[(F^+(\theta=0,\phi))^2 + (F^\times(\theta=0,\phi))^2\right]_L = 1, \quad F^T(0) = \frac{9}{4}, \quad \kappa_T = \left(\frac{3}{2}\right)^2 > 1, \tag{3.2.10a}$$

$$\left[(F^x(\theta=\frac{\pi}{2},\phi=\frac{\pi}{4}))^2 + (F^y(\theta=\frac{\pi}{2},\phi=\frac{\pi}{4}))^2\right]_L = 1, \quad F^V(\frac{\pi}{2}) = \frac{9}{8}, \quad \kappa_V = \frac{1}{2}\left(\frac{3}{2}\right)^2 > 1, \tag{3.2.10b}$$

$$\left[(F^b(\theta=\frac{\pi}{2},\phi=0))^2 + (F^l(\theta=\frac{\pi}{2},\phi=0))^2\right]_L = \frac{27}{32}, \quad F^V(\frac{\pi}{2}) = \frac{3}{4}, \quad \kappa_S = \frac{1}{2}\left(\frac{3}{2}\right)^2 > 1, \tag{3.2.10c}$$

where the subscript "L" denotes a single L-shaped interferometer.

At the time of writing (2020) there are two possible Earth locations where ET can be placed [82, 84] the first one is in Italy, in the Sos Enattos mine in the city of Lula in Sardinia (ETS), while the second one is in Netherland in the city of Limburg (ETN). If we consider the Earth-based frame of reference introduced in Appendix C, then these locations are denoted by

$$\hat{\mathbf{x}}_{\mathbf{ETS}} = (0.750, 0.125, 0.649), \qquad \hat{\mathbf{x}}_{\mathbf{ETN}} = (0.631, -0.089, 0.770). \tag{3.2.11}$$
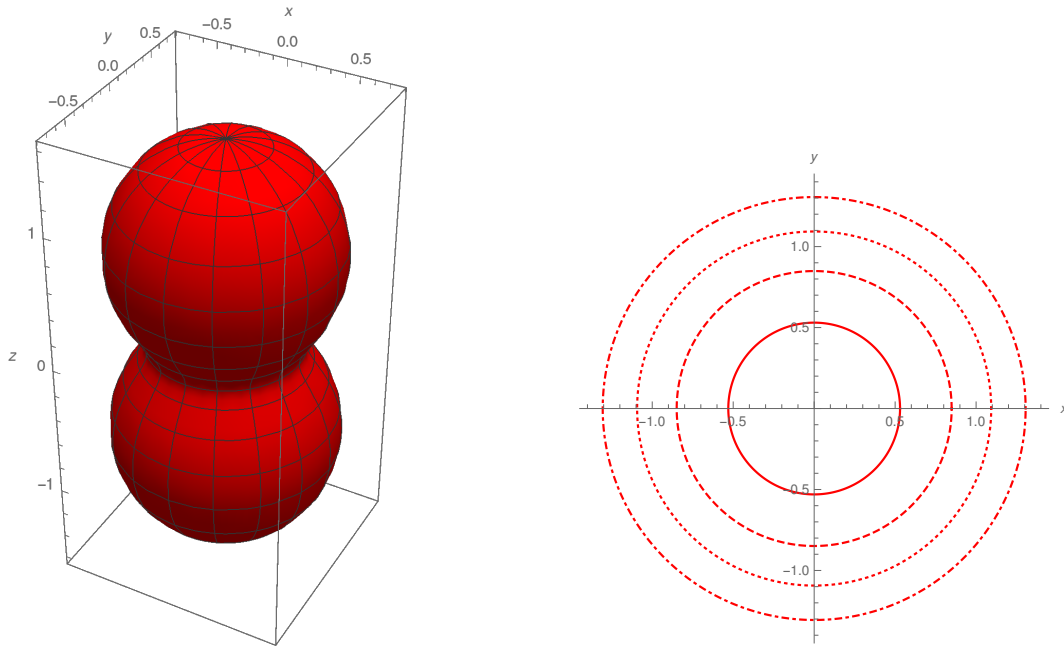
Figure 3.3: $3D$ plot of $\sqrt{F^T(\theta)}$, and relative projection on a $2D$ plane for different fixed values of θ (($\frac{\pi}{6}$, dot-dashed), ($\frac{\pi}{4}$, dotted), ($\frac{\pi}{3}$, dashed), ($\frac{\pi}{2}$, solid). In terms of tensor modes, there are no blind directions and ET can cover the whole sky. Due to ET triangular configuration, the maximum detection reach is enhanced by $\frac{3}{2}$ with respect to a single L-shaped interferometer.
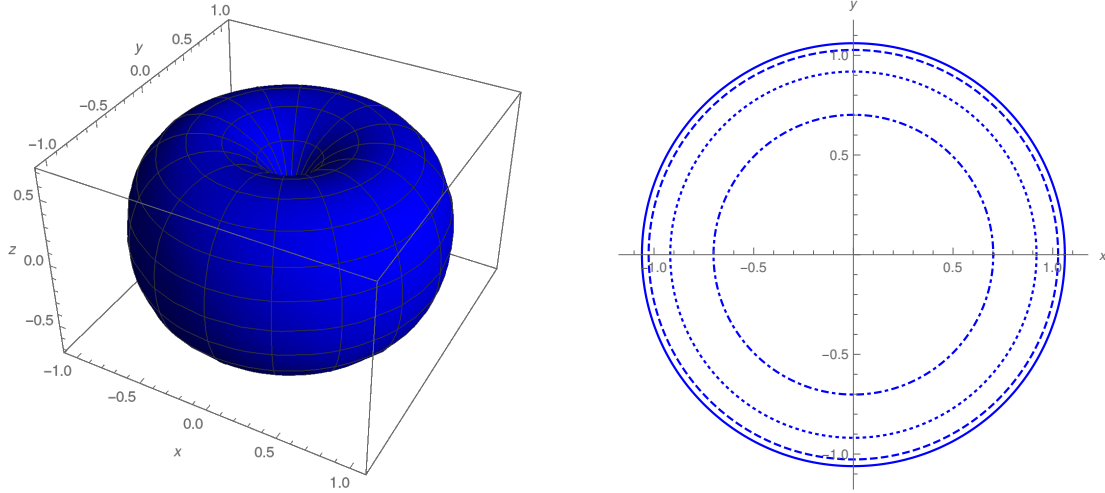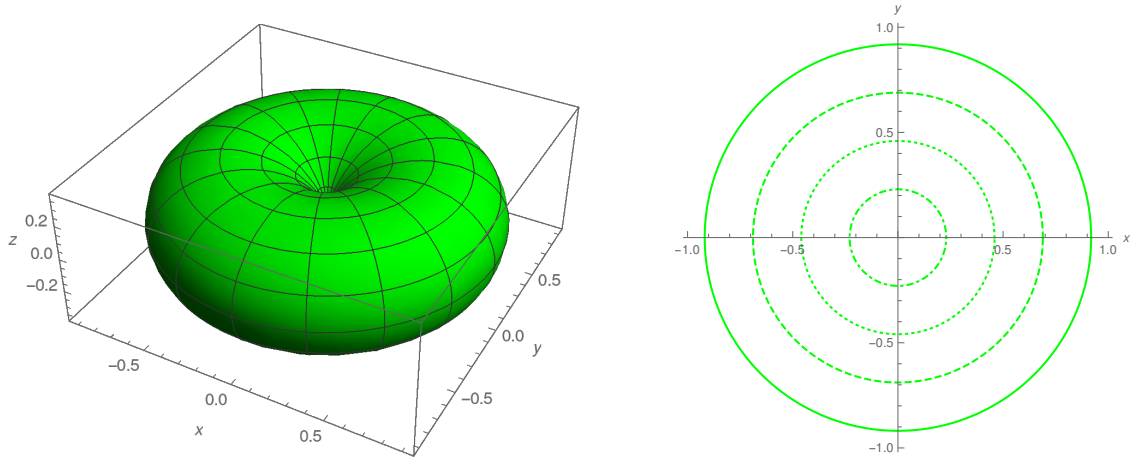
Figure 3.4: $3D$ plot of $\sqrt{F^V(\theta)}$ and relative projection on a $2D$ plane for different fixed values of θ (($\frac{\pi}{6}$, dot-dashed), ($\frac{\pi}{4}$, dotted), ($\frac{\pi}{3}$, dashed), ($\frac{\pi}{2}$, solid). In terms of cector modes blind directions are present for $\theta = 0, \pi$. Due to ET triangular configuration, the maximum detection reach for tensor modes is enhanced by $\frac{3}{2\sqrt{2}}$ with respect to a single L-shaped interferometer.

Figure 3.5: $3D$ plot of $\sqrt{F^S(\theta)}$ and relative projection on a $2D$ plane for different fixed values of θ (($\frac{\pi}{6}$, dot-dashed), ($\frac{\pi}{4}$, dotted), ($\frac{\pi}{3}$, dashed), ($\frac{\pi}{2}$, solid). In terms of scalar modes blind directions are present for $\theta = 0, \pi$. Due to ET triangular configuration, the maximum detection reach for tensor modes is enhanced by $\frac{3}{2\sqrt{2}}$ with respect to a single L-shaped interferometer.

We further consider Earth rotation around its axis with constant angular velocity $\omega = 7.29 \times 10^{-5} rad/s$ and we wish to understand how this motion affects the detector joint response to GWs. Let us focus on the Sardinia site for a concrete example: the Einstein Telescope lies on the plane π orthogonal to the direction denoted by $\hat{\mathbf{x}}_{\mathbf{ETS}}$, thus we have

$$\pi : \quad (0.750)x + (0.125)y + (0.649)z + \omega = 0, \tag{3.2.12}$$

where ω can be set to zero once we pick the plane containing the origin $O = (0,0,0)^T$. We showed in Eqs.(3.2.7)-(3.2.9) that joint responses do not depend on ϕ. This is a general result due to ET triangular configuration, thus we can pick any unit vector lying on π to be the one directed along the first interferometer arm; a simple example may be

$$\hat{\mathbf{e}}_{\mathbf{1}} = \frac{(1, -\frac{0.750}{0.125}, 0)^T}{\|(1, -\frac{0.750}{0.125}, 0)\|} = (0.1644, -0.9864, 0)^T. \tag{3.2.13}$$

We want to account for Earth rotation and we do that rotating $\hat{\mathbf{e}}_{\mathbf{1}}$ by ωt around Earth axis, thus

$$\hat{\mathbf{e}}_{\mathbf{1}}(t) = \begin{pmatrix} \cos(\omega t) & -\sin(\omega t) & 0 \\ \sin(\omega t) & \cos(\omega t) & 0 \\ 0 & 0 & 1 \end{pmatrix} \begin{pmatrix} 0.1644 \\ -0.9864 \\ 0 \end{pmatrix}. \tag{3.2.14}$$

It is then straightforward to find unit vectors related to all interferometer arms rotating[4] $\hat{\mathbf{e}}_{\mathbf{1}}(t)$ around $\hat{\mathbf{x}}_{\mathbf{ETS}}$ by $\alpha = m\frac{\pi}{3}$, with $m = 1, 2, 3, 4, 5$; this procedure can be easily extended to the Netherland site. This allow us to investigate ET joint responses to tensor, vector and scalar modes merely by knowing its location on Earth: indeed we can build detector tensors and solve Eq.(2.1.4) numerically. In Fig. 3.6, 3.7 and 3.8 we show the Mollweide projections at 6 hours intervals of the joint responses relative to the Einstein Telescope located at the Sardinia site, while in Fig. 3.9, 3.10 and 3.11 we show the ones relative to the Netherland site. Since these two sites are very close together, we get very similar results. It is worth noting that Earth rotation allows ET vector and scalar responses to cover the whole sky along one day period, thus overcoming the blind directions issue; this problem does not arise for plus and cross polarized GWs since in terms of tensor modes ET has no blind directions.

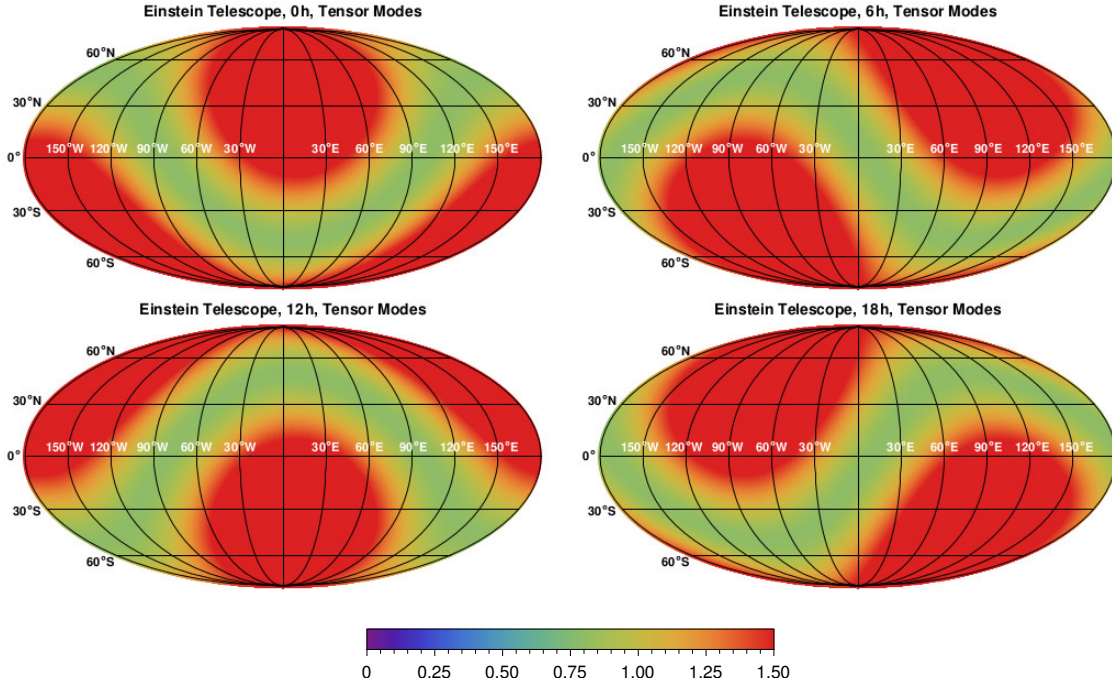[4]Since $L \ll R_E$ we can assume ET detectors lay on the same plane.

Figure 3.6: Mollweide projections of the Einstein Telescope (Sardinia site) joint response for tensor modes for $f \ll f_*$. The Earth-based coordinate system used is described in Appendix C. Earth rotation was also considered and plots are given every 6 hours. In the context of tensor modes, the Einstein Telescope has all-sky coverage, with best detection reach for GWs coming along orthogonal directions to the detector plane.
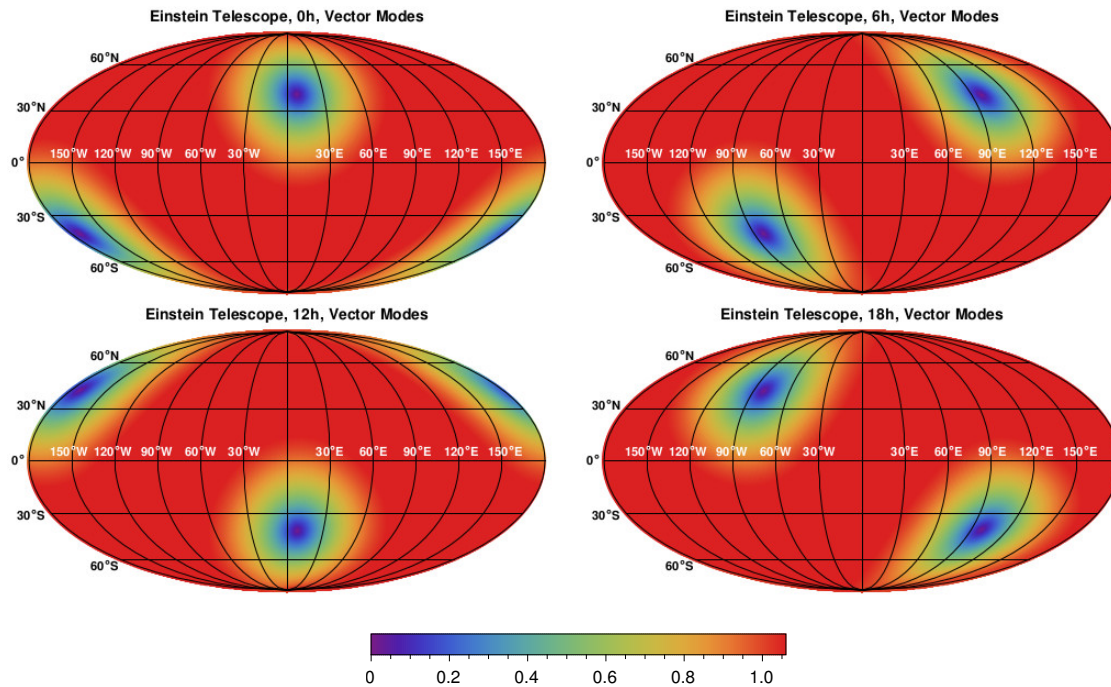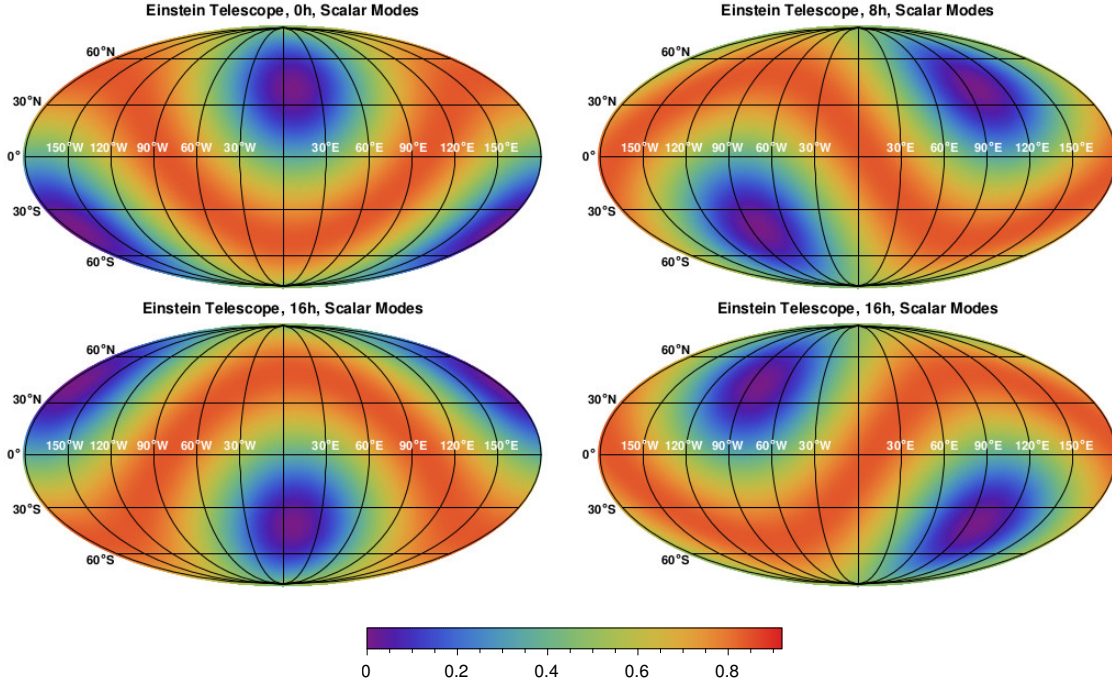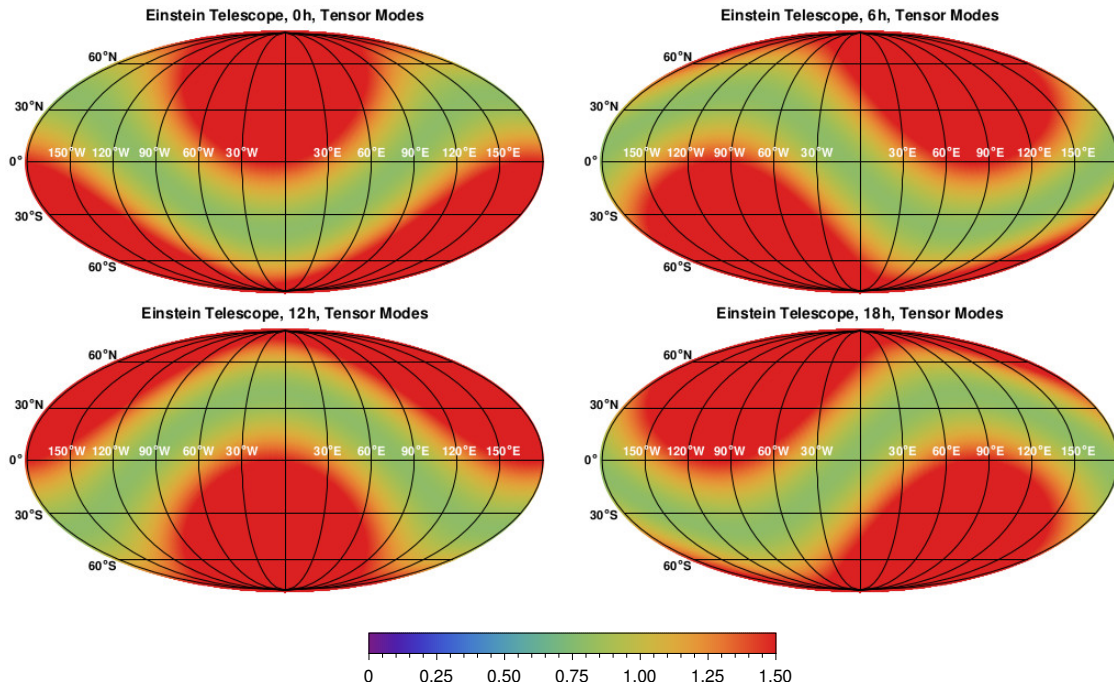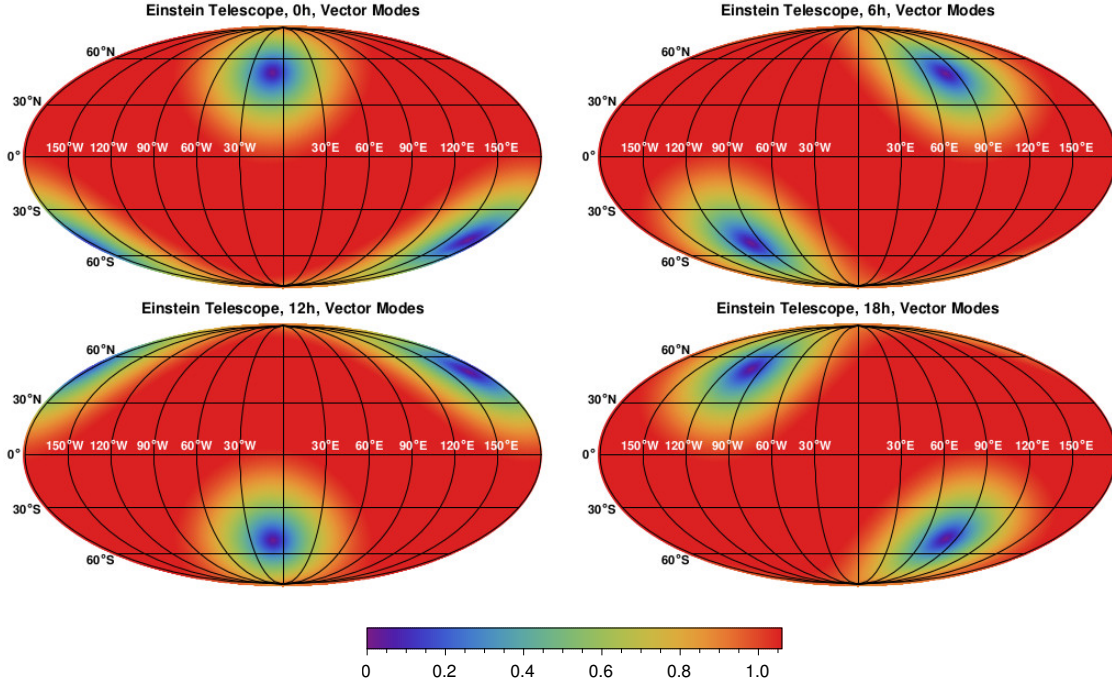
85

Figure 3.7: Mollweide projections of the Einstein Telescope (Sardinia site) joint response for vector modes for $f \ll f_*$. The Earth-based coordinate system used is described in Appendix C. Earth rotation was also considered and plots are given every 6 hours. In the context of vector modes, the Einstein Telescope has only one blind spot along the orthogonal direction to the detector plane. The best detection reach is for GWs coming along parallel directions to the detector plane.
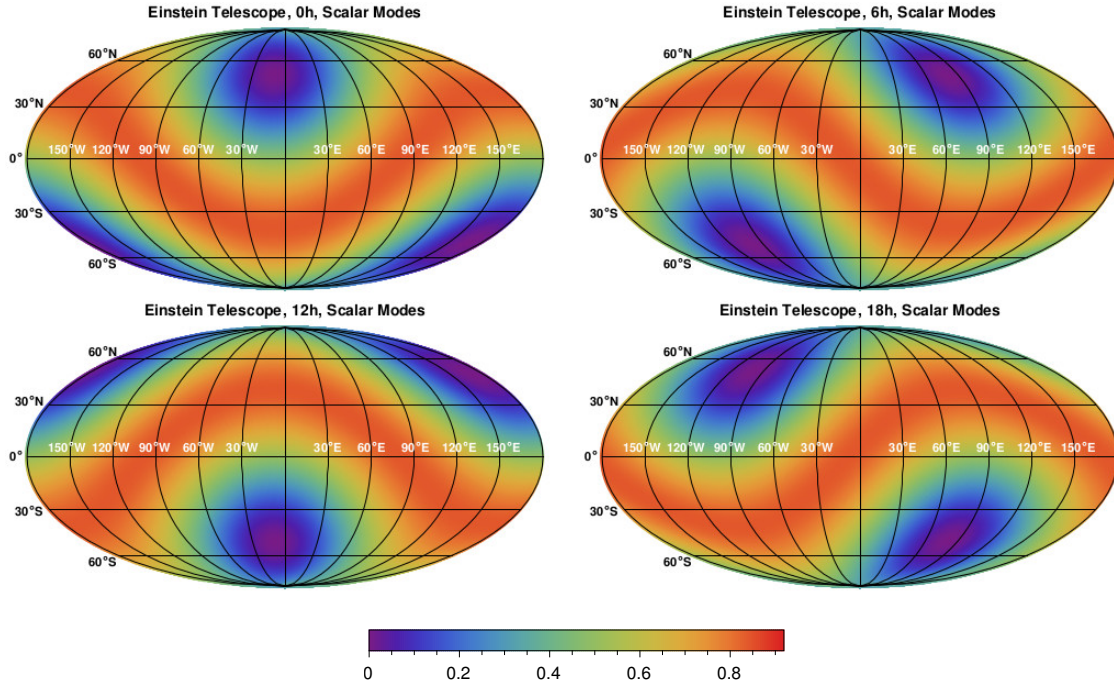
Figure 3.8: Mollweide projections of the Einstein Telescope (Sardinia site) joint response for scalar modes for $f \ll f_*$. The Earth-based coordinate system used is described in Appendix C. Earth rotation was also considered and plots are given every 6 hours. In the context of scalar modes, the Einstein Telescope has only one blind spot along the orthogonal direction to the detector plane. The best detection reach is for GWs coming along parallel directions to the detector plane.

Figure 3.9: Mollweide projections of the Einstein Telescope (Netherland site) joint response to tensor modes for $f \ll f_*$. The Earth-based coordinate system used is described in Appendix C. Earth rotation was also considered and plots are given every 6 hours. In the context of tensor modes, the Einstein Telescope has all-sky coverage, with best detection reach for GWs coming along the orthogonal direction to the detector plane.

Figure 3.10: Mollweide projections of the Einstein Telescope (Netherland site) joint response to vector modes for $f \ll f_*$. The Earth-based coordinate system used is described in Appendix C. Earth rotation was also considered and plots are given every 6 hours. In the context of vector modes, the Einstein Telescope has only one blind spot along the orthogonal direction to the detector plane. The best detection reach is for GWs coming along parallel directions to the detector plane.

Figure 3.11: Mollweide projections of the Einstein Telescope (Netherland site) joint response to scalar modes for $f \ll f_*$. The Earth-based coordinate system used is described in Appendix C. Earth rotation was also considered and plots are given every 6 hours. In the context of scalar modes, the Einstein Telescope has only one blind spot along the orthogonal direction to the detector plane. The best detection reach is for GWs coming along parallel directions to the detector plane.

3.2.2 Einstein Telescope at High Frequencies

Let us now focus on GW frequencies $f \gtrsim f_*$. This time we need to consider detector tensors accounting for transfer functions effects, thus their expressions are given by Eq.(2.2.18) or (2.3.19) depending on which configuration we are using. We can keep the discussion general for the time being, thus we do not write down explicit expressions for transfer functions. Once again we begin by considering unit vectors given by Eq.(3.2.1), although this time we have three different frequency-dependent detector tensors, one for each ET interferometer

$$D^A = \begin{pmatrix} \frac{1}{2}\left(\mathcal{T}_{A1} - \frac{\mathcal{T}_{A2}}{4}\right) & -\frac{\sqrt{3}}{8}\mathcal{T}_{A2} & 0 \\ -\frac{\sqrt{3}}{8}\mathcal{T}_{A2} & -\frac{3}{8}\mathcal{T}_{A2} & 0 \\ 0 & 0 & 0 \end{pmatrix}, \tag{3.2.15a}$$

$$D^B = \begin{pmatrix} \frac{1}{2}\left(\frac{\mathcal{T}_{B1}}{4} - \mathcal{T}_{B2}\right) & -\frac{\sqrt{3}}{8}\mathcal{T}_{B1} & 0 \\ -\frac{\sqrt{3}}{8}\mathcal{T}_{B1} & \frac{3}{8}\mathcal{T}_{B1} & 0 \\ 0 & 0 & 0 \end{pmatrix}, \tag{3.2.15b}$$

$$D^C = \begin{pmatrix} \frac{1}{8}(\mathcal{T}_{C1} - \mathcal{T}_{C2}) & \frac{\sqrt{3}}{8}(\mathcal{T}_{C1} + \mathcal{T}_{C2}) & 0 \\ \frac{\sqrt{3}}{8}(\mathcal{T}_{C1} + \mathcal{T}_{C2}) & \frac{3}{8}(\mathcal{T}_{C1} - \mathcal{T}_{C2}) & 0 \\ 0 & 0 & 0 \end{pmatrix}, \tag{3.2.15c}$$

where we have defined the transfer functions $\mathcal{T}_{M1}(\hat{\mathbf{\Omega}} \cdot \hat{\mathbf{e}}_{\mathbf{M1}}, f)$ and $\mathcal{T}_{M2}(\hat{\mathbf{\Omega}} \cdot \hat{\mathbf{e}}_{\mathbf{M2}}, f)$, with $M = A, B, C$. As we mentioned, this implies frequency dependent angular pattern functions for each polarization mode. Starting from the tensor ones we get

$$F_A^+(\theta, \phi, \psi, f) = \frac{1}{4}\Big(\cos 2\psi\big(\cos^2\theta(\cos 2\phi(\mathcal{T}_{A1} - \mathcal{T}_{A2}\cos 2\frac{\pi}{3}) + \mathcal{T}_{A1} - \mathcal{T}_{A2}) + \cos 2\phi(\mathcal{T}_{A1} - \mathcal{T}_{A2}\cos 2\frac{\pi}{3}) +$$
$$- \mathcal{T}_{A1} - \mathcal{T}_{A2}\sin\frac{\pi}{3}\cos\frac{\pi}{3}(\cos 2\theta + 3)\sin 2\phi +$$
$$+ \mathcal{T}_{A2}) - 2\cos\theta\sin 2\psi(\mathcal{T}_{A1}\sin 2\phi + \mathcal{T}_{A2}\sin\left(2(\frac{\pi}{3} - \phi)\right)))) \tag{3.2.16a}$$

$$F_B^+(\theta, \phi, \psi, f) = \frac{1}{8}\Big(\cos 2\psi\big((\mathcal{T}_{B1} - \mathcal{T}_{B2})\cos 2\theta + \mathcal{T}_{B1}(\cos 2\theta + 3)\cos\left(2(\frac{\pi}{3} + \phi)\right) +$$
$$- \mathcal{T}_{B1} - \mathcal{T}_{B2}(\cos 2\theta + 3)\cos 2\phi +$$
$$+ \mathcal{T}_{B2}) + 4\cos\theta\sin 2\psi(\mathcal{T}_{B2}\sin 2\phi - \mathcal{T}_{B1}\sin\left(2(\frac{\pi}{3} + \phi)\right)))) \tag{3.2.16b}$$

$$F_C^+(\theta, \phi, \psi, f) = \frac{1}{2}\Big((\mathcal{T}_{C1} - \mathcal{T}_{C2})\cos^2\frac{\pi}{3}\big(\cos 2\psi\big(\cos^2\theta\cos^2\phi - \sin^2\phi\big) - 4\cos\theta\sin\psi\cos\psi\sin\phi\cos\phi\big) +$$
$$+ (\mathcal{T}_{C1} - \mathcal{T}_{C2})\sin^2\frac{\pi}{3}\big(\cos 2\psi\big(\cos^2\theta\sin^2\phi - \cos^2\phi\big) + \cos\theta\sin 2\psi\sin 2\phi\big) +$$
$$+ (\mathcal{T}_{C1} + \mathcal{T}_{C2})\sin 2\frac{\pi}{3}\big(\frac{1}{4}(\cos 2\theta + 3)\cos 2\psi\sin 2\phi + \cos\theta\sin 2\psi\cos 2\phi\big)\Big) \tag{3.2.16c}$$

91

$$F_A^\times(\theta,\phi,\psi,f) = \frac{1}{8}\Big(\sin 2\psi\big((\cos 2\theta + 3)\cos 2\phi(\mathcal{T}_{A2}(-\frac{1}{2}) - \mathcal{T}_{A1}) + 2(\mathcal{T}_{A1} - \mathcal{T}_{A2})\sin^2\theta+$$

$$+ \mathcal{T}_{A2}(\frac{\sqrt{3}}{2})(\cos 2\theta + 3)\sin 2\phi) - 4\cos\theta\cos 2\psi(\mathcal{T}_{A1}\sin 2\phi+$$

$$+ \mathcal{T}_{A2}\sin\Big(2(\frac{\pi}{3} - \phi)\Big)\big)\Big) \tag{3.2.17a}$$

$$F_B^\times(\theta,\phi,\psi,f) = \frac{1}{8}\big(4\cos\theta\cos 2\psi(\mathcal{T}_{B2}\sin 2\phi - \mathcal{T}_{B1}\sin\Big(2(\frac{\pi}{3} + \phi)\Big)) + \sin 2\psi((\mathcal{T}_{B2} - \mathcal{T}_{B1})\cos 2\theta+$$

$$+ \mathcal{T}_{B1}(-(\cos 2\theta + 3))\cos\Big(2(\frac{\pi}{3} + \phi)\Big) + \mathcal{T}_{B1}+$$

$$+ \mathcal{T}_{B2}(\cos 2\theta + 3)\cos 2\phi - \mathcal{T}_{B2})\big) \tag{3.2.17b}$$

$$F_C^\times(\theta,\phi,\psi,f) = \frac{1}{16}\Big(\sin 2\psi\big(-2(\mathcal{T}_{C1} - \mathcal{T}_{C2})(-\frac{1}{2})(\cos 2\theta + 3)\cos 2\phi - 2(\mathcal{T}_{C1} + \mathcal{T}_{C2})(\frac{\sqrt{3}}{2})(\cos 2\theta + 3)\sin 2\phi+$$

$$+ 4(\mathcal{T}_{C1} - \mathcal{T}_{C2})\sin^2\theta\big) + 8\cos\theta\cos 2\psi(\mathcal{T}_{C1}\sin\Big(2(\frac{\pi}{3} - \phi)\Big)+$$

$$+ \mathcal{T}_{C2}\sin\Big(2(\frac{\pi}{3} + \phi)\Big)\big)\Big), \tag{3.2.17c}$$

for breathing and longitudinal scalar modes we get

$$F_A^b(\theta,\phi,f) = \frac{1}{8}\Big(2\sin^2\theta(\mathcal{T}_{A2}\cos\Big(2(\frac{\pi}{3} - \phi)\Big) - \mathcal{T}_{A1}\cos 2\phi) + (\mathcal{T}_{A1} - \mathcal{T}_{A2})(\cos 2\theta + 3)\Big)$$
$$\tag{3.2.18a}$$

$$F_B^b(\theta,\phi,f) = \frac{1}{8}\Big(\cos 2\theta(\mathcal{T}_{B1} - \mathcal{T}_{B2}\cos 2\phi - \mathcal{T}_{B2}) - 2\mathcal{T}_{B1}\sin^2\theta\cos\Big(2(\frac{\pi}{3} + \phi)\Big)+$$

$$+ 3\mathcal{T}_{B1} + \mathcal{T}_{B2}\cos 2\phi - 3\mathcal{T}_{B2}\Big) \tag{3.2.18b}$$

$$F_C^b(\theta,\phi,f) = \frac{1}{2}\Big((\mathcal{T}_{C1} - \mathcal{T}_{C2})(\frac{1}{4})\big(\cos^2\theta\cos^2\phi + \sin^2(\phi)\big) + (\mathcal{T}_{C1} - \mathcal{T}_{C2})(\frac{3}{4})\big(\cos^2\theta\sin^2(\phi)+$$

$$+ \cos^2\phi\big) - (\mathcal{T}_{C1} + \mathcal{T}_{C2})(\frac{\sqrt{3}}{2})\sin^2\theta\sin\phi\cos\phi\Big) \tag{3.2.18c}$$

$$F_A^l(\theta,\phi,f) = \frac{\sin^2\theta(\mathcal{T}_{A1}\cos 2\phi + \mathcal{T}_{A1} - \mathcal{T}_{A2}\cos\big(2(\frac{\pi}{3} - \phi)\big) - \mathcal{T}_{A2})}{2\sqrt{2}} \tag{3.2.19a}$$

$$F_B^l(\theta,\phi,f) = \frac{\sin^2\theta(\mathcal{T}_{B1}\cos\big(2(\frac{\pi}{3} + \phi)\big) + \mathcal{T}_{B1} - \mathcal{T}_{B2}\cos 2\phi - \mathcal{T}_{B2})}{2\sqrt{2}} \tag{3.2.19b}$$

$$F_C^l(\theta,\phi,f) = \frac{\sin^2\theta(\mathcal{T}_{C1}\cos\big(2(\frac{\pi}{3} - \phi)\big) + \mathcal{T}_{C1} - \mathcal{T}_{C2}\cos\big(2(\frac{\pi}{3} + \phi)\big) - \mathcal{T}_{C2})}{2\sqrt{2}}, \tag{3.2.19c}$$

and for x and y vector modes we get

$$F_A^x(\theta, \phi, \psi, f) = \frac{1}{2}\sin\theta(\cos\theta\cos\psi(\mathcal{T}_{A1}\cos 2\phi + \mathcal{T}_{A1} - \mathcal{T}_{A2}\cos\left(2(\frac{\pi}{3} - \phi)\right) - \mathcal{T}_{A2}) +$$
$$- \sin\psi(\mathcal{T}_{A1}\sin 2\phi + \mathcal{T}_{A2}\sin\left(2(\frac{\pi}{3} - \phi)\right))) \qquad (3.2.20a)$$

$$F_B^x(\theta, \phi, \psi, f) = \frac{1}{2}\sin\theta(\cos\theta\cos\psi(\mathcal{T}_{B1}\cos\left(2(\frac{\pi}{3} + \phi)\right) + \mathcal{T}_{B1} - \mathcal{T}_{B2}\cos 2\phi - \mathcal{T}_{B2}) +$$
$$+ \sin\psi(\mathcal{T}_{B2}\sin 2\phi - \mathcal{T}_{B1}\sin\left(2(\frac{\pi}{3} + \phi)\right))) \qquad (3.2.20b)$$

$$F_C^x(\theta, \phi, \psi, f) = \frac{1}{2}\sin\theta(\cos\theta\cos\psi(\mathcal{T}_{C1}\cos\left(2(\frac{\pi}{3} - \phi)\right) + \mathcal{T}_{C1} - \mathcal{T}_{C2}\cos\left(2(\frac{\pi}{3} + \phi)\right) - \mathcal{T}_{C2}) +$$
$$+ \sin\psi(\mathcal{T}_{C1}\sin\left(2(\frac{\pi}{3} - \phi)\right) + \mathcal{T}_{C2}\sin\left(2(\frac{\pi}{3} + \phi)\right))) \qquad (3.2.20c)$$

$$F_A^y(\theta, \phi, \psi, f) = \frac{1}{2}\sin\theta(\cos\theta\sin\psi(\mathcal{T}_{A1}(-\cos 2\phi) - \mathcal{T}_{A1} + \mathcal{T}_{A2}\cos\left(2(\frac{\pi}{3} - \phi)\right) + \mathcal{T}_{A2}) +$$
$$- \cos\psi(\mathcal{T}_{A1}\sin 2\phi + \mathcal{T}_{A2}\sin\left(2(\frac{\pi}{3} - \phi)\right))) \qquad (3.2.21a)$$

$$F_B^y(\theta, \phi, \psi, f) = \frac{1}{2}\sin\theta(\cos\theta\sin\psi(\mathcal{T}_{B1}(-\cos\left(2(\frac{\pi}{3} + \phi)\right)) - \mathcal{T}_{B1} + \mathcal{T}_{B2}\cos 2\phi + \mathcal{T}_{B2}) +$$
$$+ \cos\psi(\mathcal{T}_{B2}\sin 2\phi - \mathcal{T}_{B1}\sin\left(2(\frac{\pi}{3} + \phi)\right))) \qquad (3.2.21b)$$

$$F_C^y(\theta, \phi, \psi, f) = \frac{1}{2}\sin\theta(\cos\theta\sin\psi(\mathcal{T}_{C1}(-\cos\left(2(\frac{\pi}{3} - \phi)\right)) - \mathcal{T}_{C1} + \mathcal{T}_{C2}\cos\left(2(\frac{\pi}{3} + \phi)\right) + \mathcal{T}_{C2}) +$$
$$+ \cos\psi(\mathcal{T}_{C1}\sin\left(2(\frac{\pi}{3} - \phi)\right) + \mathcal{T}_{C2}\sin\left(2(\frac{\pi}{3} + \phi)\right))). \qquad (3.2.21c)$$

Finally we consider both the Earth-based frame of reference introduced in Appendix C and Earth rotation to get Mollweide projections of ET response functions for tensor, vector and scalar modes at high frequencies. We discussed how Michelson transfer functions already contain all the information relative to both detector geometry and GW direction, which is what we are really interested in while studying ET detection reach. Joint responses still do not depend on the polarization angle ψ, but the cylindrical symmetry along ϕ is slightly broken: indeed if we retrace what we did in the long wavelength limit, then the initial arm unit vector choice (e.g. once we define each interferometer orientation) affects the detector response and the result loses its generality. In the context of cross-correlation we mostly consider situations where transfer function effects can be ignored and we can use results found for low GW frequencies. However, we give a concrete example for joint responses at high frequencies: we choose Eq.(3.2.13) to be the initial arm unit vector for ET located in Sardinia. We proceed exactly in the same way we did for $f \ll f_*$, although this time we get frequency dependent detector tensors and angular pattern functions, thus we set[5] $f = 8000$

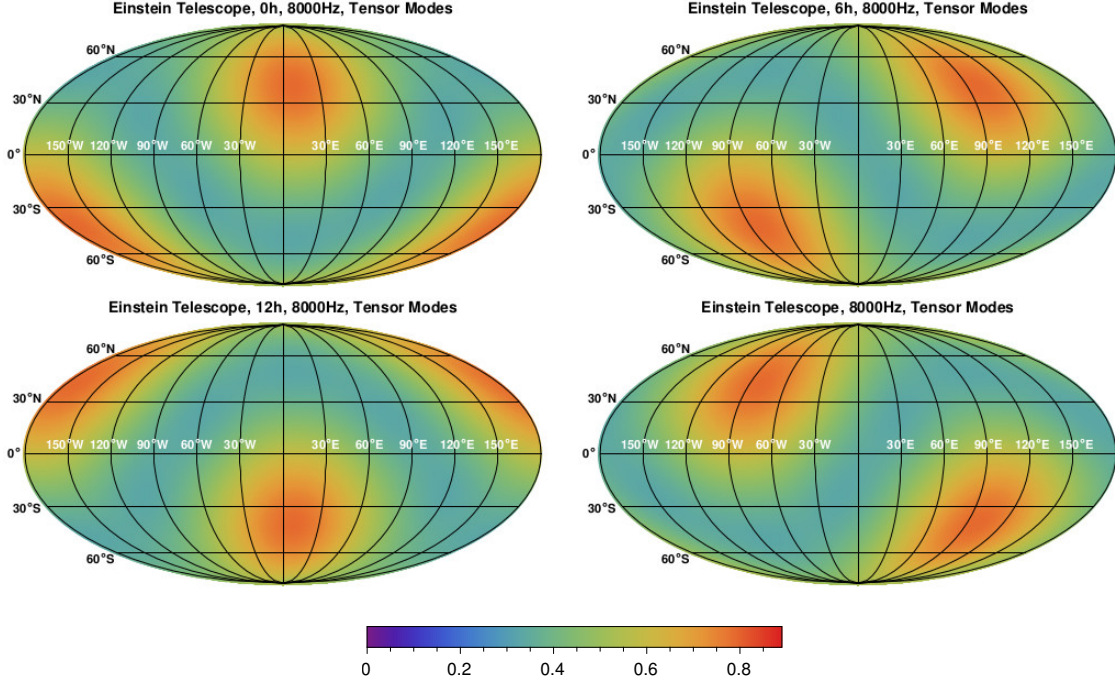[5]We recall that ET interferometer arm lengths are 10 km, thus $f_* \approx 4774.65$ Hz.

Figure 3.12: Mollweide projections of the Einstein Telescope (Sardinia site) joint response to tensor modes for $f = 8000$ Hz. The Earth-based coordinate system used is described in Appendix C. Earth rotation was also considered and plots are given every 6 hours. Unlike the long wavelength limit, the cylindrical simmetry is now slightly broken and the joint response depends on interferometer orientations. Notice how transfer functions decrease the detector sensitivity to GW of high frequencies.

Hz $> f_*$. In Fig. 3.12, 3.13 and 3.14 we show Mollweide projections at 6 hour intervals for each polarization mode.

3.3 Einstein Telescope and 2nd-generation Interferometers

We now move the subject to multiple detector correlation by building networks involving the Einstein Telescope in order to understand how ET affects the overall sensitivity. Once again we are going to consider the cosmological SGWB as a source of GWs and we retrace what we did in the previous chapter: we begin by assuming the singular existence of one between tensor, vector and scalar modes, this way we can compute energy density contributions merely considering a detector pair. We assume a frequency independent GW-spectrum and we set $SNR = 5$ and $T = 3$yrs; the sensitivity curve of the Einstein Telescope is provided [81] and is shown in Fig. 2.13. Finally, overlap reduction functions are given by Eq.(2.5.53).
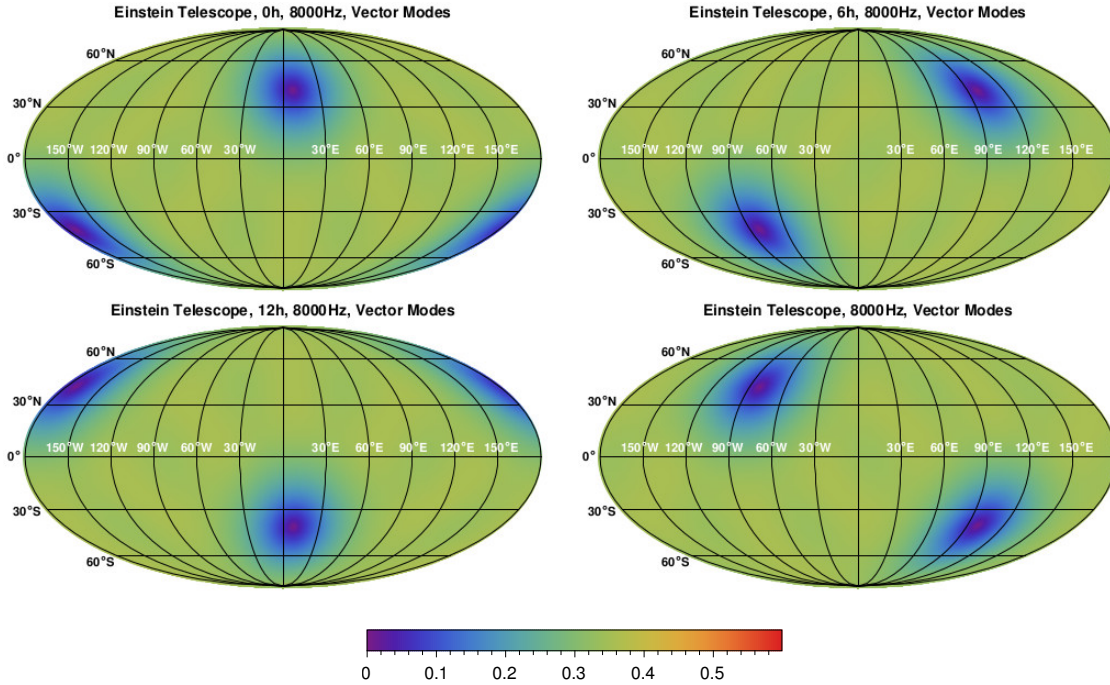
Figure 3.13: Mollweide projections of the Einstein Telescope (Sardinia site) joint response to vector modes for $f = 8000$ Hz. The Earth-based coordinate system used is described in Appendix C. Earth rotation was also considered and plots are given every 6 hours. Unlike the long wavelength limit, the cylindrical simmetry is now slightly broken and the joint response depends on interferometer orientations. Notice how transfer functions decrease the detector sensitivity to GW of high frequencies.
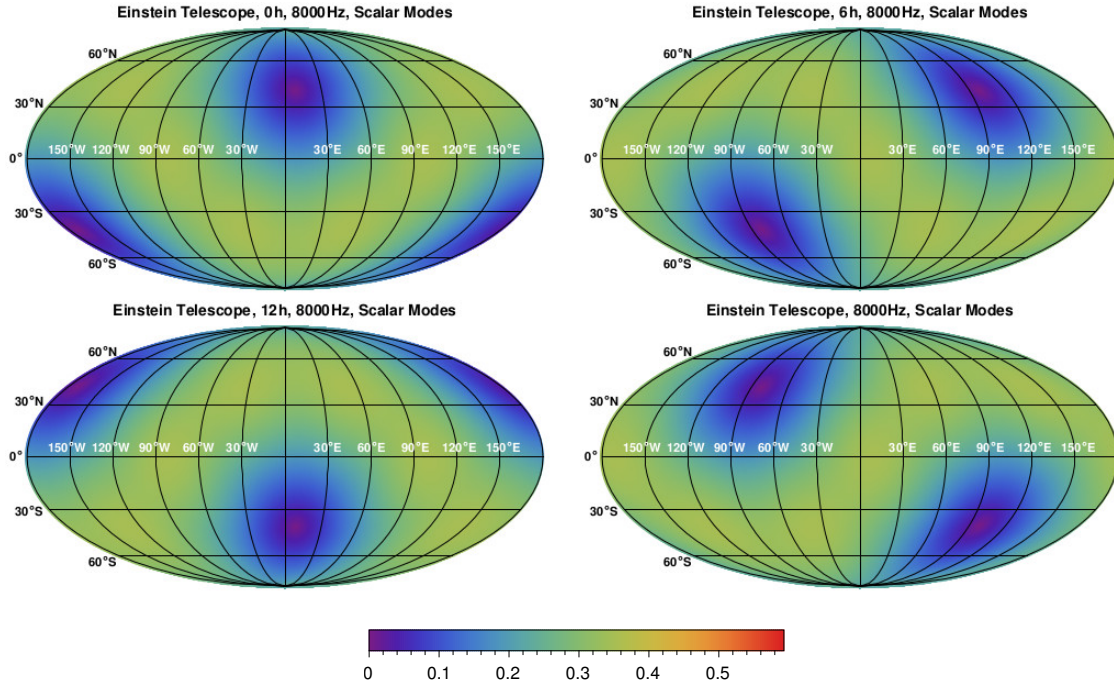
Figure 3.14: Mollweide projections of the Einstein Telescope (Sardinia site) joint response to scalar modes for $f = 8000$ Hz. The Earth-based coordinate system used is described in Appendix C. Earth rotation was also considered and plots are given every 6 hours. Unlike the long wavelength limit, the cylindrical simmetry is now slightly broken and the joint response depends on interferometer orientations. Notice how transfer functions decrease the detector sensitivity to GW of high frequencies.

	β	α	$f_c[Hz]$
ETS-LH	81.84	117.76	5.72
ETS-LL	77.66	203.00	5.97
ETS-V	3.22	40.21	133.37
ETS-K	89.38	126.4	5.32

	β	α	$f_c[Hz]$
ETN-LH	66.5	121.35	6.83
ETN-LL	62.56	198.436	7.22
ETN-V	14.27	150.80	30.17
ETN-K	87.89	142.04	5.40

Table 3.1: Detector pair orientations (α) of 2nd-generation interferometers and angular separation (β) given in decimal degrees. Both Einstein Telescope sites in Sardinia (ETS) and Netherland (ETN) are considered and characteristic frequencies for each pair are reported.
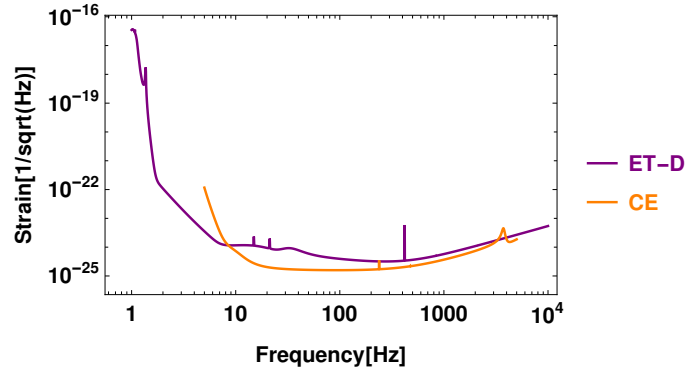

Figure 3.15: Sensitivity curves for 3rd-generation interferometers. Plots were realized with public data provided by [81, 85].

2nd-generation interferometer locations and arm orientation are shown in Tab. 2.2, thus we can compute the angular separation between each one of them and ET and their bisector orientation angle with respect to the tangent vector to the great circumference joining a detector pair together. We recall that ET has no preferred arm orientations yet, thus to overcome this issue we begin by finding the great circle of radius R_E connecting the pair together, then we decompose angular parameters σ^+ and σ^- as

$$\sigma^+ = \frac{1}{2}(\tau + \alpha), \qquad \sigma^+ = \frac{1}{2}(\tau - \alpha), \tag{3.3.1}$$

where τ is the variable ET bisector orientation angle, and α is the other interferometer known bisector orientation angle. All angular parameters are shown in Tab. 3.1 for both ET sites along with each pair characteristic frequency[6] f_c. Finally, we consider Eq.(3.1.13) and we compute the energy density as a function of ET orientation τ. Results are shown in Fig. 3.16 for each polarization mode. First of all we did not include here results relative to

---

[6]We recall thath $f_c = \frac{c}{4\pi R_E \sin\frac{\beta}{2}}$.

the Einstein Telescope-Virgo configuration: since they are very close together the characteristic frequency is very high and this instance needs a proper treatment. Other possible configurations show oscillatory behaviours and can be compared to the results shown in Tab. 2.5: assuming we can pick τ to minimize the detectable energy density, detector pairs involving ET improve the sensitivity to the SGWB approximately by a factor of 10 with respect to 2nd-generation interferometers. However, if tensor, vector and scalar modes are present at the same time we need to build detector networks in order to distinguish their energy density contributions and in the following we investigate some possible scenarios.

Einstein Telescope and Ligo Observatories. We begin by considering the Einstein Telescope-LIGO correlations: looking at Fig. 3.16 we see that peaks relative to ETS(N)-LH and ETS(N)-LL configurations show no anomalous behaviour. Moreover we can take Eq.(2.6.16)[7] to compute the energy density as a function of ET orientation τ, which we define as the bisector orientation angle with respect to the great circle connecting LL and ETS(N). We recall that the detector correlation matrix determinant, which also depends on τ, needs to statisfy $det\Lambda(f,\tau) \neq 0$ for the mode separation to be allowed. Results are shown in Fig. 3.17. Once again the correlation matrix determinant filters GW frequencies and allow mode separation in the 10-100 Hz range approximately. Tensor and vector mode energy density contributions are very similar, however it is worth noting that these configurations show better sensitivity to scalar modes. Three detector networks involving ET improve the sensitivity to the SGWB roughly by a factor of 10 for each polarization mode with respect to 2nd-generation interferometers.

Einstein Telescope and Virgo. The situation is somehow more delicate when we try to couple the Einstein Telescope and Virgo, due to their locations being very close together. To fully understand what the major concern is, let us step back and consider both the coordinate system given by Eq.(2.1.6) and two L-shaped interferometers sharing the same location ($\Delta \overline{\mathbf{x}} = 0$), but keeping different orientations: the first detector has arms directed along $\hat{\mathbf{u}} = (1,0,0)^T$ and $\hat{\mathbf{v}} = (0,1,0)^T$, while the second detector arms are given by $\hat{\mathbf{e}}_\mathbf{1} = (\frac{\sqrt{2}}{2}, \frac{\sqrt{2}}{2}, 0)^T$ and $\hat{\mathbf{e}}_\mathbf{2} = (-\frac{\sqrt{2}}{2}, \frac{\sqrt{2}}{2}, 0)^T$. We purposely set the two bisectors in a way they differ by an angle of $\frac{\pi}{4}$. We need to compute the detector tensor of the second detector, we get

$$\mathbf{D} = \frac{1}{2}\big\{\hat{\mathbf{e}}_\mathbf{1} \otimes \hat{\mathbf{e}}_\mathbf{1} - \hat{\mathbf{e}}_\mathbf{2} \otimes \hat{\mathbf{e}}_\mathbf{2}\big\} = \frac{1}{2}\begin{pmatrix} 0 & 1 & 0 \\ 1 & 0 & 0 \\ 0 & 0 & 0 \end{pmatrix}, \qquad (3.3.2)$$

---

[7]This time we have both L-shaped and V-shaped interferometers, thus overlap functions need to account for a $\sin\eta$ factor, with η opening angle of the V-shaped detector.
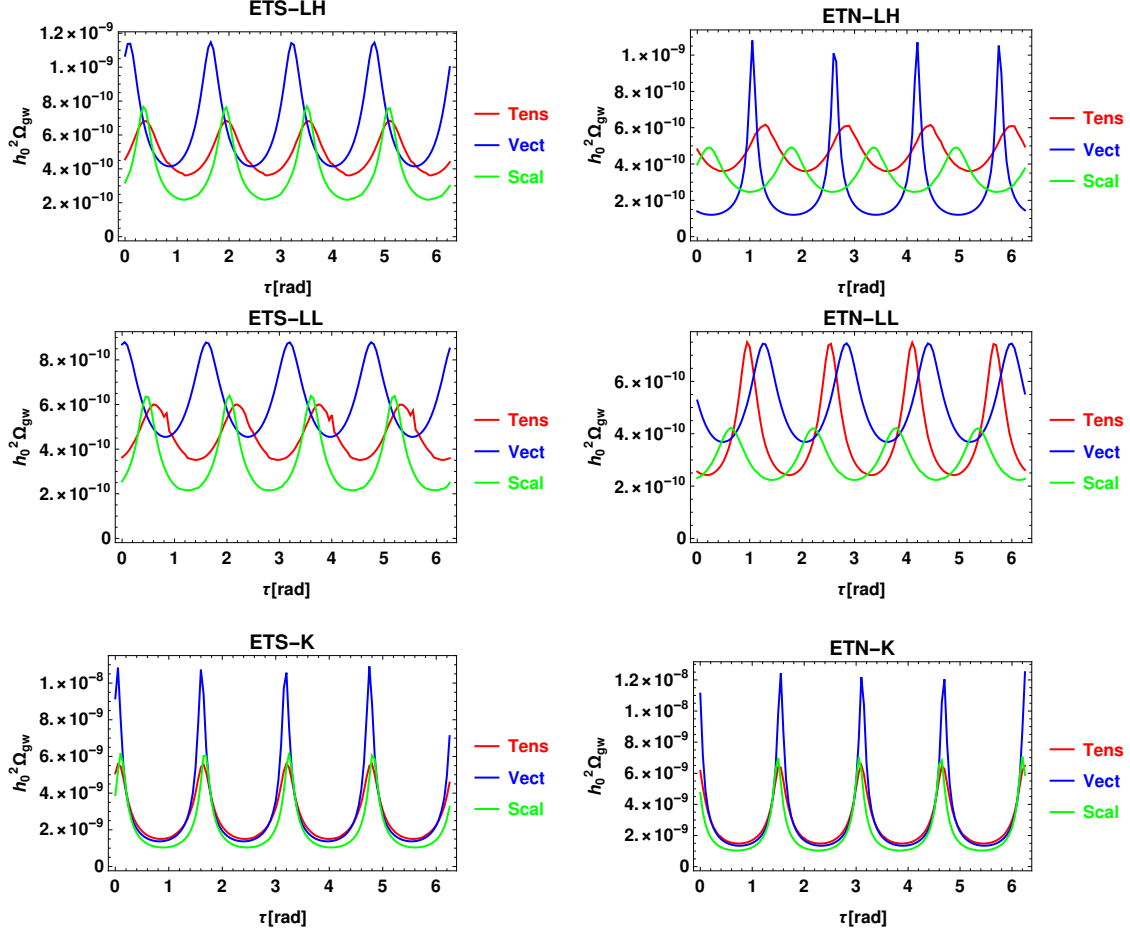
Figure 3.16: SGWB detectable energy density contributions for tensor, vector and scalar modes as a function of the Einstein Telescope orientaion τ if only one of these is present. A frequency independent GW-spectrum, and a total observational time of three years were assumed. The signal to noise ratio was set to 5. Vector modes show higher oscillations than the tensor and scalar ones for ET-LH and ET-LL configurations, while higher peaks are present considering the pair ET-K. In the context of scalar modes, $\tau(f)\Omega_{gw}h_0^2$ needs to be considered.
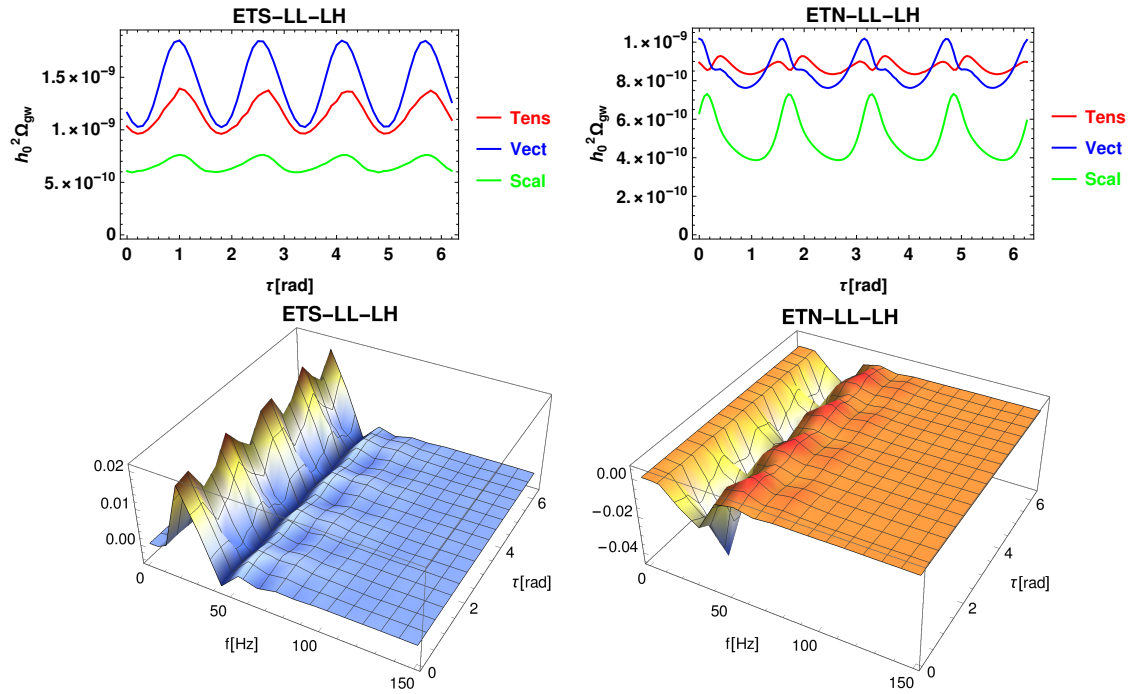
Figure 3.17: (Top) SGWB detectable energy density contributions for tensor, vector and scalar modes as a function of the Einstein Telescope bisector orientation angle τ between the great circle connecting ET and LL together. A frequency independent GW-spectrum, and a total observational time of three years were assumed. The SNR was set to 5. In the context of scalar modes, $\tau(f)\Omega_{gw}h_0^2$ needs to be considered. (Bottom) Detector correlation matrix determinant as a function of both frequency and ET orientation τ. Modes separation is allowed for frequency intervals ranging from 10-80 Hz.

and using Eq.(2.1.4) we derive the following angular pattern functions

$$\tilde{F}^+(\hat{\mathbf{\Omega}}, \psi) = \frac{1}{4}(\cos 2\theta + 3)\cos 2\psi \sin 2\phi + \cos \theta \sin 2\psi \cos 2\phi, \tag{3.3.3a}$$

$$\tilde{F}^\times(\hat{\mathbf{\Omega}}, \psi) = \cos \theta \cos 2\psi \cos 2\phi - \frac{1}{4}(\cos 2\theta + 3)\sin 2\psi \sin 2\phi, \tag{3.3.3b}$$

$$\tilde{F}^x(\hat{\mathbf{\Omega}}, \psi) = \sin \theta (\cos \theta \cos \psi \sin 2\phi + \sin \psi \cos 2\phi), \tag{3.3.3c}$$

$$\tilde{F}^y(\hat{\mathbf{\Omega}}, \psi) = \sin \theta (\cos \psi \cos 2\phi - 2\cos \theta \sin \psi \sin \phi \cos \phi), \tag{3.3.3d}$$

$$\tilde{F}^b(\hat{\mathbf{\Omega}}) = -\sin^2 \theta \sin \phi \cos \phi, \tag{3.3.3e}$$

$$\tilde{F}^l(\hat{\mathbf{\Omega}}) = \sqrt{2}\sin^2 \theta \sin \phi \cos \phi. \tag{3.3.3f}$$

Since $\Delta \overline{\mathbf{x}} = 0$, inside Eqs.(2.4.19)-(2.4.21) appear the following integral

$$\int_{S^2} \frac{d\Omega}{4\pi}\left(F_I^A(\hat{\mathbf{\Omega}})\tilde{F}_J^A(\hat{\mathbf{\Omega}})\right) = 0, \tag{3.3.4}$$

for $A = +, \times, x, y, b, l$, meaning that overlap functions are zero everywhere and from Eq.(2.4.32) the SNR is zero. If we naively attempt to isolate Ω_{gw} as in Eq.(2.6.2), we get an infinite value and we lose physical meaning. This situation is very similar to the Einstein Telescope-Virgo possible collaboration: indeed from Tab.3.1 we notice that β is very small, meaning that $\Delta \overline{\mathbf{x}} \approx 0$. We are interested in the behaviour of the overlap function given by Eq.(2.5.53). Let us consider the case where ET orientation is defined by $\tau = \alpha_V - \frac{\pi}{4}$, where α_V is Virgo known orientation listed in Tab. 3.1. Looking at the top panels of Fig. 3.18 we see how overlap functions for tensor, vector and scalar modes are very close to zero for $f < f_c$, they briefly oscillate when $f \approx f_c$, then they reduce asymptotically to zero once again. While computing the energy density using Eq.(2.6.2), we expect the denominator to become very small, thus making Ω_{gw} bigger and implying a sensitivity loss. Let us now consider the case where $\tau = \alpha_V$, which corresponds to the two detectors being perfectly aligned. Looking at the bottom panels of Fig.3.18 we see that $\gamma(f = 0) \approx 1$: this must not surprise us, since the now aligned detectors are almost sharing the same location[8] and overlap functions now start to oscillate very late in frequency due to the small distance between ET and Virgo (e.g. bigger f_c). Assuming only one between tensor, vector and scalar mode exists, we show in Tab.3.2 the numerical values of the detectable energy density for the Einstein Telescope-Virgo collaboration for the two discussed cases: notice how the orientation strongly influences the sensitivity to GWs. It might be worth investigating the scenario where ET and Virgo share the same orientation a bit further. First of all, notice that this assumption gives us the following unit vectors directed along the ET bisector

$$\hat{\mathbf{b}}_{ETS} = (-0.498, -0.539, 0.679), \qquad \hat{\mathbf{b}}_{ETN} = (-0.676, -0.549, 0.491). \tag{3.3.5}$$
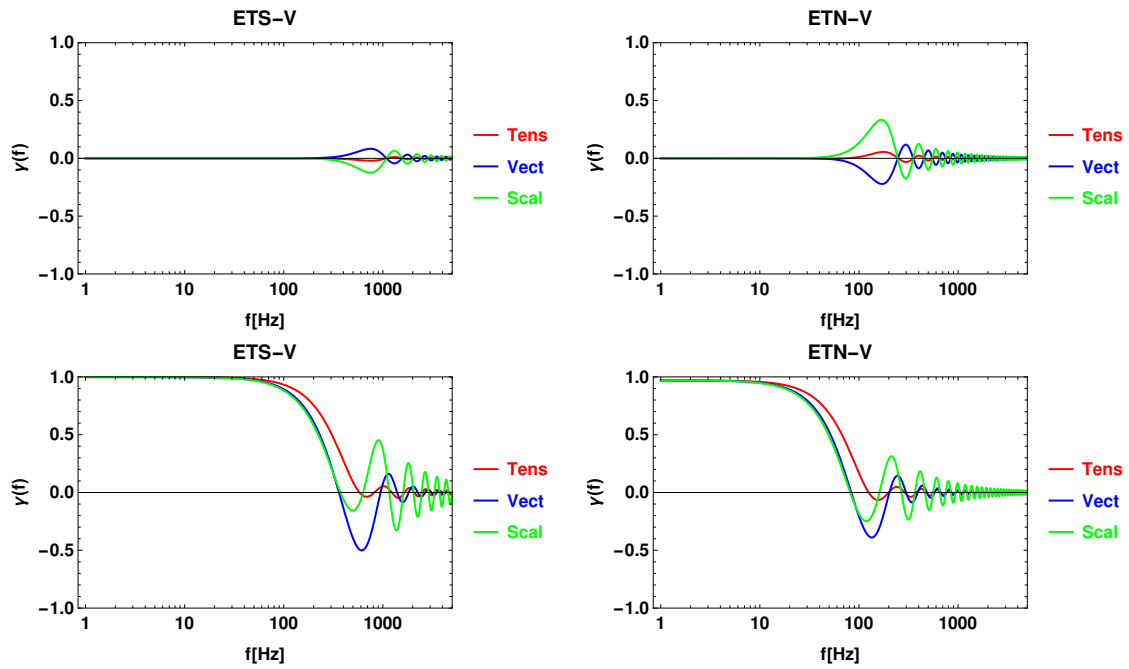
---

[8]We discussed this scenario in Eq.(2.6.1).

Figure 3.18: (Top) ETS/ETN-V overlap functions for each polarization mode with $\tau = \alpha_V - \frac{\pi}{4}$. (Bottom) ETS/ETN-V overlap functions for each polarization mode with $\alpha_V = \tau$.

	τ	$h_0^2\Omega_{gw}^T$	$h_0^2\Omega_{gw}^V$	$\tau h_0^2\Omega_{gw}^S$
ETS-V	$\alpha_V - \frac{\pi}{4}$	1.47×10^{-6}	3.53×10^{-7}	2.33×10^{-7}
ETS-V	α_V	7.05×10^{-11}	7.08×10^{-11}	7.09×10^{-11}
ETN-V	$\alpha_V - \frac{\pi}{4}$	2.41×10^{-8}	5.11×10^{-9}	3.06×10^{-9}
ETN-V	α_V	8.01×10^{-11}	8.45×10^{-11}	8.59×10^{-11}

Table 3.2: Possible orientations (τ) of the Einstein Telescope bisector as a function of Virgo orientation (α_V) and detectable energy density values for ETS/ETN-V configuration. Notice how greatly the orientation of ET influences the results.

This is exactly the information we need to extend the results in Tab.3.1 by adding the orientation of the ET bisector, which we still name τ, with respect to the tangent vector to the great circumference joining ET and a 2nd-generation interferometer together. In Tab.3.3 we show these angular values for both sites, while in Fig.3.19 we show the plots of the relative overlap functions for each possible pair. We have everything we need to

	τ
ETS-LH	173.91
ETS-LL	146.53
ETS-K	66.18

	τ
ETN-LH	175.27
ETN-LL	145.35
ETN-K	66.93

Table 3.3: Orientations (τ) of the Einstein Telescope bisector with respect to the tangent vector to the great circumference for both sites, with ET sharing the same orientation of Virgo. Numerical values are reported in decimal degrees.

compute the energy density related to each polarization mode starting from Eq.2.6.16 and creating networks involving both the Einstein Telescope and Virgo. We list our results in Tab. 3.4, while in Fig. 3.20 we show the related plots of $det\Lambda(f)$. Similarly to the previous cases, the correlation matrix determinant filters GW frequencies and allows the mode separation only for finite ranges (10-200 Hz). Once again three detector networks involving ET improve the sensitivity to the SGWB roughly by a factor of 10 for each polarization mode with respect to 2nd-generation interferometers.

Einstein Telescope and KAGRA. In the end we briefly investigate the Einstein Telescope-Kagra collaboration. In particular, we wish to better understand both energy density peaks appearing in Fig. 3.16 for both sites at $\tau \approx k\frac{\pi}{2}$, with $k \in \mathbb{N}$ and energy density minima obtained for $\tau \approx k\frac{\pi}{4}$, $k \in \mathbb{N}$. This periodic behaviour is common to all modes and can be derived once again from overlap reduction functions: while considering the great circumference joining the Einstein Telescope and Kagra overlap functions can be computed using angular parameters shown in Tab. 3.1 and choosing the orientation of ET. In Fig. 3.21 we show overlap reduction functions computed setting $\tau = 0$ and $\tau = \frac{\pi}{4}$ respectively: notice
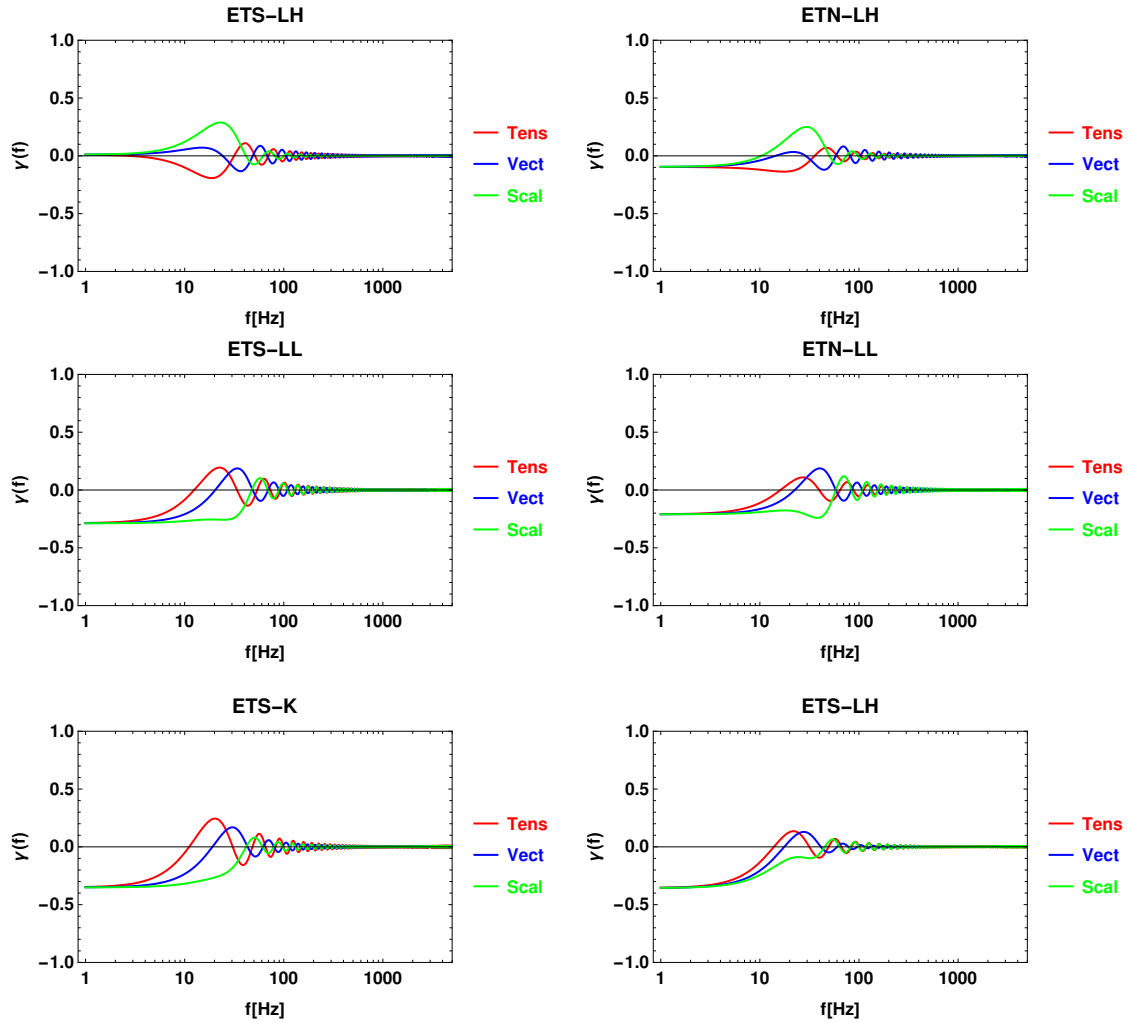
Figure 3.19: Overlap reduction functions for each possible detector pair built with ET and 2nd-generation interferometers. ET was choosen to have the same orientation of Virgo $(\tau = \alpha_V)$.
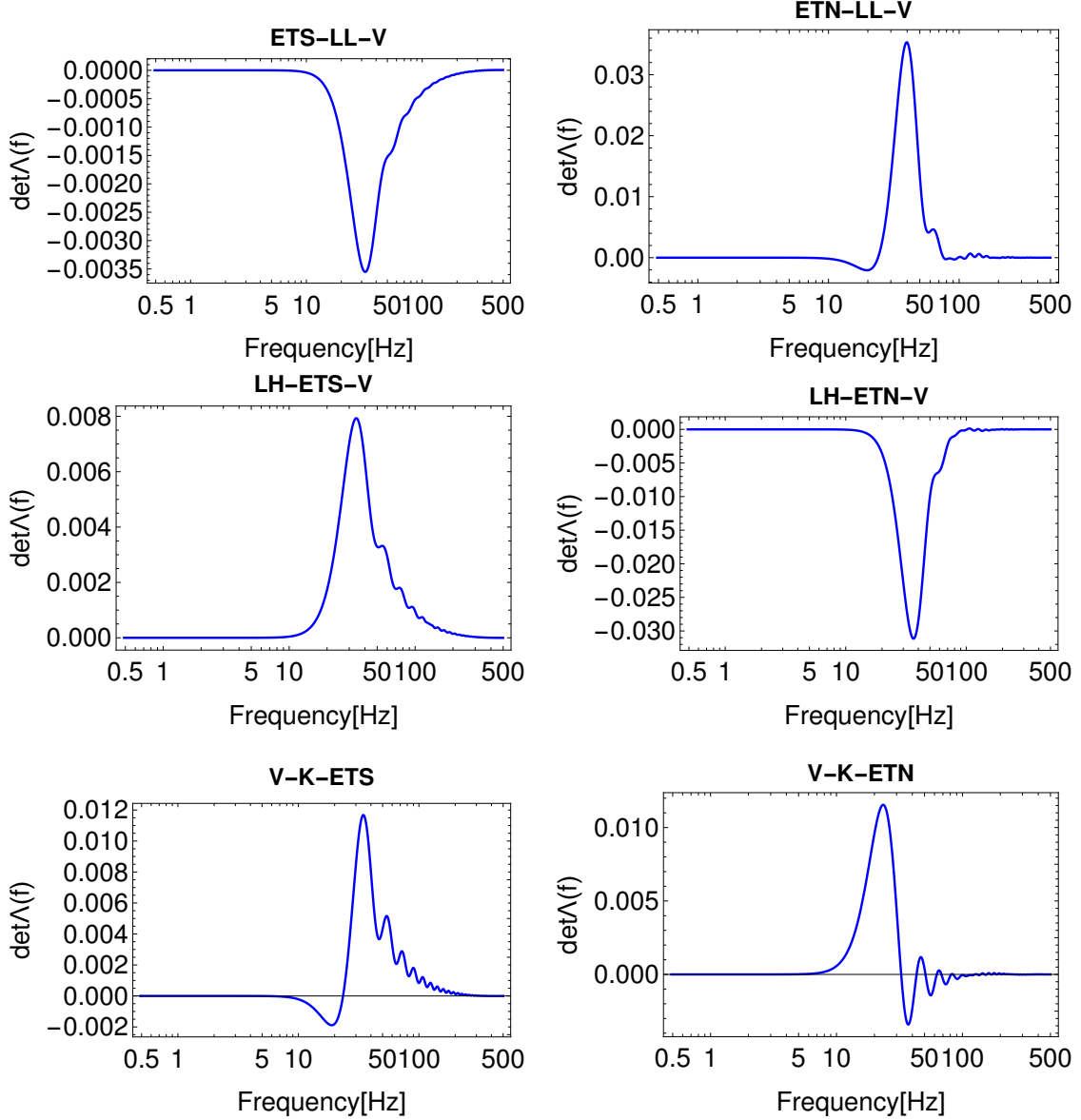
Figure 3.20: Plots of $det\Lambda(f)$ for possible detector netwroks involving ET and V, where the Einstein Telescope has the same orientation of Virgo ($\alpha = \tau$). The correlation matrix determinant filters GW frequencies and allows a true mode separation only for finite frequency ranges.

	$h_0^2\Omega_{gw}^T$	$h_0^2\Omega_{gw}^V$	$\tau h_0^2\Omega_{gw}^S$
ETS-LL-V	2.25×10^{-8}	5.86×10^{-9}	2.89×10^{-9}
LH-ETS-V	6.34×10^{-9}	3.22×10^{-9}	2.55×10^{-9}
V-K-ETS	1.67×10^{-8}	9.27×10^{-9}	1.80×10^{-8}
ETN-LL-V	5.31×10^{-9}	3.59×10^{-9}	1.28×10^{-9}
LH-ETN-V	2.73×10^{-9}	1.91×10^{-9}	1.10×10^{-9}
V-K-ETN	3.31×10^{-8}	1.57×10^{-8}	9.18×10^{-9}

Table 3.4: SGWB detectable energy density contributions for tensor, vector and scalar modes considering three detector networks with the Einstein Telescope having the same orientation of Virgo. A frequency independent GW-spectrum, and a total observational time of three years were assumed. The signal to noise ratio was set to 5. All possible networks return similar values for each polarization SGWB energy density contribution.

how when $\tau = 0$ overlap functions are very close to zero for $f < f_c$, they briefly oscillate when $f \approx f_c$, then they reduce asymptotically to zero once again. Indeed if we use this configuration to compute the energy density through Eq.(2.6.2) we get a small denominator and bigger values Ω_{gw}^N gets, thus implying a sensitivity loss to GWs and explaining the peaks.
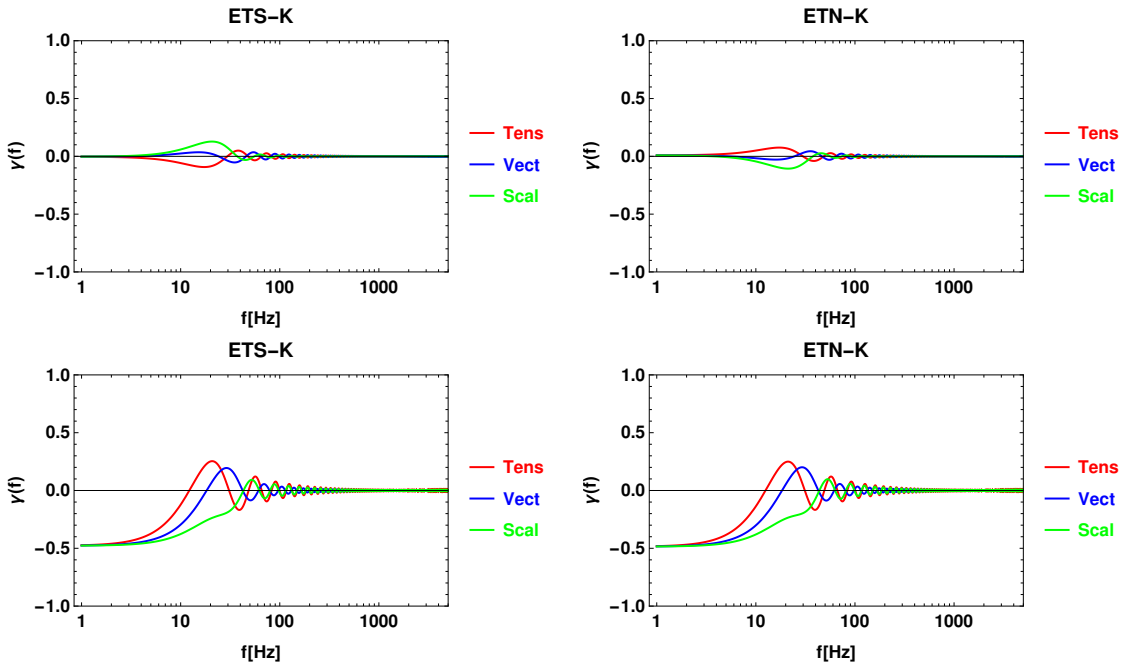
Figure 3.21: (Top) ETS/ETN-K overlap functions for each polarization mode with $\tau = 0$. (Bottom) ETS/ETN-K overlap functions for each polarization mode with $\tau = \frac{\pi}{4}$.
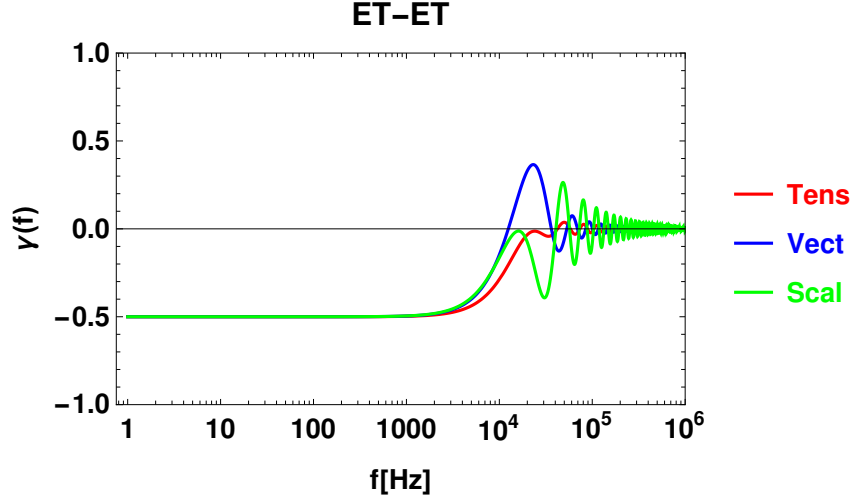
Figure 3.22: Overlap reduction function for each polarization mode considering two Einstein Telescope interferometers in the long wavelength limit. Since $f_c = f_* \approx 4774.65$ overlap functions start to oscillate ath higher frequencies with respect to previous cases considered.

3.4 Einstein Telescope Interferometers

In the previous sections we focused on networks involving ET and one or two 2nd-generation interferometers on Earth. However, 3rd-generation interferometers are expected to work together in order to greatly improve the understanding of our Universe. The Einstein Telescope offers three interferometers to work with and we now wish to understand if and how they can be exploited to detect a cosmological SGWB. Let us first consider two ET interferometers. We have already introduced its triangular configuration and we know that the two interferometers are 10 km away from each other: in this particular scenario we have $f_* = f_c \approx 4774.65$ Hz. The angular separation between two interferometers given in decimal degrees is $\beta \approx 0.089$, thus they can be considered to lie on the same plane. Let us consider detectors A and B in Fig. 3.2 as an example: let the tangent vector to the great circumference joining the interferometers together be directed along $\hat{\mathbf{e}}_{\mathbf{A1}}$, thus becoming parallel to one detector arm for each interferometer of the pair. Interferometer orientations are utterly determined independently of ET location and in the long wavelenght limit the overlap reduction function for each polarization mode is given by

$$\gamma^N(f) = \Xi_N^+(f, \beta) \cos(2\pi) + \Xi_N^-(f, \beta) \cos\left(\frac{4\pi}{3}\right). \tag{3.4.1}$$

The plot of Eq.(3.4.1) is shown in Fig. 3.22. Due to the detector configuration the overlap function is constant up to frequencies of order 10^3 Hz and it differs from zero approaching f_*. Moreover, ET is expected to be sensitive to GW frequencies up to 10 Hz

and for a proper treatment the transfer functions need to be considered. We can still use Eq.(3.4.1) to compute the energy density for tensor, vector and scalar modes supposing their singular existence one by one: these approximative results are shown in Tab. 3.5. ET pair sensitivity to the SGWB is remarkably improven roughly by a factor of 10^3 with respect to 2nd-generation interferometers. As we shall see, similar values are given by collaborations between the Einstein Telescope and the Cosmic Explorer, thus we expect transfer functions to only affect these results with small corrections, while preserving the order of magnitude. Finally we might think of using all three ET interferometers to distinguish energy density

	$h_0^2 \Omega_{gw}^T$	$h_0^2 \Omega_{gw}^V$	$\tau h_0^2 \Omega_{gw}^S$
ET-ET	2.196×10^{-12}	2.196×10^{-12}	2.196×10^{-12}

Table 3.5: SGWB detectable energy density contributions for tensor, vector and scalar modes if only one of these is present. A frequency independent GW-spectrum, and a total observational time of three years were assumed. The SNR ratio was set to 5. ET sensitivity to different polarization modes is basically the same.

contributions for each polarization mode. Consider Fig. 3.2 once again: due to its triangular configuration, the overlap reduction function of every possible pair involving detectors A, B or C is always given by Fig. 3.22. No matter what the Einstein Telescope final location will be, the tangent vector to great circumference joining ET detectors together is always parallel to one detector arm for each interferometer of the pair. Considering Eq.(2.6.8), it is clear that the correlation matrix determinant is always null[9] since $\gamma_{12}^N = \gamma_{23}^N = \gamma_{31}^N$, for $N = T, V, S$. Unforunately the Einstein Telescope alone in this configuration cannot separate polarization modes.

3.5 Einstein Telescope and Cosmic Explorer

The Cosmic Explorer (CE) [16] observatory will consist of one single L-shaped interferometer with arm length of 40 km (10 times the length of LIGO and 4 times the length of the Einstein Telescope) and a characteristic frequency $f_* \approx 1193.66$ Hz. The available sensitivity curve is provided by [85] and is shown in Fig. 3.15 for frequencies in the 5-5000 Hz range. Since the detector is an L-shaped interferometer, we can recover some previously found results: considering the coordinate system given in Eq.(2.1.6) and assuming the long wavelength limit to be valid angular pattern functions do not depend on the detector geometry and are provided by Eqs.(2.1.21)-(2.1.26); considering GW with higher frequencies and accounting for transfer functions, angular pattern functions are given instead by Eq.(3.1.4) with $\eta = \frac{\pi}{2}$. In the rest of this section we wish to understand how the Cosmic Explorer couples to 2nd-generation interferometers and then to the Einstein Telescope.

---

[9]From Eq.(2.6.16), if $det\Lambda = 0$, then $SNR = 0$.

3.5.1 The Cosmic Explorer and 2nd-generation Interferometers.

No preferred location for the Cosmic Explorer has been reported yet, thus we consider two possible sites: *a)* the Cosmic Explorer replaces LIGO H both in location and orientation (CEH) *b)* the Cosmic Explorer replaces LIGO L both in location and orientation (CEL). Once again we assume a frequency independent GW-spectrum and in our computations we set $SNR = 5$ and $T = 3$yrs. We initally consider the existence of only one between tensor, vector and scalar modes, then we proceed to separate modes and their energy density contributions considering three interferometer networks involving CE. Since we are assuming the Cosmic Explorer to have also the same orientation of the replaced LIGO interferometers, we can use the parameters listed in Tab.2.4 to compute overlap functions, which at low frequencies are exactly the ones shown in Fig.2.14 replacing LH and LL with CEH and CEL one at a time respectively. Energy density values are computed through Eq.(2.6.2) and are shown in Tab.3.6. Collaborations with the remaining LIGO observatory and Virgo improve sensitivity to GWs roughly by a factor oscillating between $10 - 10^2$ for each mode. It is then straightforward to separate polarization modes and their contribution to the stochastic background energy density as we previously did using Eq.(2.6.16). We finally list our results in Tab.3.7: Combinations of interferometers more sensitive to GWs are given by the CE, LIGO and Virgo due to their better sensitivities.

	$h_0^2\Omega_{gw}^T$	$h_0^2\Omega_{gw}^V$	$\tau h_0^2\Omega_{gw}^S$
CEH-LL	1.90×10^{-11}	2.27×10^{-11}	2.39×10^{-11}
CEL-LH	1.90×10^{-11}	2.27×10^{-11}	2.39×10^{-11}
CEL-V	1.10×10^{-10}	1.46×10^{-10}	6.42×10^{-11}
CEL-K	1.68×10^{-9}	1.73×10^{-9}	2.28×10^{-9}
CEH-V	9.50×10^{-11}	2.07×10^{-10}	5.61×10^{-11}
CEH-K	8.38×10^{-10}	6.39×10^{-10}	5.21×10^{-10}

Table 3.6: SGWB detectable energy density contributions for tensor, vector and scalar modes if only one of these is present. A frequency independent GW-spectrum, and a total observational time of three years were assumed. The signal to noise ratio was set to 5. These results were found replacing LIGO H and LIGO L observatories with the Cosmic Explorer (CEH and CEL respectively).

3.5.2 Einstein Telescope and Cosmic Explorer Cross-Correlation.

Finally we wish to investigate detector networks involving the Einstein Telescope and Cosmic Explorer in order to see how far we can push the sensitivity to GWs of upcoming ground-based interferometers. As we did previously, we consider the possibility where the Cosmic Explorer replaces one of the LIGO observatories both in location and orientation, while the Einstein Telescope can be located in Italy or Netherland with no known orienta-

	$h_0^2\Omega_{gw}^T$	$h_0^2\Omega_{gw}^V$	$\tau h_0^2\Omega_{gw}^S$
CEH-LL-V	6.02×10^{-10}	1.26×10^{-9}	4.96×10^{-10}
CEH-LL-K	2.04×10^{-8}	9.54×10^{-9}	5.66×10^{-9}
LH-CEL-V	6.72×10^{-10}	4.66×10^{-9}	4.61×10^{-10}
LH-CEL-K	5.25×10^{-9}	1.17×10^{-8}	6.65×10^{-9}
V-K-CEL	2.01×10^{-8}	1.02×10^{-8}	7.48×10^{-9}
V-K-CEH	6.79×10^{-9}	1.32×10^{-8}	4.45×10^{-9}

Table 3.7: SGWB detectable energy density contributions for tensor, vector and scalar modes considering three detector networks involving CE. A frequency independent GW-spectrum and a total observational time of three years were assumed. The signal to noise ratio was set to 5. These results were found replacing LIGO H and LIGO L observatories with the Cosmic Explorer (CEH and CEL respectively).

tion (which we denote τ) and we investigate the detection of a cosmological SGWB with a frequency independent GW-spectrum and we choose again SNR= 5 and $T = 3$yrs. Let us begin by considering the existence of only one between tensor, vector and scalar modes. Under these assumptions we can use angular parameters listed in Tab.2.4 for a concrete example: let us choose the configuration where ET and CE share the same orientation, making $\tau = \alpha_{CE}$. As usual, we can use Eq.(2.6.2) to compute the energy density for each polarization mode and we list our results in Tab. 3.8. Similarly to ET-ET pairs, collaboration between ET and CE improve sensitivity to the SGWB roughly by a factor of 10^3 with respect to 2nd-generation interferometers. Clearly we are interested in SGWB involving a

	$h_0^2\Omega_{gw}^T$	$h_0^2\Omega_{gw}^V$	$\tau h_0^2\Omega_{gw}^S$
ETS-CEL	3.90×10^{-12}	5.04×10^{-12}	5.40×10^{-12}
ETS-CEH	4.88×10^{-12}	4.62×10^{-12}	4.43×10^{-12}
ETN-CEL	2.22×10^{-12}	3.01×10^{-12}	3.29×10^{-12}
ETN-CEH	2.74×10^{-12}	2.78×10^{-12}	2.72×10^{-12}

Table 3.8: SGWB detectable energy density contributions for tensor, vector and scalar modes if only one of these is present. A frequency independent GW-spectrum, and a total observational time of three years were assumed. The signal to noise ratio was set to 5. These results were found replacing LIGO H and LIGO L observatories with the Cosmic Explorer (CEH and CEL respectively) and setting ET orientation $\tau = \alpha_{CE}$.

mixture of all possible polarization modes, thus we can use two of the Einstein Telescope interferometers (ETS1, ETS2 for the Sardinia site and ETN1, ETN2 for the Netherland site) and the Cosmic Explorer to build a 3rd-generation detector network that allow us to distinguish between tensor, vector and scalar energy density contributions. The first issue we need to deal with is ET orientation: we can choose τ to be the angle between the first

ET1 interferometer and the tangent vector to the great circumference joining ET1 and CE, thus ET2 orientation can be defined as $\tau + \frac{2\pi}{3}$ due to ET triangular configuration. Now we wish to pick τ in order to maximize the network sensitivity to GWs (e.g in order to minimize the energy density). This can be achieved by investigating the correlation matrix determinant as a function of both GW frequency and ET orientation; for all possible configurations we show the plots of $det\Lambda(f, \tau)$ in Fig. 3.23. Polarization modes can be separated roughly in the frequency range $10 - 100$ Hz almost independently by the choice of ET orientation and we now wish understand why: the overlap function between two ET interferometers is reported in Fig. 3.22 and for each polarization it appears to be equal and constant up to very high frequencies due to detectors reciprocal small distance. Indeed considering carefully Eq.(2.6.8), the ET-ET overlap function can be collected as a dominant factor, while differences between overlap functions involving CE only brings small corrections. In the end we are free to choose any value for ET orientation and we set $\tau = \frac{\pi}{3}$ for a concrete example. Overlap reduction functions for CE-ET configurations are shown in Fig. 3.24 and 3.25 for the Sardinia and Netherland site respectively, while energy density contributions for each polarization mode are listed in Tab. 3.9. Once again the result is remarkable: detector networks involving ET and CE improve sensitivity to the SGWB roughly by a factor of 10^3 with respect to 2nd-generation interferometers and by a factor of 10^2 with respect to collaborations between 3rd and 2nd-generation detectors.

	$h_0^2\Omega_{gw}^T$	$h_0^2\Omega_{gw}^V$	$\tau h_0^2\Omega_{gw}^S$
CEL-ETS1-ETS2	9.52×10^{-12}	1.38×10^{-11}	6.43×10^{-12}
CEH-ETS1-ETS2	1.03×10^{-11}	1.38×10^{-11}	6.43×10^{-12}
CEL-ETN1-ETN2	8.76×10^{-12}	1.38×10^{-11}	6.43×10^{-12}
CEH-ETN1-ETN2	8.52×10^{-12}	1.38×10^{-11}	6.43×10^{-12}

Table 3.9: SGWB detectable energy density contributions for tensor, vector and scalar modes considering three detector networks involving CE and ET only. A frequency independent GW-spectrum and a total observational time of three years were assumed. The signal to noise ratio was set to 5. These results were found replacing LIGO H and LIGO L observatories with the Cosmic Explorer (CEH and CEL respectively) and setting ET orientation $\tau = \frac{\pi}{3}$.
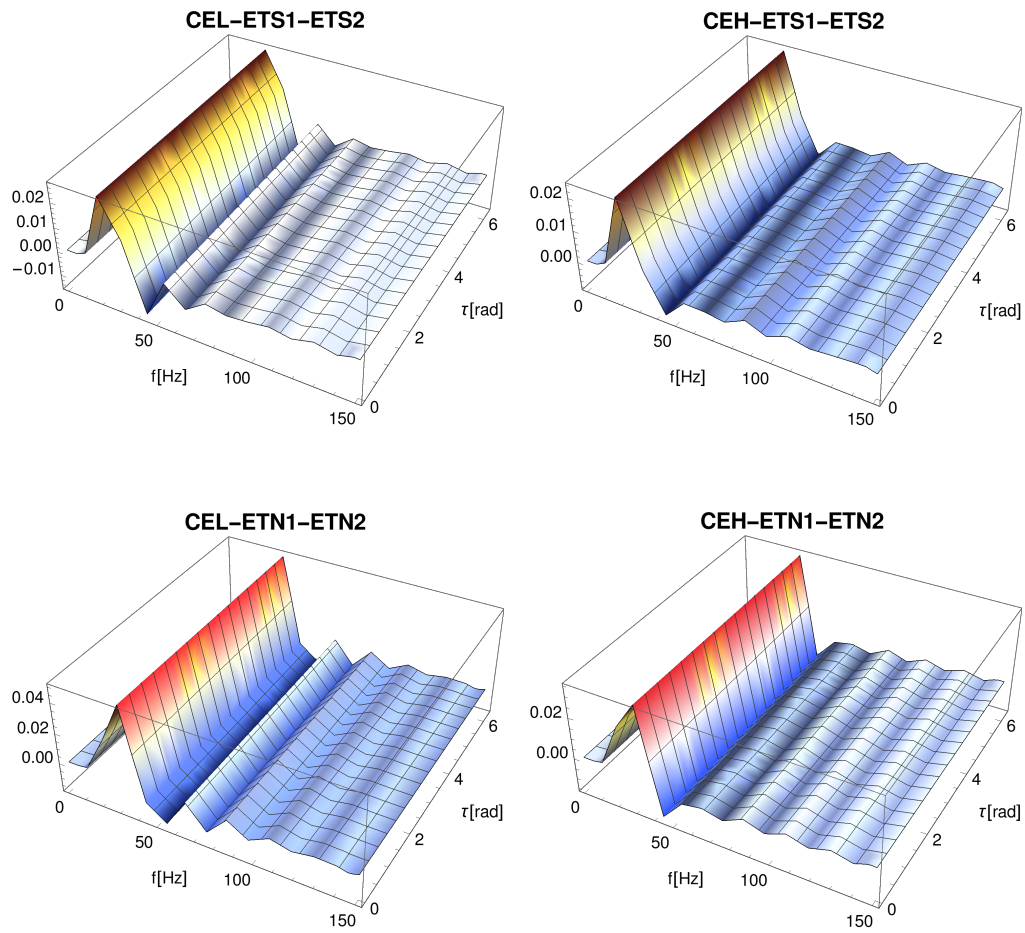
Figure 3.23: Correlation matrix determinant $det\Lambda(f,\tau)$ for all possible configurations involving ET and CE. Notice how it weakly depends on ET orientation angle.
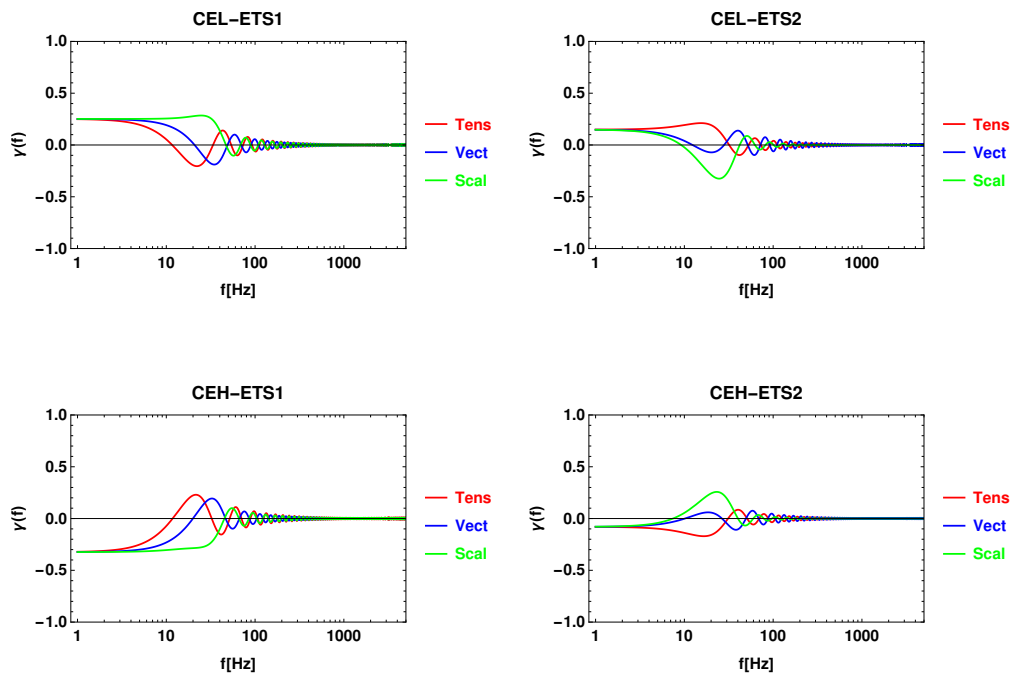
Figure 3.24: Overlap reduction functions of all possible configurations involving CEH(L) and ETS, with $\tau = \frac{\pi}{3}$.
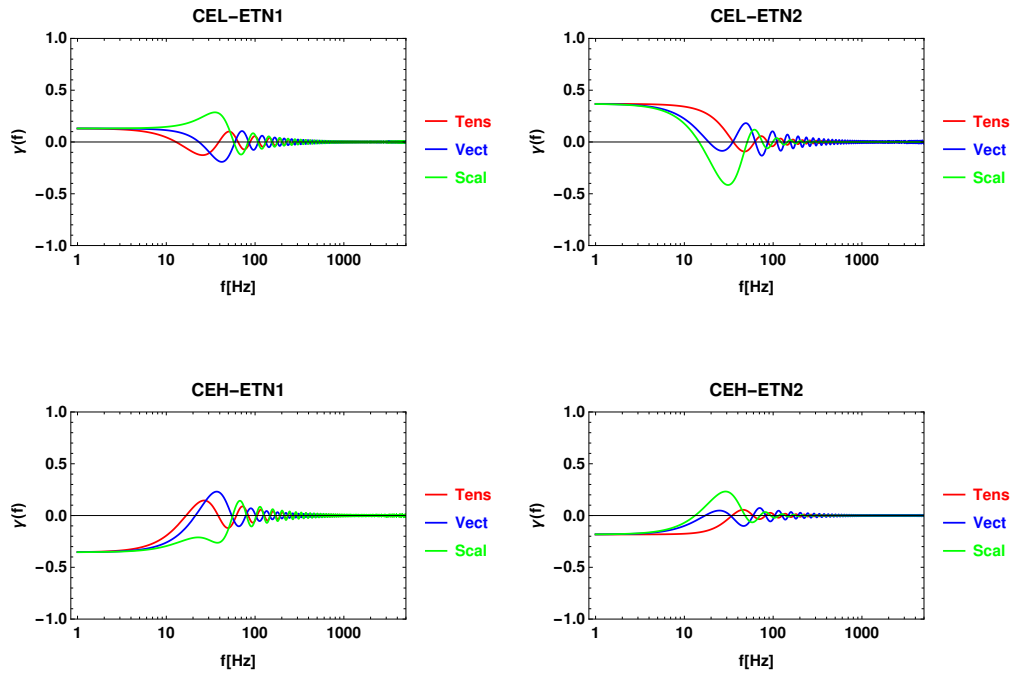
Figure 3.25: Overlap reduction functions of all possible configurations involving CEH(L) and ETN, with $\tau = \frac{\pi}{3}$.

3.6 Breaking Scalar Modes Degeneracy

While considering Eqs.(2.1.23) and (2.1.24) for L-shaped interferometers we underlined how breathing and longitudinal angular pattern functions differ from a constant factor, thus making scalar modes degenerate. Even considering V-shaped interferometers did not solve this issue. In this section we wish to show a possible way to break this degeneracy considering GW with high frequencies[10] to which upcoming ground-based detecors are expected to be sensitive. To this purpose, let us focus on the left panel of Fig.3.1: we consider the $(\hat{\mathbf{u}}, \hat{\mathbf{v}})$ plane where a generic V-shaped detector lies and we assume its bisector to form an angle of $\frac{\pi}{4}$ relative to the $\hat{\mathbf{u}}$ axis measured in a counterclockwise manner. This way we have that unit vectors along ech detector arm now are

$$\hat{\mathbf{e}}_1 = (\cos\left(\frac{\pi}{4} - \frac{\eta}{2}\right), \sin\left(\frac{\pi}{4} - \frac{\eta}{2}\right), 0), \qquad \hat{\mathbf{e}}_2 = (\cos\left(\frac{\pi}{4} + \frac{\eta}{2}\right), \sin\left(\frac{\pi}{4} + \frac{\eta}{2}\right), 0). \quad (3.6.1)$$

We choose this particular configuration in order to align the bisector of the V-shaped detector with the bisector of an hypothetical L-shaped interferometer with arms directed along $\hat{\mathbf{u}}$ and $\hat{\mathbf{v}}$: to only purpose of these assumptions is to make computations simpler. Since we are cosnidering high frequencies, the long wavelength limit is no longer valid, thus we get frequency-dependent angular pattern functions

$$F^b(f, \hat{\mathbf{\Omega}}) = D^{ij}\tilde{e}^b_{ij} = \frac{\mathcal{T}_1}{2}\left\{\cos^2(\frac{\pi}{4} - \frac{\eta}{2})(\sin^2\phi + \cos^2\phi\cos^2\theta) + \sin^2(\frac{\pi}{4} - \frac{\eta}{2})(\cos^2\phi + \sin^2\phi\cos^2\theta) + \right.$$
$$\left. - 2\sin\left(\frac{\pi}{4} - \frac{\eta}{2}\right)\cos\left(\frac{\pi}{4} - \frac{\eta}{2}\right)\sin^2\theta\sin\phi\cos\phi\right\} - \frac{\mathcal{T}_2}{2}\left\{\cos^2(\frac{\pi}{4} + \frac{\eta}{2})(\sin^2\phi + \cos^2\phi\cos^2\theta) + \right.$$
$$\left. + \sin^2(\frac{\pi}{4} + \frac{\eta}{2})(\cos^2\phi + \sin^2\phi\cos^2\theta) - 2\sin\left(\frac{\pi}{4} + \frac{\eta}{2}\right)\cos\left(\frac{\pi}{4} + \frac{\eta}{2}\right)\sin^2\theta\sin\phi\cos\phi\right\} =$$
$$= \frac{1}{4}(\mathcal{T}_1 - \mathcal{T}_2)(1 + \cos^2\theta) - \frac{1}{4}(\mathcal{T}_1 - \mathcal{T}_2)\sin^2\theta\sin 2\phi\cos\eta - \frac{1}{4}(\mathcal{T}_1 + \mathcal{T}_2)\sin^2\theta\cos 2\phi\sin\eta \quad ,$$
$$(3.6.2)$$

and

$$F^l(f, \hat{\mathbf{\Omega}}) = D^{ij}\tilde{e}^l_{ij} = \frac{\sqrt{2}\mathcal{T}_1}{2}\left\{\cos^2(\frac{\pi}{4} - \frac{\eta}{2})(\sin^2\theta\cos^2\phi) + \sin^2(\frac{\pi}{4} - \frac{\eta}{2})(\sin^2\theta\sin^2\phi) + \right.$$
$$\left. - 2\sin\left(\frac{\pi}{4} - \frac{\eta}{2}\right)\cos\left(\frac{\pi}{4} - \frac{\eta}{2}\right)\sin^2\theta\sin\phi\cos\phi\right\} - \frac{\sqrt{2}\mathcal{T}_2}{2}\left\{\cos^2(\frac{\pi}{4} + \frac{\eta}{2})(\sin^2\theta\cos^2\phi) + \right.$$
$$\left. + \sin^2(\frac{\pi}{4} + \frac{\eta}{2})(\sin^2\theta\sin^2\phi) + 2\sin\left(\frac{\pi}{4} + \frac{\eta}{2}\right)\cos\left(\frac{\pi}{4} + \frac{\eta}{2}\right)\sin^2\theta\sin\phi\cos\phi\right\} =$$
$$= \frac{\sqrt{2}}{4}(\mathcal{T}_1 - \mathcal{T}_2)(1 - \cos^2\theta) + \frac{\sqrt{2}}{4}(\mathcal{T}_1 - \mathcal{T}_2)\sin^2\theta\sin 2\phi\cos\eta + \frac{\sqrt{2}}{4}(\mathcal{T}_1 + \mathcal{T}_2)\sin^2\theta\cos 2\phi\sin\eta.$$
$$(3.6.3)$$

---

[10]In particular with $f \gtrsim f_*$

As a consistency check, if we assume $f \ll f_*$, then $\mathcal{T}_{1,2} \approx 1$ and if $\eta = \frac{\pi}{2}$ the angular pattern functions reduces to Eq. (2.1.23) and (2.1.24) respectively, while in general for $\eta \in (0, \frac{\pi}{2})$ the degeneracy cannot be broken by the interferometer opening angle choice. However, if GW frequencies approach or overcome the characteristic frequency f_*, the degeneracy is broken for every value of the angle η by the $(1 \pm \cos^2 \theta)$ factor. This can be better visualized with a concrete example using the Eart-based frame of reference introduced in Appendix C: we can consider a single Einstein Telescope detector (Sardinia site), with specific unit vectors directed along its arms given by $\hat{\mathbf{e}}_1 = (0.1644, -0.9864, 0.)$ and $\hat{\mathbf{e}}_2 = (0.6368, -0.4008, -0.6587))$, and the Cosmic Explorer replacing the LIGO Livingston observatory in both location and orientation. Both detectors are assumed to be Michelson interferometers, thus apart a frequency dependent coefficient given by Eq. (2.3.20), their transfer functions contain information relative to both detector geometry and GW direction. Finally in Fig. 3.26 and 3.27 we show the Mollweide projections of both detectors breathing and longitudinal angular pattern functions for three different GW frequency values in order to see how they behave for $f \ll f_*$, $f \approx f_*$ and $f \gg f_*$. Since 3rd-generation interferometers are expected to have longer arms (e.g. lower values of f_*) and to be sensitive to GW frequencies ranging from 1-10^4 Hz, the investigation of GWs whose frequencies are higher than f_* may be an achievable result and the degeneracy between scalar modes could be broken.
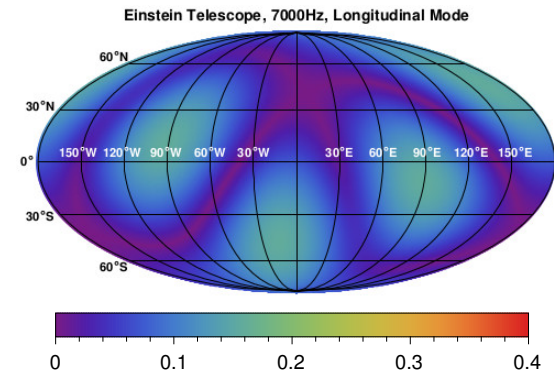
(a)

(b)

(c)

(d)

(e)

(f)
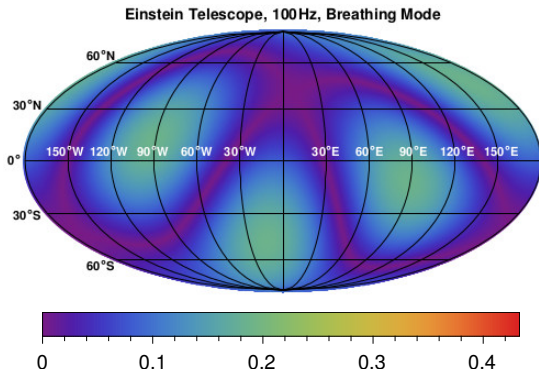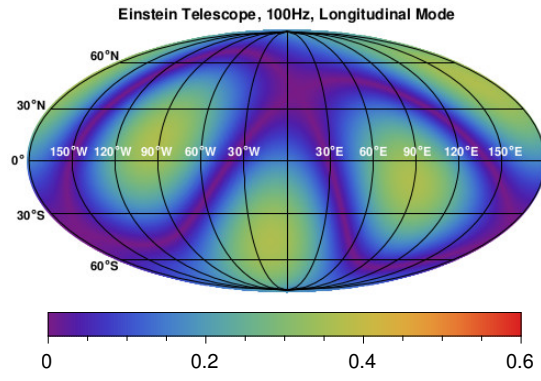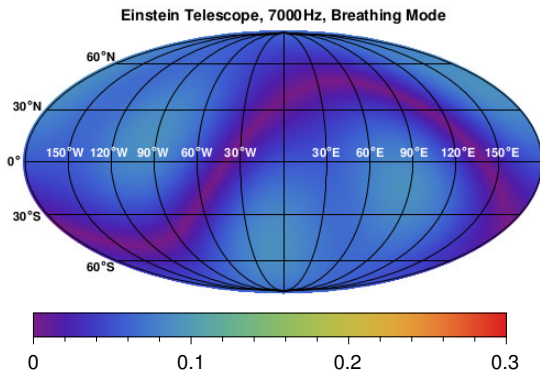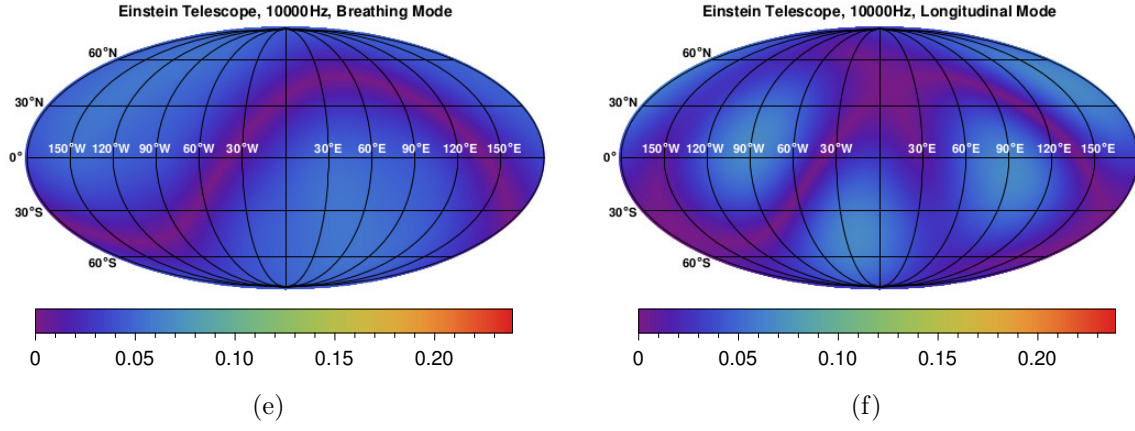
Figure 3.26: Mollweide projection of $|F^b(f, \hat{\boldsymbol{\Omega}})|$ (a), $c)$ and $e)$)and $|F^l(f, \hat{\boldsymbol{\Omega}})|$ (b), $d)$ and $f)$) for three different frequency values ($100Hz$, $7000Hz$ and $10000Hz$) using one ET Michélson interferometer. The initial intensity difference between breathing and longitudinal is due to the $\sqrt{2}$ factor that appears in the definition of F^l.

(a)

(b)
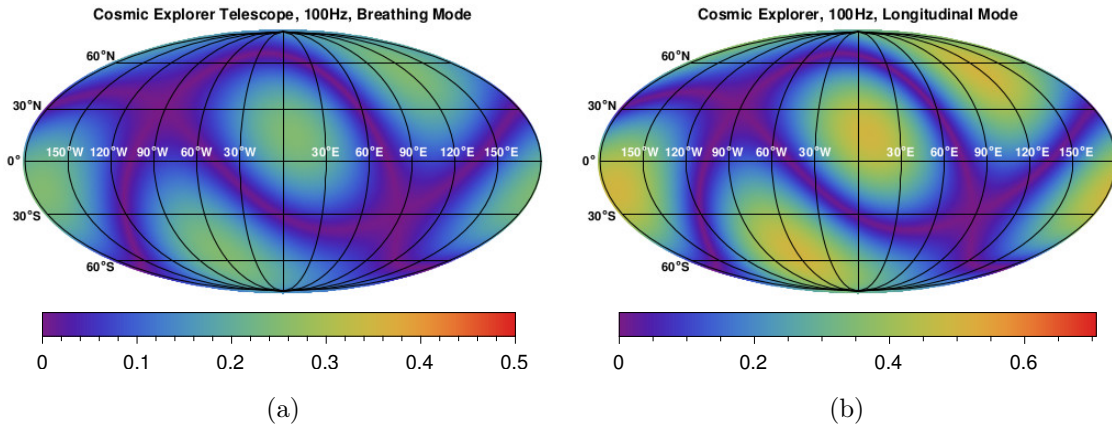
Figure 3.27: Mollweide projection of $|F^b(f,\hat{\boldsymbol{\Omega}})|$ (a), c) and e)) and $|F^l(f,\hat{\boldsymbol{\Omega}})|$ (b), d) and f)) for three different frequency values ($100Hz$, $1000Hz$ and $5000Hz$) using CE as a Michélson interferometer. The initial intensity difference between breathing and longitudinal is due to the $\sqrt{2}$ factor that appears in the definition of F^l.
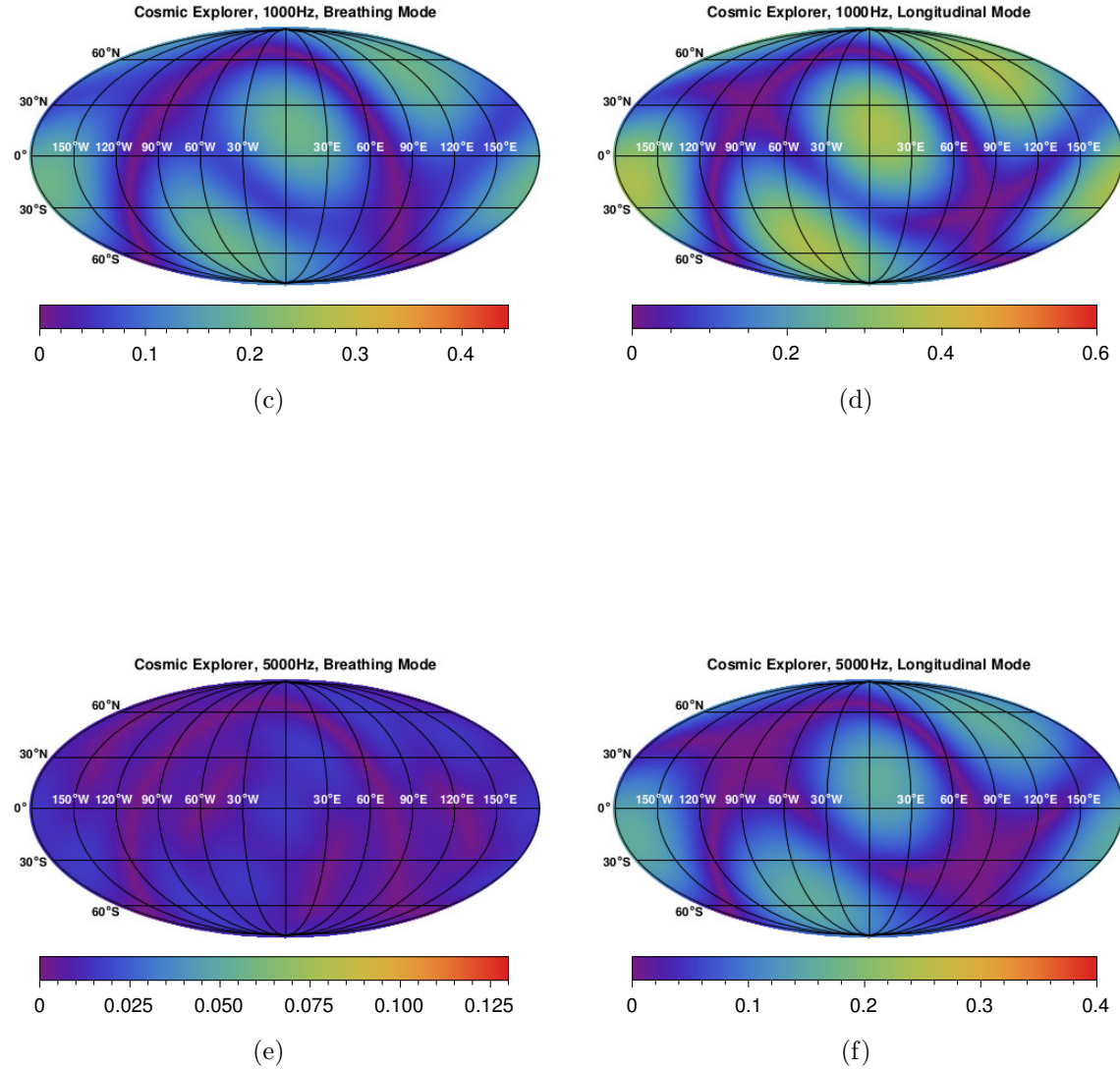
Conclusion

At the beginning of this thesis we stated that gravitational waves may represent a powerful tool to test General Relativity and at the same time to investigate proposed alternative metric theories of gravity. In particular, we focused on GW polarization modes: while GR only allows the presence of two independent tensor modes, different theories may predict also the existence of vector and scalar polarization modes, thus their detection might lead us to new physical considerations and results, causing an inevitable extension of Einstein's theory. In the context of Cosmological Stochastic Gravitational Wave Backgrounds, the detection of gravitational waves could provide us very interesting information on the status of the universe in its early phase and we showed how it is possible to distinguish between tensor, vector and scalar mode contributions to the background energy density, investigating interplays among present and future ground-based interferometers, such as the Einstein Telescope and the Cosmic Explorer.

In the context of 3rd-generation interferometers we initially discussed the proposed xylophone configuration for the Einstein Telescope, which consists of three V-shaped underground detectors displaced in a triangular way, each in turn composed of two interferometers adapted to different GW frequency ranges. Considering all three detectors, we investigated the network joint response to GWs for tensor, vector and scalar modes and we found that the Einstein Telescope maximum detection reach is overall enahanced with respect to 2nd-generation interferometers: in particular considering tensor modes ET has all-sky coverage, while in terms of vector and scalar modes only GWs coming from directions orthogonal to the detector plane cannot be detected. For sufficiently low frequencies joint responses present cylindrical symmetry with respect to the detector plane normal vector, although this simmetry is slightly broken for higher frequencies accounting for transfer function effects, which reduce ET sensitivity to GWs. We then considered how Earth rotation affects joint responses and we showed how this motion moves blind directions relative to scalar and vector joint responses and allows the detection of GWs coming from every direction along one day period.

We also considered the possibility of combining future ground-based detectors in order to

distinguish and compute the stochastic background energy density for tensor, vector and scalar modes. To separate each polarization mode contribution we need at least three interferometers, thus we began by considering the Einstein Telescope with its three detectors. Due to its geometrical configuration, we found that ET alone cannot separate polarization mode contributions to the SGWB, thus only two ET interferometers can be considered to work independently inside a network. We showed how this behaviour can be related to its proposed triangular configuration, independently of its possible locations on Earth. For this purpose, we investigated the network involving two Einstein Telescope detectors along with the Cosmic Explorer. We showed that it is possible to distinguish between tensor, vector and scalar mode energy density contributions roughly in the frequency range $10 - 100$ Hz and we found that the network sensitivity to the SGWB is overall improved by a factor of 10^{-3} with respect to 2nd-generation interferometers.

Although we mainly focus on a cosmological stochastic bacground of gravitational waves, upcoming ground-based and space-born detectors are expected to greatly improve our knowledge of both cosmology and relativistic astrophysics thanks to their higher sensitivities. Therefore we expect the following years to show us how gravitational waves are going to revolutionize our knowledge of the Universe.

A

Trigonometric identities

A.1 Sum and difference formulas for sine and cosine

$$
\begin{aligned}
\sin(\alpha + \beta) &= \sin\alpha\cos\beta + \cos\alpha\sin\beta, \\
\sin(\alpha - \beta) &= \sin\alpha\cos\beta - \cos\alpha\sin\beta, \\
\cos(\alpha + \beta) &= \cos\alpha\cos\beta - \sin\alpha\sin\beta, \\
\cos(\alpha - \beta) &= \cos\alpha\cos\beta + \sin\alpha\sin\beta.
\end{aligned}
\tag{A.1.1}
$$

A.2 Werner Formulas for sine and cosine

$$
\begin{aligned}
\sin\alpha\sin\beta &= \frac{1}{2}[\cos(\alpha - \beta) - \cos(\alpha + \beta)], \\
\cos\alpha\cos\beta &= \frac{1}{2}[\cos(\alpha - \beta) + \cos(\alpha + \beta)], \\
\sin\alpha\cos\beta &= \frac{1}{2}[\sin(\alpha - \beta) + \sin(\alpha + \beta)].
\end{aligned}
\tag{A.2.1}
$$

A.3 Double angle formulas for sine and cosine

$$
\begin{aligned}
\sin 2\alpha &= 2\sin\alpha\cos\alpha, \\
\cos 2\alpha &= \cos^2\alpha - \sin^2\alpha = 2\cos^2\alpha - 1 = 1 - \sin^2\alpha.
\end{aligned}
\tag{A.3.1}
$$

A.4   Half angle formulas for sine and cosine

$$\sin \frac{\alpha}{2} = \pm \sqrt{\frac{1 - \cos \alpha}{2}},$$
$$\cos \frac{\alpha}{2} = \pm \sqrt{\frac{1 + \cos \alpha}{2}}. \tag{A.4.1}$$

B

Spherical Bessel functions

B.1 Integral formulae

$$\int_{-1}^{+1} dx e^{i\alpha x} = 2j_0(\alpha),$$

$$\int_{-1}^{+1} dx e^{i\alpha x}(1 - x^2) = 4\frac{j_1(\alpha)}{\alpha},$$

$$\int_{-1}^{+1} dx e^{i\alpha x}(1 - x^2)^2 = 16\frac{j_2(\alpha)}{\alpha^2}. \tag{B.1.1}$$

B.2 Relations between Bessel functions

$$\frac{j_1(\alpha)}{\alpha} = \frac{1}{3}\big(j_0(\alpha) + j_2(\alpha)\big),$$

$$\frac{j_2(\alpha)}{\alpha^2} = \frac{1}{105}\big(7j_0(\alpha) + 10j_2(\alpha) + 3j_4(\alpha)\big). \tag{B.2.1}$$

Appendix C

Relative orientation and separation of two detectors on Earth

We take the Earth to be a perfect sphere of radius $R = 6.371 \cdot 10^3$ km. We consider a Cartesian coordinate system with the origin located at the center of the Earth, and with the z axis going in the direction of the North pole. The x axis goes in the direction of the point connecting the Earth Equator (latitude 0) and the Greenwich Meridian (longitude 0). The y axis is then determined by $\hat{\mathbf{e}}_{\mathbf{y}} = \hat{\mathbf{e}}_{\mathbf{z}} \times \hat{\mathbf{e}}_{\mathbf{x}}$ and is directed toward the point on the Equator at 90°E longitude. Let us then consider two detectors A and B and their positions described by the unit vectors

$$\hat{\mathbf{x}}_{\mathbf{A}} = \begin{pmatrix} a_1 \\ a_2 \\ a_3 \end{pmatrix}, \qquad \hat{\mathbf{x}}_{\mathbf{B}} = \begin{pmatrix} b_1 \\ b_2 \\ b_3 \end{pmatrix}. \tag{C.0.1}$$

Considering the great circumference of radius R wrapping the Earth and connecting A and B, we want to find the tangent vectors to the circumference itself in the detector positions: this way we are able to compute the angle that gives us the orientations σ_1 and σ_2 of the bisectors. We begin by finding the normal vector $\hat{\mathbf{q}}$ to the plane spanned by $\hat{\mathbf{x}}_{\mathbf{A}}$ and $\hat{\mathbf{x}}_{\mathbf{B}}$ and passing through the origin, we have

$$\hat{\mathbf{q}} = \hat{\mathbf{x}}_{\mathbf{A}} \times \hat{\mathbf{x}}_{\mathbf{B}} = \begin{pmatrix} q_1 \\ q_2 \\ q_3 \end{pmatrix}, \tag{C.0.2}$$

so the plane equation is

$$\pi_q : q_1 x + q_2 y + q_3 z = 0. \tag{C.0.3}$$

APPENDIX C. RELATIVE ORIENTATION AND SEPARATION OF TWO DETECTORS ON EARTH

We also need to find the planes tangent to the Earth in the detector positions, the normal vectors of which are given by $\hat{\mathbf{x}}_{\mathbf{A}}$ and $\hat{\mathbf{x}}_{\mathbf{B}}$. We can take the respective parallel planes passing through the origin, so the plane equations are

$$\pi_a : a_1 x + a_2 y + a_3 z = 0, \qquad \pi_b : b_1 x + b_2 y + b_3 z = 0. \qquad (\text{C.0.4})$$

Finally we can find the tangent vectors and their directions as the intersection between π_q and π_a or π_b considering the following systems

$$\begin{cases} q_1 x + q_2 y + q_3 z = 0 \\ a_1 x + a_2 y + a_3 z = 0 \end{cases} 0, \qquad \begin{cases} q_1 x + q_2 y + q_3 z = 0 \\ b_1 x + b_2 y + b_3 z = 0 \end{cases}. \qquad (\text{C.0.5})$$

We can choose to solve for x and then setting $x = 1$ we have

$$\bar{\mathbf{V}}_{\mathbf{A}} = \begin{pmatrix} 1 \\ -\frac{a_3 q_1 - a_1 q_3}{a_3 q_2 - a_2 q_3} \\ \frac{a_2 q_1 - a_1 q_2}{a_3 q_2 - a_2 q_3} \end{pmatrix}, \qquad \bar{\mathbf{V}}_{\mathbf{B}} = \begin{pmatrix} 1 \\ -\frac{b_3 q_1 - b_1 q_3}{b_3 q_2 - b_2 q_3} \\ \frac{b_2 q_1 - b_1 q_2}{b_3 q_2 - b_2 q_3} \end{pmatrix}, \qquad (\text{C.0.6})$$

and we can find the tangent unit vectors

$$\hat{\mathbf{v}}_{\mathbf{A}} = \frac{\overline{\mathbf{V}}_{\mathbf{A}}}{||\overline{\mathbf{V}}_{\mathbf{A}}||}, \qquad \hat{\mathbf{v}}_{\mathbf{B}} = \frac{\overline{\mathbf{V}}_{\mathbf{B}}}{||\overline{\mathbf{V}}_{\mathbf{B}}||}. \qquad (\text{C.0.7})$$

We still have to choose a convention to select the orientations: we move along the great circumference in counterclockwise manner starting from its intersection with the Greenwich meridian and so we fix the orientation of the tangent vectors $\hat{\mathbf{v}}_{\mathbf{A}}$ and $\hat{\mathbf{v}}_{\mathbf{B}}$.

Bibliography

[1] Abbott, Benjamin P., et al. "Observation of gravitational waves from a binary black hole merger." Physical review letters 116.6 (2016): 061102.

[2] Abbott, Benjamin P., et al. "GW151226: observation of gravitational waves from a 22-solar-mass binary black hole coalescence." Physical review letters 116.24 (2016): 241103.

[3] Scientific, L. I. G. O., et al. "GW170104: observation of a 50-solar-mass binary black hole coalescence at redshift 0.2." Physical Review Letters 118.22 (2017): 221101.

[4] Abbott, Benjamin P., et al. "GW170814: a three-detector observation of gravitational waves from a binary black hole coalescence." Physical review letters 119.14 (2017): 141101.

[5] Abbott, Benjamin P., et al. "GW170817: observation of gravitational waves from a binary neutron star inspiral." Physical Review Letters 119.16 (2017): 161101.

[6] Abbott, Benjamin P., et al. "Gravitational waves and gamma-rays from a binary neutron star merger: GW170817 and GRB 170817A." The Astrophysical Journal Letters 848.2 (2017): L13.

[7] Abbott, Benjamin P., et al. "Search for tensor, vector, and scalar polarizations in the stochastic gravitational-wave background." Physical review letters 120.20 (2018): 201102.

[8] Aasi, Junaid, et al. "Advanced ligo." Classical and quantum gravity 32.7 (2015): 074001.

[9] Harry, Gregory M., and LIGO Scientific Collaboration. "Advanced LIGO: the next generation of gravitational wave detectors." Classical and Quantum Gravity 27.8 (2010): 084006.

[10] Acernese, F., et al. "Advanced Virgo: a second-generation interferometric gravitational wave detector." Classical and Quantum Gravity 32.2 (2014): 024001.

[11] Somiya, Kentaro. "Detector configuration of KAGRA–the Japanese cryogenic gravitational-wave detector." Classical and Quantum Gravity 29.12 (2012): 124007.

[12] Amaro-Seoane, Pau, et al. "Laser interferometer space antenna." arXiv preprint arXiv:1702.00786 (2017).

[13] Barausse, Enrico, et al. "Prospects for Fundamental Physics with LISA." arXiv preprint arXiv:2001.09793 (2020).

[14] Punturo, M., et al. "The Einstein Telescope: a third-generation gravitational wave observatory." Classical and Quantum Gravity 27.19 (2010): 194002.

[15] Maggiore, Michele, et al. "Science case for the Einstein telescope." Journal of Cosmology and Astroparticle Physics 2020.03 (2020): 050.

[16] Cimatti, Andrea, et al. "SPACE: the spectroscopic all-sky cosmic explorer." Experimental Astronomy 23.1 (2009): 39-66.

[17] Durrer, R. (2008). The cosmic microwave background (Vol. 401). Cambridge: Cambridge University Press.

[18] Eardley, Douglas M., David L. Lee, and Alan P. Lightman. "Gravitational-wave observations as a tool for testing relativistic gravity." Physical Review D 8.10 (1973): 3308.

[19] Guzzetti, M. C., Bartolo, N., Liguori, M., Matarrese, S. (2016). Gravitational waves from inflation. arXiv preprint arXiv:1605.01615.

[20] Horowitz, Gary T. "Semiclassical relativity: The weak-field limit." Physical Review D 21.6 (1980): 1445.

[21] Shapiro, Irwin I. "Fourth test of general relativity." Physical Review Letters 13.26 (1964): 789.

[22] Everitt, CW Francis, et al. "Gravity probe B: final results of a space experiment to test general relativity." Physical Review Letters 106.22 (2011): 221101.

[23] Abbott, Benjamin P., et al. "Tests of general relativity with GW150914." arXiv preprint arXiv:1602.03841 (2016).

[24] Abbott, B. P., et al. "Tests of general relativity with GW170817." Physical review letters 123.1 (2019): 011102.

[25] Easther, Richard, John T. Giblin Jr, and Eugene A. Lim. "Gravitational wave production at the end of inflation." Physical review letters 99.22 (2007): 221301.

[26] Cook, Jessica L., and Lorenzo Sorbo. "Particle production during inflation and gravitational waves detectable by ground-based interferometers." Physical Review D 85.2 (2012): 023534.

[27] Lopez, Alejandro, and Katherine Freese. "First test of high frequency Gravity Waves from inflation using Advanced LIGO." Journal of Cosmology and Astroparticle Physics 2015.01 (2015): 037.

[28] Ölmez, S., Vuk Mandic, and X. Siemens. "Gravitational-wave stochastic background from kinks and cusps on cosmic strings." Physical Review D 81.10 (2010): 104028.

[29] Aasi, J., et al. "Constraints on cosmic strings from the LIGO-Virgo gravitational-wave detectors." Physical Review Letters 112.13 (2014): 131101.

[30] Caprini, Chiara, Ruth Durrer, and Géraldine Servant. "Gravitational wave generation from bubble collisions in first-order phase transitions: An analytic approach." Physical Review D 77.12 (2008): 124015.

[31] Caprini, Chiara, Ruth Durrer, and Géraldine Servant. "The stochastic gravitational wave background from turbulence and magnetic fields generated by a first-order phase transition." Journal of Cosmology and Astroparticle Physics 2009.12 (2009): 024.

[32] Petersen, Karl E. Ergodic theory. Vol. 2. Cambridge University Press, 1989.

[33] Bartolo, N., et al. "Anisotropies and non-Gaussianity of the cosmological gravitational wave background." Physical Review D 100.12 (2019): 121501.

[34] Rosado, Pablo A. "Gravitational wave background from binary systems." Physical Review D 84.8 (2011): 084004.

[35] Zhu, Xing-Jiang, et al. "Stochastic gravitational wave background from coalescing binary black holes." The Astrophysical Journal 739.2 (2011): 86.

[36] Abbott, Benjamin P., et al. "GW170817: implications for the stochastic gravitational-wave background from compact binary coalescences." Physical review letters 120.9 (2018): 091101.

[37] Buonanno, Alessandra, et al. "Stochastic gravitational-wave background from cosmological supernovae." Physical Review D 72.8 (2005): 084001.

[38] Zhu, Xing-Jiang, Eric Howell, and David Blair. "Observational upper limits on the gravitational wave production of core collapse supernovae." Monthly Notices of the Royal Astronomical Society: Letters 409.1 (2010): L132-L136.

[39] Rosado, Pablo A. "Gravitational wave background from rotating neutron stars." Physical Review D 86.10 (2012): 104007.

[40] Talukder, Dipongkar, et al. "Measuring neutron-star ellipticity with measurements of the stochastic gravitational-wave background." Physical Review D 89.12 (2014): 123008.

[41] Newman, Ezra, and Roger Penrose. "An approach to gravitational radiation by a method of spin coefficients." Journal of Mathematical Physics 3.3 (1962): 566-578.

[42] Alves, Marcio ES, Oswaldo D. Miranda, and Jose CN de Araujo. "Extra polarization states of cosmological gravitational waves in alternative theories of gravity." Classical and Quantum Gravity 27.14 (2010): 145010.

[43] Allen, Bruce, and Joseph D. Romano. "Detecting a stochastic background of gravitational radiation: Signal processing strategies and sensitivities." Physical Review D 59.10 (1999): 102001.

[44] Will, Clifford M. Theory and experiment in gravitational physics. Cambridge university press, 2018.

[45] Zee, Anthony. Einstein gravity in a nutshell. Vol. 14. Princeton University Press, 2013.

[46] Carroll, Sean M. "An introduction to general relativity." Spacetime and Geometry. Addison Wesley (2004).

[47] Wald, Robert M. General relativity. University of Chicago press, 2010.

[48] Fujii, Yasunori, and Kei-ichi Maeda. The scalar-tensor theory of gravitation. Cambridge University Press, 2003.

[49] Sen, D. K., and K. A. Dunn. "A scalar-tensor theory of gravitation in a modified Riemannian manifold." Journal of Mathematical Physics 12.4 (1971): 578-586.

[50] Dale, Roberto, and Diego Sáez. "On the viability of a certain vector-tensor theory of gravitation." Astrophysics and Space Science 337.1 (2012): 439-453.

[51] Dale, Roberto, and Diego Sáez. "Cosmology in a certain vector-tensor theory of gravitation." Physical Review D 89.4 (2014): 044035.

[52] Brans, Carl, and Robert H. Dicke. "Mach's principle and a relativistic theory of gravitation." Physical review 124.3 (1961): 925.

[53] Svidzinsky, Anatoly A. "Vector theory of gravity: Universe without black holes and solution of dark energy problem." Physica Scripta 92.12 (2017): 125001.

[54] Jacobson, Ted. "Extended Hořava gravity and Einstein-aether theory." Physical Review D 81.10 (2010): 101502.

[55] Gong, Yungui, and Shaoqi Hou. "The polarizations of gravitational waves." Universe 4.8 (2018): 85.

[56] Hou, Shaoqi, Yungui Gong, and Yunqi Liu. "Polarizations of gravitational waves in Horndeski theory." The European Physical Journal C 78.5 (2018): 378.

[57] Wagle, Pratik, Alexander Saffer, and Nicolás Yunes. "Polarization modes of gravitational waves in quadratic gravity." Physical Review D 100.12 (2019): 124007.

[58] Yagi, Kent, Nicolas Yunes, and Takahiro Tanaka. "Gravitational Waves from Quasicircular Black-Hole Binaries in Dynamical Chern-Simons Gravity." Physical review letters 109.25 (2012): 251105.

[59] Blázquez-Salcedo, Jose Luis, et al. "Perturbed black holes in Einstein-dilaton-Gauss-Bonnet gravity: Stability, ringdown, and gravitational-wave emission." Physical Review D 94.10 (2016): 104024.

[60] Ananda, Kishore N., S. Carloni, and P. K. S. Dunsby. "Evolution of cosmological gravitational waves in f (R) gravity." Physical Review D 77.2 (2008): 024033.

[61] Berry, Christopher PL, and Jonathan R. Gair. "Linearized f (R) gravity: gravitational radiation and solar system tests." Physical Review D 83.10 (2011): 104022.

[62] Bartolo, Nicola, et al. "Science with the space-based interferometer LISA. IV: Probing inflation with gravitational waves." Journal of Cosmology and Astroparticle Physics 2016.12 (2016): 026.

[63] Bartolo, Nicola, et al. "Probing non-Gaussian stochastic gravitational wave backgrounds with LISA." Journal of Cosmology and Astroparticle Physics 2018.11 (2018): 034.

[64] Bartolo, N., et al. "Testing primordial black holes as dark matter through LISA." arXiv preprint arXiv:1810.12224 (2018).

[65] Bartolo, N., et al. "Primordial black hole dark matter: LISA serendipity." Physical review letters 122.21 (2019): 211301.

[66] Bartolo, Nicola, et al. "Characterizing the Cosmological Gravitational Wave Background Anisotropies and non-Gaussianity." arXiv preprint arXiv:1912.09433 (2019).

[67] Bartolo, N., et al. "Gravitational wave anisotropies from primordial black holes." Journal of Cosmology and Astroparticle Physics 2020.02 (2020): 028.

[68] Alba, Vasyl, and Juan Maldacena. "Primordial gravity wave background anisotropies." Journal of High Energy Physics 2016.3 (2016): 115.

[69] Dodelson, Scott. Modern cosmology. Elsevier, 2003.

[70] Polchinski, Joseph. String theory: Volume 1, an introduction to the bosonic string. Cambridge university press, 1998.

[71] Polchinski, Joseph. String theory: Volume 2, superstring theory and beyond. Cambridge university press, 1998.

[72] Maggiore, M. (2008). Gravitational waves: Volume 1: Theory and experiments (Vol. 1). Oxford university press.

[73] Maggiore, M. (2018). Gravitational Waves: Astrophysics and Cosmology (Vol. 2). Oxford University Press.

[74] Lawrence, M. J., et al. "Dynamic response of a Fabry–Perot interferometer." JOSA B 16.4 (1999): 523-532.

[75] https://www.ligo.org/scientists/GW100916/GW100916-geometry.html

[76] Akutsu, T., et al. "Construction of KAGRA: an underground gravitational-wave observatory." Progress of Theoretical and Experimental Physics 2018.1 (2018): 013F01.

[77] Thrane, Eric, and Joseph D. Romano. "Sensitivity curves for searches for gravitational-wave backgrounds." Physical Review D 88.12 (2013): 124032.

[78] Aghanim, N., et al. "Planck 2018 results. VI. Cosmological parameters." arXiv preprint arXiv:1807.06209 (2018).

[79] https://dcc.ligo.org/LIGO-T1800042/public

[80] https://gwdoc.icrr.u-tokyo.ac.jp/cgi-bin/DocDB/ShowDocument?docid=9537

[81] http://www.et-gw.eu/index.php/etsensitivities

[82] http://www.et-gw.eu/index.php/etdsdocument

[83] Regimbau, Tania, et al. "Mock data challenge for the einstein gravitational-wave telescope." Physical Review D 86.12 (2012): 122001.

[84] https://www.einsteintelescope.nl/en/

[85] https://dcc.ligo.org/LIGO-P1600143/public

[86] Nishizawa, Atsushi, et al. "Probing nontensorial polarizations of stochastic gravitational-wave backgrounds with ground-based laser interferometers." Physical Review D 79.8 (2009): 082002.

[87] Estabrook, Frank B., and Hugo D. Wahlquist. "Response of Doppler spacecraft tracking to gravitational radiation." General Relativity and Gravitation 6.5 (1975): 439-447.

[88] Romano, Joseph D., and Neil J. Cornish. "Detection methods for stochastic gravitational-wave backgrounds: a unified treatment." Living reviews in relativity 20.1 (2017): 2.

[89] Rakhmanov, M., J. D. Romano, and John T. Whelan. "High-frequency corrections to the detector response and their effect on searches for gravitational waves." Classical and Quantum Gravity 25.18 (2008): 184017.

[90] Schilling, R. (1997). Angular and frequency response of LISA. Classical and Quantum Gravity, 14(6), 1513.